frontiers | Research Topics

Molecular and cellular mechanisms of synaptopathies: Emerging synaptic aging-related molecular pathways in neurological disorders, 2nd Edition

Edited by
Carlos Cruchaga, Laura Ibanez, Dario Maschi and Ramiro Quintá

Published in
Frontiers in Aging Neuroscience

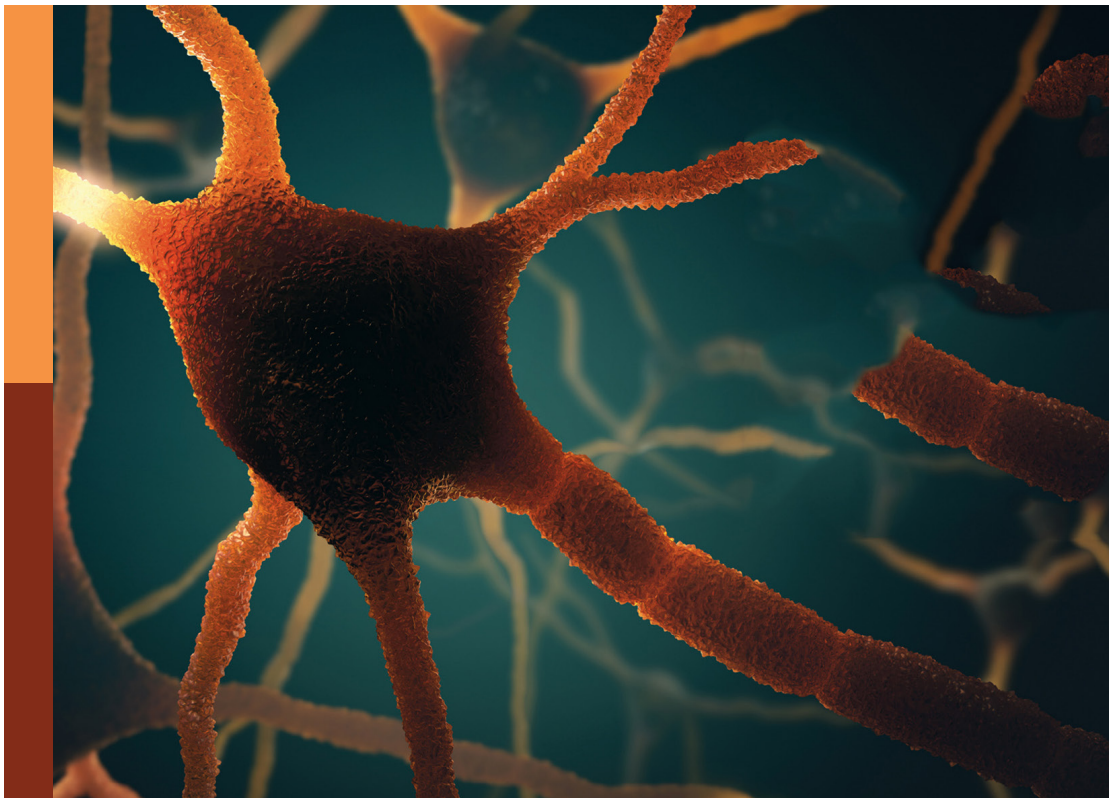

ISSN 1664-8714
ISBN 978-2-8325-4229-3
DOI 10.3389/978-2-8325-4229-3

About Frontiers

Frontiers is more than just an open access publisher of scholarly articles: it is a pioneering approach to the world of academia, radically improving the way scholarly research is managed. The grand vision of Frontiers is a world where all people have an equal opportunity to seek, share and generate knowledge. Frontiers provides immediate and permanent online open access to all its publications, but this alone is not enough to realize our grand goals.

Frontiers journal series

The Frontiers journal series is a multi-tier and interdisciplinary set of open-access, online journals, promising a paradigm shift from the current review, selection and dissemination processes in academic publishing. All Frontiers journals are driven by researchers for researchers; therefore, they constitute a service to the scholarly community. At the same time, the *Frontiers journal series* operates on a revolutionary invention, the tiered publishing system, initially addressing specific communities of scholars, and gradually climbing up to broader public understanding, thus serving the interests of the lay society, too.

Dedication to quality

Each Frontiers article is a landmark of the highest quality, thanks to genuinely collaborative interactions between authors and review editors, who include some of the world's best academicians. Research must be certified by peers before entering a stream of knowledge that may eventually reach the public - and shape society; therefore, Frontiers only applies the most rigorous and unbiased reviews. Frontiers revolutionizes research publishing by freely delivering the most outstanding research, evaluated with no bias from both the academic and social point of view. By applying the most advanced information technologies, Frontiers is catapulting scholarly publishing into a new generation.

What are Frontiers Research Topics?

Frontiers Research Topics are very popular trademarks of the *Frontiers journals series*: they are collections of at least ten articles, all centered on a particular subject. With their unique mix of varied contributions from Original Research to Review Articles, Frontiers Research Topics unify the most influential researchers, the latest key findings and historical advances in a hot research area.

Find out more on how to host your own Frontiers Research Topic or contribute to one as an author by contacting the Frontiers editorial office: frontiersin.org/about/contact

Molecular and cellular mechanisms of synaptopathies: Emerging synaptic aging-related molecular pathways in neurological disorders, 2nd Edition

Topic editors

Carlos Cruchaga — Washington University in St. Louis, United States
Laura Ibanez — Washington University in St. Louis, United States
Dario Maschi — Washington University in St. Louis, United States
Ramiro Quintá — National Scientific and Technical Research Council (CONICET), Argentina

Citation

Cruchaga, C., Ibanez, L., Maschi, D., Quintá, R., eds. (2023). *Molecular and cellular mechanisms of synaptopathies: Emerging synaptic aging-related molecular pathways in neurological disorders, 2nd Edition*. Lausanne: Frontiers Media SA. doi: 10.3389/978-2-8325-4229-3

Publisher's note: This is a 2nd edition due to an article retraction.

Table of contents

frontiers | Frontiers in Aging Neuroscience

TYPE Editorial
PUBLISHED 10 August 2023
DOI 10.3389/fnagi.2023.1267033

OPEN ACCESS

EDITED AND REVIEWED BY
Jorge Busciglio,
University of California, Irvine, United States

*CORRESPONDENCE
Dario Maschi
✉ dario.maschi@wustl.edu

RECEIVED 25 July 2023
ACCEPTED 27 July 2023
PUBLISHED 10 August 2023

CITATION
Quintá HR, Ibanez L, Cruchaga C and Maschi D (2023) Editorial: Molecular and cellular mechanisms of synaptopathies: emerging synaptic aging-related molecular pathways in neurological disorders.
Front. Aging Neurosci. 15:1267033.
doi: 10.3389/fnagi.2023.1267033

Editorial: Molecular and cellular mechanisms of synaptopathies: emerging synaptic aging-related molecular pathways in neurological disorders

Hector Ramiro Quintá[1,2,3], Laura Ibanez[4,5,6], Carlos Cruchaga[5,6,7] and Dario Maschi[8]*

[1]National Scientific and Technical Research Council (CONICET), Buenos Aires, Argentina, [2]Laboratorio de Medicina Experimental "Dr. J. Toblli", Hospital Aleman, Buenos Aires, Argentina, [3]Rehabilitation Medicine Department, University of Minnesota Twin Cities, St. Paul, MN, United States, [4]Department of Neurology, School of Medicine, Washington University in St. Louis, St. Louis, MO, United States, [5]Department of Psychiatry, School of Medicine, Washington University in St. Louis, St. Louis, MO, United States, [6]NeuroGenomics and Informatics Center, Washington University School of Medicine, St. Louis, MO, United States, [7]Hope Center for Neurological Disorders, School of Medicine, Washington University in St. Louis, St. Louis, MO, United States, [8]Department of Cell Biology and Physiology, School of Medicine, Washington University in St. Louis, St. Louis, MO, United States

KEYWORDS

neurodegenerative diseases, synaptopathies, synaptic aging, Alzheimer's disease, biomarkers, therapeutic targets

Editorial on the Research Topic
Molecular and cellular mechanisms of synaptopathies: emerging synaptic aging-related molecular pathways in neurological disorders

Despite the enormous advances made in our understanding of neurological disorders, a knowledge gap still exists that prevents the scientific community from linking clinical manifestations with actual cellular neuropathological changes. This connection is especially crucial for pathologies like Alzheimer's disease (AD), which has a 10–20 year preclinical period offering an extended window for potential interventions (McKhann et al., 1984; Sperling et al., 2011). However, the preclinical period has been challenging to explore due to the lack of specific prognostic and predictive biomarkers.

To identify disease progression biomarkers, we must diligently explore and identify new causal genes and pathways associated with the disease. Furthermore, by understanding these pathologies' mechanistic, we will speed up the development of new disease-modifying therapies. Future advances in this endeavor will necessitate the collaborative efforts of researchers from diverse backgrounds. This diversity is reflected in our editorial panel and among the contributors to this topic. Our Frontiers Research Topic, entitled "*Molecular and cellular mechanisms of synaptopathies: emerging synaptic aging-related molecular pathways in neurological disorders*", comprises original research articles from experts in the neuroscience field. These experts explore novel brain disease-related pathways that could serve as potential therapeutic targets. The number and originality of these contributions highlight the interest and ongoing activity in this area of investigation.

Among the promising new pharmacological discoveries, Bellanti et al. highlights the therapeutic potential of ultramicronized palmitoylethanolamide (um-PEA) in AD. Chronic

um-PEA treatment improved mitochondrial function and restored energy metabolism in the frontal cortex of mice, suggesting um-PEA treatment as a potential novel strategy for future clinical treatment of AD due to its bioenergetic effects.

Nan et al. offer valuable insights regarding the intersection of metabolic disorders and neurodegenerative diseases. Increasing evidence points toward a potential connection between diabetes and AD. Diabetes can lead to cognitive impairment and brain changes such as altered synaptic plasticity, aggregated amyloid-beta (Aβ) plaques, and neurofibrillary tangles composed of hyperphosphorylated tau protein. Given the demographic trend toward global aging and that the incidence of diabetes has been steadily rising, the significance of their research is clear. They examine the pathogenesis of post-menopausal diabetic encephalopathy and propose Forsythoside·B as an effective a therapeutic agent.

Expanding our understanding of the role of age in cognitive health, Li et al. present a novel research perspective on the impact of young plasma on anesthesia and surgery-induced cognitive impairment in aged rats. Their study reveals a compelling connection between young plasma preinfusion and a reduction in such cognitive impairments. Thus, young plasma emerges as a potential therapeutic strategy to mitigate cognitive dysfunction linked to surgery and anesthesia in the aged population.

A remarkable example of a promising study that uncovers new treatment possibilities for neurodegenerative pathologies is the work of León et al.. They explore the potential of c-Abl tyrosine kinase as a therapeutic target in AD pathogenesis. In previous work, Dr. Alvarez, the lead author, had collaborated with Dr. Marugan from the National Center for Advancing Translational Sciences (NCATS) to develop neurotinib, a novel c-Abl inhibitor capable of crossing the blood-brain barrier. Here, they demonstrate that down-regulating c-Abl leads to improved cognitive performance and reduced neuropathological symptoms in AD mouse models, marking neurotinib as a promising candidate for AD therapy.

Delving into the intricate mechanisms behind protein misfolding, Cazzaro et al. contribute significantly to our understanding of the disease propagation in AD. They study the mechanisms that govern the secretion of small extracellular vesicles containing misfolded proteins. Their findings reveal that Slingshot Homolog-1 augments this secretion, suggesting a promising approach to promoting the degradation of misfolded proteins and curbing the spread of intercellular pathology.

In an effort to understand how AD pathology affects neuronal activity, Martinsson et al. have shown that elevated levels of Aβ and its precursor protein, the amyloid precursor protein (APP), induce increased neuronal activity in AD. Specifically, they found impaired adaptation of calcium transients to global activity changes and observed that neurons failed to adjust the length of their axon initial segments, which typically affects excitability. They hypothesize that the close localization of APP and Aβ near synapses may play a vital role in the altered synaptic responses. These insights point to potential treatment strategies focusing on early Aβ/APP-induced hyperexcitability and synapse dysfunction.

Underscoring the importance of synaptic health in neurodegenerative disease, Olajide et al. show that amyloid beta peptide 1–42 causes significant mitochondrial dysfunction at glutamatergic synapses, leading to rapid synapse alterations, reduced energy production efficiency, and a significant reduction in key mitochondrial and synaptic protein expression. Notably, they show that lowering reactive oxygen species prevents synaptic impairments. This implies that therapies targeting reactive oxygen species might help curb the advancement of neurodegeneration in chronic models of AD.

Zhang et al. shift our attention to the protective potential of naturally occurring compounds in neurodegenerative diseases. They show that polyphenols in oolong tea have neuroprotective and anti-aging activities, nominating them as potential therapeutic agents for age-related neurodegenerative diseases.

Pursuing further insights into the role of protein aggregates, Ferrari et al. shed light on the impact of soluble α-synuclein oligomers in Parkinson's disease, finding that these oligomers play a central role in the early events leading to synaptic loss. This discovery could offer new avenues for early detection and potential therapeutic interventions, underscoring the importance of comprehending the role of these oligomers in the onset of Parkinson's disease and related disorders.

As we conclude this brief overview of the featured articles in our Research Topics, we want to draw attention to the work by Carbonell et al.. They used quantitative mass spectrometry to compare hippocampal synaptic proteomes across different Autism Spectrum Disorder (ASD) mouse models, identifying shared alterations in cellular and molecular pathways at the synapse. These results suggest that diverse ASD-related genes may converge on shared synaptic signaling pathways, paving the way for a better understanding of the pathogenesis of not just ASD but also other neuropathologies.

Addressing neurodegenerative diseases remains a critical challenge of our era, further intensified by an aging population, increasing disease prevalence, and lack of disease-modifying therapies and good biomarkers. Vital to mitigating these conditions is strategically targeting the early stages of disease progression to prevent irreversible neuronal loss and increase therapeutic effectiveness. However, this is often hindered by the fact that their symptoms frequently remain undetected until the later stages, and our knowledge of the molecular events that initiate these diseases is still limited. Despite these difficulties, the innovative approaches and unwavering commitment demonstrated by the researchers contributing to this topic reflect the ongoing strides made to unravel these diseases' complexities and propose out-of-the-box therapeutic targets advancing the field toward personalized medicine. As we continue to gain novel insights and explore new pathways, we are confident in our collective ability to advance our understanding and ultimately turn the tide against neurodegenerative diseases.

Author contributions

HRQ: Writing—original draft, Writing—review and editing. LI: Writing—original draft, Writing—review and editing. CC: Writing—original draft, Writing—review and

editing. DM: Writing—original draft, Writing—review and editing.

Conflict of interest

The authors declare that the research was conducted in the absence of any commercial or financial relationships that could be construed as a potential conflict of interest.

Publisher's note

References

McKhann, G., Drachman, D., Folstein, M., Katzman, R., Price, D., and Stadlan, E. M. (1984). Clinical diagnosis of Alzheimer's disease: report of the NINCDS-ADRDA Work Group under the auspices of Department of Health and Human Services Task Force on Alzheimer's Disease. *Neurology.* 34, 939–944. doi: 10.1212/wnl.34.7.939

Sperling, R A., Aisen, P. S., Beckett, L. A., Bennett, D. A., Craft, S., Fagan, A. M., et al. (2011). Toward defining the preclinical stages of Alzheimer's disease: recommendations from the National Institute on Aging-Alzheimer's Association workgroups on diagnostic guidelines for Alzheimer's disease. *Alzheimers Dement.* 7, 280–292. doi: 10.1016/j.jalz.2011.03.003

frontiers | Frontiers in Aging Neuroscience

ORIGINAL RESEARCH
published: 24 May 2022
doi: 10.3389/fnagi.2022.890855

Effects of Ultramicronized Palmitoylethanolamide on Mitochondrial Bioenergetics, Cerebral Metabolism, and Glutamatergic Transmission: An Integrated Approach in a Triple Transgenic Mouse Model of Alzheimer's Disease

*Francesco Bellanti[1†], Vidyasagar Naik Bukke[1†], Archana Moola[1], Rosanna Villani[1], Caterina Scuderi[2], Luca Steardo[2], Gianmauro Palombelli[3], Rossella Canese[4], Sarah Beggiato[4], Mario Altamura[5], Gianluigi Vendemiale[1], Gaetano Serviddio[1] and Tommaso Cassano[1]**

[1] Department of Medical and Surgical Sciences, University of Foggia, Foggia, Italy, [2] Department of Physiology and Pharmacology "V. Erspamer", Sapienza University of Rome, Rome, Italy, [3] MRI Unit Core Facilities, Istituto Superiore di Sanità, Rome, Italy, [4] Department of Life Sciences and Biotechnology, University of Ferrara, Ferrara, Italy, [5] Department of Clinical and Experimental Medicine, University of Foggia, Foggia, Italy

The therapeutic potential of ultramicronized palmitoylethanolamide (um-PEA) was investigated in young (6-month-old) and adult (12-month-old) 3×Tg-AD mice, which received um-PEA for 3 months *via* a subcutaneous delivery system. Mitochondrial bioenergetics, ATP homeostasis, and magnetic resonance imaging/magnetic resonance spectroscopy were evaluated in the frontal cortex (FC) and hippocampus (HIPP) at the end of um-PEA treatment. Glutamate release was investigated by *in vivo* microdialysis in the ventral HIPP (vHIPP). We demonstrated that chronic um-PEA treatment ameliorates the decrease in the complex-I respiration rate and the FoF1-ATPase (complex V) activity, as well as ATP content depletion in the cortical mitochondria. Otherwise, the impairment in mitochondrial bioenergetics and the release of glutamate after depolarization was not ameliorated by um-PEA treatment in the HIPP of both young and adult 3×Tg-AD mice. Moreover, progressive age- and pathology-related changes were observed in the cortical and hippocampal metabolism that closely mimic the alterations observed in the human AD brain; these metabolic alterations were not affected by chronic um-PEA treatment. These findings confirm that the HIPP is the most affected area by AD-like pathology and demonstrate that um-PEA counteracts mitochondrial dysfunctions and helps rescue brain energy metabolism in the FC, but not in the HIPP.

Keywords: glutamate, mitochondria, hippocampus, frontal cortex, microdialysis, Alzheimer's disease

OPEN ACCESS

Edited by:
Ashok K. Shetty, Texas A&M University College of Medicine, United States

Reviewed by:
Sandra Milena Sanabria Barrera, Fundación Cardiovascular de Colombia, Colombia
Silvia Lores Arnaiz, University of Buenos Aires, Argentina

***Correspondence:**
Tommaso Cassano
tommaso.cassano@unifg.it

[†] These authors have contributed equally to this work

Specialty section:
This article was submitted to Alzheimer's Disease and Related Dementias, a section of the journal Frontiers in Aging Neuroscience

Received: *06 March 2022*
Accepted: *19 April 2022*
Published: *24 May 2022*

Citation:
Bellanti F, Bukke VN, Moola A, Villani R, Scuderi C, Steardo L, Palombelli G, Canese R, Beggiato S, Altamura M, Vendemiale G, Serviddio G and Cassano T (2022) Effects of Ultramicronized Palmitoylethanolamide on Mitochondrial Bioenergetics, Cerebral Metabolism, and Glutamatergic Transmission: An Integrated Approach in a Triple Transgenic Mouse Model of Alzheimer's Disease. Front. Aging Neurosci. 14:890855. doi: 10.3389/fnagi.2022.890855

INTRODUCTION

Alzheimer's disease (AD) is a consequence of several detrimental processes, such as protein aggregation, oxidative stress, mitochondrial malfunction, and neuroinflammation, finally resulting in the loss of neuronal functions (Blass and Gibson, 1991; Sullivan and Brown, 2005; Yao et al., 2009; Querfurth and Laferla, 2010; Serviddio et al., 2011; Cassano et al., 2016, 2019; Carapelle et al., 2020). Starting from this evidence, multitarget drugs have been increasingly sought after over the last decades (Barone et al., 2019; Cassano et al., 2019). In this regard, palmitoylethanolamide (PEA) seems to exert neuroprotective effects by modulating more therapeutic targets at the same time (Valenza et al., 2021). In fact, it has been demonstrated that PEA, the naturally occurring amide of ethanolamine and palmitic acid, is an endogenous lipid that exerts its beneficial effects through the peroxisome proliferator-activated receptors (PPARs) involvement, transient receptor potential vanilloid type 1 channel, orphan G-protein-coupled receptor 55, and the so-called entourage effect on the endocannabinoid system (Devchand et al., 1996; Delerive et al., 2001; LoVerme et al., 2005, 2006; Scuderi et al., 2011; Tomasini et al., 2015; Bronzuoli et al., 2019; Beggiato et al., 2020a,b). In addition to its known anti-inflammatory activity, PEA protects cultured mouse cerebellar granule cells from glutamate toxicity and reduces histamine-induced cell death in hippocampal cultures (Skaper et al., 1996).

Furthermore, it has been demonstrated that PEA exerts *in vitro* and *in vivo* a combination of neuroprotective and anti-inflammatory effects in amyloid-β (Aβ)-induced toxicity by interacting at the PPAR-α nuclear site (D'Agostino et al., 2012; Scuderi et al., 2012, 2014). The neuroprotective action of PEA has been established also in transgenic animal models of AD (D'Agostino et al., 2012; Bronzuoli et al., 2018; Scuderi et al., 2018). In fact, we have previously demonstrated that ultramicronized PEA (um-PEA), a formulation endowed with better bioavailability, can rescue learning and memory impairments in a triple transgenic mouse model of AD (3×Tg-AD) by exerting anti-inflammatory properties, dampening reactive astrogliosis, and promoting the glial neurosupportive function. Moreover, um-PEA strongly suppresses Aβ(1–42) expression and reduces the abnormal phosphorylation of tau in 3×Tg-AD mice (Scuderi et al., 2018).

Mitochondrial dysfunctions are related to inflammation and other energy-dependent disturbances, where the generation of reactive oxygen species (ROS) exceeds the physiological antioxidant activity, causing cellular oxidative damage (Lin and Beal, 2006; Reddy, 2009; Romano et al., 2017). Mitochondrial dysfunction can lead to glutamatergic neurotransmission alterations (Vos et al., 2010) and excitotoxicity (Schinder et al., 1996). In fact, excessive glutamate concentration can cause excitotoxicity, leading to calcium influx, mitochondrial dysfunction, and subsequent cell death (Mahmoud et al., 2019). Therefore, considering the tight link between mitochondria and glutamate, it could be crucial to investigate their alterations in the context of AD pathology.

In the last decade, neuroimaging has been used to complement clinical assessments in the early detection of AD, showing that morphological change (such as measurement of the hippocampal volume) might be an important hallmark for the diagnosis of AD. More recently, the development of magnetic resonance spectroscopy (MRS) in the field of AD revealed that tremendous metabolic changes occur during the progression of AD correlating with cognitive abnormalities (Meyerhoff et al., 1994; Shonk et al., 1995; Frederick et al., 1997; Rose et al., 1999; Kantarci et al., 2000; Huang et al., 2001). Nevertheless, few studies with relatively small sample sizes investigated MR spectral profile alteration as a biomarker for treatment response in AD, and some of them correlated this alteration with psychiatric symptoms in patients with AD (Sweet et al., 2002; Bartha et al., 2008). Although metabolite abnormalities in AD were demonstrated in different samples and pathologically confirmed cases, the pathological significance of these changes is not fully understood. Therefore, in our study, we exploited the availability of the MRS to investigate whether it can provide complementary predictive information regarding (i) progression of the AD-like pathology and (ii) um-PEA treatment effects.

In this article, we used the 3×Tg-AD mice harboring three mutant human genes (betaAPPSwe, PS1M146V, and tauP301L) to directly test the hypothesis that (i) progressive accumulation of Aβ is closely related to mitochondrial, metabolic, and glutamatergic alterations, and (ii) chronic um-PEA administration may ameliorate such alterations. To test these hypotheses, we used an integrated approach, based on *ex vivo* studies of several mitochondrial bioenergetic parameters, *in vivo* studies of magnetic resonance imaging (MRI) and spectroscopy (MRS) to evaluate brain metabolites, as well as neurochemical analysis of extracellular levels of glutamate by microdialysis in 3×Tg-AD vs. non-Tg control mice tested at two different stages (mild and severe) of AD-like pathology and subcutaneously treated for 3 months with um-PEA.

MATERIALS AND METHODS

Animals and Treatment

A total of 3×Tg-AD male mice and their sex- and age-matched wild-type littermates (non-Tg) (C57BL6/129SvJ) were maintained in controlled conditions (12 h light/12 h dark cycle, temperature 22°C, humidity 50–60%, fresh food, and water *ad libitum*). All procedures were conducted in accordance with the guidelines of the Italian Ministry of Health (D.L. 26/2014) and the European Parliamentary directive 2010/63/EU. All efforts were made to minimize the number of animals used and their suffering. In addition, 3- and 9-month-old mice were subcutaneously implanted with a 90-day-release pellet containing either 28 mg of um-PEA (Innovative Research of America, Sarasota, Florida; cat# NX-999) or vehicle (cat# NC-111), as previously described (Scuderi et al., 2018). Briefly, an um-PEA or a vehicle pellet was surgically positioned in a subcutaneous pocket created with a blunt probe between the shoulder blades. um-PEA (EPT2110/1) was obtained from the Epitech group (Saccolongo, Italy), and both dosage and administration routes were chosen according to previous data (Costa et al., 2002;

Grillo et al., 2013; Scuderi et al., 2018). Both non-Tg and 3×Tg-AD mice were randomly assigned to either vehicle or um-PEA group. At the end of the 90-day treatment, mitochondrial bioenergetics, MRI/MRS experiments, and microdialysis/high-performance liquid chromatography (HPLC) analysis were performed as previously described (Cassano et al., 2012; Scuderi et al., 2018).

Mitochondrial Bioenergetics and ATP Homeostasis

On the day of the experiment, 6- and 12-month-old mice were decapitated and brains were rapidly removed and placed on a cold surface to dissect the hippocampus (HIPP), frontal cortex (FC), and cerebellum (Cassano et al., 2012). Experiments were conducted on four samples per group per each brain area. To obtain an optimal sample amount, tissues from three animals were pooled (a total of 12 mice per group). Mitochondria were freshly isolated by using a gradient of Percoll, as previously described (Cassano et al., 2012). Briefly, brain areas were weighted (100 mg) and immersed in ice-cold mitochondrial isolation buffer (MIB) containing 0.25 M sucrose, 0.5 mM K-EDTA, and 10 mM Tris–HCl (pH 7.4). Each sample was homogenized in 3.8 ml of 12% Percoll in MIB (5% w/v) using Dounce homogenizers with glass pestles. In addition, 3 ml of homogenate was then layered onto a previously poured, 3.5 ml 26% Percoll, on 3.5 ml 40% Percoll density gradient. The gradient was centrifuged at 19,000 rpm (30,000 × *g*) in a Sorval RC-5B type rotor for 5 min. The resulting top layer containing myelin and other cellular debris was carefully removed using a Pasteur pipette and discarded. Fraction 2 containing the mitochondria was removed by pipetting with a 200 ml gel loading tip and diluted 1:4 in cold MIB and centrifuged at 14,000 (15,000 × *g*) rpm for 10 min. The resulting pellet was then resuspended in 1 ml of MIB and centrifuged at 14,000 rpm (15,000 × *g*) for 5 min. The final pellet was resuspended in 100 ml of MIB containing 10% 10 mg/ml bovine serum albumin. After isolation, mitochondria were assayed for oxygen consumption at 37°C in a thermostatically controlled oxygraph apparatus equipped with Clark's electrode and a rapid mixing device (Hansatech Instruments, Ltd., Norfolk, England, UK). Mitochondrial respiration was triggered by glutamate and malate as complex I-linked substrates, or succinate (in the presence of rotenone as complex I inhibitor) as complex II-linked substrate. Oxygen uptake in states 3 and 4 and respiratory control index (RCI) was calculated as previously reported (Cassano et al., 2012). Respiratory activity was calculated as oxygen nmol per minute per mg of protein.

The F_OF_1-ATPase activity was measured following ATP hydrolysis with an ATP-regenerating system coupled to nicotinamide adenine dinucleotide phosphate (NADPH) oxidation, as previously reported (Cassano et al., 2012).

Measurement of ATP concentration in the total homogenates and mitochondrial fractions from brain areas was performed by using a commercial bioluminescent assay kit (Sigma-Aldrich, St. Louis, MO, USA).

Magnetic Resonance Imaging and Spectroscopy

The 6- and 12-month-old mice (n = 5–7) underwent MRI/MRS scanning to evaluate genotype- and treatment-induced differences in brain metabolites of FC and HIPP. MRI/MRS analyses were conducted at 4.7 T on a Varian/Agilent Inova horizontal bore system (Agilent, Palo Alto, USA) using a combination of volume and surface coil (RAPID Biomedical, Rimpar, Germany) according to a protocol described in Scuderi et al. (2018). Briefly, mice were anesthetized with isoflurane (IsoFlo, Abbott SpA, Berkshire, UK) 1.5–2.5% in O_2 1 L/min. Anatomical T2-weighted sagittal MRIs were acquired for the positioning of the voxels for MRS. Localized 1H-MRS (PRESS TR/TE = 4,000/23 ms) were collected from HIPP and FC (volume 9.5 and 9.1 μl, respectively) as shown in **Figure 4A**, according to a quantitative protocol (Canese et al., 2012).

The following six metabolites were considered: *N*-acetyl-aspartate (NAA), myo-inositol (mINS), the sum of creatine and phosphocreatine (Cr + PCr), glutamate (Glu), glutamine (Gln), and total choline (tCho). Metabolite concentrations are expressed in mmol/L (mM). Moreover, we evaluated the NAA/Cr ratio and mINS/Cr.

In vivo Microdialysis and HPLC Analysis

In vivo microdialysis was performed in awake, freely moving mice, as previously described (Cassano et al., 2012; Romano et al., 2014). Briefly, 6- and 12-month-old anesthetized mice (n = 5–6) were stereotaxically implanted with a CMA/7 guide cannula with a stylet (CMA Microdialysis, Stockholm, Sweden) into the vHIPP (anterior-posterior, −3.0 mm; lateral, +3.0 mm; ventral, −1.8 mm from bregma, **Figure 5A**), according to the stereotaxis atlas of Franklin and Paxinos (Franklin and Paxinos, 1997). Following a 2-day recovery period, the CMA/7 probe (6-kDa cutoff; 2 mm membrane length) was inserted and dialyses were carried out, in awake, freely moving mice, perfusing each probe with Krebs-Ringer phosphate (KRP) buffer at a flow rate of 1 μl/min. The constituents of the KRP buffer were (in mM) NaCl 145, KCl 2.7, $MgCl_2$ 1, $CaCl_2$ 2.4, and Na_2HPO_4 2, buffered at pH 7.4. After a 2-h stabilization period, four baseline samples were collected every 20 min. Thereafter, the probes were perfused for 20 min with KCl (50 mM)-enriched KRP buffer, and then six samples were further collected with the previous KRP buffer. After completion of the microdialysis, the probe position was verified histologically, glutamate was quantified by HPLC coupled to fluorescence detection as previously described (Tomasini et al., 2002; Beggiato et al., 2020a,b).

Statistical Analysis

The sample size was determined based on our previous experiments and using the free software G*Power version 3.1.9.2. All data are expressed as mean ± standard error of the mean (SEM). Within-group variability was analyzed through the Levene test for homogeneity of variances.

Data from mitochondrial bioenergetics and MRI/MRS scanning were analyzed using a 2-way analysis of variance (ANOVA) with genotype and treatment as the between variables.

Dunnett's and Tukey's *post-hoc* tests were used where appropriate to perform multiple comparisons.

Regarding the microdialysis data, the overall basal glutamate levels were calculated as marginal means of the first five dialysate samples (from time −80 up to time 0) and were analyzed by two-way ANOVA with genotype and treatment as the between variables. The neurotransmitter release in response to depolarization (K^+-stimulation) (from time 0 up to time 140) was analyzed using three-way ANOVA for repeated measures with genotype (3×Tg-AD vs. non-Tg) and treatment (um-PEA vs. vehicle) as the between variable and time as the within the variable. Dunnett's and Tukey's *post-hoc* tests were used where appropriate to perform multiple comparisons.

The threshold for statistical significance was set at $p < 0.05$. The SPSS Statistics version 19 (IBM, Armonk, NY, USA) and GraphPad Prism 6 for Windows (GraphPad Software Inc., San Diego, CA, USA) were used to perform all the statistical analyses and represent graph data, respectively.

RESULTS

Mitochondrial Respiration Activity Is Altered in Aged 3×Tg-AD Mice: Effects of Chronic um-PEA Treatment

Oxygen consumption was detected in mitochondria freshly isolated from FC and HIPP of 6- and 12-month-old non-Tg and 3×Tg-AD mice chronically treated with either vehicle or um-PEA. Statistical analyses are shown in **Tables 1**, **2**.

In 6-month-old mice, no significant difference was observed among experimental groups within the different brain regions (**Figures 1A,C**). Otherwise, when the NADH-generating substrates glutamate and malate were added to the mitochondrial preparations, a lower respiration activity in state 3 was detected in the FC of vehicle-treated 12-month-old 3×Tg-AD compared to non-Tg mice (**Figure 1B**), whereas a significant increase in both state 4 and state 3 was detected in the HIPP compared to non-Tg mice (**Figure 1D**). The ratio between state 3 and state 4, named RCI, was decreased in the FC of vehicle-treated 3×Tg-AD compared to non-Tg mice (**Figure 1B**), whereas it was unaffected in the HIPP of both genotypes, regardless of treatment (**Figure 1D**). um-PEA treatment significantly increased the state 3 respiration activity and the RCI in the FC of 3×Tg-AD mice compared to the respective vehicle (**Figure 1B**).

The analysis of complex II respiration, using succinate as a substrate in the presence of rotenone, revealed that cortical (**Figure 1B**) and hippocampal (**Figure 1D**) mitochondria were unaffected by both genotype and treatment.

Finally, neither genotype nor treatment affected the respiration activity of the cerebellum when its mitochondria were incubated with either the complex I-linked substrates or complex II-linked substrates (data not shown).

Chronic um-PEA Treatment Rescues the Impaired ATP Homeostasis in the Frontal Cortex of 3×Tg-AD Mice

To investigate the effects of chronic um-PEA treatment on ATP homeostasis, F_oF_1-ATPase (complex V) activity, ADP/O ratio (which expresses the coupling between the phosphorylation activity and mitochondrial respiration), and ATP content were measured in both non-Tg and 3×Tg-AD mice at two progressive stages of the disease (6 and 12 months of age).

Both the F_oF_1-ATPase activity and the ADP/O ratio were unaffected in mitochondria from FC (**Figures 2A,E**) and HIPP (**Figures 2C,G**) of both non-Tg and 3×Tg-AD mice at 6 months of age. Different results were obtained for F_oF_1-ATPase activity and ADP/O ratio in the presence of glutamate-malate at 12 months of age, where a significant effect of genotype ($F_{(1,12)} = 15.59$, $p < 0.01$; $F_{(1,12)} = 7.98$, $p < 0.05$, respectively) and treatment ($F_{(1,12)} = 5.728$, $p < 0.05$; $F_{(1,12)} = 4.956$, $p < 0.05$, respectively) was observed in the FC (**Figures 2B,F**). Multiple *post-hoc* comparison showed a significantly lower F_oF_1-ATPase activity and ADP/O ratio for vehicle-treated 3×Tg-AD mice compared to non-Tg mice that was counteracted by um-PEA treatment (**Figures 2B,F**). Regarding the HIPP, statistical analysis revealed only a significant main effect of genotype ($F_{(1,12)} = 6.001$, $p < 0.05$; $F_{(1,12)} = 4.914$, $p < 0.05$, respectively) (**Figures 2D,H**).

To further evaluate the effects of chronic treatment on ATP homeostasis, we measured ATP levels in tissue homogenates and mitochondrial fractions from both brain regions. Statistical analysis showed a significant main effect of genotype [6 months: ($F_{(1,12)} = 9.738$, $p < 0.01$); 12 months: ($F_{(1,12)} = 34.61$, $p < 0.001$)] and treatment [6 months: ($F_{(1,12)} = 5.372$, $p < 0.05$); 12 months: ($F_{(1,12)} = 6.152$, $p < 0.001$] in the FC at both ages (**Figures 3A,B,E,F**). In particular, multiple *post-hoc* comparison showed a significant lower ATP content for vehicle-treated 3×Tg-AD mice compared to non-Tg mice that was counteracted by um-PEA treatment (**Figures 3A,B,E,F**).

Regarding the ATP content in the HIPP, no difference was observed at 6 months of age, whereas a significant main effect of genotype ($F_{(1,12)} = 33.11$, $p < 0.001$) was observed at 12 months of age (**Figures 3C,D,G,H**).

MRI/MRS Study Shows Metabolic Changes in the Frontal Cortex and Hippocampus of 3×Tg-AD Mice

Magnetic resonance imaging/spectroscopy was used to assess metabolic profiles of treated vs. untreated mice at 6 and 12 months of age. The quantitative results of all metabolite concentrations from FC and HIPP are reported in **Figure 4**. In the FC, two-way ANOVA analysis revealed no significant differences among groups in the NAA levels at both ages, whereas in the HIPP a main effect of genotype was observed at 6 ($F_{(1,19)} = 10.098$, $p < 0.01$) and 12 months ($F_{(1,22)} = 5.820$, $p < 0.05$).

Statistical analysis for mINS showed a significant main effect of genotype in the FC at 6 months of age ($F_{(1,19)} = 22.072$, $p < 0.01$), whereas a significant main effect of treatment and genotype-by-treatment interaction effect was found at 12 months of age [($F_{\text{treatment}(1,25)} = 5.040$, $p < 0.05$); ($F_{\text{genotype}\times\text{treatment}(1,25)} = 5.286$, $p < 0.05$)]. *Post-hoc* comparisons showed a significantly higher mINS level in the um-PEA-treated compared to vehicle-treated 3×Tg-AD mice. Hippocampal mINS levels showed no significant differences among groups at 6 months, whereas a

TABLE 1 | Statistical analyses of respiratory activity in mitochondria isolated from the frontal cortex.

			Non-Tg + veh	Non-Tg + um-PEA	3×Tg-AD + veh	3×Tg-AD + um-PEA	$F_{(1,12)}$ G	$F_{(1,12)}$ T	$F_{(1,12)}$ G × T	
6-month-old	Complex I	State 4	3.02 ± 1.46	3.21 ± 1.55	3.03 ± 1.49	3.73 ± 2.43	0.089	0.250	0.082	
		State 3	8.54 ± 4.42	9.04 ± 3.91	8.75 ± 4.39	9.62 ± 4.92	0.032	0.096	0.007	
		RCI	2.96 ± 0.82	3.10 ± 0.74	3.04 ± 0.69	2.88 ± 0.80	0.033	0.001	0.154	
	Complex II	State 4	8.81 ± 6.27	8.41 ± 4.10	8.06 ± 5.25	7.26 ± 4.32	0.141	0.056	0.006	
		State 3	27.0 ± 17.1	24.9 ± 12.6	23.4 ± 14.7	22.3 ± 13.1	0.183	0.049	0.005	
		RCI	3.16 ± 0.30	3.09 ± 0.91	2.98 ± 0.20	3.09 ± 0.19	0.130	0.006	0.130	
12-month-old	Complex I	State 4	2.83 ± 1.08	2.91 ± 0.85	3.59 ± 2.80	3.28 ± 1.87	0.386	0.016	0.046	
		State 3	7.21 ± 1.73	7.16 ± 1.94	**4.20 ± 1.15↓**	**8.48 ± 2.53↑**	0.789	**4.943***	**5.179***	
		RCI	2.48 ± 0.50	2.61 ± 0.49	**1.80 ± 0.23↓**	2.78 ± 0.51	4.125	**11.36****	**7.782***	
	Complex II	State 4	9.01 ± 3.39	9.55 ± 2.18	9.82 ± 6.67	9.15 ± 3.57	0.009	0.001	0.080	
		State 3	25.9 ± 13.5	26.1 ± 10.9	21.4 ± 6.85	25.7 ± 12.4	0.191	0.161	0.134	
		RCI	2.73 ± 0.52	2.80 ± 0.74	2.62 ± 0.89	2.72 ± 0.35	0.083	0.067	0.002	

*Data are expressed as mean ± SEM of four experiments. Statistical differences were assessed by two-way ANOVA. Tukey's post-hoc test was used where appropriate to perform multiple comparisons. State 4 and state 3 are expressed as nmolO_2/min/mg protein. *$p < 0.05$; **$p < 0.01$; ↑$p < 0.05$ vs. 3xTg-AD + P; ↓$p < 0.05$ vs. other study groups.*
RCI, respiratory control index; Veh, vehicle; umPEA, ultramicronized palmitoylethanolamide. Bold values are statistical significance.

TABLE 2 | Statistical analyses of respiratory activity in mitochondria isolated from the hippocampus.

			Non-Tg + veh	Non-Tg + um-PEA	3×Tg-AD + veh	3×Tg-AD + um-PEA	$F_{(1,12)}$ G	$F_{(1,12)}$ T	$F_{(1,12)}$ G × T	
6-month-old	Complex I	State 4	4.94 ± 2.26	4.82 ± 1.79	5.50 ± 0.97	2.54 ± 1.08	1.136	3.642	3.096	
		State 3	10.7 ± 3.22	9.94 ± 4.12	9.84 ± 3.62	6.17 ± 1.69	1.980	1.813	0.782	
		RCI	2.33 ± 0.61	2.29 ± 0.77	1.78 ± 0.46	2.70 ± 1.03	0.035	1.384	1.648	
	Complex II	State 4	9.45 ± 4.92	8.57 ± 5.18	9.16 ± 6.03	7.15 ± 4.09	0.112	0.321	0.049	
		State 3	27.3 ± 20.0	25.9 ± 10.7	21.7 ± 12.3	21.5 ± 12.4	0.488	0.012	0.007	
		RCI	2.66 ± 0.80	3.05 ± 0.49	2.47 ± 0.32	2.99 ± 0.05	0.254	3.363	0.069	
12-month-old	Complex I	State 4	2.00 ± 0.79	2.31 ± 0.12	4.74 ± 1.40	5.62 ± 2.38	**8.457***	1.590	0.817	
		State 3	7.03 ± 2.35	7.44 ± 1.05	11.5 ± 4.41	12.3 ± 3.77	**5.539***	0.390	0.154	
		RCI	3.57 ± 0.28	2.98 ± 0.79	2.98 ± 0.84	2.39 ± 0.83	2.656	2.656	0.000	
	Complex II	State 4	9.42 ± 6.60	10.9 ± 3.17	11.6 ± 4.07	12.4 ± 0.42	0.770	0.256	0.026	
		State 3	23.7 ± 12.9	25.1 ± 8.95	23.9 ± 3.06	30.0 ± 6.18	0.353	0.764	0.300	
		RCI	2.71 ± 0.50	2.68 ± 0.61	2.22 ± 0.72	2.42 ± 0.42	1.709	0.088	0.161	

*Data are expressed as mean ± SEM of four experiments. Statistical differences were assessed by two-way ANOVA. Tukey's post-hoc test was used where appropriate to perform multiple comparisons. State 4 and state 3 are expressed as nmolO_2/min/mg protein. *$p < 0.05$.*
RCI, respiratory control index; Veh, vehicle; Um-PEA, ultramicronized palmitoylethanolamide. Bold values are statistical significance.

significant main effect of genotype was observed at 12 months of age ($F_{(1,23)} = 6.502$, $p < 0.05$).

Regarding the sum of creatine and phosphocreatine (Cr + PCr), named total creatine (tCr), two-way ANOVA analysis revealed in the FC a significant main effect of genotype at 6 months of age ($F_{(1,20)} = 5.616$, $p < 0.05$), whereas a significant main effect of treatment was observed at 12 months ($F_{(1,25)} = 28.220$, $p < 0.01$). *Post-hoc* comparisons within genotype showed that um-PEA treatment induced a significant increase in tCr levels compared to the vehicle-treated group. Moreover, hippocampal tCr levels showed no significant differences among groups at 6 months, whereas a significant main effect of genotype was observed at 12 months of age ($F_{(1,20)} = 5.843$, $p < 0.01$).

Statistical analysis for NAA/tCr ratio revealed a significant main effect of genotype at both ages in the FC [6 months: ($F_{(1,19)} = 9.525$, $p < 0.01$); 12 months: ($F_{(1,25)} = 9.111$, $p < 0.01$)], as well as in the HIPP [6 months: ($F_{(1,19)} = 22.910$, $p < 0.01$); 12 months: ($F_{(1,18)} = 5.101$, $p < 0.05$)]. Regarding the mINS/tCr ratio, two-way ANOVA analysis showed a significant main effect of genotype at both ages in the FC [6 months: ($F_{(1,17)} = 18.179$, $p < 0.05$); 12 months: ($F_{(1,21)} = 10.820$, $p < 0.01$)], as well as at 12 months of age in the HIPP ($F_{(1,18)} = 9.217$, $p < 0.01$), whereas no significant differences among groups were found at 6 months in the HIPP.

Statistical analysis for tCho showed no significant differences among groups in the cortical levels at both ages, whereas in the HIPP a main effect of genotype was observed at 6 ($F_{(1,19)} = 14.329$, $p < 0.01$) and 12 months of age ($F_{(1,24)} = 6.007$, $p < 0.05$).

Glu concentrations showed no differences among groups at both ages in the FC, as well as at 6 months in the HIPP; a significant main effect of genotype was observed at 12 months of age in the HIPP ($F_{(1,22)} = 5.619$, $p < 0.05$). Statistical analysis for Gln revealed a significant main effect of treatment at 6 months of age in the FC ($F_{(1,18)} = 14.586$, $p < 0.01$). *Post-hoc* comparisons within genotype showed that um-PEA treatment induced a significant increase in Gln levels compared to the vehicle-treated

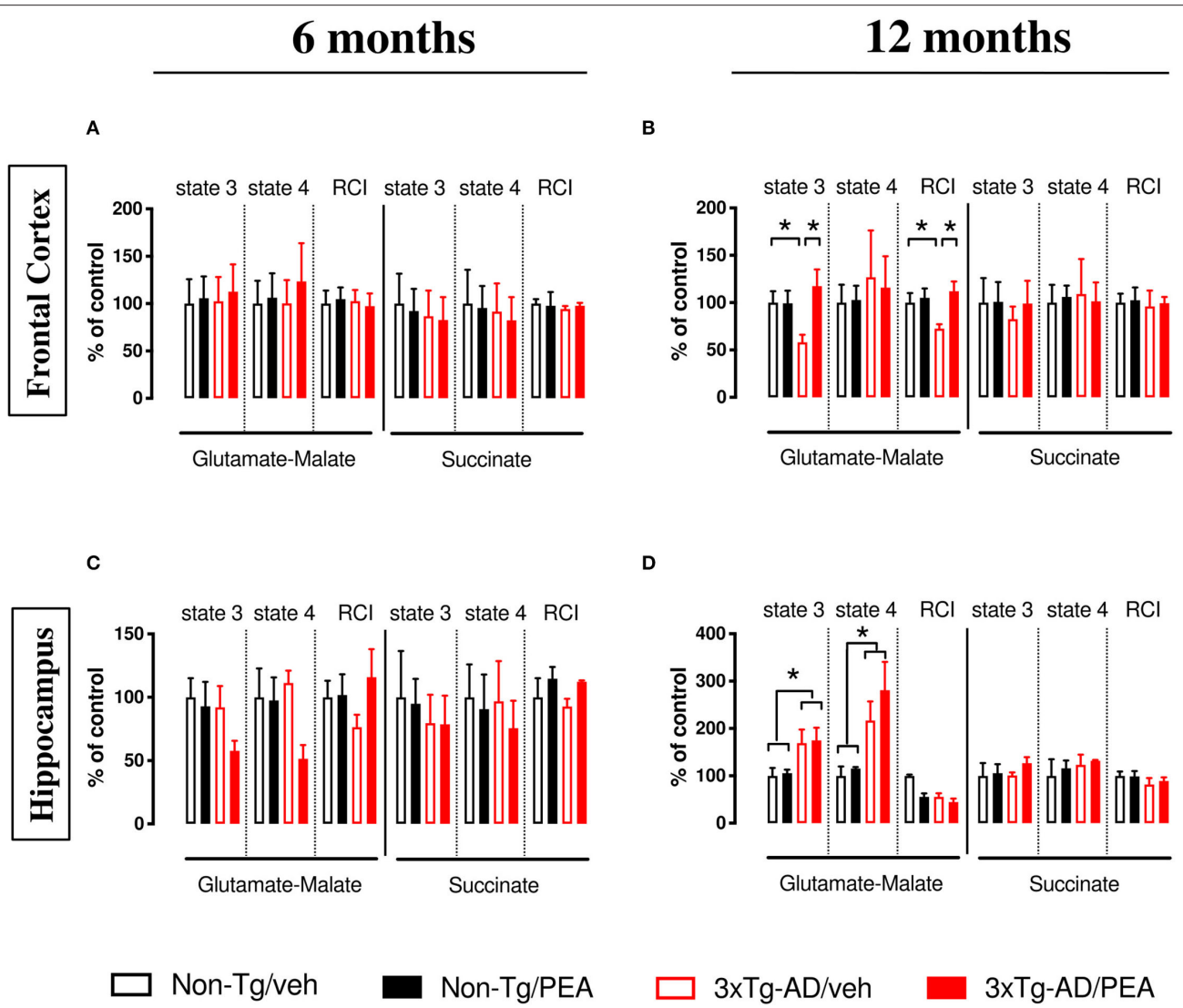

FIGURE 1 | State 4 and state 3 mitochondrial respiratory activity and respiratory control index (RCI) measured in the frontal cortex **(A,B)**, and hippocampus **(C,D)** of non-Tg (black bars) and 3×Tg-AD (red bars) 6-month-old **(A,C)** and 12-month-old **(B,D)** mice treated with vehicle (veh) (open bars) or um-PEA (filled bars), using complex I (glutamate-malate) and complex II (succinate) oxidative substrates. Data are expressed as a percentage of control ± SEM ($n = 4$). Statistical differences were assessed by two-way ANOVA and Tukey's *post-hoc* multiple comparisons test. *$p < 0.05$.

group. Moreover, no significant differences among groups were observed at 12 months in the FC, as well as in the HIPP at both ages.

Chronic um-PEA Treatment Does Not Ameliorate the Impaired K^+-Evoked Release of Glutamate in the Ventral Hippocampus of 3×Tg-AD Mice

As we have previously published (Scuderi et al., 2018), the basal extracellular glutamate levels in the vHIPP of 6-month-old 3×Tg-AD mice were significantly higher compared to age-matched non-Tg mice, whereas no significant genotype-related difference in basal glutamate levels was observed in 12-month-old mice. Moreover, chronic um-PEA treatment did not affect the basal output of glutamate at both ages (Scuderi et al., 2018). The overall basal glutamate levels are recapitulated in the insets of **Figure 5**.

After five consecutive samples, the basal extracellular levels of glutamate reached a steady state in the vHIPP of all mice. To address the impact of chronic um-PEA treatment on the impulse-driven glutamate release in the vHIPP of non-Tg and 3×Tg-AD mice, at both mild (6 months of age) and severe (12 months of age) stages of pathology, the probes were perfused with K+-enriched KRP buffer (containing KCl 50 mM) for 20 min (stimulated condition). Under the stimulated condition, the glutamate extracellular levels of non-Tg mice were increased due to the ability of neurons to increase their synaptic activity in response to depolarization. In this study, we observed the total lack of response to K+-stimulation in the vHIPP of 3×Tg-AD

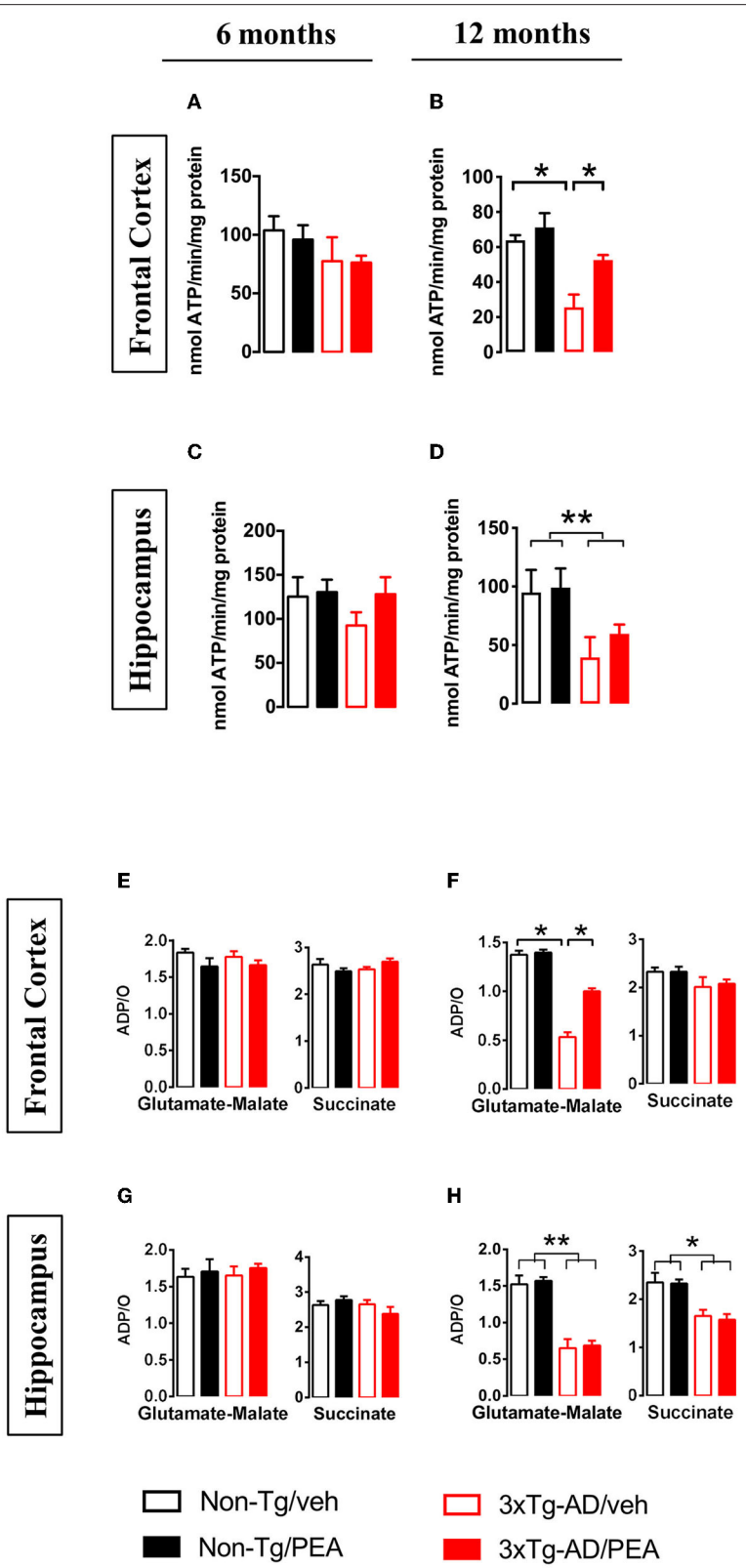

FIGURE 2 | FoF_1-ATPase activity **(A–D)** and ADP/O ratio **(E–H)** measured in mitochondria isolated from the frontal cortex **(A,B,E,F)**, and hippocampus **(C,D,G,H)** of non-Tg (black bars) and 3×Tg-AD (red bars) 6-month-old **(A,C,E,G)** and 12-month-old **(B,D,F,H)** mice treated with vehicle (open bars) or um-PEA (filled bars). Data are expressed as mean ± SEM ($n = 4$). Statistical differences were assessed by two-way ANOVA and Tukey's *post-hoc* test. *$p < 0.05$; **$p < 0.01$.

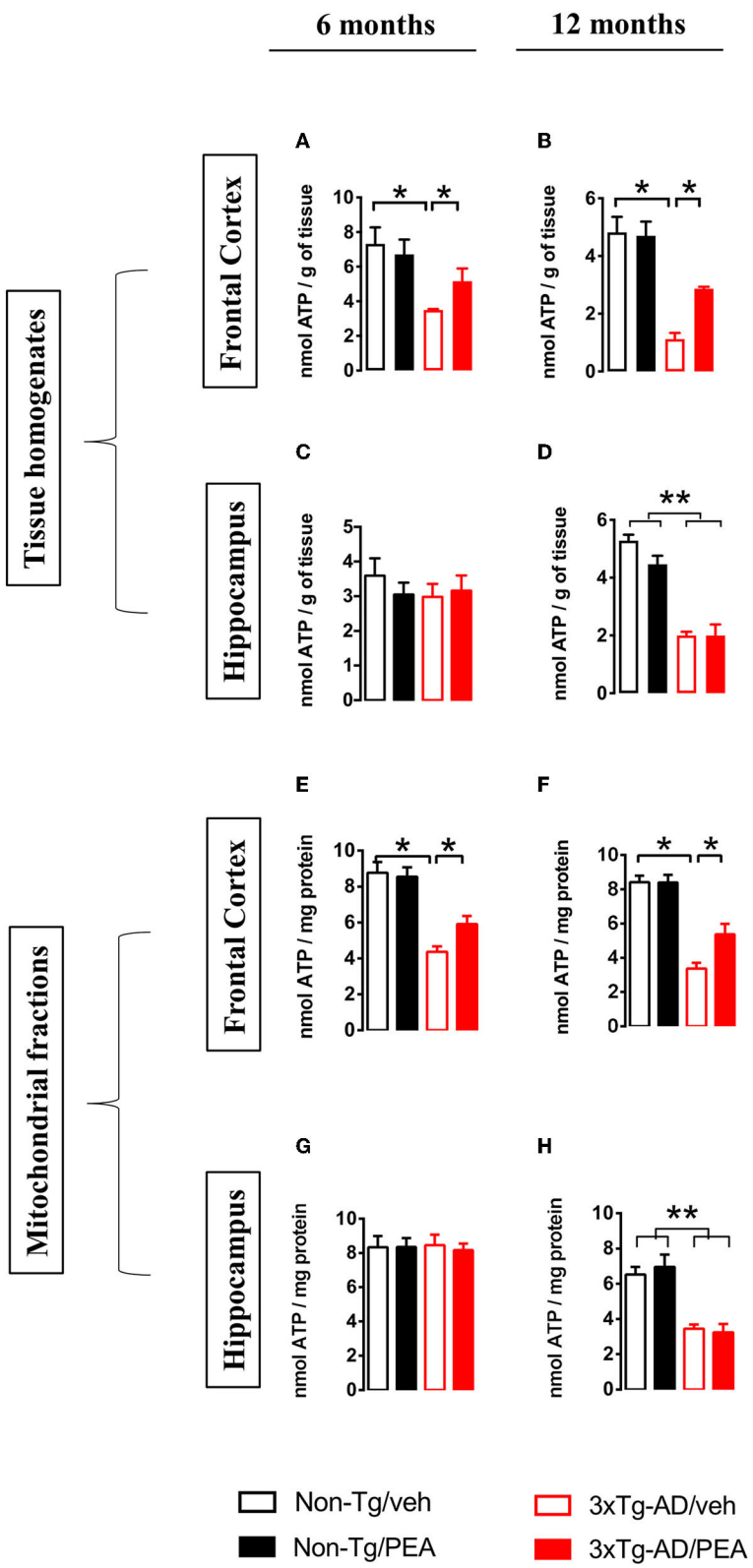

FIGURE 3 | Total homogenate ATP content measured in tissue homogenates and mitochondria isolated from frontal cortex **(A,B,E,F)** and hippocampus **(C,D,G,H)** of non-Tg (black bars) and 3×Tg-AD (red bars) 6-month-old **(A,C,E,G)** and 12-month-old **(B,D,F,H)** mice treated with vehicle (open bars) or um-PEA (filled bars). Data are expressed as mean ± SEM ($n = 4$). Statistical differences were assessed by two-way ANOVA and Tukey's *post-hoc* test. *$p < 0.05$; **$p < 0.01$.

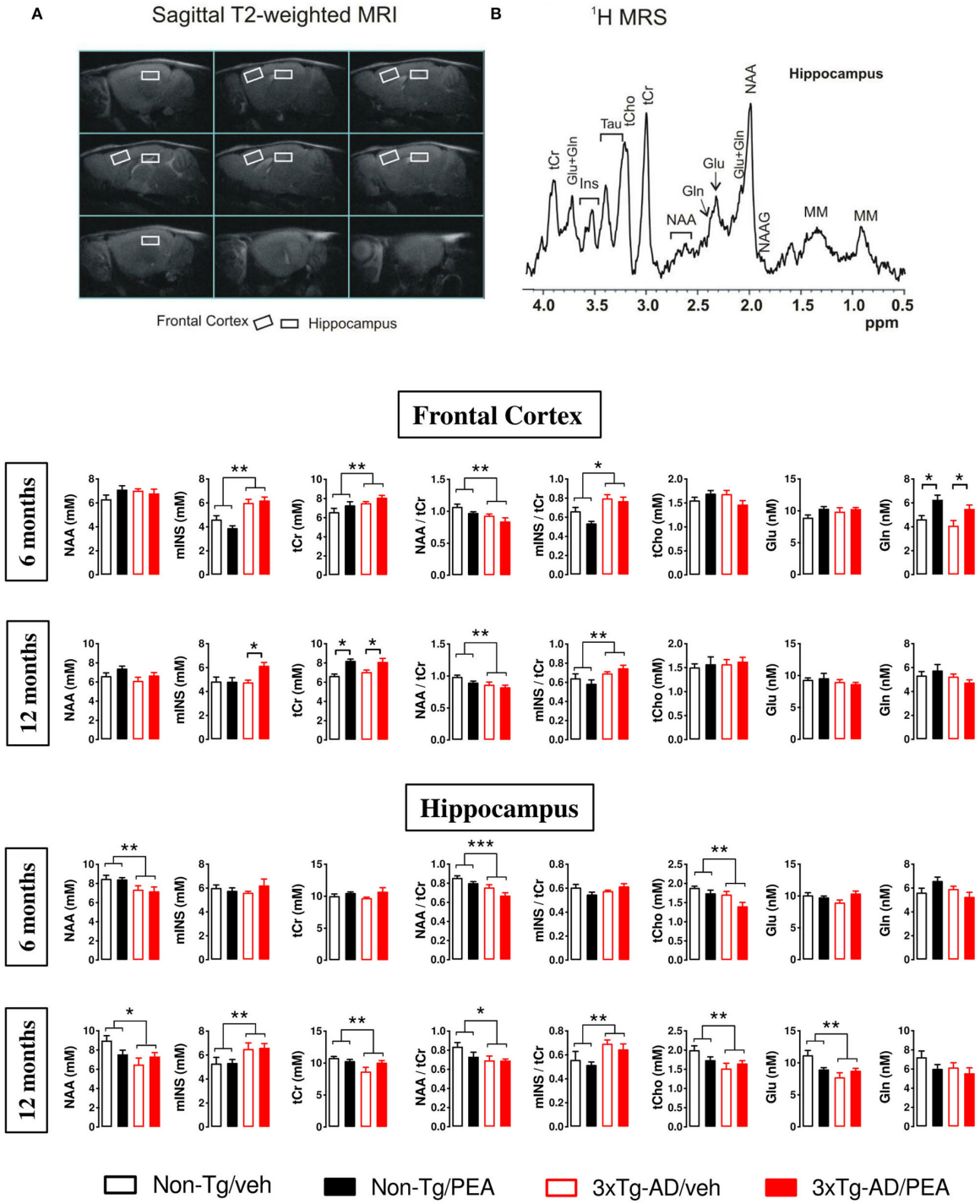

FIGURE 4 | (A) MRI panel: example of *in vivo* fast spin-echo sagittal anatomical images [repetition time (TR)/echo time (TE) = 3,200/60 ms, consecutive slices]. Voxels localized in the frontal cortex and hippocampus are indicated by white rectangles. **(B)** MRS panel: examples of *in vivo* 1 H spectra (PRESS, TR/TE = 4,000/23 ms, NS = 256). Metabolite assignments: NAA, N-acetyl-aspartate; mINS, myo-inositol; tCr, total creatine; tCho, total choline; Glu, glutamate; Gln, glutamine. Histograms showing metabolites measured from the frontal cortex (upper panel) and hippocampus (lower panel) of non-Tg (black bars) and 3×Tg-AD (red bars) 6-month-old and 12-month-old mice treated with vehicle (open bars) or um-PEA (filled bars). Data are expressed as mean ± SEM (n = 5–7). Statistical differences were assessed by two-way ANOVA and Tukey's *post-hoc* test. *$p < 0.05$; **$p < 0.01$.

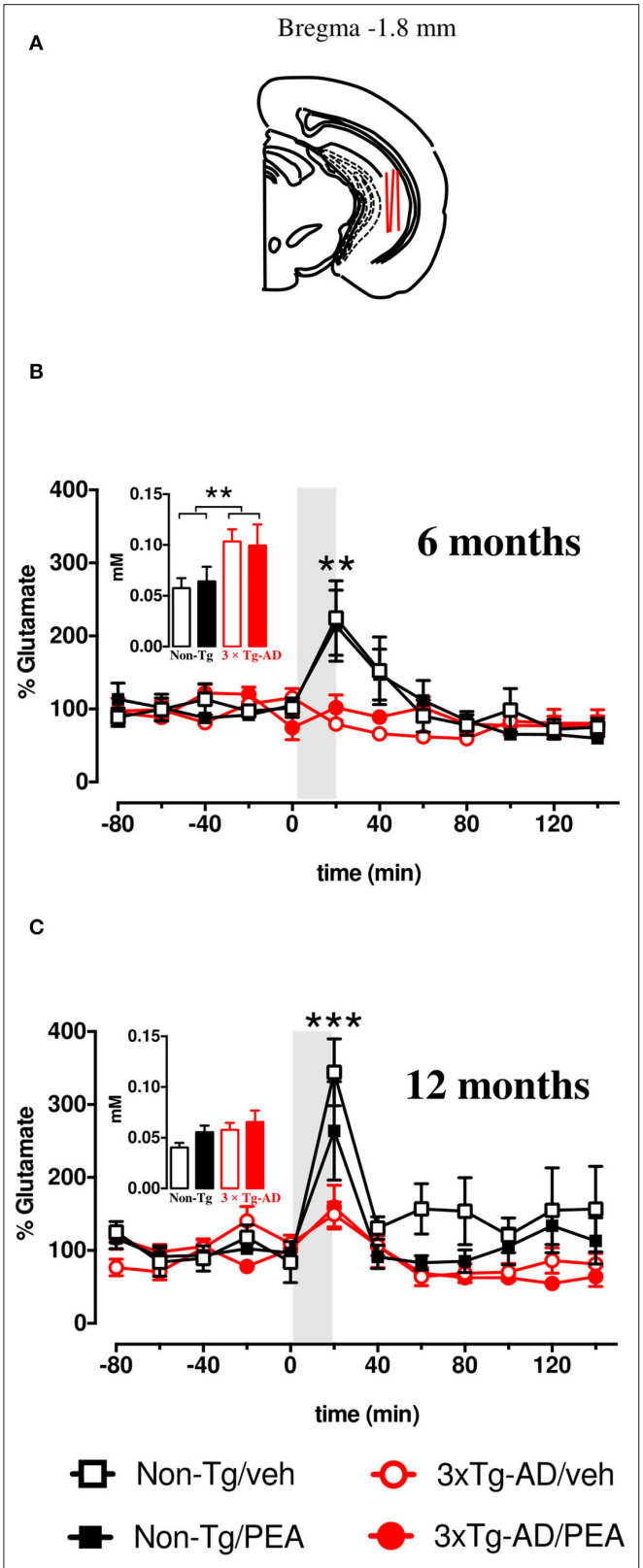

FIGURE 5 | (A) Brain diagrams illustrating the average sites (red lines) where microdialysis probes were implanted and where the representative microphotographs were taken. K^+-evoked release of glutamate in the ventral *(Continued)*

FIGURE 5 | hippocampus of 6- **(B)** and 12-month-old **(C)** freely moving non-Tg (squares) and 3×Tg-AD (circles) mice chronically treated with vehicle (empty squares and empty circles, respectively) or um-PEA (black squares and red circles, respectively); gray areas indicate the perfusion with KCl-enriched (50 mM) Krebs-Ringer phosphate (KRP) buffer. Histograms represent average baseline levels (marginal means of five consecutive dialysates: from time −80 up to time 0) observed in non-Tg (black bars) and 3×Tg-AD (red bars) mice treated with vehicle (open bars) and um-PEA (filled bars). Data are expressed as a percentage of control ± SEM ($n = 5$–6). Statistical differences were assessed by three-way ANOVA and Dunnett's multiple comparison test. $^{**}p < 0.01$; $^{***}p < 0.001$ vs. last baseline within the same group.

TABLE 3 | Statistical analyses of K^+-evoked release of glutamate in the ventral hippocampus of 3×Tg-AD mice and non-Tg mice.

	6 months of age			12 months of age		
	Df	**F**	**P**	**df**	**F**	**P**
Genotype (G)	1, 21	5,845	**0,0248**	1, 18	13,244	**0,0019**
Treatment (Tr)	1, 21	0,004	0,9517	1, 18	2,666	0.1199
G × Tr	1, 21	0,252	0,6209	1, 18	1,353	0,2599
Time (T)	7, 147	9,910	**<0,0001**	7, 126	19,526	**<0,0001**
T × G	7, 147	7,446	**<0,0001**	7, 126	5,446	**<0,0001**
T × Tr	7, 147	0,924	0,495	7, 126	0.433	0,8802
T × G × Tr	7, 147	0,477	0,8500	7, 126	0.943	0,4761

Statistical differences were assessed by three-way ANOVA for repeated measures with genotype (G) (3×Tg-AD vs. non-Tg) and treatment (Tr) (um-PEA vs. vehicle) as the between variable and time (T) as the within variable. Dunnett's and Tukey's post-hoc tests were used where appropriate to perform multiple comparisons. Bold values are statistical significance.

mice compared to the non-Tg group, at both 6 and 12 months of age. Moreover, chronic treatment of PEA did not ameliorate the impaired K+-evoked output of glutamate neurotransmission in the 6- and 12-month-old 3×Tg-AD mice (**Figures 5A,B**). The results of the statistical analyses performed by three-way ANOVA are reported in **Table 3**.

DISCUSSION

The most novel findings of our study are the demonstration that chronic um-PEA treatment can ameliorate the complex-I respiration rate, the F_oF_1-ATPase (complex V) activity, as well as ATP content in the cortical mitochondria from 3×Tg-AD mice. Otherwise, mitochondrial bioenergetics, as well as the release of glutamate after depolarization were not ameliorated by um-PEA treatment in the HIPP of both young and adult 3×Tg-AD mice. More interestingly, progressive age- and pathology-related changes were observed in the cortical and hippocampal metabolism that closely mimic the alterations observed in the human AD brain; these metabolic alterations were not affected by chronic um-PEA treatment.

We revealed for the first time that (i) AD-like pathology differently affects mitochondrial bioenergetics in the FC and HIPP and (ii) um-PEA treatment does not promote significant ameliorations simultaneously in those brain regions of 3×Tg-AD mice. This is in line with the temporal- and regional-specific

development of AD neuropathology in the brain of 3×Tg-AD mice, which closely mimics their development in the human AD brain (Oddo et al., 2003a,b; Hirata-Fukae et al., 2008).

Compared with many studies, we adopted a longitudinal study design with a sufficiently long observation period that allowed us to assess early alterations and changes over time in both non-transgenic and 3×Tg-AD mice. This study further extends the knowledge of the molecular modification during both normal aging and the progression of AD-like pathology in our murine model of AD (Oddo et al., 2003a,b). Moreover, we analyzed the modulatory effect of PEA on pathways and factors consistently associated with AD-like pathology and symptoms. In fact, we selected two different subsets of 3×Tg-AD mice, which allowed us to investigate the therapeutic potential of um-PEA in restraining the development of AD-like pathology at mild and severe stages, focusing on the mitochondrial bioenergetics, cerebral metabolism, and glutamatergic transmission. Regarding mitochondria and glutamate, we have previously demonstrated that deficits of glutamatergic transmission and mitochondrial dysfunction coexist in the FC and HIPP of 18-month-old 3×Tg-AD mice, which show a substantial number of amyloid plaques and tau pathology; the HIPP was the most affected area at that age (Cassano et al., 2012).

Despite accumulating evidence supporting the link between inflammation, mitochondria, and metabolism, several important questions remain unanswered. Furthermore, there are no studies addressing the effects of PEA on mitochondria bioenergetics in *in vivo* experimental models of AD, and only one study, to our knowledge, has assessed *in vivo* the effects of PEA on mitochondrial dysfunction observed in central nervous system pathological conditions (Cristiano et al., 2018). In this regard, Cristiano and colleagues found that PEA treatment improves hippocampal mitochondrial function and reduces oxidative stress in a genetic murine model (*BTBR T + tf/J*), which exhibits a behavioral phenotype of autism spectrum disorder. In particular, 10-day treatment with um-PEA was able to (i) restore hippocampal mitochondrial state 3 respiration using succinate as substrate, (ii) increase superoxide dismutase (SOD) activity, (iii) counteract ROS, and (iv) decline the energy efficiency, as evidenced by the decreased degree of coupling (Cristiano et al., 2018). Together, these findings demonstrate that PEA counteracts mitochondrial dysfunction and helps rescue brain energy metabolism during pathological states, balancing ROS production/antioxidant defenses, and limiting oxidative stress. Moreover, PEA-treated BTRB mice showed a low activation of pro-inflammatory cytokines at hippocampal and serum levels (Cristiano et al., 2018). Likewise, we have previously observed that 3-month treatment of um-PEA almost completely abolishes the increase in inflammatory markers observed in 6-month-old 3×Tg-AD mice and suppresses the expression of proinflammatory mediators, including interleukin (IL)-1β, IL-16, IL-5, monocyte chemotactic protein 5 (MCP-5), and macrophage colony-stimulating factor (M-CSF), but not inducible nitric oxide synthase (iNOS) and tumor necrosis factor (TNF), while enhancing the anti-inflammatory IL-10 (Scuderi et al., 2018).

In this study, 6-month-old 3×Tg-AD mice with a mild AD-like pathology showed a significant reduction of ATP content in the FC that was counteracted by um-PEA treatment. Otherwise, at 12 months of age, together with severe hallmarks of AD-like pathology, mitochondrial alterations were more evident and regional-specific. In fact, cortical mitochondria of 3×Tg-AD mice exhibited a reduced respiratory capacity, which might partially block electron flow within the respiratory chain and consequently increase oxidative stress; this effect was counteracted by um-PEA. The reduced respiratory activity was not observed after incubation with a complex II-linked substrate. The same pattern of alterations was observed in the cortical mitochondria of 18-month-old 3×Tg-AD mice, which present diffuse extracellular Aβ deposits and extensive human tau immunoreactivity (Cassano et al., 2012). Different from the latter age, at 12 months the reduced oxygen consumption observed in the transgenic cortical preparations was accompanied by alterations of F_oF_1-ATPase activity and ATP content that were counteracted by um-PEA treatment.

Regarding the HIPP, 12-month-old 3×Tg-AD mice showed the same mitochondrial dysfunctions previously observed with mice at 18 months of age (Cassano et al., 2012). In fact, here we confirmed a significant increase in state 3 and state 4 respiration rates with complex I-linked substrates and a significant impairment of ATP homeostasis. Different from FC, the pharmacological treatment with um-PEA did not ameliorate the hippocampal mitochondrial bioenergetics. Taken together, these findings suggest that um-PEA counteracts mitochondrial dysfunction, helps rescue brain energy metabolism during pathological states only in the FC, and such discrepancy might be due to the difference in Aβ/tau-linked alterations observed between these brain regions. In fact, it has been documented that Aβ and tau pathology differently impact brain regions, with HIPP showing more severe alterations compared to FC (Oddo et al., 2003a,b; Cassano et al., 2012; Bellanti et al., 2017). However, other mechanisms could underlie the regional-specific effect of um-PEA on mitochondrial bioenergetics and other experiments will be necessary to explain this phenomenon.

Brain structures undergo drastic modifications during aging, becoming progressively less interconnected and undergoing several metabolic and structural changes. A clinical scanner by MRS may serve to identify patients with AD before clinical symptom onset to help distinguish AD from other neurodegenerative disorders, as well as evaluate treatment effects.

In this regard, clinical studies demonstrated that NAA, a marker of neuronal integrity, can be detected by MRS and used to differentiate normal aging and pathological dementia (Ackl et al., 2005; Jessen et al., 2005; den Heijer et al., 2006). Besides decreased levels of NAA, several clinical studies demonstrated that mINS, a marker of glial activation, was increased in patients with AD (Glanville et al., 1989; Miller et al., 1993; Bitsch et al., 1999; Jessen et al., 2000; Kantarci et al., 2000; Huang et al., 2001).

Herein, we performed for the first time a comprehensive evaluation of six brain metabolites in the areas most involved in AD-like pathology. Interestingly, HIPP of 3×Tg-AD mice was characterized by lower concentrations of NAA and increased mINS, as seen in human patients with AD (Glanville et al., 1989; Klunk et al., 1992; Miller et al., 1993; Bitsch et al., 1999; Jessen et al., 2000; Kantarci et al., 2000, 2007; Huang et al.,

2001; Cheng et al., 2002; Schott et al., 2010). In particular, NAA reduction was observed at both ages (6 and 12 months), whereas mINS increased gradually with mouse age. Similar results were observed with APP/PS1 double transgenic mice, which is characterized by the early appearance of Aβ plaques, neuronal degeneration, and synaptic loss in the brain (Marjanska et al., 2005; Chen et al., 2009). The authors found that NAA was significantly reduced both in the FC and HIPP of 5-month-old APP/PS1 transgenic mice when pathology showed the formation of sparse Aβ plaques in these areas, and the number of neurons decreased. As the age of the mice increased, the NAA decrease was continuously accompanied by the increase in both mINS and the number of Aβ plaques (Marjanska et al., 2005; Chen et al., 2009). In our 3×Tg-AD mice, we found an increase in mINS by age only in the HIPP, but not in the FC, where a significantly higher concentration was observed only at 6 months of age compared to the non-Tg group.

Other results were obtained in the FC with different transgenic AD mice. In fact, no increase in mINS in the FC was observed in the transgenic mouse line PS2APP [PS2N141I×APP(swe)], which develops an age-related cognitive decline associated with severe amyloidosis (Von et al., 2005). Therefore, further studies need to be performed to justify the discrepancy existing in the literature, which may be attributed to the differences in the experimental parameters and animal models of AD-like pathology.

Our longitudinal study revealed a significant decrease in tCr only in the HIPP of 12-month-old 3×Tg-AD mice. This metabolic profile, together with lower NAA, is a clear indicator of the age-related hypometabolism in the HIPP of 3×Tg-AD mice, further suggesting that HIPP is the most affected area at that age (Cassano et al., 2012; Scuderi et al., 2018).

A decrease in NAA/Cr ratio accompanied by an increased mINS/Cr ratio occurs in patients with AD; the latter temporal progression of metabolite abnormalities in patients with AD correlates with the progression of the Aβ/tau-linked alterations (Glanville et al., 1989; Klunk et al., 1992; Miller et al., 1993; Bitsch et al., 1999; Jessen et al., 2000; Kantarci et al., 2000, 2007; Huang et al., 2001; Cheng et al., 2002; Schott et al., 2010). Interestingly, we found a similar pattern of changes in the metabolite ratio both in the FC and HIPP, as seen in human patients with AD.

The role of Cho metabolite in AD is more controversial since several clinical studies demonstrated an increase (Meyerhoff et al., 1994; Pfefferbaum et al., 1999; Kantarci et al., 2007), others no change (Moats et al., 1994; Schuff et al., 1997; Rose et al., 1999; Krishnan et al., 2003), whereas a decrease was reported in one study (Chantal et al., 2002). In our study, we observed a significant decrease of tCho only in the HIPP of both 6- and 12-month-old mice. The Cho cytosolic concentration derives from the breakdown products of phosphatidylcholine (Schuff et al., 1997). Therefore, it has been proposed that catabolism of the phospholipid membrane bilayer allows AD subjects to produce choline to compensate for declining acetylcholine (Wurtman et al., 1985).

Although Glu is the principal excitatory neurotransmitter involved in learning and memory, it has been less well investigated by MRS/MRI. In this regard, few clinical studies revealed a reduction of Glu levels in different brain regions of patients with AD (Antuono et al., 2001; Hattori et al., 2002; Rupsingh et al., 2011) that correlates with the severe reduction of the cerebral metabolic rate for glucose (Mosconi et al., 2008; Bedse et al., 2015; Barone et al., 2016). In fact, glutamate neurotransmission is carried out by a glial-neuronal process that includes the oxidation of glucose and the ATP-dependent glutamine-glutamate cycle. A total of 80–90% of total cerebral glucose usage is attributable to the energy requirements of glutamatergic neurotransmission (Magistretti et al., 1999; Gatta et al., 2016; Pardeshi et al., 2017; Tramutola et al., 2018; Sharma et al., 2019; Bukke et al., 2020a,b). The neurochemical changes obtained from *in vivo* human MRS studies agree with the results observed in preclinical studies. In fact, the analysis of cortex and HIPP in APP-PS1 mice showed an age-dependent reduction of Glu levels, which correlates with increasing brain amyloidosis (Marjanska et al., 2005). Similar findings were observed in the cortex of APP (Dedeoglu et al., 2004) and PS2APP mice (Von et al., 2005). This is in line with the Glu spectroscopy findings between human AD subjects and the three transgenic mouse models of AD.

In our study, we demonstrated a temporal- and regional-specific alteration of Glu in 3×Tg-AD mice with the HIPP the only affected area. In particular, at 12 months of age, we found a significant reduction (−38%) of Glu in the HIPP of vehicle-treated 3×Tg-AD vs. vehicle-treated non-Tg mice. These results, observed in the vehicle-treated 3×Tg-AD mice, together with lower hippocampal NAA (−45%), tCr (−24%), and tCho (−31%), further support the evidence of an age-related hypometabolism in the HIPP. MRS analysis might be of interest also to depict how neural correlates do change along with pharmacological treatment. In this regard, in our experimental condition, we did not observe any gross treatment-dependent differences between genotypes.

To investigate whether the decrease in hippocampal glutamate levels in the metabolic pool was paralleled by alterations in the glutamatergic nerve terminals, the pattern of glutamate release in basal condition, and in response to K^+-stimulation was explored by microdialysis sampling in the vHIPP of 6- and 12-month-old mice. We have previously demonstrated that the basal release of glutamate was significantly increased (+80%) at 6 months of age whereas a trend toward an increase (+43%) was observed in 12-month-old 3×Tg-AD compared to non-Tg mice (Scuderi et al., 2018). Here, we demonstrated that at both ages the depolarization-evoked glutamate release resulted completely disrupted in 3×Tg-AD compared to non-Tg mice, thus suggesting that the deficit of glutamate metabolic pool observed by MRS might sustain, at least in part (at 12 months of

age), the decrease of extracellular glutamate concentration in mutant mice.

CONCLUSION

Our results not only elucidate the temporal correlation among mitochondrion, metabolic alterations, and glutamatergic dysfunction but also, in future studies, allow the assessment of putative therapeutic strategies. However, this study presents some limitations. For instance, additional measurements would allow performing a tight correlation between molecular markers of bioenergetics dysfunction, for instance, hydrogen peroxide production, proton leak or membrane potential, and metabolic alterations. Finally, this study sheds additional light on the effects of PEA treatment, displaying selective bioenergetic effects. At present, the use of a PEA treatment may represent a possible novel frontier for the future clinical treatment of AD.

DATA AVAILABILITY STATEMENT

The raw data supporting the conclusions of this article will be made available by the authors, without undue reservation.

ETHICS STATEMENT

The animal study was reviewed and approved by Ethics Committee of the University of Foggia.

AUTHOR CONTRIBUTIONS

TC, CS, LS, and GS designed the research. FB, VB, MA, RV, GP, RC, and SB performed the research. FB, RC, GV, GS, and TC analyzed data and interpreted the results. FB and TC wrote the manuscript. All authors contributed to the article and approved the submitted version.

FUNDING

This project was supported by the Italian Ministry for Education, University and Research (PRIN to LS and GV), and the Department of Clinical and Experimental Medicine (Dipartimenti di eccellenza – Legge 232/2016). This paper/manuscript/study has been published with the financial support of the Department of Medical and Surgical Sciences of the University of Foggia.

REFERENCES

Ackl, N., Ising, M., Schreiber, Y. A., Atiya, M., Sonntag, A., and Auer, D. P. (2005). Hippocampal metabolic abnormalities in mild cognitive impairment and Alzheimer's disease. *Neurosci. Lett.* 384, 23–28. doi: 10.1016/j.neulet.2005.04.035

Antuono, P. G., Jones, J. L., Wang, Y., and Li, S. J. (2001). Decreased glutamate + glutamine in Alzheimer's disease detected *in vivo* with (1)H-MRS at 0.5 T. *Neurology* 56, 737–742. doi: 10.1212/WNL.56.6.737

Barone, E., Di, D. F., Cassano, T., Arena, A., Tramutola, A., Lavecchia, M. A., et al. (2016). Impairment of biliverdin reductase-A promotes brain insulin resistance in Alzheimer disease: a new paradigm. *Free Radic. Biol. Med.* 91, 127–142. doi: 10.1016/j.freeradbiomed.2015.12.012

Barone, E., Tramutola, A., Triani, F., Calcagnini, S., Di, D. F., Ripoli, C., et al. (2019). Biliverdin Reductase-A Mediates the Beneficial Effects of Intranasal Insulin in Alzheimer Disease. *Mol. Neurobiol.* 56, 2922–2943. doi: 10.1007/s12035-018-1231-5

Bartha, R., Smith, M., Rupsingh, R., Rylett, J., Wells, J. L., and Borrie, M. J. (2008). High field (1)H MRS of the hippocampus after donepezil treatment in Alzheimer disease. *Prog. Neuropsychopharmacol. Biol. Psychiatry* 32, 786–793. doi: 10.1016/j.pnpbp.2007.12.011

Bedse, G., Di, D. F., Serviddio, G., and Cassano, T. (2015). Aberrant insulin signaling in Alzheimer's disease: current knowledge. *Front Neurosci.* 9, 204. doi: 10.3389/fnins.2015.00204

Beggiato, S., Cassano, T., Ferraro, L., and Tomasini, M. C. (2020a). Astrocytic palmitoylethanolamide pre-exposure exerts neuroprotective effects in astrocyte-neuron co-cultures from a triple transgenic mouse model of Alzheimer's disease. *Life Sci.* 257, 118037. doi: 10.1016/j.lfs.2020.118037

Beggiato, S., Tomasini, M. C., Cassano, T., and Ferraro, L. (2020b). Chronic oral palmitoylethanolamide administration rescues cognitive deficit and reduces neuroinflammation, oxidative stress, and glutamate levels in a transgenic murine model of Alzheimer's disease. *J. Clin. Med.* 9, jcm9020428 doi: 10.3390/jcm9020428

Bellanti, F., Iannelli, G., Blonda, M., Tamborra, R., Villani, R., Romano, A., et al. (2017). Alterations of Clock Gene RNA Expression in Brain Regions of a Triple Transgenic Model of Alzheimer's Disease. *J. Alzheimers. Dis.* 59, 615–631. doi: 10.3233/JAD-160942

Bitsch, A., Bruhn, H., Vougioukas, V., Stringaris, A., Lassmann, H., Frahm, J., et al. (1999). Inflammatory CNS demyelination: histopathologic correlation with *in vivo* quantitative proton MR spectroscopy. *AJNR Am. J. Neuroradiol.* 20, 1619–1627.

Blass, J. P., and Gibson, G. E. (1991). The role of oxidative abnormalities in the pathophysiology of Alzheimer's disease. *Rev. Neurol. (Paris) 147* 513–525.

Bronzuoli, M. R., Facchinetti, R., Steardo, L. Jr., Romano, A., Stecca, C., Passarella, S., et al. (2018). Palmitoylethanolamide dampens reactive astrogliosis and improves neuronal trophic support in a triple transgenic model of Alzheimer's disease: *in vitro* and *in vivo* evidence. *Oxid. Med. Cell Longev.* 2018, 4720532. doi: 10.1155/2018/4720532

Bronzuoli, M. R., Facchinetti, R., Valenza, M., Cassano, T., Steardo, L., and Scuderi, C. (2019). Astrocyte function is affected by aging and not Alzheimer's disease: a preliminary investigation in hippocampi of 3xTg-AD mice. *Front. Pharmacol.* 10, 644. doi: 10.3389/fphar.2019.00644

Bukke, V. N., Archana, M., Villani, R., Romano, A. D., Wawrzyniak, A., Balawender, K., et al. (2020a). The dual role of glutamatergic neurotransmission in Alzheimer's disease: from pathophysiology to pharmacotherapy. *Int. J. Mol. Sci.* 21, ijms21207452 doi: 10.3390/ijms21207452

Bukke, V. N., Villani, R., Archana, M., Wawrzyniak, A., Balawender, K., Orkisz, S., et al. (2020b). The glucose metabolic pathway as a potential target for therapeutics: crucial role of glycosylation in Alzheimer's disease. *Int. J. Mol. Sci.* 21, ijms21207739 doi: 10.3390/ijms21207739

Canese, R., Pisanu, M. E., Mezzanzanica, D., Ricci, A., Paris, L., Bagnoli, M., et al. (2012). Characterisation of *in vivo* ovarian cancer models by quantitative 1H magnetic resonance spectroscopy and diffusion-weighted imaging. *NMR Biomed.* 25, 632–642. doi: 10.1002/nbm.1779

Carapelle, E., Mundi, C., Cassano, T., and Avolio, C. (2020). Interaction between cognitive reserve and biomarkers in Alzheimer disease. *Int. J. Mol. Sci.* 21, ijms21176279 doi: 10.3390/ijms21176279

Cassano, T., Calcagnini, S., Carbone, A., Bukke, V. N., Orkisz, S., Villani, R., et al. (2019). Pharmacological treatment of depression in Alzheimer's disease: a challenging task. *Front Pharmacol.* 10, 1067. doi: 10.3389/fphar.2019.01067

Cassano, T., Pace, L., Bedse, G., Lavecchia, A. M., De, M. F., Gaetani, S., et al. (2016). Glutamate and mitochondria: two prominent players in the oxidative stress-induced neurodegeneration. *Curr. Alzheimer Res.* 13, 185–197. doi: 10.2174/1567205013666151218132725

Cassano, T., Serviddio, G., Gaetani, S., Romano, A., Dipasquale, P., Cianci, S., et al. (2012). Glutamatergic alterations and mitochondrial impairment in a murine model of Alzheimer disease. *Neurobiol. Aging* 33, 1121–1112. doi: 10.1016/j.neurobiolaging.2011.09.021

Chantal, S., Labelle, M., Bouchard, R. W., Braun, C. M., and Boulanger, Y. (2002). Correlation of regional proton magnetic resonance spectroscopic metabolic changes with cognitive deficits in mild Alzheimer disease. *Arch. Neurol.* 59, 955–962. doi: 10.1001/archneur.59.6.955

Chen, T. F., Chen, Y. F., Cheng, T. W., Hua, M. S., Liu, H. M., and Chiu, M. J. (2009). Executive dysfunction and periventricular diffusion tensor changes in amnesic mild cognitive impairment and early Alzheimer's disease. *Hum. Brain Mapp.* 30, 3826–3836. doi: 10.1002/hbm.20810

Cheng, L. L., Newell, K., Mallory, A. E., Hyman, B. T., and Gonzalez, R. G. (2002). Quantification of neurons in Alzheimer and control brains with ex vivo high resolution magic angle spinning proton magnetic resonance spectroscopy and stereology. *Magn Reson. Imaging* 20, 527–533. doi: 10.1016/S0730-725X(02)00512-X

Costa, B., Conti, S., Giagnoni, G., and Colleoni, M. (2002). Therapeutic effect of the endogenous fatty acid amide, palmitoylethanolamide, in rat acute inflammation: inhibition of nitric oxide and cyclo-oxygenase systems. *Br. J. Pharmacol.* 137, 413–420. doi: 10.1038/sj.bjp.0704900

Cristiano, C., Pirozzi, C., Coretti, L., Cavaliere, G., Lama, A., Russo, R., et al. (2018). Palmitoylethanolamide counteracts autistic-like behaviours in BTBR T+tf/J mice: contribution of central and peripheral mechanisms. *Brain Behav. Immun.* 74, 166–175. doi: 10.1016/j.bbi.2018.09.003

D'Agostino, G., Russo, R., Avagliano, C., Cristiano, C., Meli, R., and Calignano, A. (2012). Palmitoylethanolamide protects against the amyloid-beta25-35-induced learning and memory impairment in mice, an experimental model of Alzheimer disease. *Neuropsychopharmacology* 37, 1784–1792. doi: 10.1038/npp.2012.25

Dedeoglu, A., Choi, J. K., Cormier, K., Kowall, N. W., and Jenkins, B. G. (2004). Magnetic resonance spectroscopic analysis of Alzheimer's disease mouse brain that express mutant human APP shows altered neurochemical profile. *Brain Res.* 1012, 60–65. doi: 10.1016/j.brainres.2004.02.079

Delerive, P., Fruchart, J. C., and Staels, B. (2001). Peroxisome proliferator-activated receptors in inflammation control. *J. Endocrinol.* 169, 453–459. doi: 10.1677/joe.0.1690453

den Heijer, T., Sijens, P. E., Prins, N. D., Hofman, A., and Koudstaal, P. J., Oudkerk, M. et al. (2006). MR spectroscopy of brain white matter in the prediction of dementia. *Neurology* 66, 540–544. doi: 10.1212/01.wnl.0000198256.54809.0e

Devchand, P. R., Keller, H., Peters, J. M., Vazquez, M., Gonzalez, F. J., and Wahli, W. (1996). The PPARalpha-leukotriene B4 pathway to inflammation control. *Nature* 384, 39–43. doi: 10.1038/384039a0

Franklin, K. B. J., and Paxinos, G. (1997). *The Mouse Brain in Stereotaxic Coordinates*, San Diego: Academic Press.

Frederick, B. B., Satlin, A., Yurgelun-Todd, D. A., and Renshaw, P. F. (1997). *In vivo* proton magnetic resonance spectroscopy of Alzheimer's disease in the parietal and temporal lobes. *Biol. Psychiatry* 42, 147–150. doi: 10.1016/S0006-3223(97)00242-4

Gatta, E., Lefebvre, T., Gaetani, S., dos, S. M., and Marrocco, J., Mir, A. M. et al. (2016). Evidence for an imbalance between tau O-GlcNAcylation and phosphorylation in the hippocampus of a mouse model of Alzheimer's disease. *Pharmacol. Res.* 105, 186–197. doi: 10.1016/j.phrs.2016.01.006

Glanville, N. T., Byers, D. M., Cook, H. W., Spence, M. W., and Palmer, F. B. (1989). Differences in the metabolism of inositol and phosphoinositides by cultured cells of neuronal and glial origin. *Biochim. Biophys. Acta* 1004, 169–179. doi: 10.1016/0005-2760(89)90265-8

Grillo, S. L., Duggett, N. A., Ennaceur, A., and Chazot, P. L. (2013). Non-invasive infra-red therapy (1072 nm) reduces beta-amyloid protein levels in the brain of an Alzheimer's disease mouse model, TASTPM. *J. Photochem. Photobiol. B* 123, 13–22. doi: 10.1016/j.jphotobiol.2013.02.015

Hattori, N., Abe, K., Sakoda, S., and Sawada, T. (2002). Proton MR spectroscopic study at 3 Tesla on glutamate/glutamine in Alzheimer's disease. *Neuroreport* 13, 183–186. doi: 10.1097/00001756-200201210-00041

Hirata-Fukae, C., Li, H. F., Hoe, H. S., Gray, A. J., Minami, S. S., Hamada, K., et al. (2008). Females exhibit more extensive amyloid, but not tau, pathology in an Alzheimer transgenic model. *Brain Res.* 1216, 92–103. doi: 10.1016/j.brainres.2008.03.079

Huang, W., Alexander, G. E., Chang, L., Shetty, H. U., Krasuski, J. S., Rapoport, S. I., et al. (2001). Brain metabolite concentration and dementia severity in Alzheimer's disease: a (1)H MRS study. *Neurology* 57, 626–632. doi: 10.1212/WNL.57.4.626

Jessen, F., Block, W., Traber, F., Keller, E., Flacke, S., Papassotiropoulos, A., et al. (2000). Proton MR spectroscopy detects a relative decrease of N-acetylaspartate in the medial temporal lobe of patients with AD. *Neurology* 55, 684–688. doi: 10.1212/WNL.55.5.684

Jessen, F., Traeber, F., Freymann, N., Maier, W., Schild, H. H., Heun, R., et al. (2005). A comparative study of the different N-acetylaspartate measures of the medial temporal lobe in Alzheimer's disease. *Dement. Geriatr. Cogn. Disord.* 20, 178–183. doi: 10.1159/000087095

Kantarci, K., Jack, C. R. Jr., Xu, Y. C., Campeau, N. G., O'Brien, P. C., Smith, G. E., et al. (2000). Regional metabolic patterns in mild cognitive impairment and Alzheimer's disease: A 1H MRS study. *Neurology* 55, 210–217. doi: 10.1212/WNL.55.2.210

Kantarci, K., Weigand, S. D., Petersen, R. C., Boeve, B. F., Knopman, D. S., Gunter, J., et al. (2007). Longitudinal 1H MRS changes in mild cognitive impairment and Alzheimer's disease. *Neurobiol. Aging* 28, 1330–1339. doi: 10.1016/j.neurobiolaging.2006.06.018

Klunk, W. E., Panchalingam, K., Moossy, J., McClure, R. J., and Pettegrew, J. W. (1992). N-acetyl-L-aspartate and other amino acid metabolites in Alzheimer's disease brain: a preliminary proton nuclear magnetic resonance study. *Neurology* 42, 1578–1585. doi: 10.1212/WNL.42.8.1578

Krishnan, K. R., Charles, H. C., Doraiswamy, P. M., Mintzer, J., Weisler, R., Yu, X., et al. (2003). Randomized, placebo-controlled trial of the effects of donepezil on neuronal markers and hippocampal volumes in Alzheimer's disease. *Am. J. Psychiatry* 160, 2003–2011. doi: 10.1176/appi.ajp.160.11.2003

Lin, M. T., and Beal, M. F. (2006). Alzheimer's APP mangles mitochondria. *Nat. Med.* 12, 1241–1243. doi: 10.1038/nm1106-1241

LoVerme, J., La, R. G., Russo, R., Calignano, A., and Piomelli, D. (2005). The search for the palmitoylethanolamide receptor. *Life Sci.* 77, 1685–1698. doi: 10.1016/j.lfs.2005.05.012

LoVerme, J., Russo, R., La, R. G., Fu, J., Farthing, J., Mattace-Raso, G., et al. (2006). Rapid broad-spectrum analgesia through activation of peroxisome proliferator-activated receptor-alpha. *J. Pharmacol. Exp. Ther.* 319, 1051–1061. doi: 10.1124/jpet.106.111385

Magistretti, P. J., Pellerin, L., Rothman, D. L., and Shulman, R. G. (1999). Energy on demand. *Science* 283, 496–497. doi: 10.1126/science.283.5401.496

Mahmoud, S., Gharagozloo, M., Simard, C., and Gris, D. (2019). Astrocytes maintain glutamate homeostasis in the CNS by controlling the balance between glutamate uptake and release. *Cells* 8, 184. doi: 10.3390/cells8020184

Marjanska, M., Curran, G. L., Wengenack, T. M., Henry, P. G., Bliss, R. L., Poduslo, J. F., et al. (2005). Monitoring disease progression in transgenic mouse models of Alzheimer's disease with proton magnetic resonance spectroscopy. *Proc. Natl. Acad. Sci. U. S. A* 102, 11906–11910. doi: 10.1073/pnas.0505513102

Meyerhoff, D. J., MacKay, S., Constans, J. M., Norman, D., Van, D. C., Fein, G., et al. (1994). Axonal injury and membrane alterations in Alzheimer's disease suggested by *in vivo* proton magnetic resonance spectroscopic imaging. *Ann. Neurol.* 36, 40–47. doi: 10.1002/ana.410360110

Miller, B. L., Moats, R. A., Shonk, T., Ernst, T., Woolley, S., and Ross, B. D. (1993). Alzheimer disease: depiction of increased cerebral myo-inositol with proton MR spectroscopy. *Radiology* 187, 433–437. doi: 10.1148/radiology.187.2.8475286

Moats, R. A., Ernst, T., Shonk, T. K., and Ross, B. D. (1994). Abnormal cerebral metabolite concentrations in patients with probable Alzheimer disease. *Magn. Reson. Med.* 32, 110–115. doi: 10.1002/mrm.1910320115

Mosconi, L., Tsui, W. H., Herholz, K., Pupi, A., Drzezga, A., Lucignani, G., et al. (2008). Multicenter standardized 18F-FDG PET diagnosis of mild cognitive impairment, Alzheimer's disease, and other dementias. *J. Nucl. Med.* 49, 390–398. doi: 10.2967/jnumed.107.045385

Oddo, S., Caccamo, A., Kitazawa, M., Tseng, B. P., and Laferla, F. M. (2003a). Amyloid deposition precedes tangle formation in a triple transgenic model of Alzheimer's disease. *Neurobiol. Aging* 24, 1063–1070. doi: 10.1016/j.neurobiolaging.2003.08.012

Oddo, S., Caccamo, A., Shepherd, J. D., Murphy, M. P., Golde, T. E., Kayed, R., et al. (2003b). Triple-transgenic model of Alzheimer's disease with plaques

and tangles: intracellular Abeta and synaptic dysfunction. *Neuron* 39, 409–421. doi: 10.1016/S0896-6273(03)00434-3

Pardeshi, R., Bolshette, N., Gadhave, K., Ahire, A., Ahmed, S., Cassano, T., et al. (2017). Insulin signaling: an opportunistic target to minify the risk of Alzheimer's disease. *Psychoneuroendocrinology* 83, 159–171. doi: 10.1016/j.psyneuen.2017.05.004

Pfefferbaum, A., Adalsteinsson, E., Spielman, D., Sullivan, E. V., and Lim, K. O. (1999). *In vivo* brain concentrations of N-acetyl compounds, creatine, and choline in Alzheimer disease. *Arch. Gen. Psychiatry* 56, 185–192. doi: 10.1001/archpsyc.56.2.185

Querfurth, H. W., and Laferla, F. M. (2010). Alzheimer's disease. *N. Engl. J. Med.* 362, 329–344. doi: 10.1056/NEJMra0909142

Reddy, P. H. (2009). Role of mitochondria in neurodegenerative diseases: mitochondria as a therapeutic target in Alzheimer's disease. *CNS. Spectr.* 14, 8–13. doi: 10.1017/S1092852900024901

Romano, A., Pace, L., Tempesta, B., Lavecchia, A. M., Macheda, T., Bedse, G., et al. (2014). Depressive-like behavior is paired to monoaminergic alteration in a murine model of Alzheimer's disease. *Int. J. Neuropsychopharmacol.* 18, pyu020. doi: 10.1093/ijnp/pyu020

Romano, A., Serviddio, G., Calcagnini, S., Villani, R., Giudetti, A. M., Cassano, T., et al. (2017). Linking lipid peroxidation and neuropsychiatric disorders: focus on 4-hydroxy-2-nonenal. *Free Radic. Biol. Med.* 111, 281–293. doi: 10.1016/j.freeradbiomed.2016.12.046

Rose, S. E., de Zubicaray, G. I., Wang, D., Galloway, G. J., Chalk, J. B., Eagle, S. C., et al. (1999). A 1H MRS study of probable Alzheimer's disease and normal aging: implications for longitudinal monitoring of dementia progression. *Magn. Reson. Imaging* 17, 291–299. doi: 10.1016/S0730-725X(98)00168-4

Rupsingh, R., Borrie, M., Smith, M., Wells, J. L., and Bartha, R. (2011). Reduced hippocampal glutamate in Alzheimer disease. *Neurobiol. Aging* 32, 802–810. doi: 10.1016/j.neurobiolaging.2009.05.002

Schinder, A. F., Olson, E. C., Spitzer, N. C., and Montal, M. (1996). Mitochondrial dysfunction is a primary event in glutamate neurotoxicity. *J. Neurosci.* 16, 6125–6133. doi: 10.1523/JNEUROSCI.16-19-06125.1996

Schott, J. M., Frost, C., MacManus, D. G., Ibrahim, F., Waldman, A. D., and Fox, N. C. (2010). Short echo time proton magnetic resonance spectroscopy in Alzheimer's disease: a longitudinal multiple time point study. *Brain* 133, 3315–3322. doi: 10.1093/brain/awq208

Schuff, N., Amend, D., Ezekiel, F., Steinman, S. K., Tanabe, J., Norman, D., et al. (1997). Changes of hippocampal N-acetyl aspartate and volume in Alzheimer's disease. A proton MR spectroscopic imaging and MRI study. *Neurology* 49, 1513–1521. doi: 10.1212/WNL.49.6.1513

Scuderi, C., Bronzuoli, M. R., Facchinetti, R., Pace, L., Ferraro, L., Broad, K. D., et al. (2018). Ultramicronized palmitoylethanolamide rescues learning and memory impairments in a triple transgenic mouse model of Alzheimer's disease by exerting anti-inflammatory and neuroprotective effects. *Transl. Psychiatry* 8, 32. doi: 10.1038/s41398-017-0076-4

Scuderi, C., Esposito, G., Blasio, A., Valenza, M., Arietti, P., and Steardo, L. Jr. et al. (2011). Palmitoylethanolamide counteracts reactive astrogliosis induced by beta-amyloid peptide. *J. Cell Mol. Med.* 15, 2664–2674. doi: 10.1111/j.1582-4934.2011.01267.x

Scuderi, C., Stecca, C., Valenza, M., Ratano, P., Bronzuoli, M. R., Bartoli, S., et al. (2014). Palmitoylethanolamide controls reactive gliosis and exerts neuroprotective functions in a rat model of Alzheimer's disease. *Cell Death. Dis.* 5, e1419. doi: 10.1038/cddis.2014.376

Scuderi, C., Valenza, M., Stecca, C., Esposito, G., Carratu, M. R., and Steardo, L. (2012). Palmitoylethanolamide exerts neuroprotective effects in mixed neuroglial cultures and organotypic hippocampal slices via peroxisome proliferator-activated receptor-alpha. *J. Neuroinflammation.* 9, 49. doi: 10.1186/1742-2094-9-49

Serviddio, G., Romano, A. D., Cassano, T., Bellanti, F., Altomare, E., and Vendemiale, G. (2011). Principles and therapeutic relevance for targeting mitochondria in aging and neurodegenerative diseases. *Curr. Pharm. Des.* 17, 2036–2055. doi: 10.2174/138161211796904740

Sharma, N., Tramutola, A., Lanzillotta, C., Arena, A., Blarzino, C., Cassano, T., et al. (2019). Loss of biliverdin reductase-A favors Tau hyper-phosphorylation in Alzheimer's disease. *Neurobiol. Dis.* 125, 176–189. doi: 10.1016/j.nbd.2019.02.003

Shonk, T. K., Moats, R. A., Gifford, P., Michaelis, T., Mandigo, J. C., Izumi, J., et al. (1995). Probable Alzheimer disease: diagnosis with proton MR spectroscopy. *Radiology* 195, 65–72. doi: 10.1148/radiology.195.1.7892497

Skaper, S. D., Buriani, A., Dal, T. R., Petrelli, L., Romanello, S., Facci, L., et al. (1996). The ALIAmide palmitoylethanolamide and cannabinoids, but not anandamide, are protective in a delayed postglutamate paradigm of excitotoxic death in cerebellar granule neurons. *Proc. Natl. Acad. Sci. U. S. A.* 93, 3984–3989. doi: 10.1073/pnas.93.9.3984

Sullivan, P. G., and Brown, M. R. (2005). Mitochondrial aging and dysfunction in Alzheimer's disease. *Prog. Neuropsychopharmacol. Biol. Psychiatry* 29, 407–410. doi: 10.1016/j.pnpbp.2004.12.007

Sweet, R. A., Panchalingam, K., Pettegrew, J. W., McClure, R. J., Hamilton, R. L., Lopez, O. L., et al. (2002). Psychosis in Alzheimer disease: postmortem magnetic resonance spectroscopy evidence of excess neuronal and membrane phospholipid pathology. *Neurobiol. Aging* 23, 547–553. doi: 10.1016/S0197-4580(02)00009-X

Tomasini, M. C., Borelli, A. C., Beggiato, S., Ferraro, L., Cassano, T., Tanganelli, S., et al. (2015). Differential effects of palmitoylethanolamide against amyloid-beta induced toxicity in cortical neuronal and astrocytic primary cultures from wild-type and 3xTg-AD Mice. *J. Alzheimers Dis.* 46, 407–421. doi: 10.3233/JAD-143039

Tomasini, M. C., Ferraro, L., Bebe, B. W., Tanganelli, S., Cassano, T., Cuomo, V., et al. (2002). Delta(9)-tetrahydrocannabinol increases endogenous extracellular glutamate levels in primary cultures of rat cerebral cortex neurons: involvement of CB(1) receptors. *J. Neurosci. Res.* 68, 449–453. doi: 10.1002/jnr.10242

Tramutola, A., Sharma, N., Barone, E., Lanzillotta, C., Castellani, A., Iavarone, F., et al. (2018). Proteomic identification of altered protein O-GlcNAcylation in a triple transgenic mouse model of Alzheimer's disease. *Biochim. Biophys. Acta Mol. Basis. Dis.* 1864, 3309–3321. doi: 10.1016/j.bbadis.2018.07.017

Valenza, M., Facchinetti, R., Menegoni, G., Steardo, L., and Scuderi, C. (2021). Alternative targets to fight Alzheimer's disease: focus on astrocytes. *Biomolecules.* 11. doi: 10.3390/biom11040600

Von, K. M., Kunnecke, B., Metzger, F., Steiner, G., Richards, J. G., Ozmen, L., et al. (2005). Altered metabolic profile in the frontal cortex of PS2APP transgenic mice, monitored throughout their life span. *Neurobiol. Dis.* 18, 32–39. doi: 10.1016/j.nbd.2004.09.005

Vos, M., Lauwers, E., and Verstreken, P. (2010). Synaptic mitochondria in synaptic transmission and organization of vesicle pools in health and disease. *Front. Synaptic. Neurosci.* 2, 139. doi: 10.3389/fnsyn.2010.00139

Wurtman, R. J., Blusztajn, J. K., and Maire, J. C. (1985). "Autocannibalism" of choline-containing membrane phospholipids in the pathogenesis of Alzheimer's disease-A hypothesis. *Neurochem. Int.* 7, 369–372. doi: 10.1016/0197-0186(85)90127-5

Yao, J., Irwin, R. W., Zhao, L., Nilsen, J., Hamilton, R. T., and Brinton, R. D. (2009). Mitochondrial bioenergetic deficit precedes Alzheimer's pathology in female mouse model of Alzheimer's disease. *Proc. Natl. Acad. Sci. U. S. A.* 106, 14670–14675. doi: 10.1073/pnas.0903563106

Conflict of Interest: The authors declare that the research was conducted in the absence of any commercial or financial relationships that could be construed as a potential conflict of interest.

frontiers | Frontiers in Aging Neuroscience

ORIGINAL RESEARCH
published: 06 July 2022
doi: 10.3389/fnagi.2022.946297

Aβ/Amyloid Precursor Protein-Induced Hyperexcitability and Dysregulation of Homeostatic Synaptic Plasticity in Neuron Models of Alzheimer's Disease

Isak Martinsson[1,2], Luis Quintino[3], Megg G. Garcia[1,2], Sabine C. Konings[1], Laura Torres-Garcia[1,4], Alexander Svanbergsson[4], Oliver Stange[1], Rebecca England[1], Tomas Deierborg[2], Jia-Yi Li[4], Cecilia Lundberg[3] and Gunnar K. Gouras[1]**

[1] Experimental Dementia Research Unit, Department of Experimental Medical Science, Lund University, Lund, Sweden, [2] Experimental Neuroinflammation Unit, Department of Experimental Medical Science, Lund University, Lund, Sweden, [3] CNS Gene Therapy, Department of Experimental Medical Science, Lund University, Lund, Sweden, [4] Neural Plasticity and Repair, Department of Experimental Medical Science, Lund University, Lund, Sweden

OPEN ACCESS

Edited by:
Jorge Busciglio,
University of California, Irvine,
United States

Reviewed by:
Agenor Limon,
University of Texas Medical Branch at Galveston, United States
Rakez Kayed,
University of Texas Medical Branch at Galveston, United States
Alfredo Lorenzo,
Instituto Ferreyra – INIMEC-CONICET-UNC, Argentina

***Correspondence:**
Isak Martinsson
isak.martinsson@med.lu.se
Gunnar K. Gouras
gunnar.gouras@med.lu.se

Specialty section:
This article was submitted to Cellular and Molecular Mechanisms of Brain-aging, a section of the journal Frontiers in Aging Neuroscience

Received: 17 May 2022
Accepted: 16 June 2022
Published: 06 July 2022

Citation:
Martinsson I, Quintino L, Garcia MG, Konings SC, Torres-Garcia L, Svanbergsson A, Stange O, England R, Deierborg T, Li J-Y, Lundberg C and Gouras GK (2022) Aβ/Amyloid Precursor Protein-Induced Hyperexcitability and Dysregulation of Homeostatic Synaptic Plasticity in Neuron Models of Alzheimer's Disease. Front. Aging Neurosci. 14:946297. doi: 10.3389/fnagi.2022.946297

Alzheimer's disease (AD) is increasingly seen as a disease of synapses and diverse evidence has implicated the amyloid-β peptide (Aβ) in synapse damage. The molecular and cellular mechanism(s) by which Aβ and/or its precursor protein, the amyloid precursor protein (APP) can affect synapses remains unclear. Interestingly, early hyperexcitability has been described in human AD and mouse models of AD, which precedes later hypoactivity. Here we show that neurons in culture with either elevated levels of Aβ or with human APP mutated to prevent Aβ generation can both induce hyperactivity as detected by elevated calcium transient frequency and amplitude. Since homeostatic synaptic plasticity (HSP) mechanisms normally maintain a setpoint of activity, we examined whether HSP was altered in AD transgenic neurons. Using methods known to induce HSP, we demonstrate that APP protein levels are regulated by chronic modulation of activity and that AD transgenic neurons have an impaired adaptation of calcium transients to global changes in activity. Further, AD transgenic compared to WT neurons failed to adjust the length of their axon initial segments (AIS), an adaptation known to alter excitability. Thus, we show that both APP and Aβ influence neuronal activity and that mechanisms of HSP are disrupted in primary neuron models of AD.

Keywords: amyloid, APP – amyloid precursor protein, synapse, calcium imaging, homeostatic synaptic plasticity (HSP), neuron

INTRODUCTION

Alzheimer's disease (AD) is the leading cause of dementia and the most common neurodegenerative disease. AD is characterized by the progressive, age-related accumulation and aggregation of disease-associated proteins, in particular amyloid-β (Aβ), which is cleaved from the amyloid precursor protein (APP). Multiple lines of genetic, clinical and biological evidence support the

involvement of Aβ in driving the loss of synapses and neurons that characterize the disease. However, preceding the massive neurodegeneration, AD features aberrant regional neuronal activity in the form of both hyper- and hypo-excitability, and evidence supports that the occurrence of network hyper-excitability early in the disease process is tied to elevated Aβ levels (Vossel et al., 2013; Zott et al., 2019). However, the precise mechanisms underlying this early Aβ-induced hyper-excitability remain unclear. In addition, the normal roles of Aβ/APP in brain physiology and their roles in pathophysiology during AD remain incompletely understood. Numerous lines of evidence indicate that synapses are sites of early pathogenesis in AD. APP mRNA is locally translated at post-synapses (Westmark and Malter, 2007) and APP protein is transported by fast axonal transport down axons (Koo et al., 1990), and the machinery to process APP to Aβ is localized to both pre- and post-synaptic sites. The presynaptic site is generally considered to process more APP to Aβ (Sadleir et al., 2016), although the role of neuron subtypes and anatomy in the subcellular location and generation of Aβ in brain remain poorly understood. The CA3 mossy fiber axonal terminals in the hippocampus, for example, are a site of high BACE1 levels and therefore could lead to high APP processing at presynapses (Sadleir et al., 2016). Numerous studies have reported detrimental electrophysiological, biological and behavioral effects of exogenously added Aβ on primary neurons, brain slices or murine brains *in vivo* (Abramov et al., 2009; Minkeviciene et al., 2009; Faucher et al., 2016). Emerging work indicates a complex interrelationship between intra- and extra-neuronal pools of Aβ, with the intraneuronal pool accumulating early on, prior to plaques (Roos et al., 2021). Aβ was shown to accumulate aberrantly in endosomes near synapses (Takahashi et al., 2002), where it can impair important endocytic pathways at synapses (Almeida et al., 2006). Normal synaptic function relies on regulated recycling, retrograde transport, secretion and degradation *via* endosomes that can be impaired by such aberrant protein aggregation (Perdigão et al., 2020). It is of considerable importance to parse out the earliest molecular steps in this synaptic dysfunction with AD. Primary cultures of neurons from AD transgenic mice have replicated *in vivo* phenotypes seen in AD, including increased endosome size (Willén et al., 2017) and loss of spines (Kashyap et al., 2019), and have shown Aβ-dependent reductions in important synaptic proteins, such as glutamate receptors, PSD-95 and synaptophysin (Almeida et al., 2005). Untangling the relative roles of Aβ and APP in AD also remains incomplete.

The coordinated firing of neurons across networks is considered to be crucial for cognitive function. To maintain their proper function and levels of activity, neurons employ homeostatic synaptic plasticity (HSP) and homeostatic intrinsic plasticity (HIP), which are means by which neurons can tune their activity to the global tonus of activity. Homeostatic scaling is an example of one such a tuning mechanism (Turrigiano et al., 1998), and other mechanisms of regulation are being investigated. These modulatory processes enable neuronal communication to be maintained within an appropriate window, allowing meaningful information transfer (Turrigiano, 2012). Recently, both APP and Aβ were implicated in the regulation of HSP (Gilbert et al., 2016; Galanis et al., 2021), indicating that these proteins play important roles beyond AD pathophysiology. Further, prior *in vivo* work in AD transgenic mice has suggested that HSP mechanisms might be impaired, since chronic hypo- or hyper-activity *via* either long term sleep deprivation or induction, or unilateral whisker removal, conditions in which HSP should be engaged, negatively impacted AD transgenic compared to wild-type (WT) mice (Kang et al., 2009; Tampellini et al., 2010). Recently, firing rate homeostasis was shown to be defective in APP/PS1 mice during sleep (Zarhin et al., 2022).

In this study, we set out to further elucidate the effects of APP and Aβ on calcium homeostasis in cultured primary neurons, a model system that allows for the exploration of underlying molecular and cellular biology more easily than *in vivo* in brain. To that end, we utilized primary neuronal cultures from APP/PS1 AD mutant transgenic mice and their WT counterparts and live-cell calcium imaging as a proxy for activity analyses of neuronal networks. We demonstrate that a general increase in transient calcium frequencies occurs both in the context of elevated APP or Aβ. Furthermore, we show that specifically CaMKII-positive excitatory neurons from AD transgenic mice exhibit higher amplitude calcium transients. Finally, we demonstrate the impaired ability of AD transgenic compared to WT neurons to properly initiate homeostatic plasticity mechanisms to adapt to global activity changes.

MATERIALS AND METHODS

Antibodies

The antibodies employed in this study were the following: mouse anti-beta-actin (Sigma-Aldrich, Sweden), rabbit anti-OC against high molecular weight Aβ (Merck Millipore, Sweden), mouse anti-6E10 for human Aβ/APP (BioLegend, Sweden), APPY188 rabbit anti C-terminal APP (Abcam, Sweden), rabbit anti-somatostatin (Abbexa, United Kingdom), mouse anti-GAD67 (Merck Millipore, Sweden), mouse anti-CaMKII (Merck Millipore, Sweden), mouse anti-ankyrin-G (Thermo Scientific, Sweden), guinea pig anti-Vglut1 (Synaptic Systems, Germany), rabbit anti-VGAT (Synaptic systems, Germany), rabbit anti-Gephyrin (Synaptic Systems, Germany), and chicken anti-MAP2 (Abcam, United Kingdom).

Neuronal Cell Culture

Primary neurons were cultured from the cortices and hippocampi of APP/PS1 AD transgenic mouse (APPswe, PSEN1dE9)85Dbo/Mmjax; Jackson Labs, Bar Harbor, ME, United States) and APP KO (Jackson labs, Bar Harbor, ME, United States, JAX 004133) mouse embryos at embryonic days 15–17 (E15-17). Neurons were cultured as previously described (Willén et al., 2017). Briefly, pregnant mice were anesthetized using isoflurane (MSD Animal Health, Stockholm, Sweden) and sacrificed. Embryos were quickly removed, and biopsies were taken for genotyping. Brains were dissected under constant cooling with chilled (∼4°C) Hanks balanced salt solution (HBSS; Thermo Scientific, Sweden) supplemented with 0.45% glucose (Thermo Scientific, Sweden). Cortices and hippocampi were

retrieved and incubated in 0.25% trypsin (Thermo Scientific, Sweden), followed by 2 washes with HBSS. Brain tissue was then triturated in 10% fetal bovine serum (FBS) supplemented Dulbecco's modified Eagle medium (DMEM; Thermo Scientific, Sweden) with 1% penicillin-streptomycin (Thermo Scientific, Sweden) using glass pipettes until neurons were dissociated. Neurons were plated onto 8 well- plates (for calcium imaging; Ibidi), 6 well plates (for Western blot; Sarstedt, Germany) or glass coverslips in 24 well plates (for immunolabeling; Sarstedt, Germany) coated with Poly-D-lysine (Sigma-Aldrich, Sweden). Neurons were plated with 10% FBS and 1% penicillin-streptomycin in DMEM; following 3–5 h incubation, media was exchanged for complete Neurobasal solution, consisting of Neurobasal medium, B27 supplement, penicillin-streptomycin, and L-glutamine (Thermo Scientific, Sweden). One embryo corresponds to one set of cultures. All animal experiments were performed in accordance with the ethical guidelines and were approved by the Animal Ethical Committee at Lund University ethical permit number 5.8.18-05983/2019.

Genotyping

Genotyping was carried out using the PCRbio Rapid Extract PCR kit (Techtum, Sweden). In brief, biopsies were incubated with 70 μl distilled H_2O, 20 μl 5× PCRbio buffer A (lysis buffer) and 10 μl 10× PCRbio buffer B (protease containing buffer) per vial at 75°C for 5 min, followed by heating to 95°C for 10 min. The vials were placed on ice and allowed to cool before vortexing for 3–4 s and centrifuged at 10,000 rpm for 1 min to pellet the debris. The DNA supernatant was then transferred to a new vial. The DNA supernatant was either used directly or stored at −20°C. For PCR, 1 μl of DNA was incubated with 9.5 μl distilled H_2O, 12.5 μl 2× PCRbio rapid PCR mix (containing Taq polymerase for DNA amplification), 1 μl primer-set F (APP knockout) and 1 μl primer-set G (APP WT; both 10 μM) for 3 min at 95°C. The temperature was decreased to 55°C for 15 s to allow for the annealing of primers. The temperature was then increased to 72°C for 5 min to allow for the extension of DNA. DNA bands were detected using agarose gel electrophoresis.

Viral Vectors

We used lentiviral vectors carrying TdTomato, hAPPwt, or hAPPmv (mutant APP resistant to BACE cleavage) under a CaMKII promoter; the genes were inserted *via* Gene synthesis (Thermo Fischer Scientific, United Kingdom) into a plasmid compatible with Gateway technology to serve as an entry clone. Production and titration were performed as previously described (Quintino et al., 2013). Primary neurons were transduced at 12–13 days *in vitro* (DIV) at a multiplicity of infection (MOI) of 5 and analyzed at 19–21 DIV.

Treatments

Cultured neurons at 19–21 DIV were treated with different compounds before live cell imaging, immunofluorescence or western blot experiments: thiorphan (500 nM, 1 h; Sigma-Aldrich, Sweden), TTX [1 μM, acute (0–1 h) or 48 h], bicuculline [20 μM, acute (0–1 h) or 48 h], picrotoxin (10 μM, 1 h), CNQX (10 μM, 1 h) (Sigma-Aldrich, Sweden), and synthetic Aβ1-42 (Tocris, United Kingdom) and synthetic reverse Aβ42-1 (Tocris, United Kingdom) reconstituted in dimethyl sulfoxide (DMSO) to 250 mM, sonicated 10 min and then centrifuged at 10,000 g for 15 min before adding the supernatant to cell culture media.

Western Blot

Cell lysates were prepared using modified RIPA buffer containing 50 mM Tris-HCl (pH 7.4), 150 mM NaCl, 1 mM EGTA, 1% NP-40, 0.25% sodium deoxycholate with added protease and phosphatase inhibitor cocktail II (Sigma-Aldrich, Sweden). BCA protein assay kit (Thermo Scientific, Sweden) was used to determine protein concentrations. Equal amounts of protein from each sample were loaded into 10–20% Tricine sodium dodecyl sulfate–polyacrylamide gel electrophoresis (SDS-PAGE; Sigma-Aldrich, Sweden), followed by immunoblotting on polyvinylidene difluoride (PVDF) membranes (Sigma-Aldrich, Sweden) and intensity quantification was carried out using Image Lab 5.2.1.

Live-Cell Imaging

Cultured neurons at 19–21 DIV were incubated with 3 μM of the calcium dye Fluo-4 AM (Thermo Scientific, Sweden) in DMSO (Sigma-Aldrich, Sweden) for 30 min before imaging. Cells were imaged under a Nikon Eclipse Ti microscope at 10× with 1.4 NA. Live cell imaging chamber (Okolab, Italy) was kept at 5% CO_2 and 37°C. Cells were imaged every 100 ms for a duration of 2 min with an iXon Ultra CCD camera (ANDOR Technology, United Kingdom). Multiple 2 min timestacks were captured from each experimental group.

Calcium Imaging Analysis

Time-stacks of calcium imaging files were opened in FiJi; individual Regions of interest (ROIs) were drawn around cell bodies and ROIs were determined to be CaMKII+ or CaMKII- based on TdTomato labeling. Fluorescence intensity over time was extracted, processed and normalized in the MatLab script PeakCaller (Artimovich et al., 2017). Spike frequencies and amplitudes were extracted, and raster plots were generated in MatLab. Spike detection threshold was set to 10% above baseline; for calculation of frequency all neurons including silent (<1 Peak per 2 min) were included in analysis. For calculation of amplitude heights and interspike intervals, however; silent neurons were excluded as these would bias the measurement and underestimate the amplitude heights and give misleading values in interspike intervals. Therefore number of neurons differ between frequency measurements and amplitude/interspike interval measurements.

Immunofluorescence

Cultured neurons at 19–21 DIV were fixed in 4% paraformaldehyde (PFA) in PBS with 0.12 M sucrose for 20 min, at room temperature (RT). Cells were then blocked in 0.1% saponin (Sigma-Aldrich, Sweden), 1% bovine serum albumin (BSA; Sigma-Aldrich, Sweden) and 2% normal goat serum (NGS; Thermo Scientific, Sweden) in PBS for 1 h at RT. Cells were incubated in primary antibody (diluted in 2% NGS in PBS) overnight at 4°C. Cells were rinsed in PBS and incubated

with secondary antibodies diluted in 2% NGS in PBS. Cells were rinsed in PBS and counterstained with DAPI diluted at 1:2000 (Sigma-Aldrich, Sweden). Imaging was performed with an inverted Olympus IX70 epifluorescence or an inverted Leica SP8 confocal microscope.

Image Analysis

Neurons were labeled for inhibitory or excitatory pre- and post-synaptic markers; CaMKII and VGLUT1 for excitatory synapses and Gephyrin and VGAT for inhibitory synapses. Images were then processed in the ImageJ plugin: SynaptcountJ. SynaptCountJ is a semi-automated plugin for measuring synapse density (Mata et al., 2017). By colocalization of two different excitatory or inhibitory synaptic markers one can count the number of excitatory and inhibitory synapses per neuron along with other morphological parameters such as dendritic length. For CaMKII cell quantification 19–21 DIV APP/PS1 and WT neuronal cultures were labeled with DAPI, CaMKII, and MAP2. Images were sampled at 20× in an inverted Olympus IX70 epifluorescence microscope and analyzed with the "cell-counter" plugin in ImageJ as percent CaMKII positive out of all MAP2 positive neurons. For analysis of axon initial segment length, ankyrin-G positive axon initial segments were traced and measured in ImageJ by a blinded experimenter.

Experimental Design and Statistical Analysis

All statistical analyses were performed with GraphPad Prism 8.3. Sample size was denoted as n = number of cells analyzed and N = sets of cultures. Data was first tested for normality using D'Agostino-Pearson omnibus K2 normality test to determine the appropriate statistical test. No specific statistical analysis was performed to determine sample size. Mann–Whitney (two groups) or Kruskal–Wallis (3 or more groups) tests were used to compare distribution of data between groups unless otherwise stated. Correction for multiple testing was performed with Dunn's correction unless otherwise stated. Graphs are expressed as mean ± 95% confidence interval (CI) with individual values plotted as dots unless otherwise stated in figure legend. Differences were considered significant at $^{*}p < 0.05$, $^{**}p < 0.01$, $^{***}p < 0.001$; $^{****}p < 0.0001$, n.s., not significant.

RESULTS

Characterization of Corticohippocampal Amyloid Precursor Protein/PS1 Transgenic Cultures

To study AD-related neuronal activity alterations *in vitro*, primary cortico-hippocampal neurons from APP/PS1 AD transgenic mice and their WT littermates were loaded with the calcium indicator Fluo-4 AM and imaged for calcium transients using a live cell imaging microscope. Mixed cortico-hippocampal neurons were used, since AD is characterized by cortical and hippocampal pathology. Live cell calcium imaging is used as a proxy of neuronal activity, although actual neuronal excitation and firing can deviate significantly from calcium levels (Gavello et al., 2018). Representative raster plots and calcium traces demonstrate that neurons from both APP/PS1 transgenic and WT mice were spontaneously active (**Supplementary Figures 1A–D**). APP/PS1 neurons overall had increased frequencies of calcium transients and higher amplitudes of calcium spikes compared to WT neurons (**Figures 1A–D**). Inter-spike intervals were also altered in APP/PS1 neurons, which had shorter inter-spike intervals than WT neurons (**Figure 1E**). Moreover, APP/PS1 cultures had fewer inactive neurons compared to WT cultures (**Figure 1F**), consistent with the other signs of increased excitability.

During early development, GABA can have excitatory effects in culture (Doshina et al., 2017). Normally, GABA signaling in culture shifts to being primarily inhibitory at around 14 days *in vitro* (DIV). However, because APP/PS1 neurons may have altered neuronal development due to constitutively over-expressing mutant APP and presenilin (Handler et al., 2000; Rama et al., 2012), the increased activity seen in 19–21 DIV cultures could, in part, have been due to excitatory GABA signaling. Thus, we tested whether GABA signaling had inhibitory or excitatory effects in our presumably mature 19–21 DIV APP/PS1 neurons by treating them with $GABA_A$ blockers bicuculline and picrotoxin. Blocking GABA signaling in the APP/PS1 cultures led to an increased frequency and synchronicity of firing, indicating that GABA had inhibitory effects in our cultures similar to that of WT cultures (**Figure 1G**). The addition of 1 μm TTX stopped most calcium transients in both WT and APP/PS1 neurons (**Figure 1G**), indicating that the majority of calcium transients that were detected were triggered by sodium channel activity.

Hyperactivity of Excitatory Neurons in Amyloid Precursor Protein/PS1 Cultures

To parse out the contributions of excitatory and inhibitory neurons in driving the hyperactivity in APP/PS1 cultures, we transduced neurons with a vector to induce the expression of TdTomato under a CaMKII promoter (**Figure 2A**), allowing us to distinguish excitatory neurons from putative GABAergic interneurons (**Figure 2B**) in imaged FOVs. Interestingly, we detected increased activity in CaMKII-positive APP/PS1 neurons compared to CaMKII-positive WT neurons. In contrast, activity levels in CaMKII-negative neurons were similar between APP/PS1 and WT cultures (**Figure 2C**). Furthermore, CaMKII-positive neurons had higher amplitude calcium transients compared to CaMKII-negative neurons in APP/PS1 but not WT cultures (**Figure 2D**).

We next sought to investigate whether an imbalance in the proportion of excitatory to inhibitory neurons and synapses could underlie the increased levels of activity in APP/PS1 neurons. To do this, we evaluated the relative levels of select proteins known to be localized in either excitatory or inhibitory neurons. Immunoblotting against CaMKII and GAD67, markers expressed by nearly all excitatory and inhibitory neurons, respectively, showed no differences in the levels of CaMKII and GAD67 between APP/PS1 and WT neurons (**Figures 3A–C**).

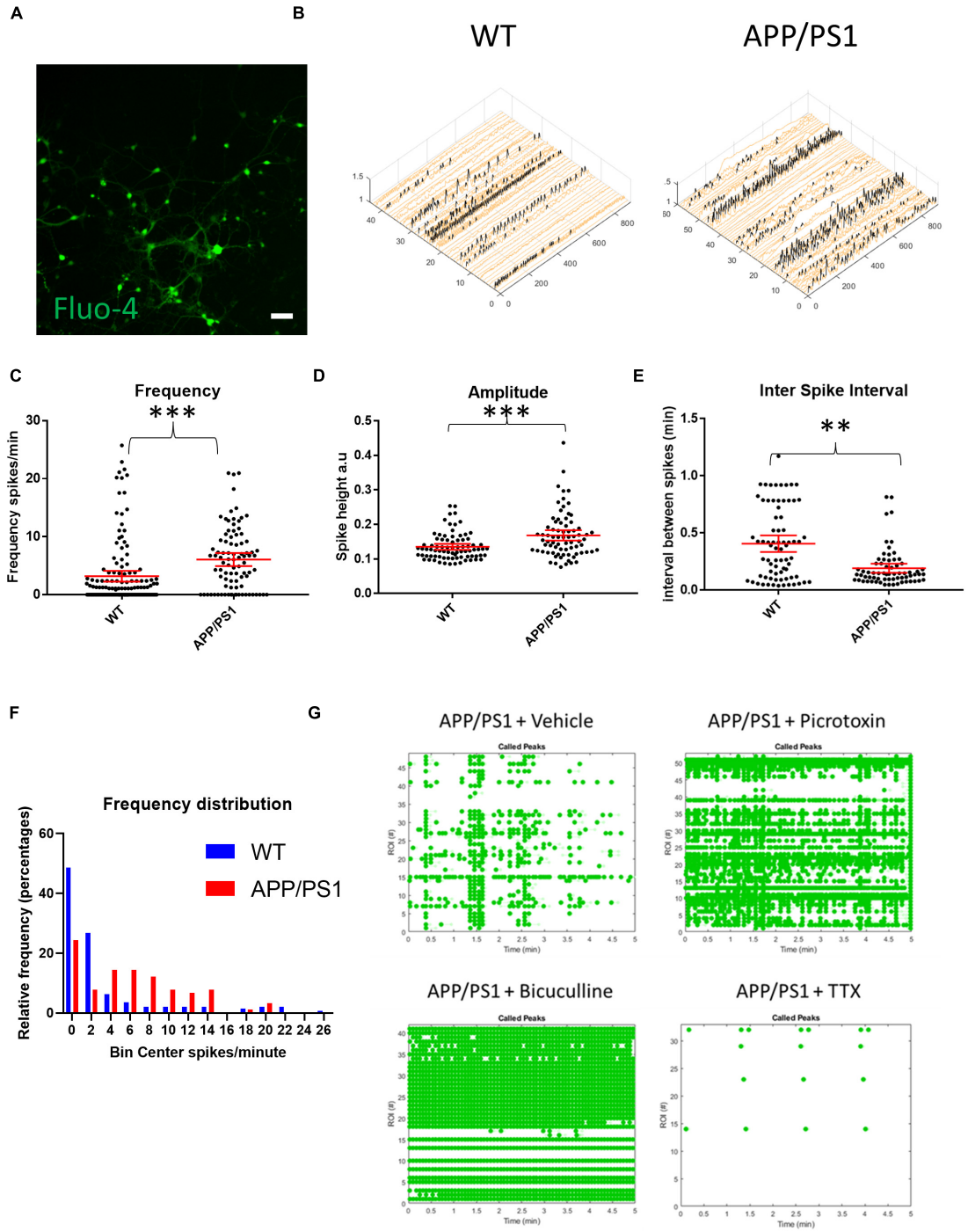

FIGURE 1 | Increased spontaneous activity in APP/PS1 primary neurons. **(A)** Representative micrograph of cultured neurons loaded with Fluo4. **(B)** Representative calcium traces from WT and APP/PS1 field of views (FOVs), black spikes are recognized by the Peakcaller algorithm. *X*-axis shows region of interest (ROI) number, *Y*-axis shows amplitude and *Z*-axis shows time point. **(C)** Frequency of firing (spikes per minute) is increased in APP/PS1 compared to WT neurons (APP/PS1 mean = 6.072, CI = 4.948–7.197, $n = 90$ compared to WT mean = 3.184, CI = 2.25–4.118, $n = 142$, $p < 0.0001$). **(D)** Amplitudes of spikes are increased in APP/PS1 compared to WT neurons (APP/PS1 mean = 0.1682, CI = 0.1532–0.1833, $n = 76$, compared to WT mean = 0.1352, CI = 0.1266–0.1437, $n = 80$, $p = 0.0003$). **(E)** Inter-spike interval distributions differ between APP/PS1 compared to WT neurons with more of the APP/PS1 neurons having low inter-spike intervals ($p = 0.0011$ using Kolmogorov–Smirnoff test). **(F)** Frequency distribution of firing frequencies of APP/PS1 compared to WT neurons shown in a graph; note higher percentage of WT neurons in the inactive bins; WT inactive = 69, APP/PS1 inactive = 22, WT active = 73 and APP/PS1 active 68, $p = 0.0003$, Fisher's exact test; $N = 4$ cultures. **(G)** Representative Raster plot of APP/PS1 neurons treated with vehicle (sterile milliQ water), 10 μM of picrotoxin, 20 μM of bicuculline or 1 μM of tetrodotoxin (TTX); neurons were imaged every 100 ms for 5 min with detected spikes represented as green dots. Mann–Whitney *U* test; $^{**}p < 0.01$, $^{***}p < 0.001$; scale bar: 50 μm.

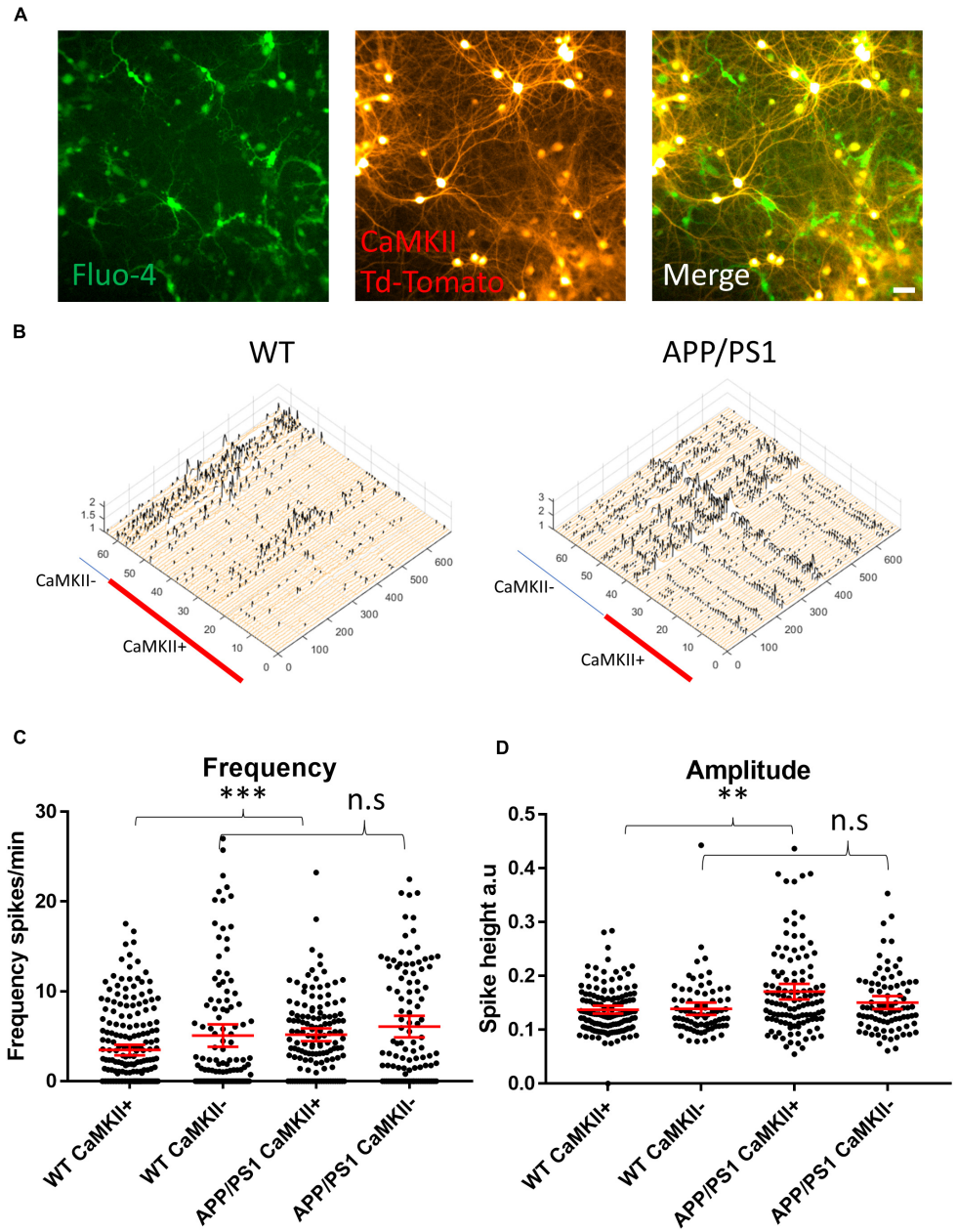

FIGURE 2 | Increased amplitude and frequency of spontaneous calcium transients in CaMKII positive excitatory neurons. **(A)** Micrograph provides an example of an image of Fluo-4 (green) and CaMKII TdTomato (red) neurons in culture. **(B)** Representative calcium traces from WT and APP/PS1 FOVs, black spikes are recognized by the Peakcaller algorithm. *X*-axis shows ROI number, *Y*-axis shows amplitude and *Z*-axis shows time point. The red line shows which ROIs belonged to CaMKII positive neurons in the representative FOVs. **(C)** Graph showing increase in spike frequency (spikes per minute) of APP/PS1 CaMKII positive compared to WT CaMKII positive neurons (APP/PS1 mean = 5.176, CI = 4.456–5.896, $n = 133$ compared to WT mean = 3.479, CI = 2.9–4.057, $n = 205$, $p = 0.0001$). In contrast, spike frequency of CaMKII negative APP/PS1 neurons did not significantly differ from WT CaMKII negative neurons (APP/PS1 mean = 6.094, CI = 4.898–7.291, $n = 108$ compared to WT mean = 5.083, CI = 3.837–6.328, $n = 114$, $p = 0.124$). **(D)** Amplitude of transients is increased specifically in APP/PS1 compared to WT CaMKII positive excitatory neurons (APP/PS1 mean = 0.171, CI 0.1566–0.1856, $n = 115$, compared to WT mean = 0.1375, CI = 0.1304–0.1446, $n = 138$, $p = 0.0024$). In contrast, the amplitude of transients in CaMKII negative neurons did not differ between APP/PS1 and WT neurons (APP/PS1 mean = 0.1505, CI = 0.1385–0.1625, $n = 85$, compared to WT mean = 0.1391, CI = 0.1275–0.1506, $n = 78$, $p = 0.302$); $N = 3$. Kruskal–Wallis test with Dunn's correction for multiple comparisons. n.s = not significant, $^{*}p < 0.05$, $^{**}p < 0.01$, $^{***}p < 0.001$; scale bar: 50 μm.

Likewise, analyses of neurons immunolabelled for glutamatergic (VGluT and CaMKII) and GABAergic (vGAT and gephyrin) synaptic markers using the image analysis plugins NeuronJ and Synapcount (Mata et al., 2017) did not show significant differences between APP/PS1 and WT cultures (**Figures 3D–F**). Similarly, counting CaMKII positive cells as a percentage of

all MAP2 positive cells per culture did not show a significant difference between the percentage of CaMKII neurons in WT and APP/PS1 neuronal cultures (**Figure 3G**). However, consistent with prior work (Siskova et al., 2014), our analyses did show decreased dendritic length in APP/PS1 compared to WT neurons (**Figures 3H,I**).

Individual Contributions of Amyloid Precursor Protein and Aβ to Neuronal Hyperactivity

To dissect out the individual role of APP on neuronal activity, we investigated whether APP over-expression alone without a concomitant elevation in Aβ could cause hyper-activity by transducing WT neurons with constructs encoding either mutant human APP resistant to BACE cleavage (hAPPmv) (Kamenetz et al., 2003) or WT human APP (hAPPwt), both under a CaMKII promoter. Remarkably, the expression of either APP construct in WT neurons led to an increase in the frequency and amplitude of calcium transients (**Figures 4A,B**), indicating an Aβ-independent effect of APP on neuronal activity in excitatory neurons.

Likewise, we sought to investigate whether increased Aβ levels alone could induce hyper-activity. We wanted to increase Aβ levels in WT cultures without affecting APP and PS1 as this could confound our results, since we provide evidence that overexpression of APP has Aβ-independent effects on neuronal activity, while PS1 has been shown to alter calcium signaling (Lerdkrai et al., 2018). Therefore, we utilized an inhibitor of the Aβ degrading enzyme neprilysin, which increases Aβ levels (Abramov et al., 2009), primarily at synapses, as neprilysin is highly expressed pre-synaptically (Iwata et al., 2004; Abramov et al., 2009). After 1 h of treatment with the neprilysin inhibitor thiorphan (500 nM), calcium transient frequencies (**Figure 4C**) and amplitudes (**Figure 4D**) were increased in WT primary neurons. Interestingly, thiorphan led to a greater increase in firing frequency in CaMKII-positive compared to CaMKII-negative neurons (**Figure 4E**). As neprilysin also degrades other peptides, such as substance P and neurokinin A, as a control, we assessed the effect of thiorphan treatment on APP knockout (KO) neurons, which lack APP and, thus, the capacity to generate Aβ. Indeed, calcium transient frequencies and amplitudes from APP KO neurons treated with thiorphan did not significantly differ from APP KO neurons treated with vehicle alone (**Figure 4F**), supporting the conclusion of elevated Aβ levels as driving the hyperactivity in WT neurons treated with thiorphan. However, APP KO neurons have been shown to have altered synaptic composition (Martinsson et al., 2019) and calcium transients (Yang et al., 2009), which could potentially mask effects by thiorphan. Therefore, as an alternative to investigate elevated Aβ levels on hyperactivity, we added exogenous synthetic Aβ peptide to WT cultures.

Immunolabeling WT neuronal cultures treated with 0.5 μM of synthetic human Aβ1–42 for 2 h with the human-specific Aβ/APP antibody 6E10 showed that the added exogenous Aβ1–42 localized to the dendritic spines of CaMKII-TdTomato expressing neurons (**Figures 5A,B**). This was consistent with prior findings showing that exogenous Aβ1–42 preferentially binds to synapses of CaMKII-immunoreactive neurons (Willen et al., 2017). Interestingly, we detected marked colocalization of the added human Aβ1–42 with the fibril and fibrillar oligomer-specific antibody OC that detects amyloid structures (Hatami et al., 2014), indicating aggregation of the exogenous Aβ1–42 at synapses, which is consistant with prior work (Willén et al., 2017). While for these experiments we added supraphysiological levels of Aβ1–42 (0.5 μM), in order to more readily visualize its localization, we next assayed what effect more physiological Aβ1–42 increases would have on calcium oscillations. Given that physiological levels of Aβ are in the picomolar range and that picomolar levels of exogenous Aβ were reported to increase LTP (Puzzo et al., 2008), we added 200 pM of synthetic human Aβ1–42 acutely to mouse WT neuronal cultures expressing CaMKII-driven TdTomato. Addition of 200 pM synthetic Aβ to WT cultures led to modest increases in the firing frequencies of both CaMKII-positive and CaMKII-negative neurons (**Figure 5C**). In addition, these picomolar levels of Aβ1–42 led to increased amplitudes of calcium oscillations in CaMKII-positive neurons but not CaMKII-negative neurons (**Figure 5D**). However, higher concentrations of synthetic Aβ1–42 (500 nM) did not lead to significantly increased calcium oscillations (**Figure 5E**), though 500 nM of synthetic Aβ1–40 did lead to a robust increase in firing frequency. In summary, our results support the concept that APP and Aβ can independently induce increases in synaptic activity, which likely plays a role under physiological and pathological conditions.

Dysregulated Homeostatic Plasticity in Amyloid Precursor Protein/PS1 Neurons

Since we showed that elevating either APP or Aβ in WT neurons can increase neuronal activity, we hypothesized that the continuously high levels of APP and Aβ in APP/PS1 neurons disrupt neuronal network activity and function, and speculated that HSP mechanisms, which help maintain synaptic firing within the boundaries of meaningful communication (Turrigiano, 2008), might be impaired in AD transgenic neurons and, as a result, may no longer be effective at returning activity levels back to a baseline. Dysfunctional HSP could explain part of the sustained hyperexcitability observed in neurons from AD transgenic mouse models. We therefore hypothesized that long-term high levels of Aβ/APP might impair homeostatic plasticity. This can be tested by manipulating neuronal firing outside of a network's set point, leading to plasticity changes that maintain the baseline activity level. We therefore initially treated APP/PS1 and WT neurons with TTX and bicuculline, which should immediately decrease network activity and increase network activity, respectively (Turrigiano et al., 1998). Indeed, acute treatment of WT and APP/PS1 neurons with TTX and bicuculline led to the expected decreased and increased activity, respectively (**Supplementary Figures 1E,F**). Next we treated WT and APP/PS1 neurons with TTX or bicuculline for a longer period of time (48 h), which are established methods for inducing HSP (Turrigiano et al., 1998). Interestingly, 48 h of TTX treatment led to a sharp decrease by western blot in total APP protein levels in both WT and APP/PS1 neurons (**Figures 6A,B**),

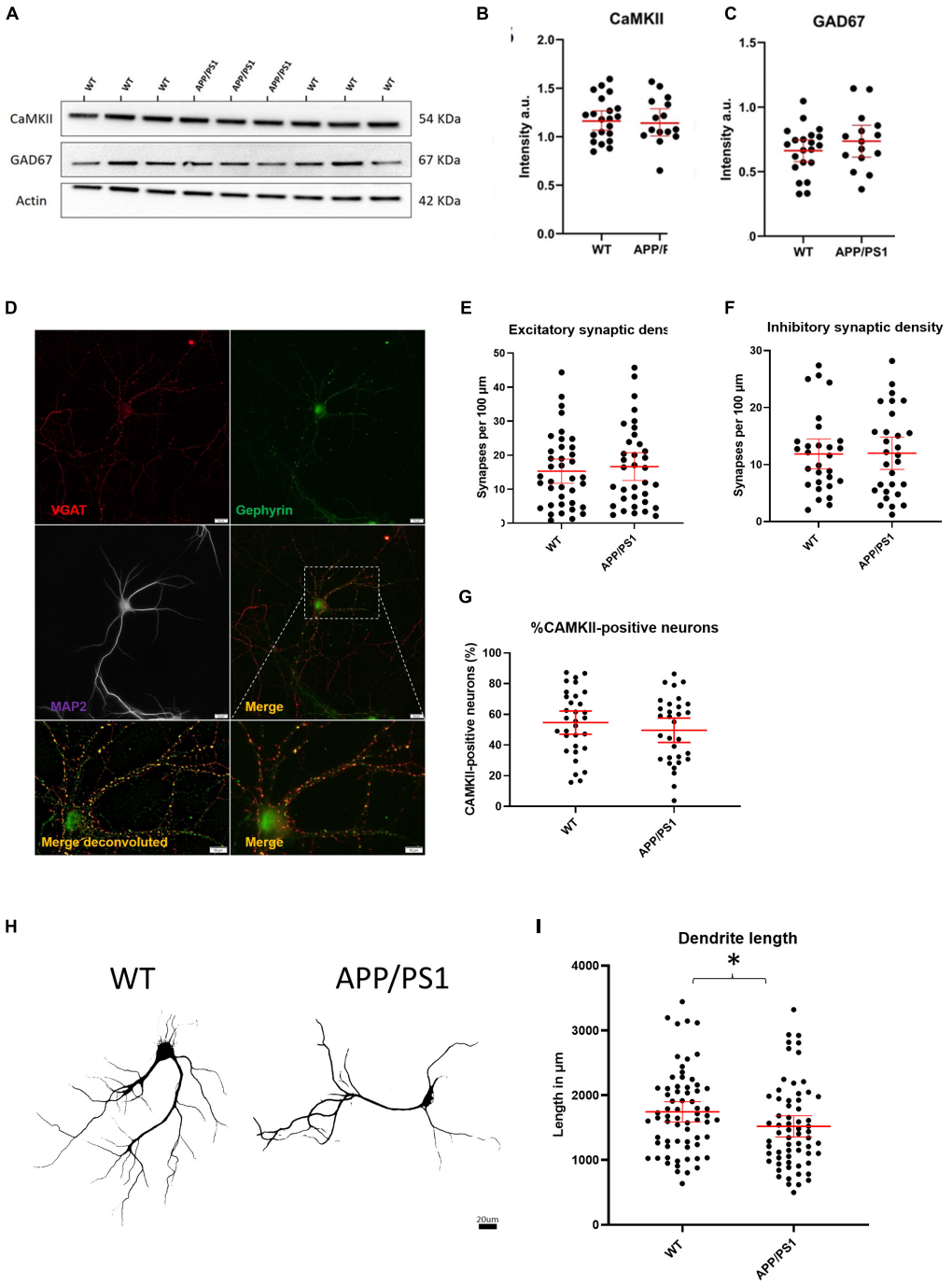

FIGURE 3 | No evidence for gross imbalances in excitatory/inhibitory neurons/synapses in APP/PS1 compared to WT neurons. **(A)** Representative western blot of CaMKII and GAD67 protein levels with actin as loading control. **(B)** Quantification of western blot of CaMKII in **(A)** (APP/PS1 mean = 1.164, CI = 1.030–1.298, n = 15 and WT mean = 1.181, CI = 1.080–1.282, n = 21, p = 0.8270). **(C)** Quantification of western blot of GAD67 in **(A)** (APP/PS1 mean = 0.7359, CI = 0.6129–0.8589, n = 15 and WT mean = 0.6620, CI = 0.5774–0.7466, n = 21, p = 0.2860, unpaired t-test). **(D)** Representative micrograph showing WT neuron labeled with VGAT (red), Gephyrin (green) and MAP2 (magenta). Lower panels show an enlarged view of neuron both with (left) and without (right) deconvolution. Scale bar = 20 µm and for Merge, 10 µm. **(E)** Graph depicting excitatory synaptic density from VGLUT/CAMKII overlap divided by neurite length (APP/PS1 mean = 16.64., CI = 12.53–20.74, n = 35 and WT mean = 15.28, CI = 11.74–18.83, n = 38, p = 0.6129, unpaired t-test). **(F)** Graph depicting inhibitory synaptic density from VGAT/Gephyrin overlap divided by neurite length (APP/PS1 mean = 12.00, CI = 9.160–14.84, n = 29 and WT mean = 11.87, CI = 9.243–14.50, n = 29 p = 0.9458). **(G)** Graph depicting quantification of percentage CaMKII neurons in WT and AD cultures. (APP/PS1 mean = 49.61% CaMKII positive neurons CI = 41.67–57.54% compared to WT mean = 54.64% CI = 47.08–62.14%, p = 0.35, unpaired t-test). **(H)** Representative binary images of WT and APP/PS1 neurons labeled for MAP2; scale bar = 20 µm. **(I)** Graph showing decreased dendrite length in APP/PS1 compared to WT neurons (APP/PS1 mean = 1518, CI = 1355–1682, n = 64, and WT mean = 1744, CI = 1588–1900. N = 67, p = 0.045, unpaired t-test). *p < 0.05.

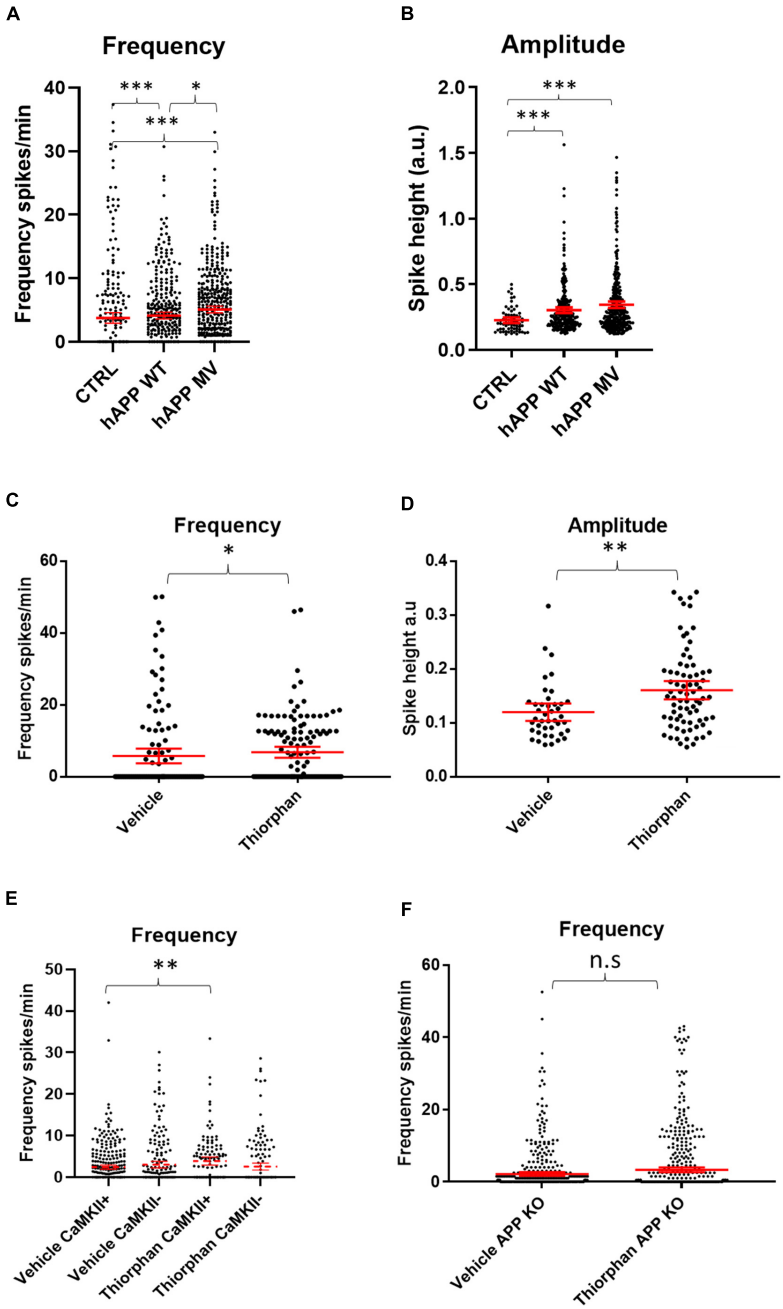

FIGURE 4 | Amyloid precursor protein and Aβ increase calcium oscillation frequency and amplitude. **(A)** Graph depicts firing frequencies in WT neurons transduced with a viral vector harboring hAPPwt or hAPPmv (BACE cleavage resistant) under a CaMKII promoter. Note that both hAPPwt and hAPPmv increase the firing frequency compared to control (CTRL), with hAPPmv having a stronger effect [hAPPmv mean = 5.087, CI = 4.542–5.633, n = 436; hAPPwt mean = 4.112, CI = 3.585–4.640, n = 375 and CTRL mean = 3.757, CI = 2.925–4.588, n = 292, p-values respective to CTRL = hAPPmv = 0.0001, hAPPwt = 0.0001, p-value hAPPmv compared to hAPPwt (p = 0.0259), Kruskal–Wallis Dunn's correction]. **(B)** Graph showing increased amplitude in neurons expressing hAPPwt and hAPPmv under CaMKII promoter (hAPPmv mean = 0.3444, CI = 0.3197–0.3691, n = 344 and hAPPwt mean = 0.3021, CI = 0.2808–0.3433, n = 278 and CTRL mean = 0.2256, CI = 0.2034–0.2479, n = 67, N = 3, p-values respective to CTRL; hAPPmv = 0.0001, hAPPwt = 0.0004, p-value, Kruskal–Wallis Dunn's correction). Kruskal–Wallis test with Dunn's correction for multiple comparisons. **(C)** WT neurons treated with 500 nM of the neprilysin inhibitor thiorphan for 1 h show increased firing frequency (thiorphan mean = 6.814, CI = 5.283–8.344, n = 133, compared to vehicle mean = 5.783, CI = 3.749–7.817, n = 125, N = 3, p = 0.0101). **(D)** The graph depicts increased spike amplitudes after 1 h of treatment of WT neurons with thiorphan (thiorphan mean = 0.1605, CI = 0.1436–0.1774, n = 76, compared to vehicle mean = 0.1198, CI = 0.1036–0.136, n = 42, p = 0.0012). **(E)** Graph showing increase in spike frequency of thiorphan treated CaMKII positive compared to vehicle treated CaMKII positive neurons (thiorphan mean = 3.905, CI = 2.942–4.869, n = 128 compared to vehicle mean = 2.432, CI = 1.934–2.931, n = 332, N = 3, p = 0.0089). In contrast, spike frequency of CaMKII negative thiorphan treated neurons did not significantly differ from vehicle treated CaMKII negative neurons (thiorphan mean = 2.566, CI = 1.726–3.406, n = 173 compared to vehicle mean = 3.018, CI = 2.243–3.794, n = 218, p = 0.0894). **(F)** Graph showing that thiorphan was ineffective at inducing increased frequency in APP KO neurons compared to vehicle (APP KO thiorphan mean = 3.329, CI = 2.692–3.967, n = 601 compared to APP KO vehicle mean = 2.196, CI = 1.689–2.704, n = 514, N = 3, p = 0.8604, Mann–Whitney U-test).; n.s = not significant, *$p < 0.05$, **$p < 0.01$, ***$p < 0.001$.

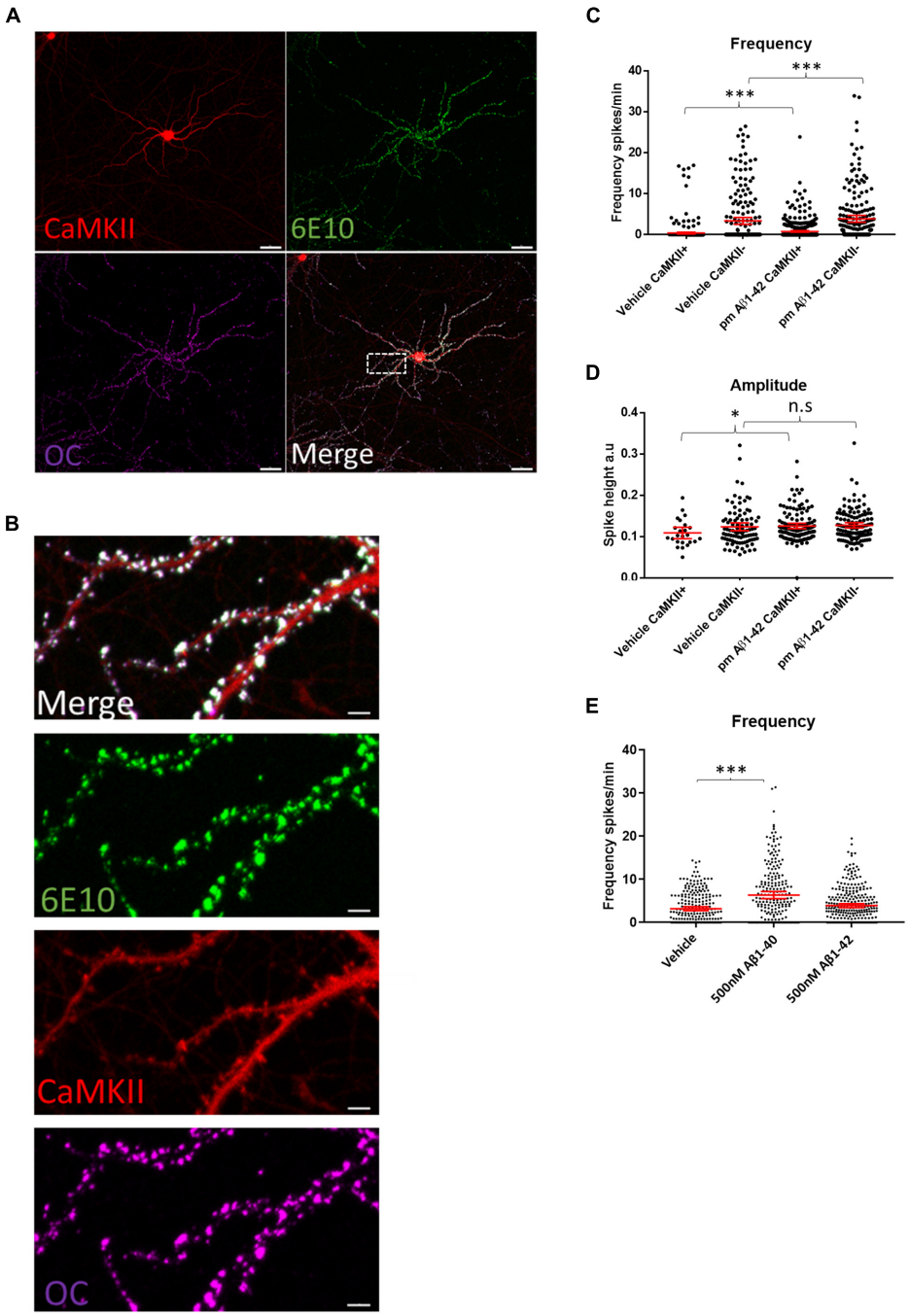

FIGURE 5 | Aβ preferentially binds synaptic compartments on CaMKII positive neurons and appears to have a dose dependent effect on spike frequency. **(A)** Micrograph showing that synthetic human Aβ1–42 preferentially binds to dendrites of CaMKII positive murine WT neurons; Td Tomato expressed through CaMKII promoter, human specific anti-Aβ antibody 6E10 (green) and conformation specific anti-amyloid antibody OC (magenta); scale bar = 50 μm. **(B)** Insert from **(A)** showing Aβ1–42 targeting synapses; note that antibody 6E10 labels the added synthetic human Aβ and that this is also labeled by the fibrillar oligomer antibody OC; scale bar = 5 μm. **(C)** WT neurons treated with 200 pM synthetic Aβ1–42 show increased spike frequency compared to DMSO treated vehicle control neurons both in CaMKII positive neurons (Aβ1–42 mean = 0.7554, CI = 0.5724–0.9383, n = 477, compared to vehicle mean = 0.367, CI = 0.1636–0.5704, n = 401, $p < 0.0001$) and in CaMKII negative neurons (Aβ1–42 mean = 3.829, CI = 3.033–4.685, n = 214, compared to vehicle mean = 3.346, CI = 2.508–4.183, n = 218). **(D)** Graph depicting increased amplitudes in CaMKII positive neurons treated with 200 pM Aβ1–42 compared with DMSO vehicle control (Aβ1–42 mean = 0.1256, CI = 0.119–0.1321, n = 128, compared to vehicle mean = 0.1087, CI = 0.09495–0.1225, n = 24, p = 0.045). However, CaMKII negative neurons did not show a significant increase in amplitude with Aβ treatment (Aβ1–42 mean = 0.1272, CI = 0.1209–0.1334, n = 133, compared to vehicle mean = 0.1235, CI = 0.114–0.133, n = 94, p = 0.2103). **(E)** Graph shows WT neurons treated with 500 nM Aβ1–42 or 500 nM Aβ1–40. While 500 nM Aβ1–42 leads to a slight but not significantly different distribution of activity, Aβ1–40 strongly increases activity (Aβ1–40 mean = 6.344, CI = 5.503–7.186, n = 235 and Aβ1–42 mean = 3.901, CI = 3.439–4.363, n = 287 compared to vehicle mean = 3.194, CI = 2.752–3.635, n = 255; p = 0.0001 and p = 0.14.); Kruskal–Wallis test, N = 3. n.s = not significant, $^{*}p < 0.05$, $^{***}p < 0.001$.

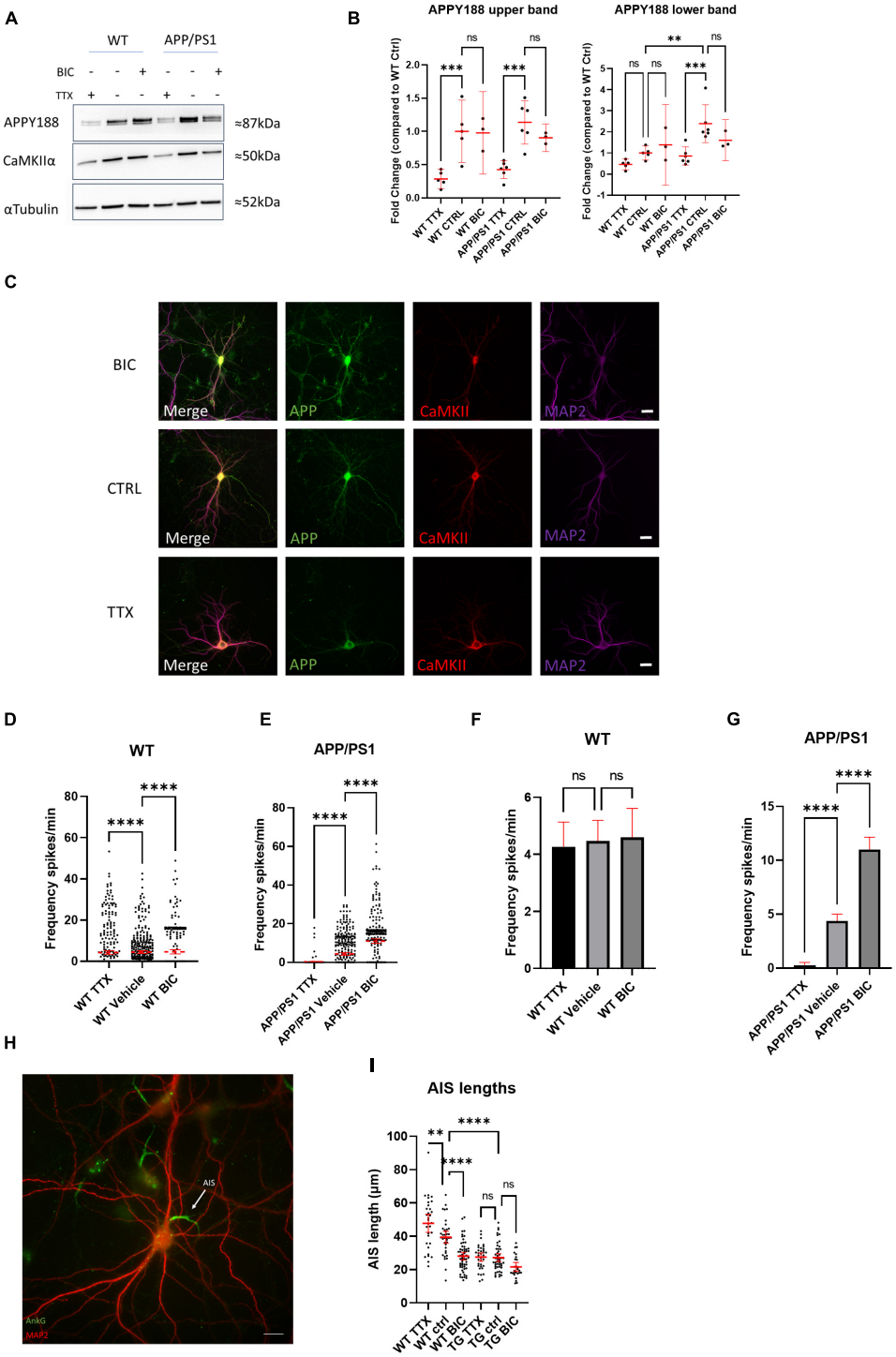

FIGURE 6 | Neurons from AD transgenic mice are unable to initiate homeostatic synaptic/intrinsic plasticity. **(A)** Representative western blot of APP (using antibody APPY188) and CaMKIIα in WT and APP/PS1 neurons treated with TTX or bicuculline for 48 h; αTubulin is used as a loading control. **(B)** Graph depicts quantification of fold change from western blots in **(A)**, APP upper band (WT TTX mean = 0.2865, CI 0.1287–0.4244, $n = 5$, WT control mean = 1.000, CI 0.5298–1.470, $n = 5$, WT bicuculline mean = 0.9782, CI 0.3574–1.599, $n = 3$, APP/PS1 TTX mean = 0.4251, CI 0.2893–0.5609, $n = 6$, APP/PS1 control mean = 1.137, CI 0.8116–1.462, $n = 6$, APP/PS1 bicuculline mean = 0.9038, CI 0.6975–1.110, $n = 3$) and the fainter APP lower band (WT TTX mean = 0.4605, CI 0.1990–0.7220, $n = 5$, WT control mean = 1.000, CI 0.6601–1.340, $n = 5$, WT bicuculline mean = 1.386, CI –0.5278–3.299, $n = 3$, APP/PS1 TTX mean = 0.8590, CI 0.4258–1.292, $n = 6$, APP/PS1 control mean = 2.239, CI 1.493–3.290, $n = 6$, APP/PS1 bicuculline mean = 1.602, CI 0.6279–2.576, $n = 3$). Note that the upper APP band is lower in TTX treated WT compared to WT control ($p = 0.0006$) and TTX treated APP/PS1 compared to APP/PS1 control ($p = 0.0002$). For the APP lower band, it was significantly higher in the APP/PS1 control than the WT control ($p = 0.0017$), while APP was lower in the APP/PS1 TTX than the APP/PS1 control ($p = 0.0003$; one-way ANOVA, Šidak

(Continued)

FIGURE 6 | correction). **(C)** Micrograph showing APP and CaMKIIα labeling after 48 h of TTX or bicuclline treatment. Note that APP labeling is relatively weaker in the TTX treated neuron consistent with the results from western blot. Scale bar = 20 μm. **(D)** Graph demonstrating HSP adaptations in WT cultures treated with TTX or bicuculline for 48 h. Note that the distribution of oscillation frequency in bicuculline treated neurons is different compared to vehicle treated (TTX mean = 4.265, CI 3.397–5.134, *n* = 442; vehicle mean = 4.467, CI = 3.741–5.192, *n* = 413; bicuculline mean = 4.593, CI = 3.574–5.611, *n* = 303, *p*-values compared to vehicle: TTX = 0.0001 and bicuculline = 0.0001, Kruskal–Wallis test, *N* = 4). **(E)** Graph showing absence of adaptation in APP/PS1 neurons in response to 48 h of TTX or bicuculline treatment. Note how both TTX or bicuculline treated APP/PS1 neurons are largely opposite from WT neurons after 48 h. (TTX mean = 0.272, CI 0.0154–0.527, *n* = 210; vehicle mean = 4.368, CI = 3.729–5.008, *n* = 464; bicuculline mean = 10.990, CI = 9.835–12.140, *n* = 368, *p*-values compared to vehicle: TTX = 0.0001 and bicuculline = 0.0001, Kruskal–Wallis test, *N* = 4). **(F)** Bar graph showing mean firing frequency from **(D)**; note that mean firing frequencies are similar between the groups. (WT TTX vs. WT vehicle $p = 0.9203$, WT bicuculline vs. WT vehicle, $p = 0.9733$, one-way ANOVA, Dunnett's test). **(G)** Bar graph showing mean firing frequency from **(E)**; note that mean firing frequencies are do not recover as in WT. (APP/PS1 TTX vs. APP/PS1 vehicle $p = 0.0001$, APP/PS1 bicuculline vs. APP/PS1 vehicle, $p = 0.0001$, one-way ANOVA, Dunnett's test). **(H)** Micrograph depicting WT neuron labeled with MAP2 (red) and ankyrin-G (green), which labels the AIS. White arrow points to AIS; scale bar = 20 μm. **(I)** Graph shows quantification of AIS lengths after treatment with TTX or bicuculline for 48 h (WT TTX mean = 47.76, CI = 42.36–53.17, *n* = 32; WT vehicle mean = 39.44, CI = 35.87–43.02, *n* = 37; WT bicuculline mean = 28.07, CI = 25.75–30.39, *n* = 57; APP/PS1 TTX mean = 27.52, CI = 25.01–30.04, *n* = 35; APP/PS1 vehicle mean = 27.20, CI = 24.85–29.55, *n* = 49; APP/PS1 bicuculline mean = 21.57, CI = 18.86–24.27, *n* = 26); ordinary one way ANOVA, Tukey's multiple comparisons test. ns = not significant, $^{*}p < 0.05$, $^{***}p < 0.001$, $^{****}p < 0.0001$.

in particular in the upper band, which corresponds to mature APP, as visualized by the APPY188 antibody. Although a similar trend was seen for the lower, immature APP band this did not reach statistical significance. The decrease in APP levels was also evident in WT primary neuron cultures immunolabelled after 48 h treatment with TTX or Bicuculline (**Figure 6C**). There was also a trend for a decrease in CaMKIIα, which was previously reported to be downregulated with TTX induced homeostatic scaling (Thiagarajan et al., 2002). To determine whether HSP mechanisms were induced by the long-term treatments, we measured the calcium transients after HSP induction. Treating WT neurons with TTX or bicuculline for 48 h led to the expected changes in excitability; most TTX treated WT neurons recover their ability to fire and while the distribution of firing rates is altered (**Figure 6D** and **Supplementary Figures 2A,B**), the mean firing frequency does not differ significantly from WT vehicle treated neurons after 48 h (**Figure 6F**). In response to the 48 h of treatment with bicuculline, which acutely elevates activity, most WT neurons, as expected, significantly decreased their firing frequency. Of note, the extended bicuculline treatment in WT neurons appears to lead to two types of firing, with one group of neurons maintaining a high firing frequency and another group that is silent (**Figures 6D,F**). In contrast, the firing frequency of APP/PS1 neurons treated for 48 h with bicuculline remained increased, while the firing frequency of APP/PS1 neurons after chronic TTX treatment remained low (**Figures 6E,G**). Thus, APP/PS1 neurons did not respond to the prolonged bicuculline or TTX exposure as the WT neurons, indicating that the APP/PS1 neurons were unable to compensate to these pharmacologically-induced changes in neuronal activity. Note that vehicle treated APP/PS1 and WT were not significantly different in this experiment although here we did not do direct comparisons.

To explore a mechanistic aspect of these HSP alterations we investigated axon initial segment (AIS) modifications in the chronic TTX and bicuculline treated cultures, as lengthening or shortening of the AIS modifies the excitability of neurons. By immunolabeling for ankyrin-G, a protein involved in linking voltage-gated channels to the AIS, we could identify the AIS and measure its length (Hedstrom et al., 2008). In WT neurons, 48 h of treatment with either bicuculline or TTX led to the expected decreased and increased AIS lengths, respectively (**Figures 6H,I**). In contrast, APP/PS1 neurons did not display adjustments of the AIS length upon either of these HSP-inducing treatments. Interestingly, the AIS lengths of APP/PS1 neurons were already shorter than those of WT neurons at baseline. Together these experiments demonstrate an inability of APP/PS1 neurons to use HSP mechanisms to adapt to extrinsic changes in activity.

DISCUSSION

Here we demonstrate that inhibition of Aβ degradation, application of synthetic Aβ, APP overexpression and familial AD-causing mutations all cause an increase in somatic calcium transients during spontaneous neuronal activity, in particular in excitatory CaMKII positive neurons. Moreover, we present evidence that homeostatic plasticity mechanisms are disrupted in APP/PS1 AD transgenic neurons, as these were unable to compensate their spontaneous calcium transient activity after chronic activity or inactivity. APP/PS1 neurons were shown to have shorter AIS and a lack of change in AIS length in response to chronic activity or chronic activity blockade. The proper function of neuronal networks depends on maintaining homeostatic set points and limiting activity within functional windows. Deviations from these set-points lead to network dysfunction. Structural homeostatic synaptic plasticity is known to occur at three main locations: (1) at the post-synapse involving reduced or increased levels of surface receptors (Turrigiano et al., 1998); (2) at the axon initial segment (AIS) by either increasing or decreasing its length or by shifting the AIS further out into the axon (Wefelmeyer et al., 2016); or (3) at the pre-synapse by modifying how much neurotransmitter is stored in synaptic vesicles or through homeostatic maintenance of presynaptic exocytosis (Delvendahl et al., 2019). Of note, Aβ was suggested to overshoot normal homeostatic scaling in response to sensory deprivation *in vivo* or TTX-mediated inhibition *in vitro* (Gilbert et al., 2016), and Aβ was recently shown to regulate homeostatic synaptic upscaling after activity blockade in dentate gyrus *in vivo* (Galanis et al., 2021). Our findings that APP/PS1 neurons do not increase their activity after 48 h of TTX treatment nor decrease firing rate after 48 h of bicuculline treatment suggest that Aβ/APP play important roles

not only in adjusting to activity blockade but also have roles in homeostatic downscaling in response to excessive activity. Interestingly, we found that 48 h of bicuculline treatment led to a strong reduction in firing in the majority of neurons in WT cultures with, however, another population of neurons that maintained a high firing frequency; a related observation was reported on visual cortex homeostatic plasticity following visual deprivation (Barnes et al., 2015), where differential adaptations by excitatory and inhibitory neuron populations were described. Interestingly, we observed that the mean firing rates were similar between TTX, vehicle and bicuculline treated WT neurons after 48 h consistent with findings suggesting that while single unit firing is unstable, networks maintain surprisingly stable firing frequencies (Slomowitz et al., 2015). Aβ and APP have been implicated in normal HSP (Gilbert et al., 2016; Galanis et al., 2021), and APP/PS1 mice were recently shown to have defective downscaling during sleep (Zarhin et al., 2022). Defective HSP could help explain why AD transgenic mice are more susceptible to pharmacologically-induced and spontaneous seizures (Minkeviciene et al., 2009; Reyes-Marin and Nuñez, 2017) and could provide a framework for explaining the increased sensitivity to seizures in AD patients (Pandis and Scarmeas, 2012).

We provide evidence that the AIS is lengthened with TTX treatment and shortened after treatment with bicuculline in WT neurons, which, however, did not occur in APP/PS1 neurons. Shortening the AIS is a way to decrease intrinsic excitability and previous work in slice cultures has shown that 1 h of bicuculline treatment was sufficient to decrease the length of the AIS (Jamann et al., 2021). Since the average lengths of the AIS in APP/PS1 neurons are shorter at baseline than in WT neurons, and are not altered by chronic treatments known to induce HSP, our findings could indicate that APP/PS1 neurons have attempted to adapt to reduce excitability (reduced baseline AIS) but are unable to do so to treatments that normally would induce HSP. It should be noted, however, that the shortening of the AIS occurs within 1 h while complete downscaling takes closer to 48 h. Thus, the role of the AIS shortening in the regulation of activity in APP/PS1 neurons is likely minor. We previously showed in primary neurons from Tg2576 AD transgenic mice, which overexpress human APP with the Swedish familial AD mutation, reduced AMPA receptor levels in culture (Almeida et al., 2005). Whether this is the result of adaptation to higher basal activity levels or a consequence of synaptotoxicity remains to be determined. Moreover, we demonstrate here that APP protein levels decrease with chronic TTX treatment. It has been previously reported that conditional APP family triple knockout increases excitability of excitatory neurons (Lee et al., 2020). Thus, the reduction we see in APP protein levels could be related to increasing excitability in the chronic TTX treatment as we also demonstrated in a previous paper that APP knockout and knockdown led to increased GluA1 protein levels both in cultured neurons and brains of APP KO mice (Martinsson et al., 2019). However, while TTX decreased levels of APP, bicuculline treatment did not significantly alter APP levels.

Our data demonstrates hyperexcitability in APP/PS1 transgenic compared to WT neurons, which we now show occurs mainly in excitatory neurons. Similar to previous studies, we found that exogenously added Aβ1–42 primarily targeted synapses of CaMKII-positive neurons, specifically in a dendritic rather than axonal pattern (Lacor et al., 2004; Willen et al., 2017). However, this does not exclude the possibility of Aβ binding to presynaptic terminals proximal to dendrites. The binding of Aβ1–42 to CaMKII-positive synapses might explain why excitatory neurons, in particular, are affected. The increased frequencies and amplitudes of calcium oscillations that we observed with neprilysin inhibition as a means to elevate endogenous Aβ are consistent with results from Abramov et al. (2009), showing increased release probability with thiorphan treatment in cultured hippocampal neurons. However, since neprilysin also degrades various enkephalins and peptide neurotransmitters, such as substance P, which can influence calcium stores (Heath et al., 1994), we additionally showed a lack of effect on calcium oscillations with neprilysin inhibition in APP KO neurons.

As the calcium oscillations were increased in APP/PS1 compared to wild type neurons, we also considered whether this might be due to decreased inhibitory interneurons/synapses. However, we did not see significant differences in the protein levels of GAD67 and CaMKII, markers of GABAergic interneurons and excitatory neurons, respectively. Further, we did not detect significant differences in the synaptic density of either excitatory or inhibitory synapses. While neuropathological studies have emphasized the vulnerability of select classes of excitatory projection neurons (Stranahan and Mattson, 2010), the relative involvement of different inhibitory and excitatory neurons in early Aβ-induced hyperactivity remains less well defined. However, while there is no evidence for differences in the proportion of different subclasses of neurons in cortical versus hippocampal neurons of AD transgenic versus WT primary cultures, we also cannot exclude this possibility. Increasing evidence suggests that alterations in inhibitory neuron connectivity lead to changes in network functions in AD. For example, increased parvalbumin and gephyrin labeling perisomatically in CA1 neurons of young APP/PS1 transgenic mice was shown (Hollnagel et al., 2019), which might represent an adaptation to increased Aβ/APP and, therefore, increased activity in these mice.

Cortical neurons in proximity to plaques were reported to have higher basal calcium levels in spines and dendrites (Kuchibhotla et al., 2008). Aβ oligomers of different varieties have been reported to bind various cell surface receptors such as PrP (Lauren et al., 2009), alpha7 nicotinic receptor (Sadigh-Eteghad et al., 2014), NMDA receptors (Texidó et al., 2011), and Ephrins (Vargas et al., 2018), leading to an influx of calcium. Yet another hypothesis proposes that Aβ increases the cell membrane permeability for calcium (Kawahara and Kuroda, 2000; Kagan et al., 2002). To complicate matters, presenilins have also been implicated in the handling of Ca^{2+} stores independently of γ-secretase in AD transgenic mouse models (Lerdkrai et al., 2018). A recent study suggested that Aβ dimers could cause hyperactivity by inhibiting glutamate reuptake (Zott et al., 2019).

Further, it was reported that Aβ oligomers can impair synaptic activity by repressing P/Q calcium channels (Nimmrich et al., 2008). While we prepared synthetic Aβ in DMSO, which prevents the formation of fibrils, Aβ forms amyloids with time in culture (Takahashi et al., 2004) and progressively aggregates at synapses (Takahashi et al., 2002, 2004; Willén et al., 2017), consistent with Aβ aggregation at synaptic compartments (Bilousova et al., 2016). Moreover, while Aβ and APP influence synaptic activity, neuronal activity also regulates APP cleavage and Aβ generation (Kamenetz et al., 2003); increased neuronal activity can increase both the generation and degradation of Aβ (Kamenetz et al., 2003; Tampellini et al., 2009). Thus, converging data indicate that both APP and Aβ are important for regulating neuronal activity. Among questions that remain to be answered are which specific aspects of neuronal activity APP and Aβ regulate/influence. Many transgenic models of AD exhibit epileptic seizures and hyperactivity (Scharfman, 2012; Born et al., 2014), and even models overexpressing wild-type human APP develop seizures (Born et al., 2014). Importantly, hyper-synchrony in AD transgenic mice could be rescued by genetic suppression of APP over-expression (Born et al., 2014). We hypothesize that the localization of APP and accumulating Aβ in endosomes near synapses (Takahashi et al., 2002) play a key role in the altered responses of synapses in the setting of AD. A better understanding of the neuron subtypes and molecular mechanisms involved in early Aβ/APP-induced hyperexcitability and synapse dysfunction should provide not only new insights into the disease, but also to new treatment strategies for AD.

DATA AVAILABILITY STATEMENT

The raw data supporting the conclusions of this article will be made available by the authors, without undue reservation, to any qualified researcher.

ETHICS STATEMENT

The animal study was reviewed and approved by Animal Ethical Committee at Lund University ethical permit number 5.8.18-05983/2019.

AUTHOR CONTRIBUTIONS

IM and GKG wrote and conceptualized the manuscript. IM, SCK, OS, and RE performed the experiments. IM, GKG, MGG, LT-G, and SCK edited the manuscript. IM, AS, OS, and RE performed the data analysis. LQ and CL performed cloning and prepared vectors. GKG, TD, and J-YL contributed funding to the project. All authors commented and edited the final version of the manuscript.

FUNDING

This study was supported by MultiPark, Hjärnfonden, Alzheimerfonden, Kockska stiftelsen, the Swedish Research Council (Grant #2019-01125), and the Olav Thon Foundation.

ACKNOWLEDGMENTS

We thank Bodil Israelsson for technical assistance as well as master's students Ainoa Pilkati and Mohammed Rahman for help with analyzing data. We appreciate the support of MultiPark, Hjärnfonden, Alzheimerfonden, Kockska stiftelsen, the Swedish Research Council (Grant #2019-01125), and the Olav Thon Foundation.

SUPPLEMENTARY MATERIAL

The Supplementary Material for this article can be found online at: https://www.frontiersin.org/articles/10.3389/fnagi.2022.946297/full#supplementary-material

Supplementary Figure 1 | Live-cell imaging method for assaying spontaneous calcium transients. **(A,B)** Representative traces of spontaneous activity over a 2 min period in neurons from WT and APP/PS1 mice, respectively. **(C,D)** Raster plots showing overall calcium transients (spikes represented as green dots) in WT and APP/PS1 neuron field of views (FOVs); ROI# or neuron number on the *Y*-axis and time in minutes on the *X*-axis. **(E)** Graph shows frequency from WT neurons treated with 1 μM TTX or 20 μM bicuculline. Note that TTX significantly reduces calcium oscillations whereas bicuculline significantly increases them compared to vehicle treated CTRL (TTX mean = 0.01429 CI = −0.01421–0.04278, $n = 70$; vehicle mean = 2.923, CI = 2.094–3.752, $n = 209$; bicuculline mean = 25.00, CI = 23.04–26.97, $n = 104$, p-values compared to vehicle: TTX = 0.0001 and bicuculline = 0.0001, Kruskal–Wallis test). **(F)** Graph demonstrating acute effects of TTX and bicuculline in APP/PS1 neurons. Note that similar to in WT neurons, TTX blocks activity while bicuculline raises activity (TTX mean = 0.1644 CI −0.07614–0.4050, $n = 118$; vehicle mean = 5.164, CI = 4.140–6.188, $n = 188$; bicuculline mean = 13.77, CI = 10.49–17.06, $n = 97$, p-values compared to vehicle: TTX = 0.0001 and bicuculline = 0.0379, Kruskal–Wallis test). $^{*}p < 0.05$, $^{***}p < 0.001$.

Supplementary Figure 2 | Frequency distribution of WT and APP/PS1 after 48 h treatment with TTX or bicuculline. **(A)** Frequency distribution of firing frequencies of WT neurons treated with TTX, bicuculline or vehicle for 48 h; neurons shown in a graph; $N = 3$ cultures. **(B)** Frequency distribution of firing frequencies of APP/PS1 neurons treated with TTX, bicuculline or vehicle for 48 h; neurons shown in a graph; $N = 3$ cultures.

REFERENCES

Abramov, E., Dolev, I., Fogel, H., Ciccotosto, G. D., Ruff, E., and Slutsky, I. (2009). Amyloid-β as a positive endogenous regulator of release probability at hippocampal synapses. *Nat. Neurosci.* 12:1567. doi: 10.1038/nn.2433

Almeida, C. G., Takahashi, R. H., and Gouras, G. K. (2006). Beta-amyloid accumulation impairs multivesicular body sorting by inhibiting the ubiquitin-proteasome system. *J. Neurosci.* 26, 4277–4288.

Almeida, C. G., Tampellini, D., Takahashi, R. H., Greengard, P., Lin, M. T., Snyder, E. M., et al. (2005). Beta-amyloid accumulation in APP mutant neurons reduces PSD-95 and GluR1 in synapses. *Neurobiol. Dis.* 20, 187–198. doi: 10.1016/j.nbd.2005.02.008

Artimovich, E., Jackson, R. K., Kilander, M. B. C., Lin, Y. C., and Nestor, M. W. (2017). PeakCaller: an automated graphical interface for the quantification of intracellular calcium obtained by high-content screening. *BMC Neurosci.* 18:72. doi: 10.1186/s12868-017-0391-y

Barnes, S. J., Sammons, R. P., Jacobsen, R. I., Mackie, J., Keller, G. B., and Keck, T. (2015). Subnetwork-specific homeostatic plasticity in mouse visual cortex *in vivo*. *Neuron* 86, 1290–1303. doi: 10.1016/j.neuron.2015.05.010

Bilousova, T., Miller, C. A., Poon, W. W., Vinters, H. V., Corrada, M., Kawas, C., et al. (2016). Synaptic amyloid-β oligomers precede p-tau and differentiate high pathology control cases. *Am. J. Pathol.* 186, 185–198. doi: 10.1016/j.ajpath.2015.09.018

Born, H. A., Kim, J. Y., Savjani, R. R., Das, P., Dabaghian, Y. A., Guo, Q., et al. (2014). Genetic suppression of transgenic APP rescues Hypersynchronous network activity in a mouse model of Alzeimer's disease. *J. Neurosci.* 34, 3826–3840. doi: 10.1523/JNEUROSCI.5171-13.2014

Delvendahl, I., Kita, K., and Müller, M. (2019). Rapid and sustained homeostatic control of presynaptic exocytosis at a central synapse. *Proc. Natl. Acad. Sci. U.S.A.* 116:23783. doi: 10.1073/pnas.1909675116

Doshina, A., Gourgue, F., Onizuka, M., Opsomer, R., Wang, P., Ando, K., et al. (2017). Cortical cells reveal APP as a new player in the regulation of GABAergic neurotransmission. *Sci. Rep.* 7:370. doi: 10.1038/s41598-017-00325-2

Faucher, P., Mons, N., Micheau, J., Louis, C., and Beracochea, D. J. (2016). Hippocampal injections of oligomeric Amyloid β-peptide (1–42) induce selective working memory deficits and long-lasting alterations of erk signaling pathway. *Front. Aging Neurosci.* 7:245. doi: 10.3389/fnagi.2015.00245

Galanis, C., Fellenz, M., Becker, D., Bold, C., Lichtenthaler, S. F., Müller, U. C., et al. (2021). Amyloid-beta mediates homeostatic synaptic plasticity. *J. Neurosci.* 41:5157.

Gavello, D., Calorio, C., Franchino, C., Cesano, F., Carabelli, V., Carbone, E., et al. (2018). Early alterations of hippocampal neuronal firing induced by Abeta42. *Cereb. Cortex* 28, 433–446. doi: 10.1093/cercor/bhw377

Gilbert, J., Shu, S., Yang, X., Lu, Y., Zhu, L.-Q., and Man, H.-Y. (2016). β-Amyloid triggers aberrant over-scaling of homeostatic synaptic plasticity. *Acta Neuropathol. Commun.* 4:131.

Handler, M., Yang, X., and Shen, J. (2000). Presenilin-1 regulates neuronal differentiation during neurogenesis. *Development* 127, 2593–2606.

Hatami, A., Albay, R. III, Monjazeb, S., Milton, S., and Glabe, C. (2014). Monoclonal antibodies against Aβ42 fibrils distinguish multiple aggregation state polymorphisms *in vitro* and in Alzheimer disease brain. *J. Biol. Chem.* 289, 32131–32143. doi: 10.1074/jbc.M114.594846

Heath, M. J., Womack, M. D., and Macdermott, A. B. (1994). Substance P elevates intracellular calcium in both neurons and glial cells from the dorsal horn of the spinal cord. *J. Neurophysiol.* 72, 1192–1198. doi: 10.1152/jn.1994.72.3.1192

Hedstrom, K. L., Ogawa, Y., and Rasband, M. N. (2008). AnkyrinG is required for maintenance of the axon initial segment and neuronal polarity. *J. Cell Biol.* 183, 635–640.

Hollnagel, J. O., Elzoheiry, S., Gorgas, K., Kins, S., Beretta, C. A., Kirsch, J., et al. (2019). Early alterations in hippocampal perisomatic GABAergic synapses and network oscillations in a mouse model of Alzheimer's disease amyloidosis. *PLoS One* 14:e0209228. doi: 10.1371/journal.pone.0209228

Iwata, N., Mizukami, H., Shirotani, K., Takaki, Y., Muramatsu, S.-I., Lu, B., et al. (2004). Presynaptic localization of neprilysin contributes to efficient clearance of amyloid-β peptide in mouse brain. *J. Neurosci.* 24, 991–998. doi: 10.1523/JNEUROSCI.4792-03.2004

Jamann, N., Dannehl, D., Lehmann, N., Wagener, R., Thielemann, C., Schultz, C., et al. (2021). Sensory input drives rapid homeostatic scaling of the axon initial segment in mouse barrel cortex. *Nat. Commun.* 12:23. doi: 10.1038/s41467-020-20232-x

Kagan, B. L., Hirakura, Y., Azimov, R., Azimova, R., and Lin, M. C. (2002). The channel hypothesis of Alzheimer's disease: current status. *Peptides* 23, 1311–1315. doi: 10.1016/s0196-9781(02)00067-0

Kamenetz, F., Tomita, T., Hsieh, H., Seabrook, G., Borchelt, D., Iwatsubo, T., et al. (2003). APP processing and synaptic function. *Neuron* 37, 925–937.

Kang, J. E., Lim, M. M., Bateman, R. J., Lee, J. J., Smyth, L. P., Cirrito, J. R., et al. (2009). Amyloid-beta dynamics are regulated by orexin and the sleep-wake cycle. *Science* 326, 1005–1007. doi: 10.1126/science.1180962

Kashyap, G., Bapat, D., Das, D., Gowaikar, R., Amritkar, R. E., Rangarajan, G., et al. (2019). Synapse loss and progress of Alzheimer's disease –A network model. *Sci. Rep.* 9:6555.

Kawahara, M., and Kuroda, Y. (2000). Molecular mechanism of neurodegeneration induced by Alzheimer's beta-amyloid protein: channel formation and disruption of calcium homeostasis. *Brain Res. Bull.* 53, 389–397.

Koo, E. H., Sisodia, S. S., Archer, D. R., Martin, L. J., Weidemann, A., Beyrreuther, K., et al. (1990). Precursor of amyloid protein in Alzheimer disease undergoes fast anterograde axonal transport. *Proc. Natl. Acad. Sci. U.S.A.* 87, 1561–1565.

Kuchibhotla, K. V., Goldman, S. T., Lattarulo, C. R., Wu, H. Y., Hyman, B. T., and Bacskai, B. J. (2008). Abeta plaques lead to aberrant regulation of calcium homeostasis *in vivo* resulting in structural and functional disruption of neuronal networks. *Neuron* 59, 214–225. doi: 10.1016/j.neuron.2008.06.008

Lacor, P. N., Buniel, M. C., Chang, L., Fernandez, S. J., Gong, Y., Viola, K. L., et al. (2004). Synaptic targeting by Alzheimer's-related amyloid beta oligomers. *J. Neurosci.* 24, 10191–10200.

Lauren, J., Gimbel, D. A., Nygaard, H. B., Gilbert, J. W., and Strittmatter, S. M. (2009). Cellular prion protein mediates impairment of synaptic plasticity by amyloid-beta oligomers. *Nature* 457, 1128–1132.

Lee, S. H., Kang, J., Ho, A., Watanabe, H., Bolshakov, V. Y., and Shen, J. (2020). APP family regulates neuronal excitability and synaptic plasticity but not neuronal survival. *Neuron* 108, 676.e8–690.e8.

Lerdkrai, C., Asavapanumas, N., Brawek, B., Kovalchuk, Y., Mojtahedi, N., Olmedillas del Moral, M., et al. (2018). Intracellular Ca(2+) stores control *in vivo* neuronal hyperactivity in a mouse model of Alzheimer's disease. *Proc. Natl. Acad. Sci. U.S.A.* 115, E1279–E1288. doi: 10.1073/pnas.1714409115

Martinsson, I., Capetillo-Zarate, E., Faideau, M., Willen, K., Esteras, N., Frykman, S., et al. (2019). APP depletion alters selective pre- and post-synaptic proteins. *Mol. Cell Neurosci.* 95, 86–95. doi: 10.1016/j.mcn.2019.02.003

Mata, G., Cuesto, G., Heras, J., Morales, M., Romero, A., and Rubio, J. (2017). "SynapCountJ: a validated tool for analyzing synaptic densities in neurons," in *Biomedical Engineering Systems and Technologies*, eds A. Fred and H. Gamboa (Cham: Springer International Publishing), 41–55. doi: 10.1002/jnr.23353

Minkeviciene, R., Rheims, S., Dobszay, M. B., Zilberter, M., Hartikainen, J., Fülöp, L., et al. (2009). Amyloid beta-induced neuronal hyperexcitability triggers progressive epilepsy. *J. Neurosci.* 29, 3453–3462. doi: 10.1523/JNEUROSCI.5215-08.2009

Nimmrich, V., Grimm, C., Draguhn, A., Barghorn, S., Lehmann, A., Schoemaker, H., et al. (2008). Amyloid beta oligomers (A beta(1-42) globulomer) suppress spontaneous synaptic activity by inhibition of P/Q-type calcium currents. *J. Neurosci.* 28, 788–797. doi: 10.1523/JNEUROSCI.4771-07.2008

Pandis, D., and Scarmeas, N. (2012). Seizures in Alzheimer disease: clinical and epidemiological data. *Epilepsy Curr.* 12, 184–187.

Perdigão, C., Barata, M. A., Araújo, M. N., Mirfakhar, F. S., Castanheira, J., and Guimas Almeida, C. (2020). Intracellular trafficking mechanisms of synaptic dysfunction in Alzheimer's disease. *Front. Cell Neurosci.* 14:72. doi: 10.3389/fncel.2020.00072

Puzzo, D., Privitera, L., Leznik, E., Fa, M., Staniszewski, A., Palmeri, A., et al. (2008). Picomolar amyloid-beta positively modulates synaptic plasticity and memory in hippocampus. *J. Neurosci.* 28, 14537–14545. doi: 10.1523/JNEUROSCI.2692-08.2008

Quintino, L., Manfre, G., Wettergren, E. E., Namislo, A., Isaksson, C., and Lundberg, C. (2013). Functional neuroprotection and efficient regulation of GDNF using destabilizing domains in a rodent model of Parkinson's disease. *Mol. Ther.* 21, 2169–2180. doi: 10.1038/mt.2013.169

Rama, N., Goldschneider, D., Corset, V., Lambert, J., Pays, L., and Mehlen, P. (2012). Amyloid precursor protein regulates netrin-1-mediated commissural axon outgrowth. *J. Biol. Chem.* 287, 30014–30023. doi: 10.1074/jbc.M111.324780

Reyes-Marin, K. E., and Nuñez, A. (2017). Seizure susceptibility in the APP/PS1 mouse model of Alzheimer's disease and relationship with amyloid β plaques. *Brain Res.* 1677, 93–100.

Roos, T. T., Garcia, M. G., Martinsson, I., Mabrouk, R., Israelsson, B., Deierborg, T., et al. (2021). Neuronal spreading and plaque induction of intracellular Aβ and its disruption of Aβ homeostasis. *Acta Neuropathol.* 142, 669–687.

Sadigh-Eteghad, S., Talebi, M., Farhoudi, M., Golzari, S. E. J., Sabermarouf, B., and Mahmoudi, J. (2014). Beta-amyloid exhibits antagonistic effects on alpha 7 nicotinic acetylcholine receptors in orchestrated manner. *J. Med. Hypothes. Ideas* 8, 49–52.

Sadleir, K. R., Kandalepas, P. C., Buggia-Prévot, V., Nicholson, D. A., Thinakaran, G., and Vassar, R. (2016). Presynaptic dystrophic neurites surrounding amyloid

plaques are sites of microtubule disruption, BACE1 elevation, and increased Aβ generation in Alzheimer's disease. *Acta Neuropathol.* 132, 235–256. doi: 10.1007/s00401-016-1558-9

Scharfman, H. E. (2012). Alzheimer's disease and epilepsy: insight from animal models. *Future Neurol.* 7, 177–192.

Siskova, Z., Justus, D., Kaneko, H., Friedrichs, D., Henneberg, N., Beutel, T., et al. (2014). Dendritic structural degeneration is functionally linked to cellular hyperexcitability in a mouse model of Alzheimer's disease. *Neuron* 84, 1023–1033. doi: 10.1016/j.neuron.2014.10.024

Slomowitz, E., Styr, B., Vertkin, I., Milshtein-parush, H., Nelken, I., Slutsky, M., et al. (2015). Interplay between population firing stability and single neuron dynamics in hippocampal networks. *eLife* 4:e04378. doi: 10.7554/eLife.04378

Stranahan, A. M., and Mattson, M. P. (2010). Selective vulnerability of neurons in layer II of the entorhinal cortex during aging and Alzheimer's disease. *Neural Plast.* 2010:108190.

Takahashi, R. H., Almeida, C. G., Kearney, P. F., Yu, F., Lin, M. T., Milner, T. A., et al. (2004). Oligomerization of Alzheimer's beta-amyloid within processes and synapses of cultured neurons and brain. *J. Neurosci.* 24, 3592–3599.

Takahashi, R. H., Milner, T. A., Li, F., Nam, E. E., Edgar, M. A., Yamaguchi, H., et al. (2002). Intraneuronal Alzheimer abeta42 accumulates in multivesicular bodies and is associated with synaptic pathology. *Am. J. Pathol.* 161, 1869–1879.

Tampellini, D., Capetillo-Zarate, E., Dumont, M., Huang, Z., Yu, F., Lin, M. T., et al. (2010). Effects of synaptic modulation on beta-amyloid, synaptophysin, and memory performance in Alzheimer's disease transgenic mice. *J. Neurosci.* 30, 14299–14304.

Tampellini, D., Rahman, N., Gallo, E. F., Huang, Z., Dumont, M., Capetillo-Zarate, E., et al. (2009). Synaptic activity reduces intraneuronal Abeta, promotes APP transport to synapses, and protects against Abeta-related synaptic alterations. *J. Neurosci.* 29, 9704–9713. doi: 10.1523/JNEUROSCI.2292-09.2009

Texidó, L., Martín-Satué, M., Alberdi, E., Solsona, C., and Matute, C. (2011). Amyloid β peptide oligomers directly activate NMDA receptors. *Cell Calcium* 49, 184–190. doi: 10.1016/j.ceca.2011.02.001

Thiagarajan, T. C., Piedras-Renteria, E. S., and Tsien, R. W. (2002). alpha- and betaCaMKII. Inverse regulation by neuronal activity and opposing effects on synaptic strength. *Neuron* 36, 1103–1114. doi: 10.1016/s0896-6273(02)01049-8

Turrigiano, G. (2012). Homeostatic synaptic plasticity: local and global mechanisms for stabilizing neuronal function. *Cold Spring Harb. Perspect. Biol.* 4:a005736.

Turrigiano, G. G. (2008). The self-tuning neuron: synaptic scaling of excitatory synapses. *Cell* 135, 422–435. doi: 10.1016/j.cell.2008.10.008

Turrigiano, G. G., Leslie, K. R., Desai, N. S., Rutherford, L. C., and Nelson, S. B. (1998). Activity-dependent scaling of quantal amplitude in neocortical neurons. *Nature* 391, 892–896.

Vargas, L. M., Cerpa, W., Munoz, F. J., Zanlungo, S., and Alvarez, A. R. (2018). Amyloid-beta oligomers synaptotoxicity: the emerging role of EphA4/c-Abl signaling in Alzheimer's disease. *Biochim. Biophys. Acta Mol. Basis Dis.* 1864, 1148–1159. doi: 10.1016/j.bbadis.2018.01.023

Vossel, K. A., Beagle, A. J., Rabinovici, G. D., Shu, H., Lee, S. E., Naasan, G., et al. (2013). Seizures and epileptiform activity in the early stages of Alzheimer disease. *JAMA Neurol.* 70, 1158–1166.

Wefelmeyer, W., Puhl, C. J., and Burrone, J. (2016). Homeostatic plasticity of subcellular neuronal structures: from inputs to outputs. *Trends Neurosci.* 39, 656–667. doi: 10.1016/j.tins.2016.08.004

Westmark, C. J., and Malter, J. S. (2007). FMRP mediates mGluR5-dependent translation of amyloid precursor protein. *PLoS Biol.* 5:e0050052. doi: 10.1371/journal.pbio.0050052

Willén, K., Edgar, J. R., Hasegawa, T., Tanaka, N., Futter, C. E., and Gouras, G. K. (2017). Aβ accumulation causes MVB enlargement and is modelled by dominant negative VPS4A. *Mol. Neurodegener.* 12:61. doi: 10.1186/s13024-017-0203-y

Willen, K., Sroka, A., Takahashi, R. H., and Gouras, G. K. (2017). Heterogeneous association of alzheimer's disease-linked amyloid-beta and amyloid-beta protein precursor with synapses. *J. Alzheimers. Dis.* 60, 511–524. doi: 10.3233/JAD-170262

Yang, L., Wang, Z., Wang, B., Justice, N. J., and Zheng, H. (2009). Amyloid precursor protein regulates Cav1.2 L-type calcium channel levels and function to influence GABAergic short-term plasticity. *J. Neurosci.* 29, 15660–15668. doi: 10.1523/JNEUROSCI.4104-09.2009

Zarhin, D., Atsmon, R., Ruggiero, A., Baeloha, H., Shoob, S., Scharf, O., et al. (2022). Disrupted neural correlates of anesthesia and sleep reveal early circuit dysfunctions in Alzheimer models. *Cell Rep.* 38:110268. doi: 10.1016/j.celrep.2021.110268

Zott, B., Simon, M. M., Hong, W., Unger, F., Chen-Engerer, H. J., Frosch, M. P., et al. (2019). A vicious cycle of β amyloid-dependent neuronal hyperactivation. *Science* 365, 559–565. doi: 10.1126/science.aay0198

Conflict of Interest: The authors declare that the research was conducted in the absence of any commercial or financial relationships that could be construed as a potential conflict of interest.

Publisher's Note: All claims expressed in this article are solely those of the authors and do not necessarily represent those of their affiliated organizations, or those of the publisher, the editors and the reviewers. Any product that may be evaluated in this article, or claim that may be made by its manufacturer, is not guaranteed or endorsed by the publisher.

frontiers | Frontiers in Aging Neuroscience

TYPE Original Research
PUBLISHED 25 August 2022
DOI 10.3389/fnagi.2022.933979

OPEN ACCESS

EDITED BY
Rodrigo Morales,
University of Texas Health Science Center at Houston, United States

REVIEWED BY
Melissa Calegaro Nassif,
Universidad Mayor, Chile
Irene Benito Cuesta,
Karolinska Institutet (KI), Sweden
Tadanori Hamano,
University of Fukui, Japan

*CORRESPONDENCE
David E. Kang
dek94@case.edu
Jung-A. A. Woo
jaw330@case.edu

SPECIALTY SECTION
This article was submitted to Alzheimer's Disease and Related Dementias, a section of the journal Frontiers in Aging Neuroscience

RECEIVED 01 May 2022
ACCEPTED 08 August 2022
PUBLISHED 25 August 2022

CITATION
Cazzaro S, Fang C, Khan H, Witas R, Kee TR, Woo J-AA and Kang DE (2022) Slingshot homolog-1 mediates the secretion of small extracellular vesicles containing misfolded proteins by regulating autophagy cargo receptors and actin dynamics. *Front. Aging Neurosci.* 14:933979. doi: 10.3389/fnagi.2022.933979

Slingshot homolog-1 mediates the secretion of small extracellular vesicles containing misfolded proteins by regulating autophagy cargo receptors and actin dynamics

Sara Cazzaro[1,2], Cenxiao Fang[2], Hirah Khan[2], Richard Witas[2], Teresa R. Kee[1,2], Jung-A. A. Woo[1]* and David E. Kang[1,3]*

[1]Department of Pathology, School of Medicine, Case Western Reserve University, Cleveland, OH, United States, [2]Department of Molecular Medicine, USF Health Morsani College of Medicine, Tampa, FL, United States, [3]Louis Stokes Cleveland VA Medical Center, Cleveland, OH, United States

Increasing evidence indicates that the accumulation misfolded proteins in Alzheimer's disease (AD) arises from clearance defects in the autophagy-lysosome pathway. Misfolded proteins such as Aβ and tau are secreted in small extracellular vesicles (i.e., exosomes) and are propagated from cell to cell in part through secreted small extracellular vesicles (sEVs). Recent studies suggest that autophagic activity and exosome secretion are coregulated events, and multiple autophagy-related proteins are found in sEVs, including the cargo receptors Sqstm1/p62 and optineurin. However, whether and how autophagy cargo receptors *per se* regulate the secretion of sEVs is unknown. Moreover, despite the prominent role of actin dynamics in secretory vesicle release, its role in EV secretion is unknown. In this study, we leveraged the dual axes of Slingshot Homolog-1 (SSH1), which inhibits Sqstm1/p62-mediated autophagy and activates cofilin-mediated actin dynamics, to study the regulation of sEV secretion. Here we show that cargo receptors Sqstm1/p62 and optineurin inhibit sEV secretion, an activity that requires their ability to bind ubiquitinated cargo. Conversely, SSH1 increases sEV secretion by dephosphorylating Sqstm1/p62 at pSer403, the phospho-residue that allows Sqstm1/p62 to bind ubiquitinated cargo. In addition, increasing actin dynamics through the SSH1-cofilin activation pathway also increases sEV secretion, which is mimicked by latrunculin B treatment. Finally, Aβ42 oligomers and mutant tau increase sEV secretion and are physically associated with secreted sEVs. These findings suggest that increasing cargo receptor engagement with autophagic cargo and reducing actin dynamics (i.e., SSH1 inhibition) represents an attractive strategy to promote misfolded protein degradation while reducing sEV-mediated cell to cell spread of pathology.

KEYWORDS

SSH1, amyloid, tau, exosome, p62, optineurin, actin dynamics, autophagy

Introduction

Emerging evidence indicates that the release and uptake of extracellular vesicles (EVs) represents an important form of intercellular communication that could transmit beneficial or pathogenic signals across different cells (Rajendran et al., 2014). Normal EVs have been shown to regulate neuronal neurite outgrowth, survival, and synaptic activity (Wang et al., 2011; Antonucci et al., 2012) as well as microglial activation (Verderio et al., 2012; Prada et al., 2013). EVs are secreted by all cell types and contain specific sets of RNA and proteins (membrane and cytosolic) (Valadi et al., 2007; Skog et al., 2008). Large microvesicles (MVs) (150–1000 nm) are derived from evagination and excision of the plasma membrane, whereas the smaller exosomes (30–150 nm) are intraluminal vesicles (ILVs) formed by inward budding of the limiting membrane of late endosomes or multivesicular bodies (MVBs), and are secreted by fusion with the plasma membrane (Raposo and Stoorvogel, 2013). Despite their ubiquitous presence in the brain, the role of EVs in brain cells and their potential effects on neurodegenerative processes are relatively unknown. In pathological settings, proteins prone to aggregation (i.e., Aβ, Tau, α-synuclein, and prion) are secreted in EVs, potentially providing an avenue for spreading such misfolded proteins to neighboring healthy cells (Rajendran et al., 2006; Vella et al., 2007; Danzer et al., 2012; Saman et al., 2012). For example, the spread of tau requires neighboring microglia and exosomes (Asai et al., 2015), and tau overexpression also abnormally recruits other proteins to exosomes (Saman et al., 2014). Alzheimer's disease (AD) brain-derived exosomes contain tau and Aβ oligomers that can seed and propagate pathology (Sardar Sinha et al., 2018; Miyoshi et al., 2021). Other studies have shown beneficial effects of certain exosomes in reducing amyloid load and protecting against synaptic plasticity deficits (An et al., 2013; Yuyama et al., 2014).

Recent studies suggest that EV secretion of pathological proteins and autophagy pathways may be linked. For example, autophagy activation with the mTOR inhibitor rapamycin inhibits exosomal prion release, whereas inhibition of autophagy increases exosomal prion secretion (Abdulrahman et al., 2018). In a similar vein, inhibition of lysosome function by bafilomycin A1 increases TDP-43 and α-synuclein release in EVs (Iguchi et al., 2016; Minakaki et al., 2018), suggesting that failure of the autophagy-lysosome pathway (ALP) directs autophagosomes containing misfolded proteins for secretion in association with EVs. This secretory pathway has been proposed to involve the fusion of autophagosomes with MVBs to form amphisomes, which are then secreted by fusion with the plasma membrane (Gordon et al., 1992; Liou et al., 1997; Fader et al., 2008; Ganesan and Cai, 2021). Interestingly, autophagy cargo receptors, such as Sqstm1/p62 and optineurin, are often found in secreted exosomes (Gudbergsson and Johnsen, 2019), while they play vital roles in the clearance of misfolded proteins such as tau in AD (Xu et al., 2019; Woo et al., 2020; Fang et al., 2021; Roca-Agujetas et al., 2021a,b). However, whether prototypic autophagy cargo receptors regulate exosome secretion is unknown. Moreover, despite the crucial role of actin dynamics in secretory vesicle docking and secretion (Li et al., 2018), how actin dynamics regulate exosome secretion is also unknown. We and others previously showed that the protein phosphatase Slingshot Homolog-1 (SSH1) contains two major separable activities in the control of actin dynamics through cofilin activation through dephosphorylation at Ser3 (Niwa et al., 2002) and autophagy inhibition through p62 dephosphorylation at pSer403 (Fang et al., 2021). In this study, using a combination of DiI labeling of EVs and differential centrifugation, we explored the role of autophagy cargo receptors and actin dynamics regulated by SSH1 in small EV (sEV, aka exosome) secretion. Our findings highlight the roles of autophagy cargo receptors and actin dynamics in regulating sEV secretion through mechanisms impacting AD pathogenesis.

Materials and methods

Cell lines

Mouse hippocampus-derived neuroblastoma cells HT22, mouse embryonic fibroblast-derived NIH3T3, and tetracycline-inducible human embryonic kidney 293 cells overexpressing tau P301L (iHEK P301L) were cultured in Dulbecco's modified Eagle's medium (DMEM 1X) (Gibco, 11965-092) supplemented with 10% fetal bovine serum (FBS) (Sigma, 12306C) and 1% penicillin-streptomycin (P/S) (Gibco, 15140-122), and BM cyclin (Roche, 10799050001). iHEKP301L cells were induced with 1 μg/mL tetracycline when seeded, and cells were grown for 48 h before performing experimental assays. Cells were maintained at 37°C with 5% CO_2 levels.

Abbreviations: Aβ42o, Aβ42 oligomers; Arp2/3, actin related protein 2/3 complex; AD, Alzheimer's disease; ALS, amyotrophic lateral sclerosis; ALP, autophagy-lysosome pathway; CK2, casein kinase 2; EVs, extracellular vesicles; sEVs, small EVs; F-actin, fllamentous actin; FTDP-17, frontotemporal dementia with parkinsonism-17; Hsc70, heat shock cognate 70 kDa protein; FP, green fluorescent protein; ILVs, intraluminal vesicles; LIR, LC3 interacting region; LC3, microtubule-associated protein light chain 3; MVs, microvesicles; MVBs, multivesicular bodies; mTOR, mammalian target of rapamycin; NTA, nanoparticle tracking analysis; SSH1, slingshot homolog-1; sequestosome-1, Sqstm1/p62; TBK1, tank binding kinase 1; TSG101, tumor susceptibility gene 101 protein; UBA, ubiquitin association; ULK1, Unc-51 like autophagy activating kinase 1.

Primary neurons

Cortical primary neurons were cultured from C57BL6 or tauP301S P0 mouse pups as previously described (Woo et al., 2015b; Fang et al., 2021). Briefly, the cortex was dissected in ice-cold HBSS and digested with 0.25% Trypsin-EDTA (1X) (Gibco, 25200-056), then plated in culture-treated plates with neurobasal medium (Invitrogen, 21103049) supplemented with 2% GlutaMAX (Invitrogen, 35050061) and 2% B27 supplement (Invitrogen, 17504044). Cells were maintained at 37°C with 5% CO_2 levels.

DNA constructs

pMXs-puro GFP-p62 (Addgene, 38277) (Itakura and Mizushima, 2011), pMXs-puro GFP-p62ΔC (addgene, 38282) (Itakura and Mizushima, 2011), ECFP-SSH1ΔC (Kurita et al., 2008), pEGFP-N1 human cofilin WT (addgene, 50859) (Garvalov et al., 2007), pEGFP-N1 human cofilin S3A (addgene, 50860) (Garvalov et al., 2007), pEGFP-N1 human cofilin S3E (addgene, 50861) (Garvalov et al., 2007), pOPTN-EGFP (addgene, 27052) (Park et al., 2006), pOPTN E478G-EGFP (addgene, 68848) (Turturro et al., 2014) were obtained from corresponding sources. Plasmids p3xFlag-SSH1 and p3xFlag-SSH1ΔN, and GFP-p62 403E were generated in the Kang lab as previously documented (Fang et al., 2021).

DNA transfections

DNA plasmids were transiently transfected using Lipofectamine 2000 (Invitrogen, 11668-019) and reduced serum media Opti-MEM I (Gibco, 31985-070). After 4–6 h post-transfection, the media was replaced with new complete medium. Cells were grown for 48 h after transfection.

Small extracellular vesicle (exosome) isolation

Small extracellular vesicles within the size range of exosomes were isolated by serial centrifugation as previously described (Witas et al., 2017). Briefly, 48 h after transfection, cells were washed twice with PBS (Gibco, 10010-023), and media was replaced with DMEM 1X supplemented with 10% exosome-depleted fetal bovine serum (FBS) (Gibco, A27208-03) and 1% P/S. Twenty-four hours later, media was collected for EV isolation. Samples were centrifuged at 4°C at 800 × *g* for 10 min to remove cells and large bodies, and supernatants were centrifuged at 4°C at 2,500 × *g* for 15 min to remove cell debris. Supernatants were then centrifuged at 4°C at 10,000 × *g* for 30 min to separate pellet microvesicles. Finally, the resulting supernatants were labeled with DiI and centrifuged 4°C at 100,000 × *g* for 1 h to pellet small EVs. Small EV pellets were washed with PBS and used for analysis.

DiI staining

Vesicles were stained with DiI as previously described (Witas et al., 2017). Briefly, post-microvesicle supernatants were rocked for 15 min in 5 μM DiI (Thermo Fisher, D3911) solution at 37°C. After EVs isolation and washing, pellets were resuspended in 5 μl of fluorochrome mounting solution (Thermo scientific, TA-030-FM), and the entire volume was placed on a glass slide and covered with a glass coverslip for imaging and analysis.

Nanoparticle tracking analysis

Isolated EVs were resuspended in 500 μl of PBS and ran on NanoSight™ LM10 with nanoparticle tracking analysis (Malvern). Using the NanoSight software, three videos of 60 s each were taken and analyzed for particle size distribution.

Protein extraction

For cell protein extraction, cells were washed with 1× PBS and then resuspended in RIPA lysis buffer (50 mM Tris–HCl, pH 7.4, 150 mM NaCl, 2 mM EDTA, and 1% Triton X-100 [Amresco, 0694–1 L], 0.1% SDS) with protease inhibitor (GeneDEPOT, P3100-010) and phosphatase inhibitor (GeneDEPOT, P3200-005). Sample concentrations were determined and equalized using Pierce BCA Protein Assay Kit (Thermo Scientific, 23225), and then used for immunoblotting. For EV protein extraction, EVs isolated from the media of two 10 cm plates were resuspended in RIPA buffer with protease and phosphatase inhibitors. The samples were equalized based on corresponding protein concentrations in cell lysates.

Western blotting

Equal protein amounts were loaded and ran in SDS-PAGE gels, then transferred to nitrocellulose membranes (GE Healthcare, 10600002). Blots were probed with primary antibodies overnight at 4°C (1:1000 dilution in TBS-T) and with HRP-conjugated secondary antibodies overnight at 4°C (1:1000 dilution in TBS-T) before detection with ECL western blot reagents (Pierce, 34578) and imaged with Fuji LAS-4000 imager (LAS-4000, Pittsburgh, PA, United States). All images were quantified using NIH ImageJ software.

Antibodies

Antibodies were purchased from the following commercial sources: Aβ (Cell Signaling Technology, 8243S), Tau (Santa Cruz Biotech, sc-390476), Hsc70 (Enzo Life Sciences, ADI-SPA-815-F), TSG101 (Thermo Fisher, PA5-31260), GFP (Cell Signaling Technology, 2956S), β-Actin (Santa Cruz Biotech, sc-47778), p62 (Cell Signaling Technology, 5114), Flag (Sigma Aldrich, F1804), SSH1 (ECM Biosciences, SP1711) (Cell Signaling Technology, 13578), Cofilin (Cell Signaling Technology, 5175s), Peroxidase-Conjugated AffiniPure Goat anti-mouse IgG (Jackson ImmunoResearch, 115-035-033), Peroxidase-conjugated AffiniPure Goat anti-rabbit IgG (Jackson ImmunoResearch, 111-035-033), donkey anti-rat IgG-HRP (Southern Biotech, 6430-05).

Drugs, reagents, and oligonucleotides

Amyloid-β 1-42 (GenicBio, A-42-T-1), Rapamycin (Sigma Aldrich, R0395), Bafilomycin A1 (Sigma Aldrich, B1793), Latrunculin B (Sigma Aldrich, L5288), Jasplakinolide (AdipoGen Life Sciences, 102396-24-7), p62 siRNA (Cell Signaling Technology, 6399S), SSH1 siRNA (Dharmacon GE Healthcare, 5′-GAG GAG CUG UCC CGA UGA C-3′), Cofilin siRNA (Dharmacon GE Healthcare, 5′-GGA GGA CCU GGU GUU CAU C-3′).

Imaging and quantification

Confocal images were captured with the Olympus FV10i confocal microscope (Tokyo, Japan). All images were quantified using NIH ImageJ software.

Results

Rapamycin decreases and bafilomycin increases small extracellular vesicle secretion

To measure the secretion of exosomes, hereafter referred to as small EVs (sEVs), we used medium containing exosome-depleted (exo-free) FBS to collect conditioned medium from cells. Post-microvesicle (10,000 × *g*) supernatant was labeled with the fluorescent lipophilic dye DiI and ultracentrifuged at 100,000 × *g* to pellet sEVs (**Figure 1A**). We then visualized and quantified isolated sEVs on microscopic slides by fluorescence confocal microscopy. A similar method of DiI-labeling of EVs has previously been documented (Lehmann et al., 2008; Beer et al., 2015; Witas et al., 2017). As earlier studies showed that the autophagy activator and mTOR inhibitor rapamycin significantly inhibits sEV secretion (Fader et al., 2008; Abdulrahman et al., 2018; Bhat et al., 2021), we first tested the effects of rapamycin on sEV secretion in NIH3T3 cells. Indeed, rapamycin treatment for 24 h significantly reduced sEV secretion by ∼30% (**Figures 1B,C**). Western blotting for exosome markers Hsc70 and TSG101 showed corresponding reductions of both proteins in isolated sEVs but not in whole-cell lysates (**Figure 1D**). Nanoparticle tracking analysis (NTA) showed that the isolated sEVs are within the expected size range, the vast majority of which were under ∼150 nm in diameter with a minor proportion in the 150–250 nm range (**Figure 1E**). By contrast, inhibition of lysosomes with bafilomycin A1 treatment for 6 h significantly increased sEV release into the conditioned medium by ∼45% (**Figures 1F,G**), in agreement with previous studies (Iguchi et al., 2016; Minakaki et al., 2018).

Autophagy cargo receptors, Sqstm1/p62 and optineurin, suppress secreted small extracellular vesicle secretion through the ubiquitin association domain

While previous studies have observed autophagy cargo receptors such as Sqstm1/p62 and optineurin in isolated sEVs (Gudbergsson and Johnsen, 2019), whether such cargo receptors regulate sEV secretion is unknown. Hence, we tested if overexpression of Sqstm1/p62 or optineurin alters sEV secretion. Hereafter, we use p62 in reference to Sqstm1/p62. The C-terminal region of p62 contains the UBA and LIR domains essential for binding to ubiquitinated cargo and LC3, respectively (**Figure 2A**; Katsuragi et al., 2015). The UBA region of p62 is subject to phosphorylation at Ser403 by ULK1, CK2, and/or TBK1, allowing p62 to bind ubiquitinated cargo (Pilli et al., 2012; Katsuragi et al., 2015; Lim et al., 2015; Matsumoto et al., 2015; Sanchez-Martin and Komatsu, 2018). GFP-p62 transfection significantly decreased sEV secretion by ∼50% compared to control GFP transfection (**Figures 2B–D**). However, transfection of p62 lacking the UBA and LIR domains (p62ΔC) failed to alter sEV secretion (**Figures 2B–D**), suggesting that p62 engagement with ubiquitinated cargo and/or LC3 binding are necessary to inhibit sEV release. Like p62, transfection of optineurin also suppressed sEV secretion. However, the ALS-linked optineurin E478G mutant, which fails to bind ubiquitin (Nakazawa et al., 2016), also failed to alter sEV secretion (**Figures 2E–G**), indicating that ubiquitin binding is a necessary step in suppressing sEV secretion by optineurin. To determine if endogenous p62 normally inhibits sEV secretion, we transfected cells with p62 siRNA. As expected, p62 knockdown significantly increased sEV secretion by ∼40% (**Figures 2H–J**). Hence, these observations indicate that autophagy cargo receptors, p62 and optineurin, inhibit sEV secretion by engaging ubiquitinated cargo.

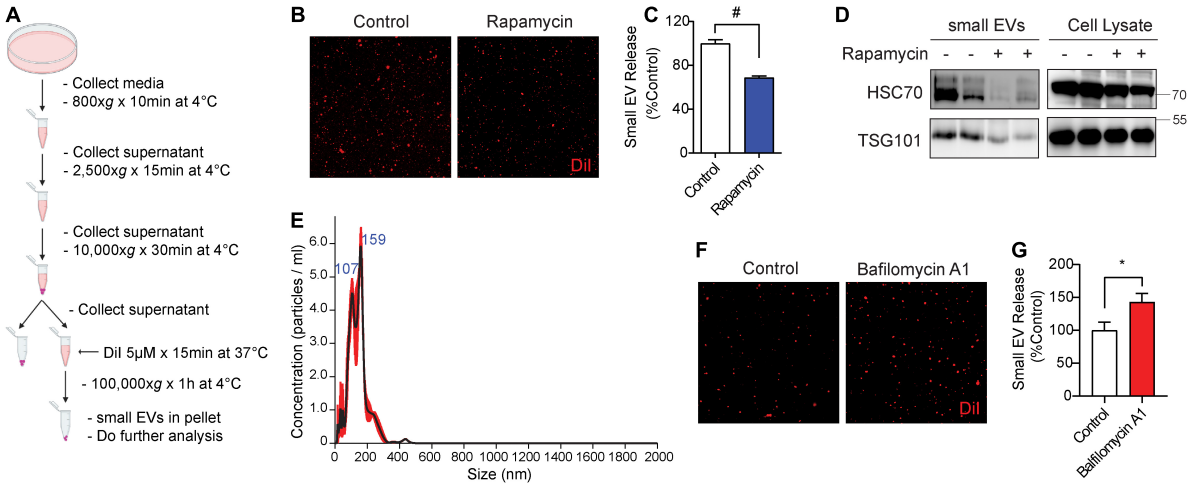

FIGURE 1
Rapamycin decreases and bafilomycin A1 increases small EV secretion. **(A)** Schematic of small EV isolation method. **(B)** Representative images of DiI-stained small EVs secreted from NIH3T3 cells with or without 200 nM rapamycin treatment for 24 h. **(C)** Quantification of secreted small EVs for **(B)**. Data are presented as means ± SEM. n = 3 independent experiments, t-test, $^{\#}P < 0.0001$. **(D)** Representative immunoblots for the indicated proteins in secreted small EVs and cell lysates from NIH3T3 cells with or without 200 nM rapamycin treatment for 24 h. **(E)** Representative NTA analysis of small EVs isolated from NIH3T3 cells. The black line indicates concentration and size of particles, and the red line indicates standard error. **(F)** Representative images of DiI-stained small EVs secreted from NIH3T3 cells with or without 200 nM bafilomycin A1 treatment for 6 h. **(G)** Quantification of secreted small EVs for **(F)**. Data are presented as means ± SEM. n = 4 independent experiments, t-test, $^{*}P = 0.02$.

Slingshot homolog-1-mediated p62 inhibition at pSer403 increases secreted small extracellular vesicle secretion

We recently showed that SSH1 contains a modular activity in inhibiting p62 autophagy flux by dephosphorylating p62 at pSer403, the phospho-residue that allows p62 binding to ubiquitinated cargo (Fang et al., 2021). SSH1 siRNA significantly decreased sEV secretion by nearly ∼40% (**Figures 3A–C**), indicating that endogenous SSH1 promotes sEV secretion. Conversely, forced expression of SSH1 significantly increased sEV secretion (**Figures 3D–F**). In p62 depleted cells, which exhibited significantly elevated sEV secretion (**Figures 3G–I**), SSH1 failed to increase sEV secretion (**Figures 3G–I**), indicating that SSH1-induced sEV secretion requires p62. To determine if SSH1-induced sEV secretion is specifically through p62 dephosphorylation at pSer403, we co-transfected cells with or without SSH1 and GFP control, GFP-p62, or GFP-p62-S403E, the latter mutant which mimics constitutive p62 phosphorylation at Ser403 (Fang et al., 2021). As expected, SSH1 overexpression significantly increased sEV secretion in the setting of GFP transfection and significantly reversed the decline in sEV secretion induced by GFP-p62 (**Figures 3J–L**). However, SSH1 failed to change the reduction in sEV secretion caused by GFP-p62-S403E (**Figures 3J–L**), indicating that SSH1 increases sEV secretion by dephosphorylating p62 at pSer403, a step that renders p62 inactive for binding to ubiquitinated cargo. Hence, these results indicate that the ability of p62 to engage ubiquitinated cargo is critical to SSH1-regulated sEV secretion. We did not investigate SSH1-mediated effects on optineurin-induced inhibition of sEV secretion, as SSH1 does not alter optineurin-mediated autophagy (Fang et al., 2021).

Slingshot homolog-1 increases secreted small extracellular vesicle secretion partially through cofilin activation and F-actin disruption

Slingshot homolog-1 was initially discovered as the major phosphatase that activates the actin severing and depolymerizing protein cofilin by its dephosphorylation at pSer3, increasing actin dynamics (Niwa et al., 2002; Kurita et al., 2007, 2008). SSH1-mediated dephosphorylation of cofilin and p62 are separable activities, as SSH1ΔN lacking the cofilin binding site dephosphorylates p62 but not cofilin, while the SSH1ΔC lacking the p62 binding site dephosphorylates cofilin but not p62 (Fang et al., 2021; **Figure 4A**). Hence, we tested if SSH1ΔN and SSH1ΔC increase sEV secretion compared to vector control and full-length SSH1. Surprisingly, SSH1ΔN or SSH1ΔC overexpression significantly increased sEV secretion compared to vector control, albeit less effectively than full-length SSH1 (**Figures 4B–D**). Given that SSH1ΔC increases cofilin activation, we next tested whether cofilin *per se* increases sEV secretion. Indeed, cofilin overexpression alone

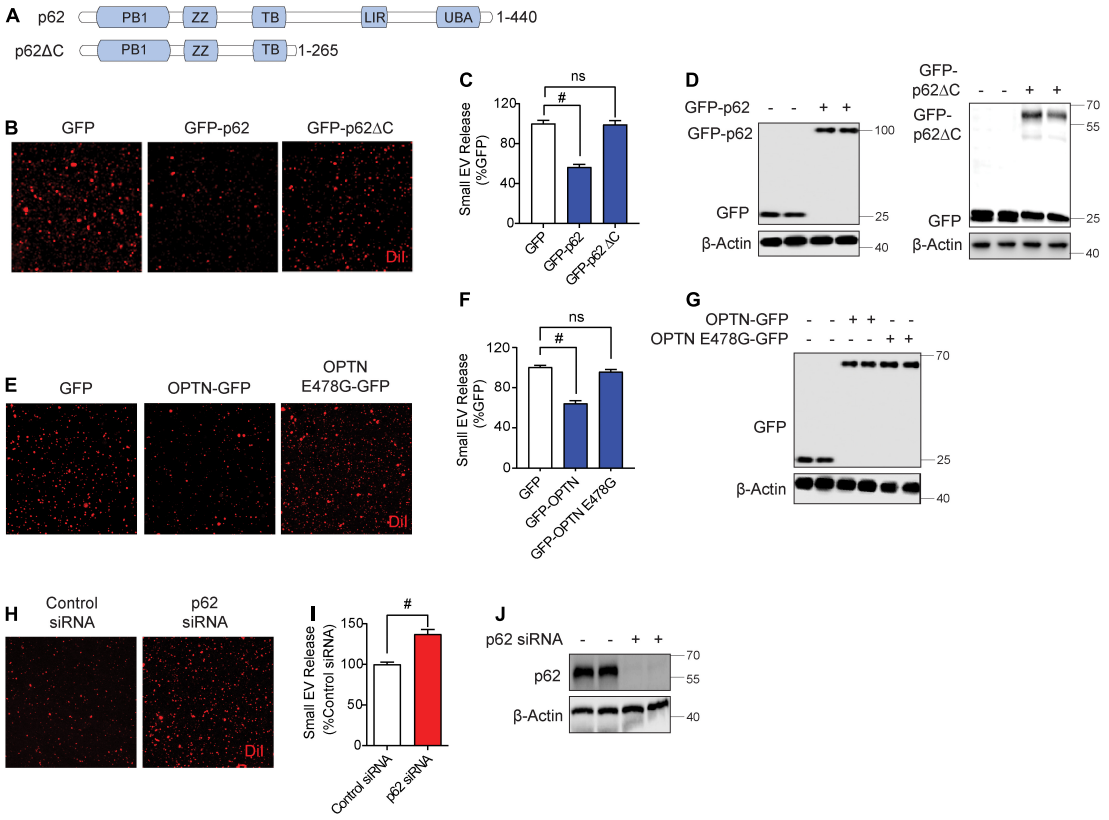

FIGURE 2
Autophagy cargo receptors, p62 and optineurin, inhibit small EV secretion through the ubiquitin association domain. **(A)** Schematic of p62 full length and p62ΔC proteins with their respective domains. **(B)** Representative images of DiI-stained small EVs secreted from NIH3T3 cells expressing GFP, GFP-p62, or GFP-p62ΔC. **(C)** Quantification of secreted small EVs for **(B)**. Data are presented as means ± SEM. $n = 3$ independent experiments, 1-way ANOVA, followed by Dunnett's *post-hoc*, $^{\#}P < 0.0001$. **(D)** Representative immunoblots of GFP-p62, GFP-p62ΔC, GFP, and β-Actin protein levels in lysates from cells for **(B)**. **(E)** Representative images of DiI-stained small EVs secreted from NIH3T3 cells expressing GFP, GFP-OPTN, or GFP-OPTN E478G. **(F)** Quantification of secreted small EVs for **(E)**. Data are presented as means ± SEM. $n = 3$ independent experiments, 1-way ANOVA, followed by Dunnett's *post-hoc*, $^{\#}P < 0.0001$. n.s. = not significant. **(G)** Representative immunoblots for GFP, GFP-OPTN, and β-Actin protein levels in cell lysates for **(E)**. **(H)** Representative images of DiI-stained small EVs secreted from NIH3T3 cells transfected with control siRNA or p62 siRNA. **(I)** Quantification of secreted small EVs for **(H)**. Data are presented as means ± SEM. $n = 4$ independent experiments, *t*-test, $^{\#}P < 0.0001$. **(J)** Representative immunoblots for p62 and β-Actin protein levels in cell lysates for **(H)**.

significantly increased sEV secretion by ∼30% (**Figures 4E–G**). The constitutively active cofilin-S3A similarly increased sEV secretion, whereas the inactive and dominant-negative cofilin-S3E (Liu et al., 2017; Shaw and Bamburg, 2017; Woo et al., 2019), which mimics the phosphorylated state, significantly decreased sEV secretion by ∼40% (**Figures 4H–J**). Moreover, cofilin siRNA significantly reduced sEV secretion by ∼35% (**Figures 4K–M**), indicating that endogenous cofilin promotes sEV secretion.

As actin filament severing and depolymerization activity of cofilin promoted sEV secretion, we tested if latrunculin B and jasplakinolide, drugs known to inhibit actin polymerization (Wakatsuki et al., 2001) and nucleate actin (Bubb et al., 2000), respectively, alter sEV secretion. Compared to the vehicle control, preventing actin polymerization by latrunculin B significantly increased sEV secretion by ∼50%, whereas promoting actin nucleation by jasplakinolide had no significant effect on sEV secretion (**Figures 4N,O**). These results are consistent with the observation that activated cofilin, which severs and depolymerizes F-actin, increases sEV release.

Aβ42 oligomers and misfolded tau increase secreted small extracellular vesicle secretion and are associated with secreted small extracellular vesicles

Aβ42 oligomers (Aβ42o) increase cofilin activation *via* SSH1, disrupt F-actin (Woo et al., 2015b) and enhance mTOR signaling (Caccamo et al., 2010). Moreover, misfolded mutant tau inhibits p62-mediated autophagy flux (Fang et al.,

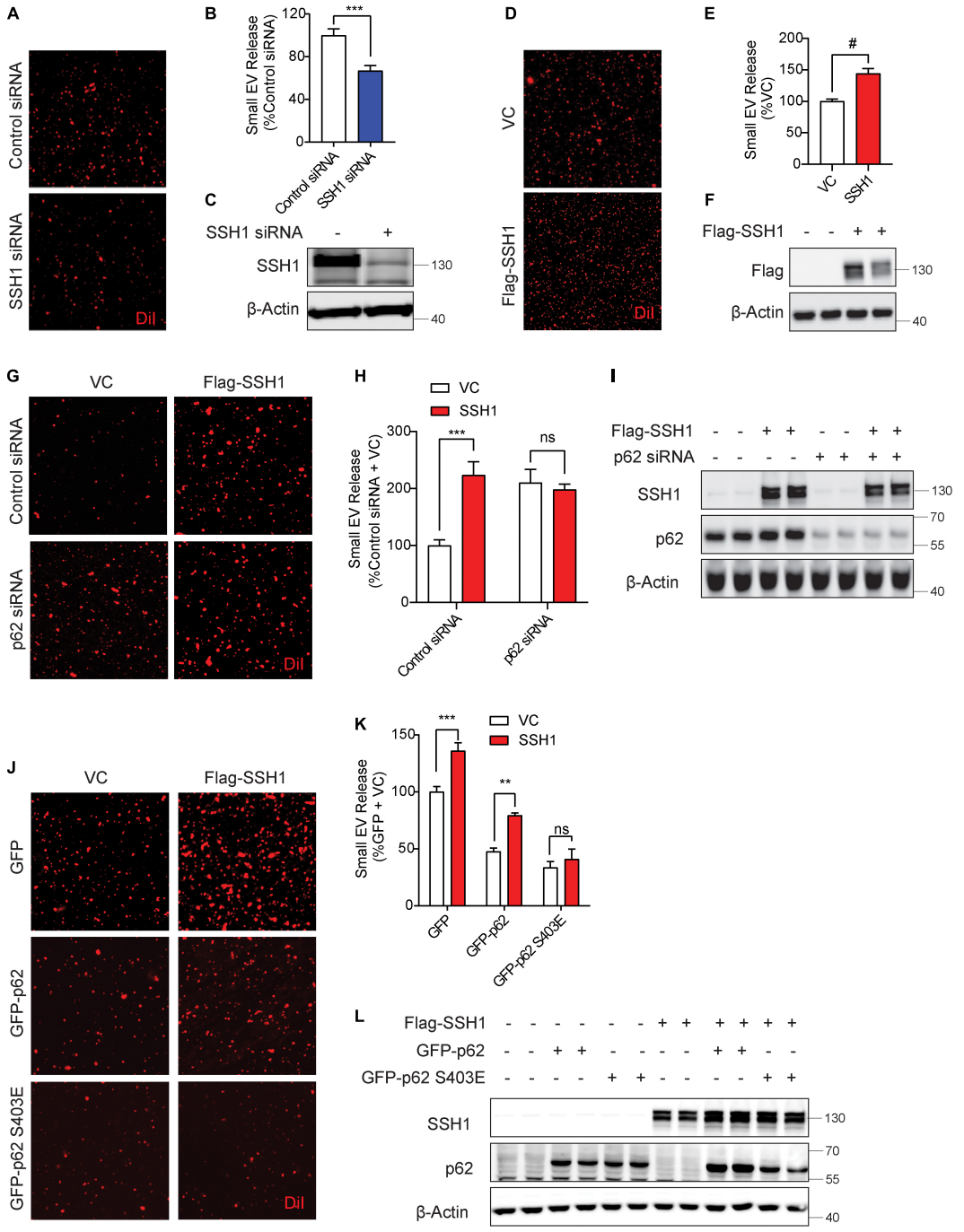

FIGURE 3
Slingshot homolog-1 (SSH1)-mediated p62 inhibition at pSer403 increases small EV secretion. **(A)** Representative images of DiI-stained small EVs secreted from NIH3T3 cells transfected with control siRNA or SSH1 siRNA. **(B)** Quantification of secreted small EVs for **(A)**. Data are presented as means ± SEM. $n = 3$ independent experiments, t-test, $^{***}P = 0.0005$. **(C)** Representative immunoblots for SSH1 and β-Actin protein levels in cell lysates for **(A)**. **(D)** Representative images of DiI-stained small EVs secreted from NIH3T3 cells expressing VC or Flag-SSH1 **(E)** Quantification of secreted small EVs for **(D)**. Data are presented as means ± SEM. $n = 3$ independent experiments, t-test, $^{\#}P < 0.0001$ **(F)** Representative immunoblots for Flag and β-Actin protein levels in cell lysates for **(D)**. **(G)** Representative images of DiI-stained small EVs secreted from NIH3T3 cells co-transfected with VC or Flag-SSH1 and control siRNA or p62 siRNA. **(H)** Quantification of secreted small EVs for **(G)**. Data are presented as means ± SEM. $n = 3$ independent experiments, 2-way ANOVA, followed by Sidak's *post-hoc*, $^{***}P = 0.0004$. n.s. = not significant. **(I)** Representative immunoblots showing SSH1, p62, and β-Actin protein levels in cell lysates for **(G)**. **(J)** Representative images of DiI-stained small EVs secreted from NIH3T3 cells co-transfected with VC or Flag-SSH1 and GFP, GFP-p62, or GFP-p62 S403E. **(K)** Quantification of secreted small EVs for **(J)**. Data are presented as means ± SEM. $n = 3$ independent experiments, 2-way ANOVA, followed by Sidak's *post-hoc*, $^{***}P = 0.0007$, $^{**}P = 0.001$. n.s. = not significant. **(L)** Representative immunoblots for SSH1, p62, and β-Actin protein levels in cell lysates for **(J)**.

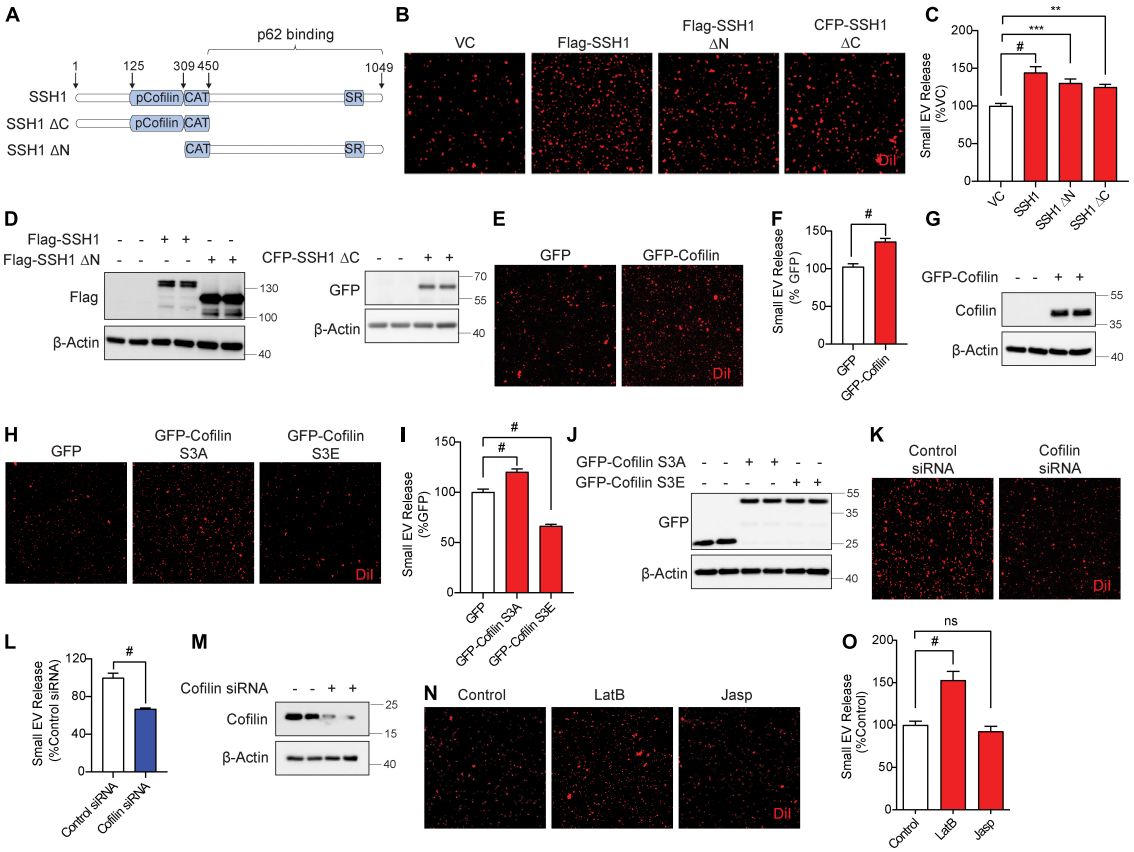

FIGURE 4
Slingshot homolog-1 (SSH1) increases small EV secretion partially through cofilin activation and F-actin disruption. **(A)** Schematic of SSH1 full length, SSH1ΔC, and SSH1ΔN proteins. **(B)** Representative images of DiI-stained small EVs secreted from NIH3T3 cells expressing VC, Flag-SSH1, Flag-SSH1ΔN, or CFP-SSH1ΔC. **(C)** Quantification of secreted small EVs for **(B)**. Data are presented as means ± SEM. $n = 3$ independent experiments, 1-way ANOVA, followed by Dunnett's *post-hoc*, $^{\#}P < 0.0001$, $^{***}P = 0.001$, $^{**}P = 0.0069$. **(D)** Representative immunoblots for Flag, GFP, and β-Actin protein levels in cell lysates for **(B)**. **(E)** Representative images of DiI-stained small EVs secreted from NIH3T3 cells expressing GFP or GFP-Cofilin. **(F)** Quantification of secreted small EVs for **(E)**. Data are presented as means ± SEM. $n = 3$ independent experiments, *t*-test, $^{\#}P < 0.0001$. **(G)** Representative immunoblots for cofilin and β-Actin protein levels in cell lysates for **(E)**. **(H)** Representative images of DiI-stained small EVs secreted from NIH3T3 cells expressing GFP, GFP-cofilin-S3A, or GFP-cofilin-S3E. **(I)** Quantification of secreted small EVs for **(H)**. Data are presented as means ± SEM. $n = 3$ independent experiments, 1-way ANOVA, followed by Dunnett's *post-hoc*, $^{\#}P < 0.0001$. **(J)** Representative immunoblots for GFP and β-Actin protein levels in cell lysates for **(H)**. **(K)** Representative images of DiI-stained small EVs secreted from NIH3T3 cells transfected with control siRNA or cofilin siRNA. **(L)** Quantification of secreted small EVs for **(K)**. Data are presented as means ± SEM. $n = 3$ independent experiments, *t*-test, $^{\#}P < 0.0001$. **(M)** Representative immunoblots for cofilin and β-Actin protein levels in cell lysates for **(K)**. **(N)** Representative images of DiI-stained small EVs secreted from NIH3T3 cells with or without 100 nM Latrunculin B (LatB) or 100 nM Jasplakinolide (Jasp) treatment for 8 h. **(O)** Quantification of secreted small EVs for **(N)**. Data are presented as means ± SEM. $n = 3$ independent experiments, 1-way ANOVA, followed by Dunnett's *post-hoc*, $^{\#}P < 0.0001$. n.s. = not significant.

2021) and promotes F-actin bundling (Fulga et al., 2007; Cabrales Fontela et al., 2017). We tested if these AD signature pathologies alter sEV secretion and are in turn associated with sEVs. For treatment with Aβ42o, we used mouse hippocampus-derived HT22 neuroblastoma cells, as HT22 cells are responsive to Aβ42o-induced cofilin activation (Woo et al., 2015b). Aβ42o were prepared as previously described (Woo et al., 2015b). Aβ42o (250 nM) treatment to HT22 cells for 24 h significantly increased sEV secretion by nearly ∼3-fold (**Figures 5A,B**). Likewise, Western blotting for Hsc70 and TSG101 also demonstrated significant increases in these exosome markers by Aβ42o treatment in isolated sEVs but not in cell lysates (**Figures 5C,D**). The treated Aβ42o were readily detected in isolated sEVs (**Figure 5C**). Like in NIH3T3 cells, isolation of DiI-labeled sEVs in HT22 cells yielded the vast majority of nanovesicles <150 nm in diameter by NTA (**Figure 5E**), consistent with the range for exosomes. To determine whether misfolded tau alters sEV secretion, we utilized Frontotemporal dementia with Parkinsonism-17 (FTDP-17) tau^{P301S} mutant and littermate WT neurons from P0 pups grown for 9 days *in vitro* (DIV9). On DIV9, the media was replaced with fresh media and collected after 24 h. Tau^{P301S} neurons exhibited significantly increased sEV secretion compared to littermate WT neurons (**Figures 5F,G**). To confirm this

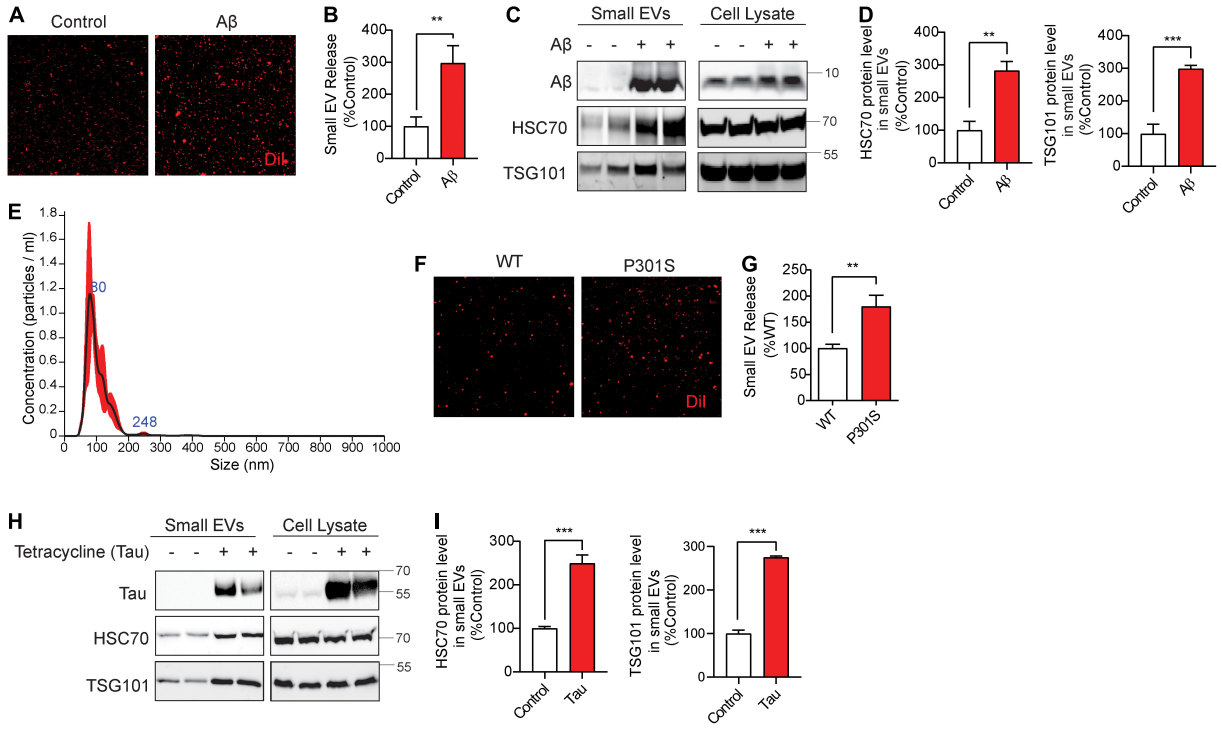

FIGURE 5
Aβ42 oligomers (Aβ42) oligomers and misfolded tau increase small EV secretion and are associated with secreted small EVs. **(A)** Representative images of DiI-stained small EVs secreted from HT22 cells with or without 250 nM Aβ treatment for 24 h. **(B)** Quantification of secreted small EVs for **(A)**. Data are presented as means ± SEM. n = 3 independent experiments, t-test, $^{**}P < 0.005$. **(C)** Representative immunoblots for the indicated proteins in secreted small EVs and cell lysates from HT22 cells with or without 250 nM Aβ treatment for 24 h. **(D)** Quantification of Hsc70 and TSG101 (small EV markers) for **(C)**. Data are presented as means ± SEM. n = 4 independent experiments, t-test, $^{***}P = 0.0007$, $^{**}P < 0.004$. **(E)** Representative NTA analysis of vesicle size distribution of small EVs isolated from HT22 cells. The black line indicates concentration and size of particles, and the red line indicates standard error. **(F)** Representative images of DiI-stained small EVs secreted by DIV10 cortical primary neurons derived from C57BL6 (WT) or tau^{P301S} (P301S) mice. **(G)** Quantification of secreted small EVs for **(F)**. Data are presented as means ± SEM. n = 3 independent experiments, t-test, $^{**}P = 0.002$. **(H)** Representative immunoblots for the indicated proteins in secreted small EVs and cell lysates from tet-inducible iHEK-P301L cells expressing tau^{P301L}, with or without tetracycline. **(I)** Quantification of Hsc70 and TSG101 (small EV markers) for **(H)**. Data are presented as means ± SEM. n = 4 independent experiments, t-test, $^{***}P < 0.0003$.

finding in a different way using another FTDP-17-linked tau mutation, we utilized tetracycline-inducible HEK293 expressing the tau^{P301L} mutation. Tetracycline-inducible expression of tau^{P301L} significantly increased exosome markers Hsc70 and TSG101 in isolated sEVs but not in cell lysates (**Figures 5H,I**), indicating that misfolded tau increases sEV secretion in neurons and HEK293 cells. Tau^{P301L} was also readily detected in association with isolated sEVs (**Figure 5H**), indicating that misfolded tau not only drives sEV release but is also a content of sEVs.

Discussion

Multiple studies have implicated the involvement of the SSH1-cofilin pathway in Aβ-induced dendritic spine shrinkage and F-actin loss (Zhao et al., 2006; Shankar et al., 2007) as well as the accumulation of multiple pathologies, including cofilin-actin pathology (Minamide et al., 2000; Rahman et al., 2014), Aβ pathology (Liu et al., 2019), and tau pathology (Woo et al., 2019). Cofilin activity is increased in the brains of AD patients (Zhao et al., 2006; Kim et al., 2013) and the APP/PS1 mouse model (Woo et al., 2015b). At the same time, the autophagy-lysosome pathway is overwhelmed and impaired in AD (Lin et al., 2003; Nixon et al., 2005; Salminen et al., 2012; Hebron et al., 2014; Rea et al., 2014; Tanji et al., 2014; Feng et al., 2019; Roca-Agujetas et al., 2021a,b), which contributes to the accumulation of misfolded proteins and dysfunctional mitochondria (Ramesh Babu et al., 2008; Xu et al., 2019; Woo et al., 2020; Fang et al., 2021; Roca-Agujetas et al., 2021a,b). Meanwhile, AD pathological proteins Aβ and tau are secreted in exosomes and are propagated from cell to cell in part *via* exosomes (Asai et al., 2015; Sardar Sinha et al., 2018; Miyoshi et al., 2021). Yet, the pathobiological relationship between these drivers of AD pathogenesis and sEV secretion are unknown. In this study, we took advantage of the dual axes of SSH1 signaling in the inhibition of autophagy (Fang et al., 2021) and the promotion of actin dynamics (Niwa et al., 2002; Kurita et al., 2007, 2008)

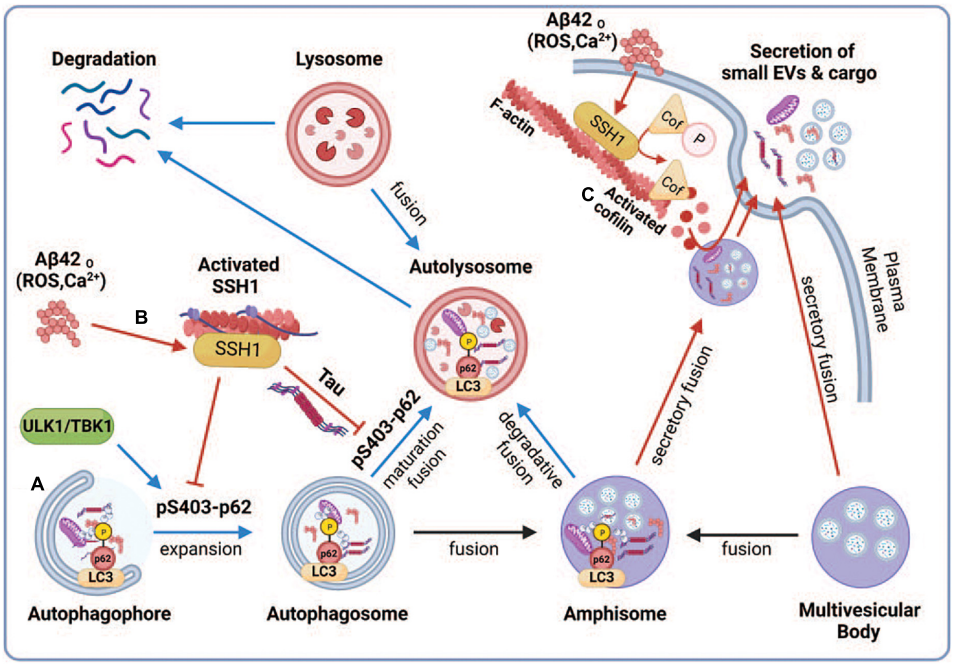

FIGURE 6
Proposed model depicting the regulation of small EV secretion by p62-mediated autophagy and cofilin-mediated actin dynamics through the SSH1 pathway. Note that blue lines/arrows favor lysosomal degradation, whereas red lines/arrows favor secretory clearance. **(A)** Accumulation of misfolded proteins or dysfunctional mitochondria activates autophagy through ULK1 and TBK1, which phosphorylate p62 at Ser403, resulting in p62 binding to ubiquitinated cargo and activation of LC3 to drive autophagosome maturation. This promotes autophagy flux and fusion of autophagosomes and amphisomes with lysosomes, resulting in the degradation of ubiquitinated cargo together with intraluminal vesicles from amphisomes, thereby reducing small EV secretion. **(B)** Oxidative stress (ROS) or calcium elevation induced by Aβ oligomers or otherwise activates SSH1, which dephosphorylates p62 at pSer403 and inhibits p62 autophagy flux. Dephosphorylated p62 is less able to bind ubiquitinated cargo and activate LC3, which slows autophagy flux and fusion of autophagosomes and amphisomes with lysosomes. This process diverts amphisomes toward the secretory fusion pathway and increases small EV secretion. Like SSH1, inhibition of p62 autophagy flux by misfolded tau (Fang et al., 2021) also likely contributes to increased small EV secretion. **(C)** Actin filaments serve to recruit vesicles and create a diffusion barrier for vesicles to gain access to the plasma membrane. SSH1 activation by ROS or calcium also activates cofilin, which severs and depolymerizes the F-actin network near the plasma membrane. This process allows large secretory amphisomes to access membrane docking sites, facilitating small EV secretion. This illustration was generated at Biorender.com.

to study the corresponding pathways in sEV secretion. We used the neutral term sEVs to place no bias on the origin of the EVs; however, sEVs are largely equivalent to exosomes based on their predominant size range. Here we showed for the first time that autophagy cargo receptors, p62 and optineurin, inhibit sEV secretion, an activity that requires their ability to engage ubiquitinated cargo. SSH1, which inhibits p62 binding to cargo (Fang et al., 2021), increased sEV secretion, but not in p62-depleted cells or cells expressing the p62-S403E mutation. However, the N-terminal domain of SSH1 (SSH1ΔC), which activates cofilin but does not inhibit p62 (Fang et al., 2021), increased sEV secretion through the cofilin activation pathway. Accordingly, latrunculin B, which prevents actin polymerization and indirectly promotes F-actin depolymerization (Wakatsuki et al., 2001), mimicked the effect of cofilin in enhancing sEV secretion. Finally, we showed that AD pathological proteins, Aβ oligomers and mutant tau, both of which impact autophagy and F-actin dynamics pathways (Fulga et al., 2007; Caccamo et al., 2010; Woo et al., 2015b; Cabrales Fontela et al., 2017; Fang et al., 2021), increased sEV secretion and are also contents of secreted sEVs. These findings, therefore, implicate autophagy cargo receptor-cargo interactions and actin dynamics in regulating sEV secretion through mechanisms contributing to AD pathogenesis.

Multiple studies have shown that autophagosomes accumulate in AD brains (Lin et al., 2003; Nixon et al., 2005; Hebron et al., 2014; Feng et al., 2019), indicative of impairment in the autophagy-lysosome pathway. Autophagosomes can fuse with multivesicular bodies (MVBs) containing intraluminal vesicles to form amphisomes or fuse directly with lysosomes for degradation (Ganesan and Cai, 2021; **Figure 6**). Our observations that the ability of p62 and optineurin to inhibit sEV secretion depends on their ability to engage ubiquitinated cargo are intriguing in light of the significantly reduced p62 Ser403 phosphorylation in AD brains (Tanji et al., 2014), a phospho-residue required for p62 to bind ubiquitinated cargo (Pilli et al., 2012; Katsuragi et al., 2015; Lim et al., 2015; Matsumoto et al., 2015; Sanchez-Martin and Komatsu, 2018).

We interpret this to indicate that the binding of autophagy cargo receptors to ubiquitinated cargo promotes autophagy flux and fusion of autophagosomes and amphisomes with lysosomes (Fang et al., 2021), which diverts amphisomes away from fusing with the plasma membrane and are instead degraded by lysosomes (**Figure 6A**). Indeed, cargo binding to p62 promotes autophagosome maturation by enhancing the synthesis of LC3 and its conversion to LC3-II (Cha-Molstad et al., 2017; **Figure 6A**). In support of this notion, SSH1 increased sEV secretion through its ability to dephosphorylate p62 at pSer403, which reduces cargo binding and inhibits p62 autophagy flux (Fang et al., 2021; **Figure 6B**). Interestingly, calcium elevation or reactive oxygen species (ROS) induced by Aβ oligomers or other stressors activate SSH1 (Davis et al., 2011; Woo et al., 2015a,b) through calcineurin activation (Wang et al., 2005; Tu et al., 2014) and/or 14-3-3 oxidation (Wang et al., 2005), respectively, the latter which releases SSH1 from 14-3-3 inhibitory control (**Figure 6B**). Such calcium and reactive oxygen species (ROS)-mediated control of SSH1 activation is consistent with our observation that Aβ42 oligomers also increase sEV secretion (**Figure 6B**). Like SSH1, inhibition of p62-mediated autophagy flux by misfolded tau (Fang et al., 2021) is also consistent with increased sEV secretion by mutant tau in this study, likely by diverting autophagosomes away from lysosomes toward secretory amphisomes (**Figure 6B**).

Control of actin dynamics is critical to maintaining cell morphology and other cellular processes, including membrane protein trafficking, endocytosis, phagocytosis, and exocytosis (Carlsson, 2018; Li et al., 2018; Liu et al., 2019). However, the role of actin dynamics in sEV secretion is essentially unknown. The actin-binding protein cortactin positively regulates sEV secretion by binding to F-actin and Arp2/3, stabilizing docking sites at the plasma membrane (Sinha et al., 2016). Like exocytosis of secretory vesicles, sEV secretion is increased by calcium elevation (Savina et al., 2003). At the microscale level, the actin-based cytoskeleton serves to both recruit vesicles and function as a diffusion barrier that prevents vesicles from gaining access to docking sites on the plasma membrane (Li et al., 2018). Hence, a dense network of actin filaments would serve as a far more significant barrier to the much larger MVBs or amphisomes. As SSH1-mediated cofilin activation is increased by calcium elevation (Wang et al., 2005), the F-actin severing and depolymerizing cofilin activities would be expected to trim the dense F-actin network, allowing MVBs and amphisomes to gain access to plasma membrane docking sites (**Figure 6C**). However, excessive depolymerization of F-actin could also hinder sEV secretion by failing to recruit MVBs or amphisomes to the F-actin mesh close to the plasma membrane. Studies on secretory vesicles have shown that it is the oscillation of calcium signals and actin dynamics (depolymerization and polymerization) that coordinately control vesicle access to docking sites and exocytosis (Li et al., 2018). Indeed, cofilin-S3A, which is far more active than wild-type (WT) cofilin, was slightly less effective than WT cofilin in increasing sEV secretion, which may be due to the excessive actin disruptive activity of this mutant. On the other hand, the inactive and dominant-negative cofilin-S3E significantly decreased sEV secretion, likely due to the inhibition of endogenous SSH1 (Liu et al., 2017; Shaw and Bamburg, 2017; Woo et al., 2019). Like cofilin, 100 nM latrunculin B treatment for 8 h, a dose that partially disrupts F-actin (Wakatsuki et al., 2001), had a net positive effect on sEV secretion.

Our studies showed that Aβ oligomers and misfolded tau not only increase sEV secretion but are also secreted in association with sEVs. This coupling appears to be a way for cells to efficiently expel misfolded proteins, which otherwise would impede and congest the autophagy machinery. Excessive secretion of misfolded proteins by "secretory autophagy" in association with sEVs or otherwise could then serve as seeds for the propagation of pathology from cell to cell (Rajendran et al., 2006; Vella et al., 2007; Danzer et al., 2012; Saman et al., 2012, 2014; Asai et al., 2015; Sardar Sinha et al., 2018; Miyoshi et al., 2021).

Conclusion

Our data suggest that increasing cargo receptor engagement with autophagic cargo and reducing actin dynamics (i.e., SSH1 inhibition) represents an attractive strategy to promote misfolded protein degradation while reducing sEV-mediated cell to cell spread of pathology.

Data availability statement

The original contributions presented in this study are included in the article/supplementary material, further inquiries can be directed to the corresponding authors.

Ethics statement

The animal study was reviewed and approved by the Institutional Animal Care and Use Committee (IACUC) at the University of South Florida (USF) and Case Western Reserve University (CWRU).

Author contributions

SC: investigation, methodology, and writing. CF, HK, and RW: investigation and methodology. TK: data analysis and visualization. JW: investigation, writing, review, and funding acquisition. DK: conceptualization, writing,

visualization, and funding acquisition. All authors have read and approved the manuscript.

Funding

This work was supported in part by grants from the National Institutes of Health (NIH) (R01AG059721, JW; R01AG067741, DK and JW; R01NS122350, DK; and RF1AG053060, DK) and Veterans Affairs (BX004680, DK).

Acknowledgments

We thank Dr. Laura Blair and Dr. Chad Dickey for providing the iHEK-tau^{P301L} cells.

Conflict of interest

The authors declare that the research was conducted in the absence of any commercial or financial relationships that could be construed as a potential conflict of interest.

Publisher's note

References

Abdulrahman, B. A., Abdelaziz, D. H., and Schatzl, H. M. (2018). Autophagy regulates exosomal release of prions in neuronal cells. *J. Biol. Chem.* 293, 8956–8968. doi: 10.1074/jbc.RA117.000713

An, K., Klyubin, I., Kim, Y., Jung, J. H., Mably, A. J., O'Dowd, S. T., et al. (2013). Exosomes neutralize synaptic-plasticity-disrupting activity of Abeta assemblies in vivo. *Mol. Brain* 6:47. doi: 10.1186/1756-6606-6-47

Antonucci, F., Turola, E., Riganti, L., Caleo, M., Gabrielli, M., Perrotta, C., et al. (2012). Microvesicles released from microglia stimulate synaptic activity via enhanced sphingolipid metabolism. *EMBO J.* 31, 1231–1240. doi: 10.1038/emboj.2011.489

Asai, H., Ikezu, S., Tsunoda, S., Medalla, M., Luebke, J., Haydar, T., et al. (2015). Depletion of microglia and inhibition of exosome synthesis halt tau propagation. *Nat. Neurosci.* 18, 1584–1593. doi: 10.1038/nn.4132

Beer, L., Zimmermann, M., Mitterbauer, A., Ellinger, A., Gruber, F., Narzt, M. S., et al. (2015). Analysis of the Secretome of Apoptotic Peripheral Blood Mononuclear Cells: Impact of Released Proteins and Exosomes for Tissue Regeneration. *Sci. Rep.* 5:16662. doi: 10.1038/srep16662

Bhat, O. M., Yuan, X., Kukreja, R. C., and Li, P. L. (2021). Regulatory role of mammalian target of rapamycin signaling in exosome secretion and osteogenic changes in smooth muscle cells lacking acid ceramidase gene. *FASEB J.* 35:e21732. doi: 10.1096/fj.202100385R

Bubb, M. R., Spector, I., Beyer, B. B., and Fosen, K. M. (2000). Effects of jasplakinolide on the kinetics of actin polymerization. An explanation for certain in vivo observations. *J. Biol. Chem.* 275, 5163–5170. doi: 10.1074/jbc.275.7.5163

Cabrales Fontela, Y., Kadavath, H., Biernat, J., Riedel, D., Mandelkow, E., and Zweckstetter, M. (2017). Multivalent cross-linking of actin filaments and microtubules through the microtubule-associated protein Tau. *Nat. Commun.* 8:1981. doi: 10.1038/s41467-017-02230-8

Caccamo, A., Majumder, S., Richardson, A., Strong, R., and Oddo, S. (2010). Molecular interplay between mammalian target of rapamycin (mTOR), amyloid-beta, and Tau: effects on cognitive impairments. *J. Biol. Chem.* 285, 13107–13120. doi: 10.1074/jbc.M110.100420

Carlsson, A. E. (2018). Membrane bending by actin polymerization. *Curr. Opin. Cell Biol.* 50, 1–7. doi: 10.1016/j.ceb.2017.11.007

Cha-Molstad, H., Yu, J. E., Feng, Z., Lee, S. H., Kim, J. G., Yang, P., et al. (2017). p62/SQSTM1/Sequestosome-1 is an N-recognin of the N-end rule pathway which modulates autophagosome biogenesis. *Nat. Commun.* 8:102. doi: 10.1038/s41467-017-00085-7

Danzer, K. M., Kranich, L. R., Ruf, W. P., Cagsal-Getkin, O., Winslow, A. R., Zhu, L., et al. (2012). Exosomal cell-to-cell transmission of alpha synuclein oligomers. *Mol. Neurodegeneration* 7:42. doi: 10.1186/1750-1326-7-42

Davis, R. C., Marsden, I. T., Maloney, M. T., Minamide, L. S., Podlisny, M., Selkoe, D. J., et al. (2011). Amyloid beta dimers/trimers potently induce cofilin-actin rods that are inhibited by maintaining cofilin-phosphorylation. *Mol. Neurodegeneration.* 6:10. doi: 10.1186/1750-1326-6-10

Fader, C. M., Sanchez, D., Furlan, M., and Colombo, M. I. (2008). Induction of autophagy promotes fusion of multivesicular bodies with autophagic vacuoles in k562 cells. *Traffic* 9, 230–250. doi: 10.1111/j.1600-0854.2007.00677.x

Fang, C. X., Woo, J. A. A., Liu, T., Zhao, X. Y., Cazzaro, S., Yan, Y., et al. (2021). SSH1 impedes SQSTM1/p62 flux and MAPT/Tau clearance independent of CFL (cofilin) activation. *Autophagy* 17, 2144–2165. doi: 10.1080/15548627.2020.1816663

Feng, Q., Luo, Y., Zhang, X. N., Yang, X. F., Hong, X. Y., Sun, D. S., et al. (2019). MAPT/Tau accumulation represses autophagy flux by disrupting IST1-regulated ESCRT-III complex formation: a vicious cycle in Alzheimer neurodegeneration. *Autophagy* 16, 641–658. doi: 10.1080/15548627.2019.1633862

Fulga, T. A., Elson-Schwab, I., Khurana, V., Steinhilb, M. L., Spires, T. L., Hyman, B. T., et al. (2007). Abnormal bundling and accumulation of F-actin mediates tau-induced neuronal degeneration in vivo. *Nat Cell Biol.* 9, 139–148. doi: 10.1038/ncb1528

Ganesan, D., and Cai, Q. (2021). Understanding amphisomes. *Biochem. J.* 478, 1959–1976. doi: 10.1042/BCJ20200917

Garvalov, B. K., Flynn, K. C., Neukirchen, D., Meyn, L., Teusch, N., Wu, X., et al. (2007). Cdc42 regulates cofilin during the establishment of neuronal polarity. *J. Neurosci.* 27, 13117–13129. doi: 10.1523/JNEUROSCI.3322-07.2007

Gordon, P. B., Hoyvik, H., and Seglen, P. O. (1992). Prelysosomal and lysosomal connections between autophagy and endocytosis. *Biochem. J.* 283, 361–369. doi: 10.1042/bj2830361

Gudbergsson, J. M., and Johnsen, K. B. (2019). Exosomes and autophagy: rekindling the vesicular waste hypothesis. *J. Cell Commun. Signal.* 13, 443–450. doi: 10.1007/s12079-019-00524-8

Hebron, M. L., Algarzae, N. K., Lonskaya, I., and Moussa, C. (2014). Fractalkine signaling and Tau hyper-phosphorylation are associated with autophagic alterations in lentiviral Tau and Abeta1-42 gene transfer models. *Exp. Neurol.* 251, 127–138. doi: 10.1016/j.expneurol.2013.01.009

Iguchi, Y., Eid, L., Parent, M., Soucy, G., Bareil, C., Riku, Y., et al. (2016). Exosome secretion is a key pathway for clearance of pathological TDP-43. *Brain* 139, 3187–3201. doi: 10.1093/brain/aww237

Itakura, E., and Mizushima, N. (2011). p62 Targeting to the autophagosome formation site requires self-oligomerization but not LC3 binding. *J. Cell Biol.* 192, 17–27. doi: 10.1083/jcb.201009067

Katsuragi, Y., Ichimura, Y., and Komatsu, M. (2015). p62/SQSTM1 functions as a signaling hub and an autophagy adaptor. *FEBS J.* 282, 4672–4678. doi: 10.1111/febs.13540

Kim, T., Vidal, G. S., Djurisic, M., William, C. M., Birnbaum, M. E., Garcia, K. C., et al. (2013). Human LilrB2 is a beta-amyloid receptor and its murine homolog PirB regulates synaptic plasticity in an Alzheimer's model. *Science* 341, 1399–1404. doi: 10.1126/science.1242077

Kurita, S., Gunji, E., Ohashi, K., and Mizuno, K. (2007). Actin filaments-stabilizing and -bundling activities of cofilin-phosphatase Slingshot-1. *Genes Cells* 12, 663–676. doi: 10.1111/j.1365-2443.2007.01078.x

Kurita, S., Watanabe, Y., Gunji, E., Ohashi, K., and Mizuno, K. (2008). Molecular dissection of the mechanisms of substrate recognition and F-actin-mediated activation of cofilin-phosphatase Slingshot-1. *J. Biol. Chem.* 283, 32542–32552. doi: 10.1074/jbc.M804627200

Lehmann, B. D., Paine, M. S., Brooks, A. M., McCubrey, J. A., Renegar, R. H., Wang, R., et al. (2008). Senescence-associated exosome release from human prostate cancer cells. *Cancer Res.* 68, 7864–7871. doi: 10.1158/0008-5472.CAN-07-6538

Li, P., Bademosi, A. T., Luo, J., and Meunier, F. A. (2018). Actin Remodeling in Regulated Exocytosis: Toward a Mesoscopic View. *Trends Cell Biol.* 28, 685–697. doi: 10.1016/j.tcb.2018.04.004

Lim, J., Lachenmayer, M. L., Wu, S., Liu, W., Kundu, M., Wang, R., et al. (2015). Proteotoxic stress induces phosphorylation of p62/SQSTM1 by ULK1 to regulate selective autophagic clearance of protein aggregates. *PLoS Genet.* 11:e1004987. doi: 10.1371/journal.pgen.1004987

Lin, W. L., Lewis, J., Yen, S. H., Hutton, M., and Dickson, D. W. (2003). Ultrastructural neuronal pathology in transgenic mice expressing mutant (P301L) human tau. *J. Neurocytol.* 32, 1091–1105. doi: 10.1023/B:NEUR.0000021904.61387.95

Liou, W., Geuze, H. J., Geelen, M. J., and Slot, J. W. (1997). The autophagic and endocytic pathways converge at the nascent autophagic vacuoles. *J. Cell Biol.* 136, 61–70. doi: 10.1083/jcb.136.1.61

Liu, T., Wang, F., LePochat, P., Woo, J. A., Bukhari, M. Z., Hong, K. W., et al. (2017). Cofilin-mediated Neuronal Apoptosis via p53 Translocation and PLD1 Regulation. *Sci. Rep.* 7:11532. doi: 10.1038/s41598-017-09996-3

Liu, T., Woo, J. A., Yan, Y., LePochat, P., Bukhari, M. Z., and Kang, D. E. (2019). Dual role of cofilin in APP trafficking and amyloid-beta clearance. *FASEB J.* 33, 14234–14247. doi: 10.1096/fj.201901268R

Matsumoto, G., Shimogori, T., Hattori, N., and Nukina, N. (2015). TBK1 controls autophagosomal engulfment of polyubiquitinated mitochondria through p62/SQSTM1 phosphorylation. *Hum. Mol. Genet.* 24, 4429–4442. doi: 10.1093/hmg/ddv179

Minakaki, G., Menges, S., Kittel, A., Emmanouilidou, E., Schaeffner, I., and Barkovits, K. (2018). Autophagy inhibition promotes SNCA/alpha-synuclein release and transfer via extracellular vesicles with a hybrid autophagosome-exosome-like phenotype. *Autophagy* 14, 98–119. doi: 10.1080/15548627.2017.1395992

Minamide, L. S., Striegl, A. M., Boyle, J. A., Meberg, P. J., and Bamburg, J. R. (2000). Neurodegenerative stimuli induce persistent ADF/cofilin-actin rods that disrupt distal neurite function. *Nat. Cell Biol.* 2, 628–636. doi: 10.1038/35023579

Miyoshi, E., Bilousova, T., Melnik, M., Fakhrutdinov, D., Poon, W. W., and Vinters, H. V. (2021). Exosomal tau with seeding activity is released from Alzheimer's disease synapses, and seeding potential is associated with amyloid beta. *Lab Invest.* 101, 1605–1617. doi: 10.1038/s41374-021-00644-z

Nakazawa, S., Oikawa, D., Ishii, R., Ayaki, T., Takahashi, H., and Takeda, H. (2016). Linear ubiquitination is involved in the pathogenesis of optineurin-associated amyotrophic lateral sclerosis. *Nat. Commun.* 7:12547. doi: 10.1038/ncomms12547

Niwa, R., Nagata-Ohashi, K., Takeichi, M., Mizuno, K., and Uemura, T. (2002). Control of actin reorganization by Slingshot, a family of phosphatases that dephosphorylate ADF/cofilin. *Cell* 108, 233–246. doi: 10.1016/s0092-8674(01)00638-9

Nixon, R. A., Wegiel, J., Kumar, A., Yu, W. H., Peterhoff, C., Cataldo, A., et al. (2005). Extensive involvement of autophagy in Alzheimer disease: an immuno-electron microscopy study. *J. Neuropathol. Exp. Neurol.* 64, 113–122. doi: 10.1093/jnen/64.2.113

Park, B. C., Shen, X., Samaraweera, M., and Yue, B. Y. (2006). Studies of optineurin, a glaucoma gene: Golgi fragmentation and cell death from overexpression of wild-type and mutant optineurin in two ocular cell types. *Am. J. Pathol.* 169, 1976–1989. doi: 10.2353/ajpath.2006.060400

Pilli, M., Arko-Mensah, J., Ponpuak, M., Roberts, E., Master, S., and Mandell, M. A. (2012). TBK-1 promotes autophagy-mediated antimicrobial defense by controlling autophagosome maturation. *Immunity* 37, 223–234. doi: 10.1016/j.immuni.2012.04.015

Prada, I., Furlan, R., Matteoli, M., and Verderio, C. (2013). Classical and unconventional pathways of vesicular release in microglia. *Glia* 61, 1003–1017. doi: 10.1002/glia.22497

Rahman, T., Davies, D. S., Tannenberg, R. K., Fok, S., Shepherd, C., Dodd, P. R., et al. (2014). Cofilin rods and aggregates concur with tau pathology and the development of Alzheimer's disease. *J. Alzheimer's Dis.* 42, 1443–1460. doi: 10.3233/JAD-140393

Rajendran, L., Bali, J., Barr, M. M., Court, F. A., Kramer-Albers, E. M., Picou, F., et al. (2014). Emerging roles of extracellular vesicles in the nervous system. *J. Neurosci.* 34, 15482–15489. doi: 10.1523/JNEUROSCI.3258-14.2014

Rajendran, L., Honsho, M., Zahn, T. R., Keller, P., Geiger, K. D., Verkade, P., et al. (2006). Alzheimer's disease beta-amyloid peptides are released in association with exosomes. *Proc. Natl. Acad. Sci. U.S.A.* 103, 11172–11177. doi: 10.1073/pnas.0603838103

Ramesh Babu, J., Lamar Seibenhener, M., Peng, J., Strom, A. L., Kemppainen, R., Cox, N., et al. (2008). Genetic inactivation of p62 leads to accumulation of hyperphosphorylated tau and neurodegeneration. *J. Neurochem.* 106, 107–120. doi: 10.1111/j.1471-4159.2008.05340.x

Raposo, G., and Stoorvogel, W. (2013). Extracellular vesicles: exosomes, microvesicles, and friends. *J. Cell Biol.* 200, 373–383. doi: 10.1083/jcb.201211138

Rea, S. L., Majcher, V., Searle, M. S., and Layfield, R. (2014). SQSTM1 mutations–bridging Paget disease of bone and ALS/FTLD. *Exp. Cell Res.* 325, 27–37. doi: 10.1016/j.yexcr.2014.01.020

Roca-Agujetas, V., Barbero-Camps, E., de Dios, C., Podlesniy, P., Abadin, X., Morales, A., et al. (2021a). Cholesterol alters mitophagy by impairing optineurin recruitment and lysosomal clearance in Alzheimer's disease. *Mol. Neurodegeneration* 16:15. doi: 10.1186/s13024-021-00435-6

Roca-Agujetas, V., de Dios, C., Abadin, X., and Colell, A. (2021b). Upregulation of brain cholesterol levels inhibits mitophagy in Alzheimer disease. *Autophagy* 17, 1555–1557. doi: 10.1080/15548627.2021.1920814

Salminen, A., Kaarniranta, K., Haapasalo, A., Hiltunen, M., Soininen, H., and Alafuzoff, I. (2012). Emerging role of p62/sequestosome-1 in the pathogenesis of Alzheimer's disease. *Progress Neurobiol.* 96, 87–95. doi: 10.1016/j.pneurobio.2011.11.005

Saman, S., Kim, W., Raya, M., Visnick, Y., Miro, S., Saman, S., et al. (2012). Exosome-associated tau is secreted in tauopathy models and is selectively phosphorylated in cerebrospinal fluid in early Alzheimer disease. *J. Biol. Chem.* 287, 3842–3849. doi: 10.1074/jbc.M111.277061

Saman, S., Lee, N. C., Inoyo, I., Jin, J., Li, Z., Doyle, T., et al. (2014). Proteins recruited to exosomes by tau overexpression implicate novel cellular mechanisms linking tau secretion with Alzheimer's disease. *J. Alzheimer's Dis.* 40:S47–S70. doi: 10.3233/JAD-132135

Sanchez-Martin, P., and Komatsu, M. (2018). p62/SQSTM1 - steering the cell through health and disease. *J. Cell Sci.* 131:jcs222836. doi: 10.1242/jcs.222836

Sardar Sinha, M., Ansell-Schultz, A., Civitelli, L., Hildesjo, C., Larsson, M., Lannfelt, L., et al. (2018). Alzheimer's disease pathology propagation by exosomes containing toxic amyloid-beta oligomers. *Acta Neuropathol.* 136, 41–56. doi: 10.1007/s00401-018-1868-1

Savina, A., Furlan, M., Vidal, M., and Colombo, M. I. (2003). Exosome release is regulated by a calcium-dependent mechanism in K562 cells. *J. Biol. Chem.* 278, 20083–20090. doi: 10.1074/jbc.M301642200

Shankar, G. M., Bloodgood, B. L., Townsend, M., Walsh, D. M., Selkoe, D. J., and Sabatini, B. L. (2007). Natural oligomers of the Alzheimer amyloid-beta protein induce reversible synapse loss by modulating an NMDA-type glutamate receptor-dependent signaling pathway. *J. Neurosci.* 27, 2866–2875. doi: 10.1523/JNEUROSCI.4970-06.2007

Shaw, A. E., and Bamburg, J. R. (2017). Peptide regulation of cofilin activity in the CNS: A novel therapeutic approach for treatment of multiple neurological disorders. *Pharmacol. Ther.* 175, 17–27. doi: 10.1016/j.pharmthera.2017.02.031

Sinha, S., Hoshino, D., Hong, N. H., Kirkbride, K. C., Grega-Larson, N. E., Seiki, M., et al. (2016). Cortactin promotes exosome secretion by controlling branched actin dynamics. *J. Cell Biol.* 214, 197–213. doi: 10.1083/jcb.201601025

Skog, J., Wurdinger, T., van Rijn, S., Meijer, D. H., Gainche, L., Sena-Esteves, M., et al. (2008). Glioblastoma microvesicles transport RNA and proteins that promote tumour growth and provide diagnostic biomarkers. *Nat. Cell Biol.* 10, 1470–1476. doi: 10.1038/ncb1800

Tanji, K., Miki, Y., Ozaki, T., Maruyama, A., Yoshida, H., Mimura, J., et al. (2014). Phosphorylation of serine 349 of p62 in Alzheimer's disease brain. *Acta Neuropathol. Commun.* 2:50. doi: 10.1186/2051-5960-2-50

Tu, S., Okamoto, S., Lipton, S. A., and Xu, H. (2014). Oligomeric Abeta-induced synaptic dysfunction in Alzheimer's disease. *Mol. Neurodegeneration* 9:48. doi: 10.1186/1750-1326-9-48

Turturro, S., Shen, X., Shyam, R., Yue, B. Y., and Ying, H. (2014). Effects of mutations and deletions in the human optineurin gene. *Springerplus* 3:99. doi: 10.1186/2193-1801-3-99

Valadi, H., Ekstrom, K., Bossios, A., Sjostrand, M., Lee, J. J., and Lotvall, J. O. (2007). Exosome-mediated transfer of mRNAs and microRNAs is a novel mechanism of genetic exchange between cells. *Nat. Cell Biol.* 9, 654–659. doi: 10.1038/ncb1596

Vella, L. J., Sharples, R. A., Lawson, V. A., Masters, C. L., Cappai, R., and Hill, A. F. (2007). Packaging of prions into exosomes is associated with a novel pathway of PrP processing. *J. Pathol.* 211, 582–590. doi: 10.1002/path.2145

Verderio, C., Muzio, L., Turola, E., Bergami, A., Novellino, L., Ruffini, F., et al. (2012). Myeloid microvesicles are a marker and therapeutic target for neuroinflammation. *Ann. Neurol.* 72, 610–624. doi: 10.1002/ana.23627

Wakatsuki, T., Schwab, B., Thompson, N. C., and Elson, E. L. (2001). Effects of cytochalasin D and latrunculin B on mechanical properties of cells. *J. Cell Sci.* 114, 1025–1036. doi: 10.1242/jcs.114.5.1025

Wang, S., Cesca, F., Loers, G., Schweizer, M., Buck, F., and Benfenati, F. (2011). Synapsin I is an oligomannose-carrying glycoprotein, acts as an oligomannose-binding lectin, and promotes neurite outgrowth and neuronal survival when released via glia-derived exosomes. *J. Neurosci.* 31, 7275–7290. doi: 10.1523/JNEUROSCI.6476-10.2011

Wang, Y., Shibasaki, F., and Mizuno, K. (2005). Calcium signal-induced cofilin dephosphorylation is mediated by Slingshot via calcineurin. *J. Biol. Chem.* 280, 12683–12689. doi: 10.1074/jbc.M411494200

Witas, R., Chaput, D., Khan, H., Stevens, S. M. Jr., and Kang, D. (2017). Isolation and Proteomic Analysis of Microvesicles and Exosomes from HT22 Cells and Primary Neurons. *Methods Mol. Biol.* 1598, 255–267. doi: 10.1007/978-1-4939-6952-4_12

Woo, J. A., Boggess, T., Uhlar, C., Wang, X., Khan, H., and Cappos, G. (2015a). RanBP9 at the intersection between cofilin and Abeta pathologies: rescue of neurodegenerative changes by RanBP9 reduction. *Cell Death Dis.* 6:1676. doi: 10.1038/cddis.2015.37

Woo, J. A., Liu, T., Fang, C. C., Castano, M. A., Kee, T., Yrigoin, K., et al. (2020). beta-Arrestin2 oligomers impair the clearance of pathological tau and increase tau aggregates. *Proc. Natl. Acad. Sci. U.S. A.* 117, 5006–5015. doi: 10.1073/pnas.1917194117

Woo, J. A., Liu, T., Fang, C. C., Cazzaro, S., Kee, T., LePochat, P., et al. (2019). Activated cofilin exacerbates tau pathology by impairing tau-mediated microtubule dynamics. *Commun. Biol.* 2:112. doi: 10.1038/s42003-019-0359-9

Woo, J. A., Zhao, X., Khan, H., Penn, C., Wang, X., Joly-Amado, A., et al. (2015b). Slingshot-Cofilin activation mediates mitochondrial and synaptic dysfunction via Abeta ligation to beta1-integrin conformers. *Cell Death Differ.* 22, 1069–1070. doi: 10.1038/cdd.2015.41

Xu, Y., Zhang, S., and Zheng, H. (2019). The cargo receptor SQSTM1 ameliorates neurofibrillary tangle pathology and spreading through selective targeting of pathological MAPT (microtubule associated protein tau). *Autophagy* 15, 583–598. doi: 10.1080/15548627.2018.1532258

Yuyama, K., Sun, H., Sakai, S., Mitsutake, S., Okada, M., Tahara, H., et al. (2014). Decreased amyloid-beta pathologies by intracerebral loading of glycosphingolipid-enriched exosomes in Alzheimer model mice. *J. Biol. Chem.* 289, 24488–24498. doi: 10.1074/jbc.M114.577213

Zhao, L., Ma, Q. L., Calon, F., Harris-White, M. E., Yang, F., Lim, G. P., et al. (2006). Role of p21-activated kinase pathway defects in the cognitive deficits of Alzheimer disease. *Nat. Neurosci.* 9, 234–242. doi: 10.1038/nn1630

frontiers | Frontiers in Aging Neuroscience

TYPE Original Research
PUBLISHED 07 September 2022
DOI 10.3389/fnagi.2022.967316

OPEN ACCESS

EDITED BY
Nibaldo C. Inestrosa,
Pontificia Universidad Católica de Chile, Chile

REVIEWED BY
Yalong Lu,
Shaanxi Normal University, China
Cleverton Roberto De Andrade,
São Paulo State University, Brazil

*CORRESPONDENCE
Michael Wink
wink@uni-hd.de
Jinke Lin
ljk213@163.com

†These authors have contributed equally to this work

SPECIALTY SECTION
This article was submitted to Alzheimer's Disease and Related Dementias, a section of the journal Frontiers in Aging Neuroscience

RECEIVED 12 June 2022
ACCEPTED 22 August 2022
PUBLISHED 07 September 2022

CITATION
Zhang S, Duangjan C, Tencomnao T, Wu L, Wink M and Lin J (2022) Oolonghomobisflavans exert neuroprotective activities in cultured neuronal cells and anti-aging effects in *Caenorhabditis elegans*. *Front. Aging Neurosci.* 14:967316. doi: 10.3389/fnagi.2022.967316

Oolonghomobisflavans exert neuroprotective activities in cultured neuronal cells and anti-aging effects in *Caenorhabditis elegans*

Shaoxiong Zhang[1,2,3†], Chatrawee Duangjan[2,3,4†], Tewin Tencomnao[2], Liangyu Wu[1], Michael Wink[3*] and Jinke Lin[1,5*]

[1]College of Horticulture, Fujian Agriculture and Forestry University, Fuzhou, China, [2]Natural Products for Neuroprotection and Anti-Ageing Research Unit, Department of Clinical Chemistry, Faculty of Allied Health Sciences, Chulalongkorn University, Bangkok, Thailand, [3]Institute of Pharmacy and Molecular Biotechnology, Heidelberg University, Heidelberg, Germany, [4]Leonard Davis School of Gerontology, University of Southern California, Los Angeles, Los Angeles, CA, United States, [5]Anxi College of Tea Science, Fujian Agriculture and Forestry University, Fuzhou, China

Potential health benefits of tea has attracted significant scientific and public attention worldwide. Tea polyphenols are considered as natural promising complementary therapeutical agents for neurodegenerative diseases. However, the anti-neurodegeneration or anti-aging activities of oolong tea polyphenols have not been investigated. The current study aims to document beneficial effects of oolong tea polyphenols [dimers of epigallocatechin gallate (EGCG), oolonghomobisflavan A (OFA), and oolonghomobisflavan B (OFB)] with neuroprotective and neuritogenesis properties in cultured neuronal (Neuro-2a and HT22) cells and *Caenorhabditis elegans* models. *In vitro*, we found that the compounds (EGCG, OFA, and OFB) protect against glutamate-induced neurotoxicity *via* scavenging radical activity, suppression intracellular ROS and up-regulation of antioxidant enzymes. Moreover, the compounds induce neurite outgrowth *via* up-regulate Ten-4 gene expression. Interestingly, OFA and OFB exert stronger neuroprotective and neurite outgrowth properties than EGCG known as an excellent antioxidant agent in tea. *In vivo*, we found that the compounds protect against *C. elegans* Aβ-induced paralysis, chemotaxis deficiency and α-synuclein aggregation. Moreover, the compounds are capable of extending the lifespan of *C. elegans*. OFA and OFB possess both anti-neurodegeneration and anti-aging activities, supporting its therapeutic potential for the treatment of age-related neurodegenerative diseases which need to be studied in more detail in intervention studies.

KEYWORDS

oolonghomobisflavans, oxidative stress, antioxidants, anti-aging, neuroprotective, neurite outgrowth

Introduction

As aging populations increase rapidly, millions of people around the world are currently affected by neurodegenerative diseases and the disease treatment is expected to grow rapidly as more people live longer (Pérez-Hernández et al., 2016). The most common of neurodegenerative diseases is Alzheimer's disease (AD) which is associated with age (Pérez-Hernández et al., 2016).

Glutamate is the main excitatory neurotransmitter in the brain while excessive levels of glutamate can cause neuronal cell death through mitochondrial function impairment and accumulation of reactive oxygen species (ROS) (Tobaben et al., 2011; Rocha et al., 2020). Oxidative stress has been reported as a factor in neurodegenerative diseases as well as AD. The accumulation of ROS during aging is closely related with mitochondrial dysfunction leading to neuro-inflammation and neuronal cell death which plays an important role in neurodegenerative diseases especially AD (Bonaterra et al., 2017).

Neuritogenesis involves the growth, differentiation and regeneration of neurites. The impairment of the neurogenesis process affects neurons cell survival and differentiation leading to various neurodegenerative diseases (Park et al., 2015). Neurite outgrowth is an initial process for functional neuron networks including neuronal differentiation and regeneration (Read and Gorman, 2009). Regulation of neurite outgrowth can promote neuronal regeneration from nerve injury or neurological disorders and plays an valuable role in development of therapies for neurodegenerative diseases (Park et al., 2015; Rangsinth et al., 2021).

In brain, reduction of oxidative stress and induction of neuronal differentiation are the key parameters for neuroprotective effects. Moreover, current drug treatment for neurodegenerative diseases is at the risk of loss of function with many unfavorable side effects (Pérez-Hernández et al., 2016).

Plant natural bioactive compounds have turned into an alternative choice to prevent and relieve neurodegenerative diseases. Oolong tea has been reported for many beneficial effects, including anti-hyperglycemic, anti-obesity, anti-bacterial and anti-inflammatory properties (Weerawatanakorn et al., 2015). Oolonghomobisflavan A (OFA) and oolonghomobisflavan B (OFB) have a unique structure as a dimer of epigallocatechin gallate (EGCG) which could be isolated from oolong tea but not from green tea or black tea (Nakai et al., 2005; **Figure 1**). However, neuroprotective and anti-aging activity of oolong tea polyphenols, OFA and OFB, have not been reported. Anti-aging in this study is concerned with extending the lifespan. This research shows the first proof of longevity promoting effects and neuroprotective properties of OFA and OFB in cultured neuronal cells (Neuro-2a and HT22) and *C. elegans* model.

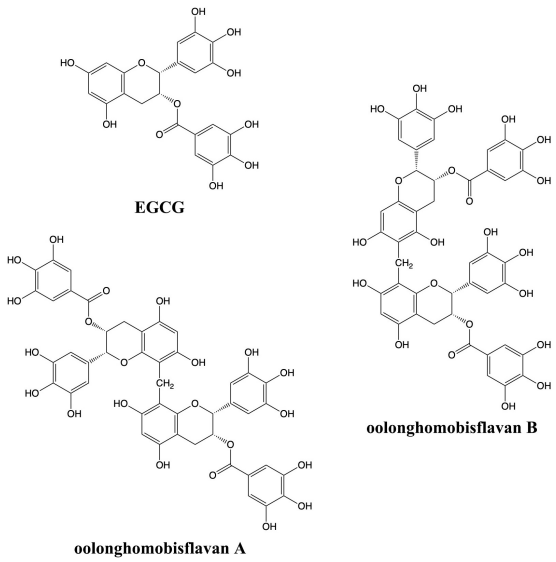

FIGURE 1
Chemical structures of EGCG, OFA, and OFB.

Materials and methods

Chemicals and reagents

OFA (≥98%) and OFB (≥98%) were purchased from Nagara Science (Japan). EGCG (≥95%), Dimethyl sulfoxide (DMSO), Dulbecco's modified eagle medium (DMEM), Fetal bovine serum (FBS), L-glutamic acid were purchased from Sigma-Aldrich (United States). Agar, tryptone, yeast extract were purchased from Becton, benzaldehyde from Merck, TRIzol® from Invitrogen, and 3-(4,5-Dimethylthiazol-2-yl)-2,5-diphenyltetrazolium bromide (MTT) from Bio Basic.

Diphenyl-2-picrylhydrazyl assay

The 1,1-diphenyl-2-picrylhydrazyl (DPPH) radical scavenging activity of the EGCG and OFA and OFB were evaluated according to the user's manual (Peixoto et al., 2016), with a minor modification. The DPPH working solution was prepared in methanol and was mixed with the EGCG and

Abbreviations: EGCG, Epigallocatechin gallate; OFA, Oolonghomobisflavan A; OFB, Oolonghomobisflavan B; MTT, 3-(4,5-Dimethylthiazol-2-yl)-2,5-diphenyltetrazolium bromide; FBS, Fetal bovine serum; DMSO, Dimethyl sulfoxide; LDH, Lactate dehydrogenase; Aβ, β-amyloid; H2DCFDA, 2′,7′-Dichlorodihydrofluorescein diacetate; AD, Alzheimer's disease; PT_{50}, Paralyzed time in 50%; ROS, Reactive oxygen species.

OFA and OFB at a 1:1 ratio by serial methanolic dilution. After 30 min incubation at room temperature under dark condition, the absorbance was measured at 517 nm using an automatic 96 wells plate reader. Radical scavenging activity against DPPH was calculated follow the formula presented below, where A_0 represent the absorbance of the control, and A_1 represent the absorbance after adding the extract.

$$DPPH\ radical\ scavenging\ effect(\%) = [(A_0 - A_1)/A_0] \times 100.$$

The results were collected from three independent experiments performed in duplicate and are showed as EC_{50} (μ g/ml).

Cell culture and treatment

Neuro-2a cell line (purchased from The JCRB Cell Bank, Japan) and HT22 cell line (purchased from The Salk Institute, United States) were used as cultured neuronal cell models in this study. Neuro-2a cell line were cultured in DMEM/HamF12 medium contain 1% penicillin-streptomycin solution and 10% FBS. HT22 cell line were cultured in DMEM medium contain 1% penicillin-streptomycin solution and 10% FBS. Neuronal cells were incubated at incubator (37°C, 5% CO_2).

Cell viability

MTT and lactate dehydrogenase (LDH) assays were used in investigating cell viability. Cells (1.5 10^4 cells/well) were seeded in plates (96-well) which contained 100 μl 10% FBS medium overnight and treated with compounds (EGCG, OFA, and OFB) for 1 h.

MTT and LDH assay were done as previously described (Zhang et al., 2020).

Measurement of neurite outgrowth and neurite-bearing cells

Neuro-2a cells (1.5 10^4 cells/well) were seeded in 6 wells plate containing 10% FBS and cultured overnight. Then the cell culture medium was removed and cells were washed with PBS. After that, cells were cultured 24 h with compounds under the condition of low nutrition (1% FBS). Photos were taken from around 100 cells/treatment group, the lengths of neurite were measured with Fiji software (NIH, Bethesda, MD, United States). The cells whose neurite length is longer than the diameter of cell body are regard as neurite bearing cells (Park et al., 2015).

Glutamate induced cell toxicity

The cells were exposed to 1.25–40 mM glutamate for 1–30 h, which decreased cell viability in a time and a dose-dependent manner (Zhang et al., 2020).

Cells were cultured overnight and then treated with or without compounds for 1 h, followed by adding 10 mM glutamate (Neuro-2a cell line) or 5 mM glutamate (HT22 cell line) for 24 or 18 h to induce cell toxicity.

Quantitative real-time PCR analysis

For neurite outgrowth assay, cells (9×10^4 cells/well) were seeded in 6 wells plates containing 10% FBS medium overnight, and then treated with compounds in 1% FBS for 24 h. For neuroprotective assay, cells (9×10^4 cells/well) were seeded in 6 wells plates containing 10% FBS medium overnight, and then treated with compounds in 10% FBS for 1 h. According to manufacturer's instructions, total RNA was extracted using TRIzol® Reagent. cDNA was synthesized from 1 μg of total RNA using AccuPower® RT Premix with oligo (dT). All Quantitative real-time PCR (qRT-PCR) reactions were performed in an Exicycler™ 96. PCR settings: 95°C for 15 min, 45–55 cycles of denaturation at 95°C for 15 s, annealing/extension at 55°C for 30 s. The mRNA expression of *GAP-43*, *Ten-4*, *GSTo1*, *GSTa2*, *GPx*, *CAT*, *SOD1*, and *SOD2* (Zhang et al., 2020) were detected by qRT-PCR, β-*actin* was selected for standardization control.

Measurement of intracellular reactive oxygen species levels in cultured neuronal cells

The protective effect against intracellular ROS accumulation was detected by H2DCFDA staining as previously described (Zhang et al., 2020). Briefly, the cells were seeded in the plates overnight and pre-treated with compounds (EGCG, OFA, and OFB) for 1 h, followed by co-treatment with glutamate for 18 h (Neuro-2a) or 12 h (HT22). The fluorescence intensity was measured under the condition of 485 nm excitation and 535 nm emission. The results are expressed as the percentage of the fluorescence intensity of treatment group compared with negative control group.

Caenorhabditis elegans strains and maintenance

Caenorhabditis elegans wild-type (N2), TJ356, TJ375, CL2166 were maintained at 20°C, while CL4176, CL802,

CL2355, CL2122 were maintained at 16°C. All the strains were maintained on nematode growth medium (NGM) with *Escherichia coli* OP50 as food source.

Lifespan assay

Lifespan assay was conducted as previously described (Duangjan et al., 2019b). Age-synchronized L4 larvae were transferred with platinum picker to NGM plates, which contained different concentrations of OFA and OFB and the transfer time was set as day 0. During the egg-laying period, the worms were transferred to a fresh corresponding concentration plate every day to ensure that the offspring produced by worms do not affect the experimental results, after that, the worms were transferred to fresh plate every second day. The numbers of survival and dead worms were recorded every other day during transfer to the fresh plate until all worms died. If there was no response after slightly touching the worm with platinum wire, they were recorded as dead. Worms that produce "internal hatch," escape from the NGM plate or lost, and were severely damaged during transfer are recorded as "censored." Each group had at least three replicates, and each replicate consisted of approximately 30 worms. The experiment was conducted in a double-blind manner.

Measurement of intracellular reactive oxygen species levels in *Caenorhabditis elegans*

Under the condition of 20°C, wild type L1 larvae wild-type (N2) were treated with OFA and OFB (5, 10, 25 μM) for 48 h and exposed to non-lethal concentration of the pro-oxidative juglone (20 μM) for 24 h. After that, 20 μM H_2DCFDA was added to the worm culture medium and then incubated in the dark for 45 min. Then worms were washed with M9 buffer to remove residual dye. Live images were captured from at least 20 worms per group by fluorescence microscopy. The fluorescence intensities were detected and analyzed (Duangjan et al., 2019b).

Survival assay under juglone-induced oxidative stress

Survival assay was done as previously described (Abbas and Wink, 2009). Briefly, age-synchronized L1 larvae wild-type (N2) worms were treated with OFA and OFB (5, 10, 25 μM) for 48 h in S-medium. Then, worms were exposed to the pro-oxidant juglone (80 μM) for 24 h, the number of survivors were examined and scored.

Fluorescence detection and image analysis

The transgenic worms with a target gene promoter fused with a GFP reporter were used in gene expression assay. The fluorescence intensity value emitted by the worm represents the relative expression of the target gene. Worms treated with OFA and OFB need to be cleaned by gently wash with M9 buffer, and then fixed on a glass slide with 100 mM tetramisole hydrochloride. After the cover glass has been placed, a fluorescence microscope (BIOREVO BZ-9000) was used for analysis. Approximately 20 worms were randomly selected for each group and each replicate to be photographed. The average fluorescence intensities value of worms were analyzed by Fiji software.

The expression of stress-related genes

The transgenic strain TJ375 (HSP-16.2:GFP) and CL2166 (GST-4:GFP) were employed in this assay. Age-synchronized L1 worms were cultured in S-medium containing OFA and OFB (5, 10, 25 μM) for 48 h, followed by exposure to 20 μM juglone for 24 h (Duangjan et al., 2019a).

Localization of DAF-16

The transgenic strain TJ356 (DAF-16:GFP) was applied to test the localization of DAF-16 in cells (Duangjan et al., 2019a). The synchronized L1 larvae TJ356 were cultured in S-medium and treated with different concentrations of OFA and OFB for 24 h. The worms were collected and photographed under a fluorescence microscope for the analysis of DAF-16 localization, respectively. Data were collected from at least three repetitions, each repetition containing about 20 worms.

Paralysis assay

Paralysis assay was conducted as previously described (Dostal and Link, 2010). Synchronized eggs of strain CL4176 and its control strain CL802 were maintained at 16°C, on the NGM plates with or without OFA and OFB. The expression of transgene (muscle-specific $A\beta_{1-42}$ in CL4176) was activated by turning up the temperature from 16 to 25°C, begin 48 h after egg laying and continued until paralysis assay finished. The record was executed at 2 h interval until the last worm became paralyzed. The worms that did not move or only moved their head when gently touched with a platinum picker were scored as paralyzed. Time required for half of the nematodes in each group to represent paralysis (PT_{50}) was used to quantify the speed of paralysis.

Chemotaxis assay

The synchronized L1 transgenic *C. elegans* CL2355 and its control strain CL2122 were treated with or without OFA and OFB at 16°C in S-medium with *E. coli* (OP50) for 36 h. The chemotaxis assay was carried out as previously described (Zhang et al., 2020).

Statistical analysis

All data come from at least three independent experiments. For comparison of two groups, Student's *t*-test was performed. For comparisons among multiple groups, one-way analysis of variance (ANOVA) followed by Dunnett's *post-hoc* test (Prism, GraphPad Software, San Diego, CA, United States) were performed. Lifespan assay were performed by Kaplan-Meier in software SPSS24, survival curves were drawn by GraphPad Prism 8 software, and the comparison between the two groups of survival curves was showed by Log Rank (Mantel-Cox) test. $P < 0.05$ is regarded as significant difference between groups.

Results

The cytotoxicity of oolonghomobisflavan A and oolonghomobisflavan B in cultured neuronal (HT22 and Neuro-2a) cells

Firstly, to investigate whether EGCG, OFA, and OFB have toxic effects in cultured neuronal (HT22 and Neuro-2a) cells, the cells were treated with the polyphenols and cell viability was analyze by the MTT assay. Different concentrations of EGCG, OFA, and OFB did not cause a significant change in cell viability in Neuro-2a and HT22 cells compared to the negative control group. For subsequent experiments, non-cytotoxic concentrations (5, 10 μM) were chosen (**Supplementary Figures 1A,B**).

Oolonghomobisflavan A and oolonghomobisflavan B promotes neurite outgrowth involved in Teneurin-4

We investigated whether EGCG, OFA, and OFB can induce neurite outgrowth in Neuro-2a cells. The Neuro-2a cells in DMEM supplemented with 10% FBS showed round shape without neurite extension, whereas Neuro-2a cells in DMEM supplemented with 1% FBS (the serum-starved condition) apparently increased the number and the length of neurite (**Figures 2A,B**).

To investigate the effect of EGCG, OFA, and OFB on neurite outgrowth activity, the cells were maintained in low-serum medium (DMEM supplemented with 1% FBS). The cells treated with EGCG (10 μM), OFA (5, 10 μM), and OFB (5, 10 μM) exhibited significantly increased neurite lengths and neurite bearing cells in a dose-dependent manner, compared to the 1% FBS control group (**Figures 2A,B**). Interestingly, higher concentrations of OFA (10 μM) and OFB (10 μM) promoted neurite lengths and neurite bearing cells more effectively and were superior to EGCG (10 μM) ($p < 0.001$) (**Figures 2A,B,E**).

In agreement with neurite outgrowth results, a marker of neurite outgrowth (GAP-43 gene expression) was significantly increased in Neuro-2a cells treated with EGCG (10 μM), OFA (5, 10 μM), and OFB (5, 10 μM), when compared to1% FBS control group (**Figure 2C**).

To investigate whether Ten-4 expression is involved in EGCG, OFA, and OFB activity to induce neurite growth, the Ten-4 gene expression was examined. The cells treated with EGCG (10 μM), OFA (5, 10 μM), and OFB (5, 10 μM) exhibited significantly increased Ten-4 gene expression, compared to the 1% FBS control group (**Figure 2D**).

The results suggest that EGCG, OFA, and OFB promote neurite outgrowth, possibly involved the Teneurin-4 transmembrane protein.

Oolonghomobisflavan A and oolonghomobisflavan B protect against glutamate-induced cytotoxicity

To investigate whether EGCG, OFA, and OFB can protect neuronal (Neuro-2a and HT22) cells against glutamate-induced cytotoxicity, the cell viability was determined. The cells treated with varying concentrations of EGCG, OFA, and OFB significantly reduced glutamate-induced cell death, compared to the negative control group (**Figures 3A,B**). The results were confirmed by the LDH assay (**Figures 3C,D**) as well as morphological examination (**Figures 3E,F**). These results suggest that EGCG, OFA, and OFB exert a potent neuroprotective effect against cytotoxicity induced by excessive glutamate in cultured neuronal (Neuro-2a and HT22) cells.

Oolonghomobisflavan A and oolonghomobisflavan B protect against glutamate-induced oxidative stress

To investigate whether EGCG, OFA, and OFB could suppress glutamate-induced oxidative stress, their antioxidant properties were explored in Neuro-2a and HT22 cells using

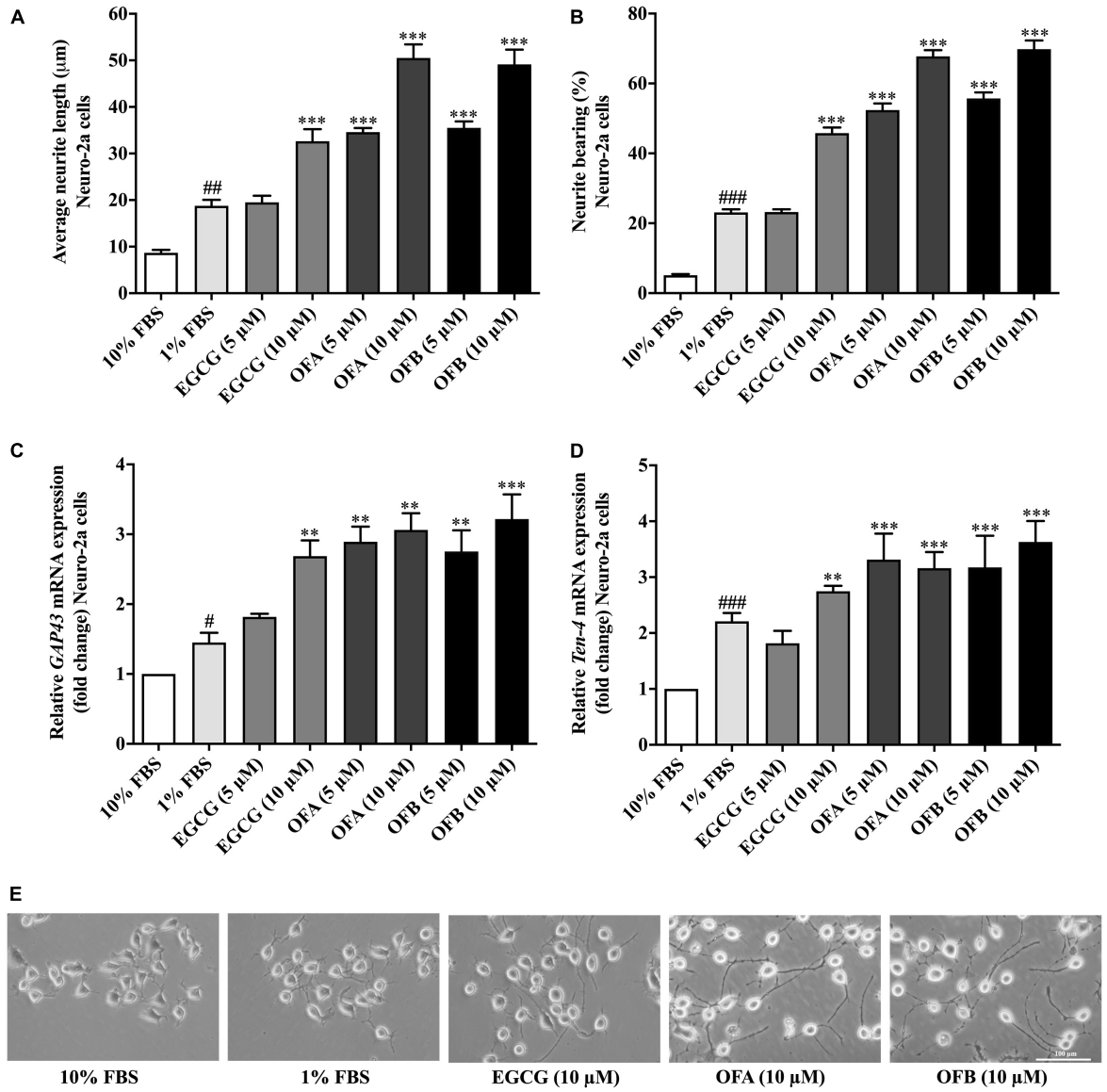

FIGURE 2
Effect of EGCG, OFA, and OFB on neurite outgrowth. After treated with EGCG, OFA, and OFB in Neuro-2a cells, the average of neurite lengths **(A)** and the percentage of neurite-bearing cells **(B)** were measured. Relative *GAP-43* **(C)** and *Ten-4* **(D)** mRNA expression levels represented as fold change compared to the 10% FBS control in Neuro-2a cells. The images of cell morphology were taken under a 10 magnification microscope **(E)**. *β-Actin* was used in RT-PCR assay as internal control. Results were normalized to 10% FBS control level and shown as the mean ± standard deviation ($n \geq 3$ independent experiments). $^{\#}p < 0.05$, $^{\#\#}p < 0.01$, and $^{\#\#\#}p < 0.001$ compared to the 10% FBS control; $^{**}p < 0.01$ and $^{***}p < 0.001$ compared to the 1% FBS control.

intracellular ROS accumulation assay. The cells were exposured to glutamate (10 mM in Neuro-2a cells and 5 mM in HT22 cells) showed significantly elevated intracellular ROS level in Neuro-2a (approximately 2 fold) and HT22 (approximately 1.9 fold) cells, compared to the negative control group (Figures 4A,B). However, the cells treated with all concentration of EGCG, OFA, and OFB significantly reduced the elevated intracellular ROS levels, compared to the glutamate treated group ($P < 0.001$) (Figures 4A,B).

In order to clarify the mechanism of action in antioxidant-mediated neuroprotective effects against glutamate toxicity, the effect of EGCG, OFA, and OFB on the expression of antioxidant as well as phase II enzyme gene were investigated.

Previous results found that EGCG, OFA, and OFB had demonstrated the protective effects against glutamate-induced oxidative stress and toxicity in a concentration-dependent manner with the maximum protective effect at 10 μM (Figures 3A,B, 4A,B). Thus, these concentrations were used

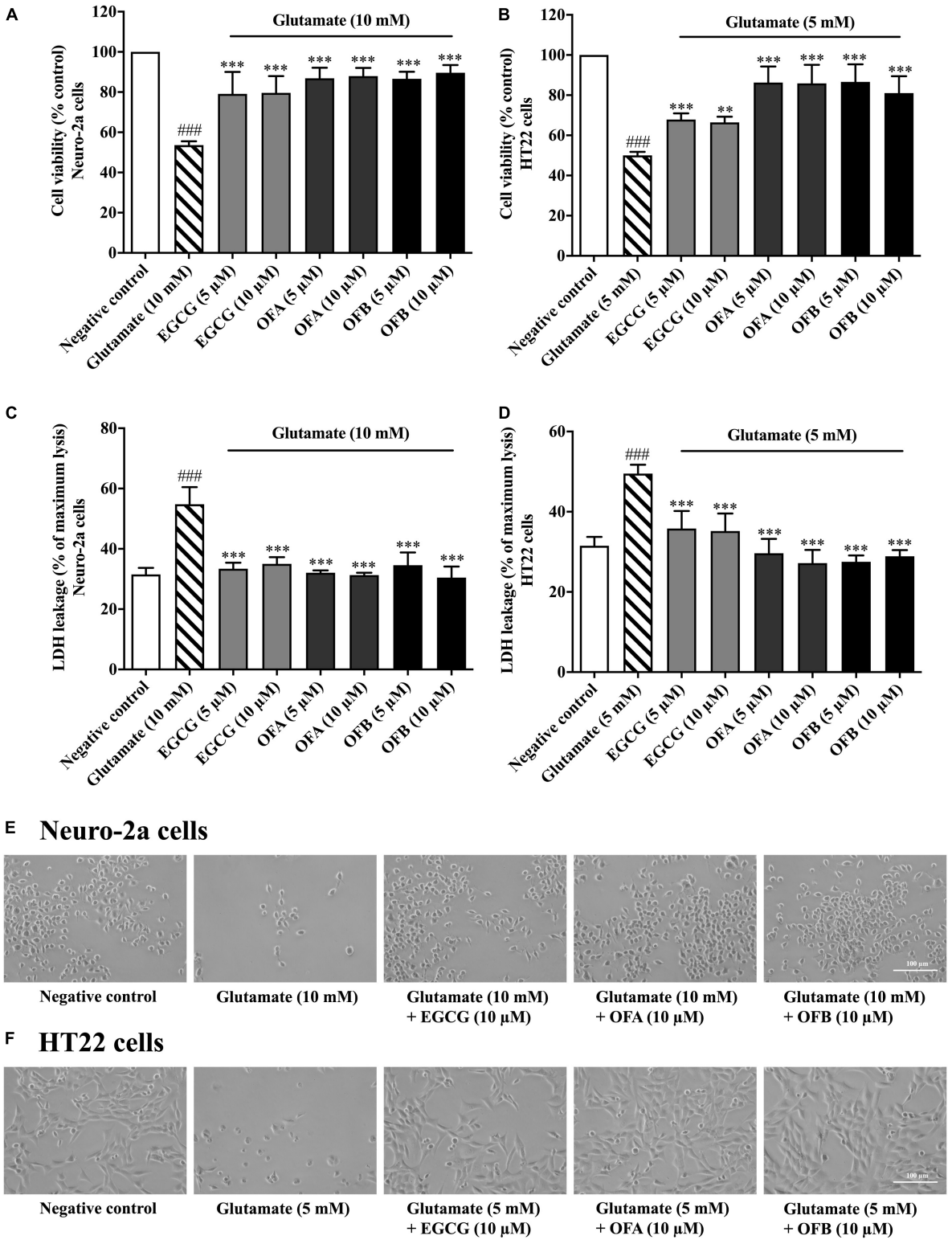

FIGURE 3
Protective effects of EGCG, OFA, and OFB against glutamate-induced toxicity in Neuro-2a and HT22 cells. Cell viability after treatment with different concentrations of EGCG, OFA, and OFB and exposed to glutamate in Neuro-2a **(A,C)** and HT22 cells **(B,D)**. Samples were exposed to glutamate (5–10 mM) to induce toxicity. Cell morphology was also checked under a 5 magnification microscope **(E,F)**. Results are shown as the mean ± standard deviation ($n \geq 3$ independent experiments). $^{###}p < 0.001$ compared to the negative control; $^{**}p < 0.01$ and $^{***}p < 0.001$, compared to the glutamate treated cells.

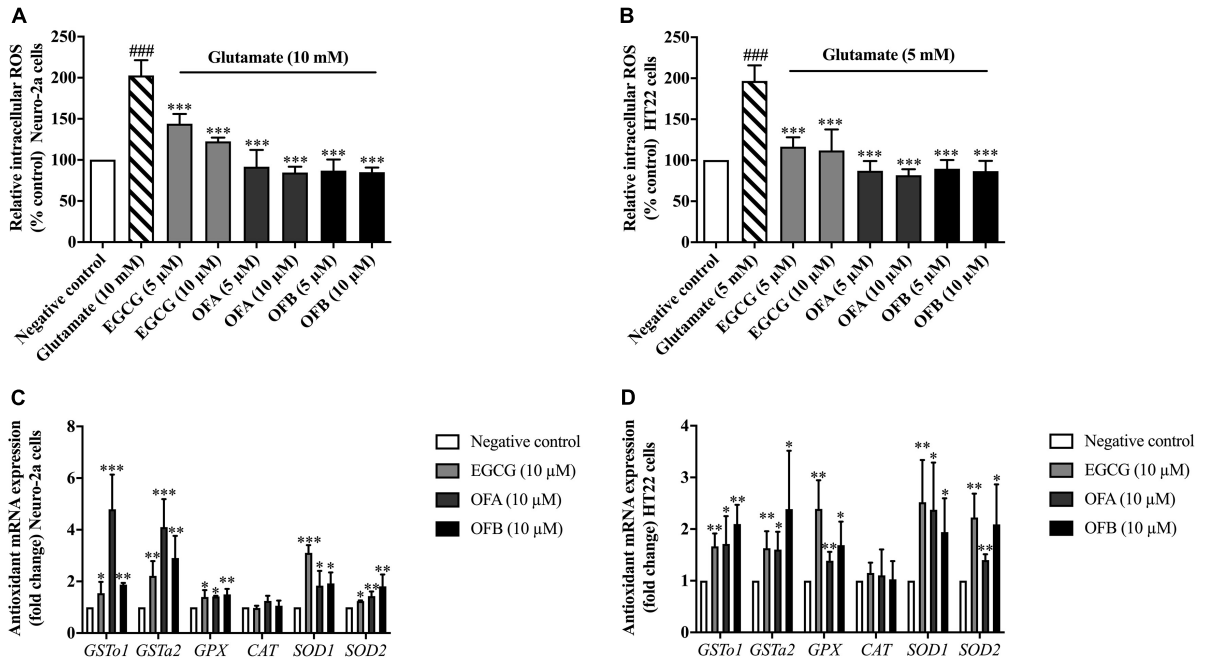

FIGURE 4
Protective effect of EGCG, OFA, and OFB in Neuro-2a and HT22 cells against glutamate-induced oxidative stress by suppressing intracellular ROS and enhancing the antioxidant gene expression. After treated with EGCG, OFA, and OFB in Neuro-2a **(A)** and HT22 cells **(B)**, the intracellular ROS were measured. Samples were exposed to glutamate (5–10 mM) to induce oxidative stress. The endogenous antioxidant gene expression in Neuro-2a **(C)** and HT22 cells **(D)**. β-*Actin* was used in RT-PCR assay as internal control. Results are shown as the mean ± standard deviation ($n \geq 3$ independent experiments). $^{###}p < 0.001$ compared to the negative control; $^{*}p < 0.05$, $^{**}p < 0.01$, and $^{***}p < 0.001$ compared to the glutamate treated control.

to detect expressions of antioxidant genes. The cells treated with EGCG, OFA, and OFB showed significantly up-regulated expressions of antioxidant genes, including *GSTo1*, *GSTa2*, *GPx*, *SOD1*, and *SOD2* (Figures 4C,D). Interestingly, the expression of CAT gene was not significant changed after treated with EGCG, OFA, and OFB in both Neuro-2a and HT22 cells (Figures 4C,D), compared to the negative control.

The results suggest that EGCG, OFA, and OFB protect against glutamate-induced cytotoxicity not only by suppressing intracellular ROS production but also through enhancing the expression of endogenous antioxidant enzymes in cultured neuronal (Neuro-2a and HT22) cells.

Oolonghomobisflavan A and oolonghomobisflavan B improve the Aβ-induced paralysis in *Caenorhabditis elegans*

We investigated whether EGCG, OFA, and OFB suppress Aβ-induced toxicity in the transgenic *C. elegans* strain CL4176. Worms of CL4176 strain, which express human $A\beta_{1-42}$ peptides, become paralyzed due to the Aβ aggregate accumulation in muscle cells at 25°C, result in oxidative stress (Drake et al., 2003). We found that EGCG, OFA, and OFB extend PT_{50} when compare to negative control. 50 μM EGCG extended PT_{50} by 8.04% ($P < 0.01$), 5 μM OFA by 7.67% ($P < 0.01$), 10 μM OFA by 9.44% ($P < 0.001$), 25 μM OFA by 8.42% ($P < 0.01$), 5 μM OFB by 8.79% ($P < 0.001$), 10 μM OFB by 9.20% ($P < 0.001$), 25 μM OFB by 7.36% ($P < 0.01$) (Figure 5 and Supplementary Table 1). These results suggest that OFA and OFB may contain the potential to protect worms against Aβ-induced toxicity.

Oolonghomobisflavan A and oolonghomobisflavan B improved the Aβ-induced chemotaxis deficit in *Caenorhabditis elegans*

The chemotaxis behavior in *C. elegans* is regulated by stimulation of sensory neurons and inters neurons to activate the motor neurons (Hobert, 2003). To investigate whether EGCG, OFA and OFB could improve Aβ-induced deficit in chemotaxis behavior, worms of CL2355 strain were used (Figure 5D). OFA and OFB show better chemotaxis ability toward benzaldehyde compare with negative control. 50 μM EGCG, 5 μM OFA, and 5 μM OFB significantly increased

10.3389/fnagi.2022.967316

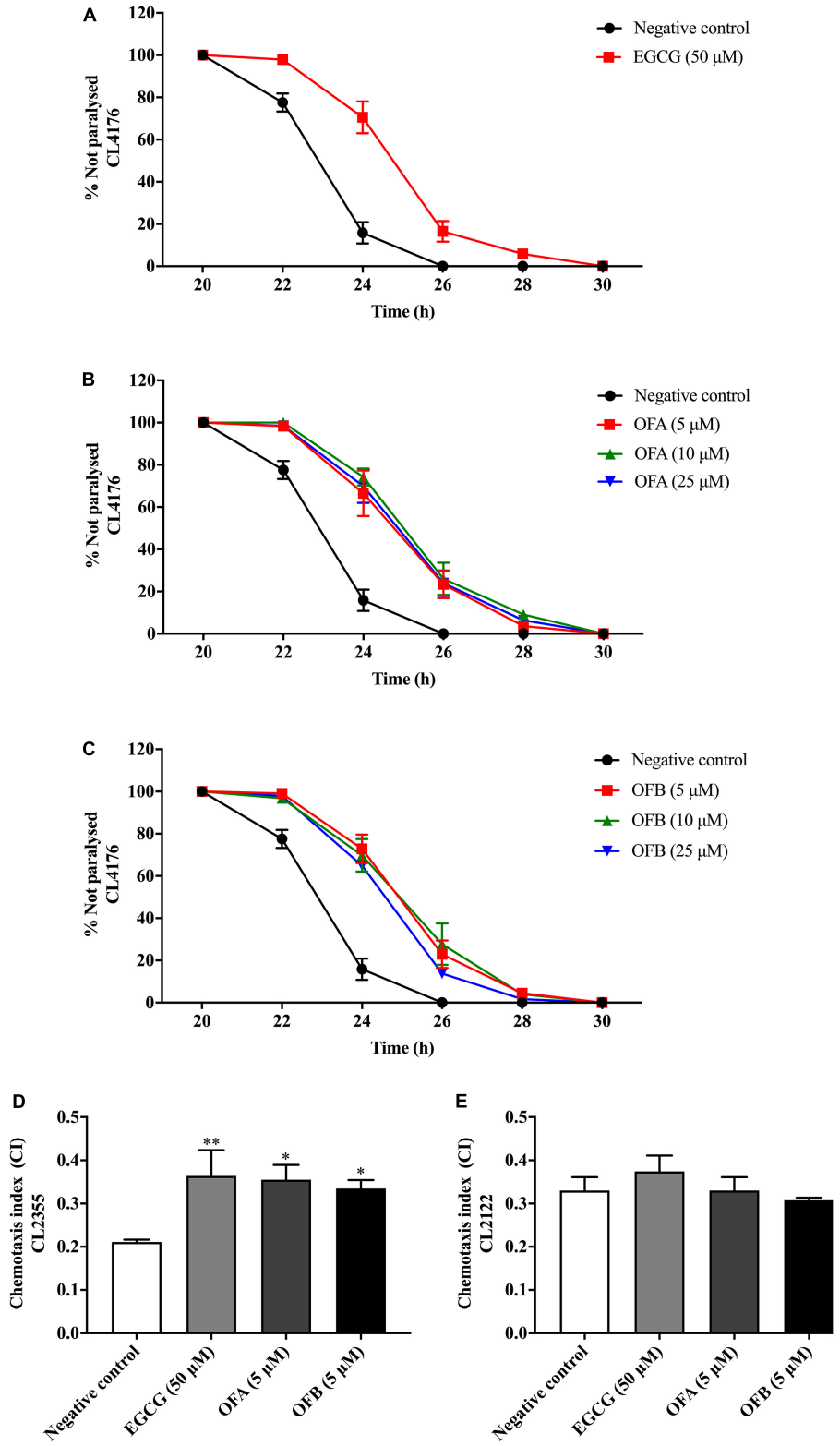

FIGURE 5
Effect of EGCG, OFA, and OFB on Aβ -induced paralysis in transgenic stain AD model CL4176 **(A–C)**. The indicated times are from the initiation of the temperature shift up. Effect of EGCG, OFA, and OFB on Aβ -induced deficit in chemotaxis behavior in transgenic strain AD model CL2355 **(D)**. EGCG, OFA, and OFB didn't affect the chemotaxis behaviour of the control strain CL2122 **(E)**. All data are shown as the mean ± SEM ($n \geq 3$ independent experiments). $^{*}p < 0.05$, $^{**}p < 0.01$ compared to the negative control.

chemotaxis index for 71.43% ($P < 0.01$), 68.25% ($P < 0.05$), and 58.77% ($P < 0.05$), respectively. Meanwhile, OFA and OFB didn't affect the chemotaxis behavior of the control strain CL2122. These results suggest that OFA and OFB contain some protective effects against Aβ-induced chemotaxis deficit.

Oolonghomobisflavan A and oolonghomobisflavan B extended the lifespan of *Caenorhabditis elegans*

In another set of experiments, we investigated whether OFA and OFB can increase the lifespan of *C. elegans* similarly as EGCG (Abbas and Wink, 2009). wild-type (N2) strain was used to detect the effect of OFA and OFB on lifespan (**Supplementary Figure 2** and **Supplementary Table 2**). The mean lifespan of negative control was 14.92 ± 0.31 d, while OFA treated worms lived to 18.71 ± 0.40 d (5 μM), 19.55 ± 0.45 d (10 μM), and 19.83 ± 0.49 d (25 μM), respectively, OFB are 19.98 ± 0.58 (5 μM), 20.01 ± 0.46 (10 μM), and 18.50 ± 0.51 d (25 μM), respectively. These results show that OFA and OFB extend the lifespan of wild-type (N2) strain under normal condition.

The antioxidant effects of oolonghomobisflavan A and oolonghomobisflavan B

OFA and OFB exhibit substantial antioxidant activity. When tested in the DPPH assay, both OFA and OFB effectively scavenged radicals (IC_{50} = 4.65 ± 0.26 μM and 4.80 ± 0.30 μM, respectively). These values are in a similar range as those of known antioxidant EGCG (**Supplementary Table 3**).

Oolonghomobisflavan A and oolonghomobisflavan B increases the stress resistance in *Caenorhabditis elegans*

To further investigate the antioxidant properties of OFA and OFB, the survival of nematodes was analyzed under oxidative stress conditions. Wild-type (N2) strain was cultured in S-medium under oxidative stress which was induced by 80 μM juglone. We found that all concentrations of OFA and OFB significant increased the survival rate when compared with negative control. OFA (5, 10, and 25 μM) increased the survival rate to 25.79% ($P < 0.05$), 54.34% ($P < 0.001$), and 50.02% ($P < 0.001$), respectively, OFB (5, 10 and 25 μM) increased the survival to 43.11 ($P < 0.001$), 48.95% ($P < 0.001$), and 44.01% ($P < 0.001$), respectively compared with negative control (**Figure 6A**). These results show that OFA and OFB can increase the survival rate of wild-type (N2) under the lethal concentration of juglone.

Oolonghomobisflavan A and oolonghomobisflavan B decreased the reactive oxygen species accumulation in *Caenorhabditis elegans*

To investigate whether EGCG, OFA, and OFB could suppress juglone-induced oxidative stress, the intracellular ROS accumulation assay was determined in wild-type (N2) worms. We found that OFA (5, 10, and 25 μM) significant decreased the ROS level 86.01, 88.12, and 90.87%, respectively compared with negative control, OFB (5, 10, and 25 μM) significant decreased the ROS level to 81.51, 87.71, and 91.13%, respectively compared with negative control (**Figure 6B**). These results suggest that OF can decrease the ROS accumulation in *C. elegans*.

Oolonghomobisflavan A and oolonghomobisflavan B modulated the expression of stress response genes in *Caenorhabditis elegans*

To elucidate mechanism of action of OFA and OFB, the expression of the stress response related genes were examined in transgenic *C. elegans* (CL2166 and TJ375) (**Figure 6**). We found that OFA (2.5, 5, 10 μM) significantly decreased the expression of GST-4:GFP by 62.92, 60.59, and 38.53% compared with negative control (**Figure 6D**). OFB (2.5, 5, 10 μM) significantly decreased the expression of GST-4:GFP by 60.29, 63.29, and 53.18% compared with negative control (**Figure 6D**). OFA (2.5, 5, 10 μM) significantly decreased the expression of HSP-16.2:GFP by 25.71, 25.91, and 25.70% compared with negative control (**Figure 6C**). OFB (2.5, 5, 10 μM) significantly decreased the expression of HSP-16.2:GFP by 18.13, 25.12, and 23.43% compared with negative control (**Figure 6C**).

Oolonghomobisflavan A and oolonghomobisflavan B increased the nuclear translocation of DAF-16 in *Caenorhabditis elegans*

DAF-16, a FOXO-family transcription factor, is the well-known regulator of aging in response to the IIS pathway in *C. elegans* (Murphy et al., 2003). The nuclear localization of DAF-16 is essential for activation stress resistance, and lifespan modulation genes. We next examined the effects of OFA and OFB on the nuclear localization of DAF-16. We found that OFA and OFB increased the nuclear translocation of DAF-16 (**Figure 6E**) in transgenic mutant *C. elegans*.

10.3389/fnagi.2022.967316

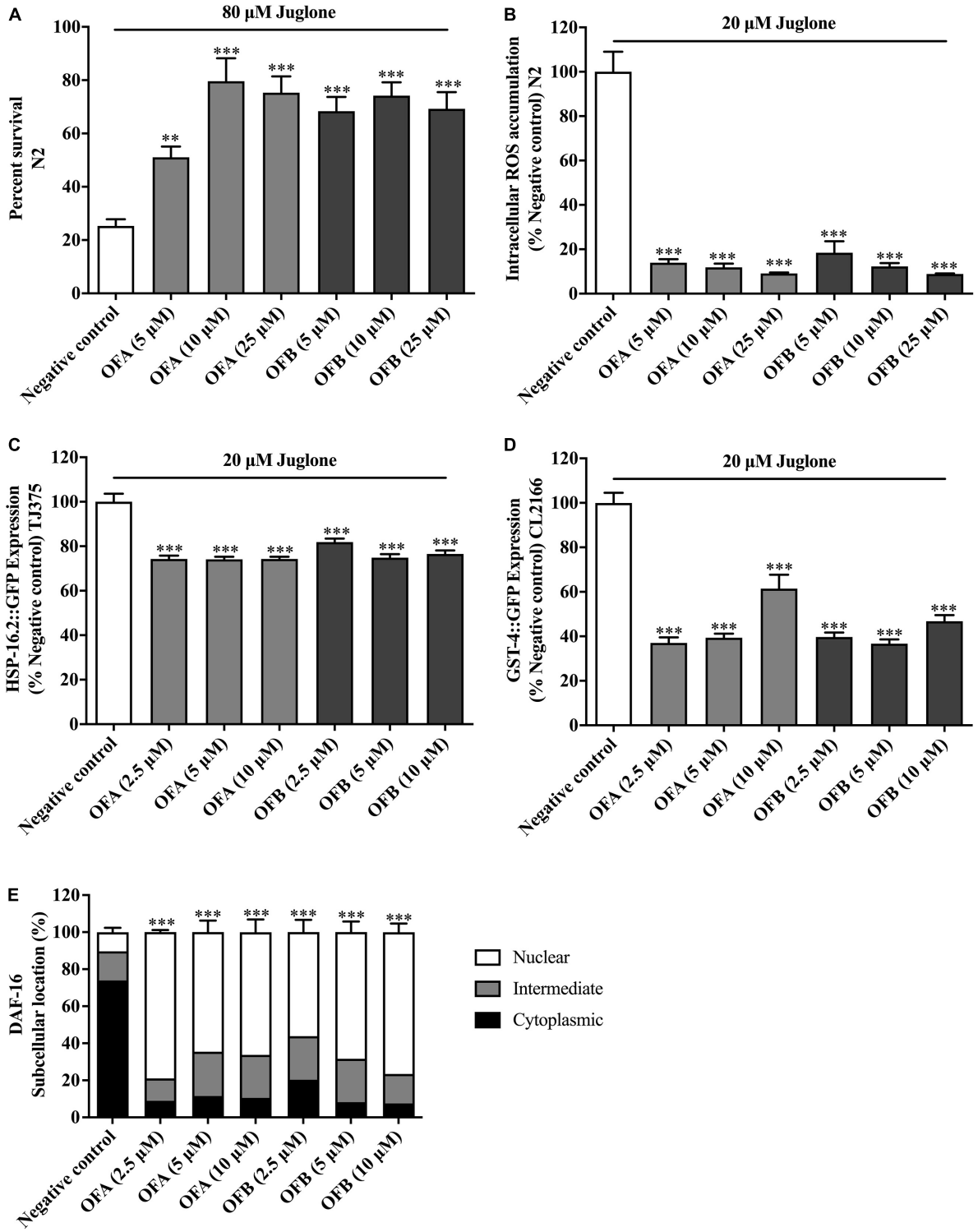

FIGURE 6

Effect of OFA and OFB on *C. elegans* under oxidative stress condition treated with juglone. Percent survival of wild-type (N2) treated with OFA and OFB under lethal juglone concentration (80 µM) condition **(A)**. OFA and OFB attenuate intracellular ROS accumulation in wild-type (N2) under 20 µM juglone condition **(B)**. Effects of OFA and OFB on the expression of *hsp-16.2* **(C)** and *gst-4* **(D)** under 20 µM juglone condition. The localization of DAF-16 transcription factors **(E)**. All data are shown as the mean ± standard deviation ($n \geq 3$ independent experiments). $^{**}p < 0.01$, $^{***}p < 0.001$ compared to the negative control.

Discussion

The accelerated aging of the population is now affecting the entire world. Neurodegenerative disorders have attracted considerable attention among the age-related disorders. Neurodegenerative diseases are linked to neuronal cell death and neurite outgrowth impairment that are often caused by oxidative stress. Plant bioactive secondary metabolites, which have antioxidative and neuroprotective properties could be potential candidates for alternative treatment of neurodegenerative diseases. This is the first report the beneficial effects of oolong tea polyphenols (OFA and OFB) promoting neuroprotective and neuritogenesis properties as well as anti-aging potential. Anti-aging in this study is concerned with extending the lifespan. Both OFA and OFB can extend the lifespan of *C. elegans* wild-type (N2) under normal cultured condition and increase the survival rate of wild-type (N2) under the lethal concentration of juglone.

Neurite outgrowth is a basal process of neuronal differentiation to promote neuronal regeneration after damage or nervous system disorder (Huang et al., 2016). In addition, neurite outgrowth is a crucial goal for the process of anti-neurodegenerative disease therapy (Hu et al., 2015). We found that OFA and OFB promoted neurite outgrowth and neurite-bearing cells in Neuro-2a cells. Besides morphological observation, neurite outgrowth marker examination was also an effective way for measuring neurite outgrowth. GAP-43 (growth-associated protein) (Korshunova and Mosevitsky, 2010) and Ten-4 (Teneurin-4) (Suzuki et al., 2014) are neuron-specific protein associated which regulates neurite outgrowth through axon growth and growth cone formation. We found that OFA and OFB increased GAP-43 and Ten-4 gene expression. Thus, OFA and OFB exhibited neuritogenesis properties by enhancing neurite outgrowth and neurite outgrowth proteins. The utilization of small molecules that interact with neurotrophic factors to stimulate neurite outgrowth at the location of nerve damage has been a potential therapeutic strategy (Bawari et al., 2019). At present, the neurotrophic factor family includes nerve growth factor (NGF), brain-derived neurotrophic factor (BDNF), neurotrophin-3 (NT-3), and neurotrophin-4 (NT-4). They mainly bind to the corresponding high-affinity tyrosine kinase receptors and initiate downstream signaling pathways to maintain neuron survival and promote nerve growth (Huang and Reichardt, 2003). Therefore, it is speculated that EGCG, OFA, and OFB may have physiological effects similar to neurotrophic factors.

The mechanism related to neuronal death in AD is still unclear, but excessive oxidative stress is regarded as major initiators or mediators of AD (Chen and Zhong, 2014). The aggregation of amyloid beta (Aβ) and neurofibrillary tangles enhanced the production of oxidative stress leading to neuronal cell death. In addition, excessive levels of glutamate can contribute to neuronal cell death through the mitochondrial function impairment and stimulation the ROS (Tobaben et al., 2011). We found that OFA and OFB exert a potent neuroprotective effects against cytotoxicity induced by excessive glutamate in cultured neuronal (Neuro-2a and HT22) cells by suppressing intracellular ROS production but also through enhancing the expression of endogenous antioxidant enzymes (*GSTo1*, *GSTa2*, *GPx*, *SOD1*, and *SOD2*).

Furthermore, we explored the neuroprotective effects *in vivo* by using transgenic worms which express human $A\beta_{1-42}$ peptides. The CL4176 strain, which expresses $A\beta_{1-42}$ peptides in muscle cells was used in paralysis assay. OFA and OFB delayed PT50 as compared to negative control. The CL2355 strain, which expresses $A\beta_{1-42}$ peptides in neuron cells was used in chemotaxis assay. OFA and OFB improved chemotaxis ability toward benzaldehyde as compared with negative control worms. These results suggest that OFA and OFB exhibit protective effects against Aβ-induced toxicity in *C. elegans*. Taken together, OFA and OFB exhibit potent neuroprotective effects against glutamate/Aβ-induced toxicity both *in vitro* (Neuro-2a and HT22 cells) and *in vivo* (*C. elegans*). Numerous naturally occurring phytochemicals reduced the level of Aβ induced ROS level through its antioxidative property (Thapa and Carroll, 2017). Our results agree with the neuroprotective properties in tea polyphenol which have been reported in several studies (Abbas and Wink, 2009; Rho et al., 2019; Zhan et al., 2020).

Oxidative stress is considered as a major risk factor for age-related diseases (Wadhwa et al., 2018). In the last decade, the correlation between antioxidant and age-related diseases has gained a lot of attention. Some researchers announced a positive correlation between antioxidants in drinks and longevity (Sadowska-Bartosz and Bartosz, 2014). EGCG could increase lifespan in several animal models such as *Drosophila melanogaster* (Wagner et al., 2015), *Caenorhabditis elegans* (Abbas and Wink, 2009), and *Rattus norvegicus* (Niu et al., 2013). These studies are in agreement with our findings that OFA and OFB have longevity effect by extending the lifespan of *C. elegans* (Duangjan and Curran, 2022). Since OFA and OFB are dimers of EGCG, this result implies that even larger polyphenols exhibit bioavailability in worms. Interestingly, OFA and OFB also exhibit oxidative stress resistance properties in *C. elegans*. We found that OFA and OFB can effectively protect worms against severe oxidative stress and reduced the amount of intracellular ROS. The antioxidant effects of OFA and OFB were further confirmed by the *in vitro* DPPH assays. OFA and OFB exhibit powerful antioxidant activity in a similar range as EGCG. These results support the neuroprotective effects of OFA and OFB in cultured neuronal (Neuro-2a and HT22) cells which suppressed intracellular ROS and induced endogenous antioxidant enzymes. DAF-16, a FOXO-family transcription factor, is the well-known regulator of aging in response to the IIS pathway in *C. elegans* (Murphy et al., 2003;

Guerrero-Rubio et al., 2020; Navarro-Hortal et al., 2021). DAF-16/FOXO remains inactive state in the cytoplasm until external factors such as stress or certain ligands motivate DAF-16/FOXO translocation from the cytoplasm to the nucleus, inducing the expression of stress response gene including *sod-3*, *gst-4,* and *hsp-16.2* (Peixoto et al., 2016; Wang and Wink, 2016; Duangjan et al., 2019b; Li et al., 2019). We found that OFA and OFB increased the nuclear translocation of DAF-16. Moreover, OFA and OFB modulated the expression of stress response genes by down-regulation of *hsp-16.2* and *gst-4* gene expression under juglone induced-oxidative in *C. elegans*. Potential antioxidant activities of tea polyphenols such as EGCG, catechin and caffeine in *C. elegans* were also reported from previous studies (Abbas and Wink, 2009, 2014; Li et al., 2019). Tea has been shown a potential therapeutic agent for preventing age-related diseases such as cancer, cardiovascular diseases and neurodegenerative diseases. This ability is mostly attributed to their antioxidant activity of polyphenols, including the major component EGCG. However, we found that OFA and OFB exhibited the higher neuroprotective than EGCG. The enhanced anti-oxidant activity, is possibly due to existence of more hydroxyl groups, and cytoprotective effects of bi-flavonoids compared to flavonoid monomers (Shin et al., 2006; Hamaguchi et al., 2009; Thapa and Chi, 2015). Dimers of apigenin revealed enhanced anti-cancer effects compared to apigenin (flavonoid monomer) alone (Chan et al., 2006; Hadden and Blagg, 2008). Both OFA and OFB contain a methylene bridge linking the 8,8'-positons of two flavan units. Maybe it is the key why OFA and OFB showed a better neuroprotective effect than EGCG. Taken together, this study provides the first evidence of OFA and OFB in neuritogenesis and neuroprotective potential both *in vitro* (Neuro-2a and HT22 neuronal cells model) and *in vivo* (*C. elegans* model). OFA and OFB protected Neuro-2a and HT22 neuronal cells against glutamate-induced toxicity and of *C. elegans* against juglone/Aβ-induced toxicity. OFA and OFB significantly reduced the intracellular ROS accumulation and regulated the gene expression of antioxidant enzymes in these models. According to an examination of 302 neurons, the neurotransmitters, vesicle circulation and synaptic transmission of the nematode are highly conserved. Thus, *C. elegans* has been used as an *in vivo* model for neurotoxicity (Link et al., 2016). Amyloid-β, a well-known hallmark of AD, can induce oxidative stress and neuronal cell death, which plays an important role in AD (Yankner and Lu, 2009). Moreover, we got the positive results from paralysis assay (CL4176 model, which expresses $A\beta_{1-42}$ peptides in muscle cells) and chemotaxis assay (CL2355 model, which expresses $A\beta_{1-42}$ peptides in neuron cells) treated with OFA and OFB, which proved the neuroprotective effect against Aβ-induced toxicity. Considering the AD is age-related neurodegenerative disease, we deduced that OFA and OFB may contain the anti-aging effect. And it's consistent with our findings that OFA and OFB significantly extend the lifespan of wild type (N2) *C. elegans*. The oolong tea polyphenols (OFA and OFB) possesses both longevity promoting effects and neuroprotective activity supporting its therapeutic potential for the treatment of age-associated neurodegenerative diseases. Further studies are required to study the molecular mechanism of OFA and OFB on longevity and neuroprotective properties, and *in vivo* tests with more complex model organisms and intervention studies.

Conclusion

In conclusion, OFA and OFB increased the neurite length of Neuro-2a, decreased the accumulation of ROS in cultured neuronal cells (Neuro-2a and HT22), up-regulated the expression of antioxidant mRNA expression (*GPx*, *GSTs,* and *SODs*). Moreover, OFA and OFB delayed the Aβ-induced paralysis in transgenic strain CL4176 and counteracted the chemotaxis deficit in strain CL2355. Similar with EGCG, OFA, and OFB can extend the lifespan of *C. elegans*. OFA and OFB maybe become promising candidates agents for treating the age-related neuroprotective diseases in the future.

Data availability statement

The original contributions presented in this study are included in the article/**Supplementary material**, further inquiries can be directed to the corresponding author/s.

Authors contributions

SZ and CD performed the experiments, analyzed the data, and were major contributors in writing the manuscript. SZ, CD, TT, and LW designed the study and prepared media and reagents. JL and MW provided materials for the study, conceived and supervised the research, and reviewed and edited the manuscript. JL, MW, TT, and LW corrected the manuscript. All authors contributed to manuscript revision, read, and approved the submitted version.

Funding

SZ thanked the support from the China Scholarship Council. This research was also supported by grants from the Natural Science Foundation of Anxi Government, China (KH1500790), the Modern Agricultural and Industrial Park for Anxi County in Fujian Province, Ministry of Agriculture and Rural Affairs, China (KMD18003A), the Industry-University-Research Collaboration Program of

Fujian Science and Technology Department, China (2016N5001), the Fujian Agriculture and Forestry University Construction Project for Technological Innovation and Service System of Tea Industry Chain (K152005A07), and the Natural Science Foundation of Fujian Agriculture and Forestry (CXZX2020079A).

Conflict of interest

MW was an editor for the Frontiers journal.

The remaining authors declare that the research was conducted in the absence of any commercial or financial relationships that could be construed as a potential conflict of interest.

Publisher's note

Supplementary material

The Supplementary Material for this article can be found online at: https://www.frontiersin.org/articles/10.3389/fnagi.2022.967316/full#supplementary-material

References

Abbas, S., and Wink, M. (2009). Epigallocatechin gallate from green tea (*Camellia sinensis*) increases lifespan and stress resistance in *Caenorhabditis elegans*. *Planta Med.* 75, 216–221. doi: 10.1055/s-0028-1088378

Abbas, S., and Wink, M. (2014). Green tea extract induces the resistance of *Caenorhabditis elegans* against oxidative stress. *Antioxidants* 3, 129–143. doi: 10.3390/antiox3010129

Bawari, S., Tewari, D., Argüelles, S., Sah, A. N., Nabavi, S. F., Xu, S., et al. (2019). Targeting BDNF signaling by natural products: Novel synaptic repair therapeutics for neurodegeneration and behavior disorders. *Pharmacol. Res.* 148:104458. doi: 10.1016/j.phrs.2019.104458

Bonaterra, G. A., Schwendler, A., Hüther, J., Schwarzbach, H., Schwarz, A., Kolb, C., et al. (2017). Neurotrophic, cytoprotective, and anti-inflammatory effects of St. John's wort extract on differentiated mouse hippocampal HT-22 neurons. *Front. Pharmacol.* 8:955. doi: 10.3389/fphar.2017.00955

Chan, K.-F., Zhao, Y., Burkett, B. A., Wong, I. L. K., Chow, L. M. C., and Chan, T. H. (2006). Flavonoid dimers as bivalent modulators for P-glycoprotein-based multidrug resistance: Synthetic apigenin homodimers linked with defined-length poly(ethylene glycol) spacers increase drug retention and enhance chemosensitivity in resistant cancer cells. *J. Med. Chem.* 49, 6742–6759. doi: 10.1021/jm060593

Chen, Z., and Zhong, C. (2014). Oxidative stress in Alzheimer's disease. *Neurosci. Bull.* 30, 271–281. doi: 10.1007/s12264-013-1423-y

Dostal, V., and Link, C. D. (2010). Assaying β-amyloid toxicity using a transgenic *C. elegans* model. *J. Vis. Exp.* 44:2252. doi: 10.3791/2252

Drake, J., Link, C. D., and Butterfield, D. A. (2003). Oxidative stress precedes fibrillar deposition of Alzheimer's disease amyloid beta-peptide (1-42) in a transgenic *Caenorhabditis elegans* model. *Neurobiol. Aging* 24, 415–420. doi: 10.1016/s0197-4580(02)00225-7

Duangjan, C., and Curran, S. P. (2022). Oolonghomobisflavans from Camellia sinensis increase Caenorhabditis elegans lifespan and healthspan. *Geroscience* 44, 533–545. doi: 10.1007/s11357-021-00462-7

Duangjan, C., Rangsinth, P., Gu, X., Zhang, S., Wink, M., and Tencomnao, T. (2019b). *Glochidion zeylanicum* leaf extracts exhibit lifespan extending and oxidative stress resistance properties in *Caenorhabditis elegans* via DAF-16/FoxO and SKN-1/Nrf-2 signaling pathways. *Phytomedicine* 64:153061. doi: 10.1016/j.phymed.2019.153061

Duangjan, C., Rangsinth, P., Gu, X., Wink, M., and Tencomnao, T. (2019a). Lifespan extending and oxidative stress resistance properties of a leaf extracts from Anacardium occidentale L. in *Caenorhabditis elegans*. *Oxid. Med. Cell. Longev.* 2019:9012396. doi: 10.1155/2019/9012396

Guerrero-Rubio, M. A., Hernández-García, S., Escribano, J., Jiménez-Atiénzar, M., Cabanes, J., García-Carmona, F., et al. (2020). Betalain health-promoting effects after ingestion in *Caenorhabditis elegans* are mediated by DAF-16/FOXO and SKN-1/Nrf2 transcription factors. *Food Chem.* 330:127228. doi: 10.1016/j.foodchem.2020.127228

Hadden, M. K., and Blagg, B. S. J. (2008). Dimeric approaches to anti-cancer chemotherapeutics. *Anticancer Agents Med. Chem.* 8, 807–816. doi: 10.2174/187152008785914743

Hamaguchi, T., Ono, K., Murase, A., and Yamada, M. (2009). Phenolic compounds prevent Alzheimer's pathology through different effects on the amyloid-beta aggregation pathway. *Am. J. Pathol.* 175, 2557–2565. doi: 10.2353/ajpath.2009.090417

Hobert, O. (2003). Behavioral plasticity in *C. elegans*: Paradigms, circuits, genes. *J. Neurobiol.* 54, 203–223. doi: 10.1002/neu.10168

Hu, S., Cui, W., Mak, S., Xu, D., Hu, Y., Tang, J., et al. (2015). Substantial neuroprotective and neurite outgrowth-promoting activities by bis(propyl)-cognitin via the activation of α7-nAChR, a promising anti-Alzheimer's dimer. *ACS Chem. Neurosci.* 6, 1536–1545. doi: 10.1021/acschemneuro.5b00108

Huang, E. J., and Reichardt, L. F. (2003). Trk receptors: Roles in neuronal signal transduction. *Annu. Rev. Biochem.* 72, 609–642. doi: 10.1146/annurev.biochem.72.121801.161629

Huang, L., Liu, L.-F., Liu, J., Dou, L., Wang, G.-Y., Liu, X.-Q., et al. (2016). Ginsenoside Rg1 protects against neurodegeneration by inducing neurite outgrowth in cultured hippocampal neurons. *Neural Regen. Res.* 11, 319–325. doi: 10.4103/1673-5374.177741

Korshunova, I., and Mosevitsky, M. (2010). Role of the growth-associated protein GAP-43 in NCAM-mediated neurite outgrowth. *Adv. Exp. Med. Biol.* 663, 169–182. doi: 10.1007/978-1-4419-1170-4_11

Li, H., Roxo, M., Cheng, X., Zhang, S., Cheng, H., and Wink, M. (2019). Pro-oxidant and lifespan extension effects of caffeine and related methylxanthines in *Caenorhabditis elegans*. *Food Chem. X* 1:100005. doi: 10.1016/j.fochx.2019.100005

Link, P., Roth, K., Sporer, F., and Wink, M. (2016). Carlina acaulis exhibits antioxidant activity and counteracts Aβ toxicity in *Caenorhabditis elegans*. *Molecules* 21:871. doi: 10.3390/molecules21070871

Murphy, C. T., McCarroll, S. A., Bargmann, C. I., Fraser, A., Kamath, R. S., Ahringer, J., et al. (2003). Genes that act downstream of DAF-16 to influence the lifespan of *Caenorhabditis elegans*. *Nature* 424, 277–283. doi: 10.1038/nature01789

Nakai, M., Fukui, Y., Asami, S., Toyoda-Ono, Y., Iwashita, T., Shibata, H., et al. (2005). Inhibitory effects of oolong tea polyphenols on pancreatic lipase in vitro. *J. Agric. Food Chem.* 53, 4593–4598. doi: 10.1021/jf047814

Navarro-Hortal, M. D., Romero-Márquez, J. M., Esteban-Muñoz, A., Sánchez-González, C., Rivas-García, L., Llopis, J., et al. (2021). Strawberry (Fragaria × ananassa cv. *Romina*) methanolic extract attenuates Alzheimer's beta amyloid production and oxidative stress by SKN-1/NRF and DAF-16/FOXO mediated mechanisms in *C. elegans*. *Food Chem.* 372:131272. doi: 10.1016/j.foodchem.2021.131272

Niu, Y., Na, L., Feng, R., Gong, L., Zhao, Y., Li, Q., et al. (2013). The phytochemical, EGCG, extends lifespan by reducing liver and kidney function

damage and improving age-associated inflammation and oxidative stress in healthy rats. *Aging Cell* 12, 1041–1049. doi: 10.1111/acel.12133

Park, S. J., Jin, M. L., An, H. K., Kim, K. S., Ko, M. J., Kim, C. M., et al. (2015). Emodin induces neurite outgrowth through PI3K/Akt/GSK-3β-mediated signaling pathways in Neuro2a cells. *Neurosci. Lett.* 588, 101–107. doi: 10.1016/j.neulet.2015.01.001

Peixoto, H., Roxo, M., Krstin, S., Röhrig, T., Richling, E., and Wink, M. (2016). An anthocyanin-rich extract of Acai (*Euterpe precatoria* Mart.) increases stress resistance and retards aging-related markers in *Caenorhabditis elegans*. *J. Agric. Food Chem.* 64, 1283–1290. doi: 10.1021/acs.jafc.5b05812

Pérez-Hernández, J., Zaldívar-Machorro, V. J., Villanueva-Porras, D., Vega-Ávila, E., and Chavarría, A. (2016). A potential alternative against neurodegenerative diseases: Phytodrugs. *Oxid. Med. Cell. Longev.* 2016:8378613. doi: 10.1155/2016/8378613

Rangsinth, P., Duangjan, C., Sillapachaiyaporn, C., Isidoro, C., Prasansuklab, A., and Tencomnao, T. (2021). *Caesalpinia mimosoides* leaf extract promotes neurite outgrowth and inhibits BACE1 activity in mutant APP-Overexpressing Neuronal Neuro2a Cells. *Pharmaceuticals* 14:901. doi: 10.3390/ph14090901

Read, D. E., and Gorman, A. M. (2009). Involvement of Akt in neurite outgrowth. *Cell. Mol. Life Sci.* 66, 2975–2984. doi: 10.1007/s00018-009-0057-8

Rho, T., Choi, M. S., Jung, M., Kil, H. W., Hong, Y. D., and Yoon, K. D. (2019). Identification of fermented tea (*Camellia sinensis*) polyphenols and their inhibitory activities against amyloid-beta aggregation. *Phytochemistry* 160, 11–18. doi: 10.1016/j.phytochem.2018.12.013

Rocha, L., Neves, D., Valentão, P., Andrade, P. B., and Videira, R. A. (2020). Adding value to polyvinylpolypyrrolidone winery residue: A resource of polyphenols with neuroprotective effects and ability to modulate type 2 diabetes-relevant enzymes. *Food Chem.* 329:127168. doi: 10.1016/j.foodchem.2020.127168

Sadowska-Bartosz, I., and Bartosz, G. (2014). Effect of antioxidants supplementation on aging and longevity. *Biomed Res. Int.* 2014:404680. doi: 10.1155/2014/404680

Shin, D. H., Bae, Y. C., Kim-Han, J. S., Lee, J. H., Choi, I. Y., Son, K. H., et al. (2006). Polyphenol amentoflavone affords neuroprotection against neonatal hypoxic-ischemic brain damage via multiple mechanisms. *J. Neurochem.* 96, 561–572. doi: 10.1111/j.1471-4159.2005.03582.x

Suzuki, N., Numakawa, T., Chou, J., de Vega, S., Mizuniwa, C., Sekimoto, K., et al. (2014). Teneurin-4 promotes cellular protrusion formation and neurite outgrowth through focal adhesion kinase signaling. *FASEB J.* 28, 1386–1397. doi: 10.1096/fj.13-241034

Thapa, A., and Carroll, N. J. (2017). Dietary modulation of oxidative stress in Alzheimer's disease. *Int. J. Mol. Sci.* 18:1583. doi: 10.3390/ijms18071583

Thapa, A., and Chi, E. Y. (2015). Biflavonoids as potential small molecule therapeutics for Alzheimer's disease. *Adv. Exp. Med. Biol.* 863, 55–77. doi: 10.1007/978-3-319-18365-7_3

Tobaben, S., Grohm, J., Seiler, A., Conrad, M., Plesnila, N., and Culmsee, C. (2011). Bid-mediated mitochondrial damage is a key mechanism in glutamate-induced oxidative stress and AIF-dependent cell death in immortalized HT-22 hippocampal neurons. *Cell Death Differ.* 18, 282–292. doi: 10.1038/cdd.2010.92

Wadhwa, R., Gupta, R., and Maurya, P. K. (2018). Oxidative stress and accelerated aging in neurodegenerative and neuropsychiatric disorder. *Curr. Pharm. Des.* 24, 4711–4725. doi: 10.2174/1381612825666190115121018

Wagner, A. E., Piegholdt, S., Rabe, D., Baenas, N., Schloesser, A., Eggersdorfer, M., et al. (2015). Epigallocatechin gallate affects glucose metabolism and increases fitness and lifespan in *Drosophila melanogaster*. *Oncotarget* 6, 30568–30578. doi: 10.18632/oncotarget.5215

Wang, E., and Wink, M. (2016). Chlorophyll enhances oxidative stress tolerance in *Caenorhabditis elegans* and extends its lifespan. *PeerJ* 4:e1879. doi: 10.7717/peerj.1879

Weerawatanakorn, M., Hung, W.-L., Pan, M.-H., Li, S., Li, D., Wan, X., et al. (2015). Chemistry and health beneficial effects of oolong tea and theasinensins. *Food Sci. Hum. Wellness* 4, 133–146. doi: 10.1016/j.fshw.2015.10.002

Yankner, B. A., and Lu, T. (2009). Amyloid β-protein toxicity and the pathogenesis of Alzheimer disease. *J. Biol. Chem.* 284, 4755–4759. doi: 10.1074/jbc.R800018200

Zhan, C., Chen, Y., Tang, Y., and Wei, G. (2020). Green tea extracts EGCG and EGC display distinct mechanisms in disrupting Aβ42 protofibril. *ACS Chem. Neurosci.* 11, 1841–1851. doi: 10.1021/acschemneuro.0c00277

Zhang, S., Duangjan, C., Tencomnao, T., Liu, J., Lin, J., and Wink, M. (2020). Neuroprotective effects of oolong tea extracts against glutamate-induced toxicity in cultured neuronal cells and β-amyloid-induced toxicity in *Caenorhabditis elegans*. *Food Funct.* 11, 8179–8192. doi: 10.1039/d0fo01072c

frontiers | Frontiers in Aging Neuroscience

TYPE Original Research
PUBLISHED 06 October 2022
DOI 10.3389/fnagi.2022.960314

OPEN ACCESS

EDITED BY
Panteleimon Giannakopoulos,
Université de Genève, Switzerland

REVIEWED BY
Natali Lujan Chanaday Ricagni,
University of Pennsylvania,
United States
Guy Perkins,
University of California, San Diego,
United States

*CORRESPONDENCE
Clifton Andrew Chapman
andrew.chapman@concordia.ca

SPECIALTY SECTION
This article was submitted to Alzheimer's Disease and Related Dementias,
a section of the journal
Frontiers in Aging Neuroscience

RECEIVED 02 June 2022
ACCEPTED 20 September 2022
PUBLISHED 06 October 2022

CITATION
Olajide OJ, La Rue C, Bergdahl A and Chapman CA (2022) Inhibiting amyloid beta (1–42) peptide-induced mitochondrial dysfunction prevents the degradation of synaptic proteins in the entorhinal cortex.
Front. Aging Neurosci. 14:960314.
doi: 10.3389/fnagi.2022.960314

Inhibiting amyloid beta (1–42) peptide-induced mitochondrial dysfunction prevents the degradation of synaptic proteins in the entorhinal cortex

Olayemi Joseph Olajide[1,2], Claudia La Rue[1], Andreas Bergdahl[3] and Clifton Andrew Chapman[1]*

[1]Department of Psychology, Center for Studies in Behavioral Neurobiology, Concordia University, Montreal, QC, Canada, [2]Division of Neurobiology, Department of Anatomy, College of Health Sciences, University of Ilorin, Ilorin, Nigeria, [3]Department of Health, Kinesiology and Applied Physiology, Concordia University, Montreal, QC, Canada

Increasing evidence suggests that mitochondrial dysfunction and aberrant release of mitochondrial reactive oxygen species (ROS) play crucial roles in early synaptic perturbations and neuropathology that drive memory deficits in Alzheimer's disease (AD). We recently showed that solubilized human amyloid beta peptide 1–42 ($hA\beta_{1-42}$) causes rapid alterations at glutamatergic synapses in the entorhinal cortex (EC) through the activation of both GluN2A- and GluN2B-containing NMDA receptors. However, whether disruption of mitochondrial dynamics and increased ROS contributes to mechanisms mediating $hA\beta_{1-42}$-induced synaptic perturbations in the EC is unknown. Here we assessed the impact of $hA\beta_{1-42}$ on mitochondrial respiratory functions, and the expression of key mitochondrial and synaptic proteins in the EC. Measurements of mitochondrial respiratory function in wild-type EC slices exposed to 1 μM $hA\beta_{1-42}$ revealed marked reductions in tissue oxygen consumption and energy production efficiency relative to control. $hA\beta_{1-42}$ also markedly reduced the immunoexpression of both mitochondrial superoxide dismutase (SOD2) and mitochondrial-cytochrome c protein but had no significant impact on cytosolic-cytochrome c expression, voltage-dependent anion channel protein (a marker for mitochondrial density/integrity), and the immunoexpression of protein markers for all five mitochondrial complexes. The rapid impairments in mitochondrial functions induced by $hA\beta_{1-42}$ were accompanied by reductions in the presynaptic marker synaptophysin, postsynaptic density protein (PSD95), and the vesicular acetylcholine transporter, with no significant changes in the degradative enzyme acetylcholinesterase. We then assessed whether reducing $hA\beta_{1-42}$-induced increases in ROS could prevent dysregulation of entorhinal synaptic proteins, and found that synaptic impairments induced by $hA\beta_{1-42}$ were prevented by the mitochondria-targeted antioxidant drug mitoquinone

mesylate, and by the SOD and catalase mimetic EUK134. These findings indicate that hAβ_{1-2} can rapidly disrupt mitochondrial functions and increase ROS in the entorhinal, and that this may contribute to synaptic dysfunctions that may promote early AD-related neuropathology.

KEYWORDS

Alzheimer's disease, mitochondria, acetylcholine, entorhinal cortex, oxidative stress, reactive oxygen species, synaptic proteins

Introduction

Alzheimer's disease (AD) is a debilitating neurodegenerative disorder that results from the progressive loss of neurons in selective brain areas, and is the primary cause of dementia worldwide (Fan et al., 2020; Guo et al., 2020; Olajide et al., 2021). Neuropathology in AD is hallmarked by abnormal accumulation of amyloid beta peptide (Aβ), a highly neurotoxic derivative of the amyloid precursor protein (APP) which is a transmembrane protein that is particularly concentrated in synapses (Haass and Selkoe, 2007; Masters and Selkoe, 2012; Mucke and Selkoe, 2012; Hampel et al., 2021). Aβ is thought to interact with multiple biological mechanisms to incite AD-related modifications in neurons, and several lines of experimental evidence, including our own, have shown that Aβ can rapidly dysregulate proteins mediating excitatory synaptic transmission (Selkoe, 2002; Coleman and Yao, 2003; Shankar and Walsh, 2009; Overk and Masliah, 2014; Tu et al., 2014; Olajide and Chapman, 2021; Olajide et al., 2021). These synaptic changes are thought to lead to cognitive deficits and memory failure early in AD (Arendt, 2009; Mucke and Selkoe, 2012; Marsh and Alifragis, 2018; Guo et al., 2020), but the molecular mechanisms through which Aβ induces excitotoxicity and neurodegeneration are still poorly understood.

Synaptic transmission relies heavily on mitochondria that generate energy through ATP and nicotinamide adenine dinucleotide (NAD +), maintain calcium homeostasis and buffering, and regulate cell signaling (Calkins et al., 2011; Akhter et al., 2017; Pickett et al., 2018). Perturbation of mitochondrial functions may contribute directly to impaired synaptic transmission in early AD (Cavallucci et al., 2013; Akhter et al., 2017; Olajide et al., 2017a; Xiao et al., 2017; Pickett et al., 2018; Khosravi and Harner, 2020), and Aβ can disrupt mitochondrial energy production and lead to increases in the synthesis of reactive oxygen species (ROS) and oxidative damage (Calkins et al., 2011; Hampel et al., 2021; Olajide et al., 2021; Ashleigh et al., 2022). Cellular ROS are natural by-products of mitochondrial aerobic respiration that result predominantly from leakage of electrons at complexes I and III of the electron transport chain. While ROS serve essential cellular functions, excess ROS can induce oxidative damage and AD-related neuropathology (Murphy, 2009; Patten et al., 2010; Wang et al., 2020). Under physiological conditions, oxidative damage by the major ROS, superoxide (O^2-), is prevented by mitochondrial superoxide dismutase (SOD2), an antioxidant enzyme that catalyzes the dismutation of O^2- to hydrogen peroxide (Murphy, 2009). However, Aβ can induce mitochondrial dysfunction both by increasing O^2- production and by depleting the cellular antioxidant defense system, which causes degeneration of synaptic elements and alters neurotransmission processes in neurons (Tönnies and Trushina, 2017; Wang et al., 2020; Ionescu-Tucker and Cotman, 2021; Misrani et al., 2021). The overexpression of SOD2 in AD mouse models reportedly reduces Aβ deposition and prevents memory deficits (Dumont et al., 2009; Massaad et al., 2009), whereas mutant AD mice with depleted SOD2 expression show increased Aβ levels and accelerated synaptic dysfunction and cognitive decline (Li et al., 2004; Esposito et al., 2006).

The entorhinal cortex (EC) is important for cognitive functions including memory and is among the first cortical regions to be affected by AD pathology (van Hoesen et al., 1991; Velayudhan et al., 2013; Khan et al., 2014; Zhou et al., 2016; Grubman et al., 2019; Olajide et al., 2021). Subpopulations of neurons are differentially vulnerable to the toxicity of oxidative stress (Wang and Michaelis, 2010), and the EC is one of the earliest temporal lobe structures to show both oxidative impairment and Aβ accumulation (Nunomura et al., 2001; Terni et al., 2010; Olajide et al., 2021). Armand-Ugon et al. (2017) reported reduced expression of mitochondrial complexes I, II, IV, and V in the EC, but not in the frontal cortex, during the initial stages of AD, and this mitochondrial dysfunction and oxidative impairment may drive early synaptic failure in AD (Tönnies and Trushina, 2017). We have shown recently that human Aβ_{1-42} (hAβ_{1-42}) rapidly alters elements of glutamatergic synapses in the EC through activation of both GluN2A and GluN2B subunit-containing NMDA receptors (Olajide and Chapman, 2021). This may drive the selective vulnerability of the EC to AD-type neurodegeneration (Olajide et al., 2021), but whether increased ROS and mitochondrial dysfunction contribute to the susceptibility of EC to early AD-related synaptic degeneration has not been explored.

Here, we investigated how mitochondrial proteins, respiratory function, and key synaptic proteins are affected in the EC of brain slices from wild-type rats following exposure to soluble $hA\beta_{1-42}$. We then assessed the ability of two novel and specific pharmacological ROS scavengers and inhibitors, the mitochondria-targeted antioxidant mitoquinone mesylate (MitoQ) and the SOD and catalase mimetic EUK134, to block the degradation of synaptic proteins induced by $hA\beta_{1-42}$ in the EC. Our results support the idea that mitochondrial alterations induced by $hA\beta_{1-42}$ are a central factor in early synaptic degeneration in the EC, and contribute to a more detailed understanding of the molecular mechanisms driving neurodegeneration in the EC during early AD.

Materials and methods

Animals and tissue preparation

Experiments were conducted according to the guidelines of the Canadian Council on Animal Care, and experimental procedures were approved by the Concordia University Animal Research Ethics Committee (Permit Number: 30000253). Six to ten-week-old male Long-Evans rats (Charles River) were housed and placed on a reverse 12 h: 12 h light-dark cycle, with free access to rat chow and water. Acute brain slices were obtained following isoflurane anesthesia and decapitation as previously described (Glovaci and Chapman, 2019). Brains were rapidly removed and cooled (4°C) in high-sucrose ACSF containing (in mM) 250 sucrose, 2 KCl, 1.25 NaH_2PO_4, 7 $MgCl_2$, 26 $NaHCO_3$, 0.5 $CaCl_2$ and 10 dextrose, saturated with 95% O_2 and 5% CO_2. Horizontal slices (400 μm thick) were obtained throughout the ventral to the dorsal extent of the brain in cooled high-sucrose ACSF using a vibratome (Leica, VT1200). The EC was carefully excised from each slice, using a flat blade in contact with the vibratome blade (Paxinos and Watson, 1997; Olajide and Chapman, 2021). Obtained tissue was placed in normal ACSF consisting (in mM) of 124 NaCl, 5 KCl, 1.25 NaH_2PO_4, 2 $MgSO_4$, 2 $CaCl_2$, 26 $NaHCO_3$, and 10 dextrose saturated with 95% O_2 and 5% CO_2 at 32°C for 30 min. Assignment of EC slices taken from the right or left hemispheres were alternated between treatment groups at each consecutive level, so that tissue in the control and treated conditions was obtained from both hemispheres across the dorso-ventral extent of the EC.

Drug preparation and treatments

Drugs were prepared as stock solutions and diluted to final concentrations just before use. Tissue was incubated for 3 h in submersion chambers containing ACSF at 22–24°C, saturated with 95% O_2 and 5% CO_2. EC slices were incubated in 1 μM $hA\beta_{1-42}$ (MW 4514.08; Abcam, AB120301) with a final concentration of DMSO of 0.1%, while control EC slices were exposed to 0.1% DSMO in ACSF. Solubilization and preparation of $hA\beta_{1-42}$ were done as previously described (Olajide and Chapman, 2021). $hA\beta_{1-42}$ was first solubilized in DMSO at 500 μM, sonicated for 15 min at room temperature, and then centrifuged at 15,000 × g at 4°C for 20 min. The supernatant was stored at −80°C in 10 μL aliquots and diluted in ACSF just before use. This method is known to result in low molecular weight β-oligomers including monomers to tetramers (Bitan et al., 2003; Stine et al., 2003) which are the most neurotoxic (Masters and Selkoe, 2012; Guo et al., 2020). It is possible for some protofibrils to develop following this preparation, but significant fibrillary aggregation requires longer incubation times and higher concentrations (>10 μM; O'Nuallain et al., 2004; Wogulis et al., 2005).

The role of mitochondrial ROS and oxidative stress was assessed by applying the mitochondria-targeted antioxidant drug mitoquinone mesylate (MitoQ, 500 nM; Toronto Research Chemicals; M372215), and SOD/catalase mimetic drug EUK134 (250 nM; Cayman Chemical; 10006329) during incubation of slices in $hA\beta_{1-42}$ or DMSO. Each treatment group included slices from at least 6 animals.

Mitochondrial respiration measurements

A sequential substrate addition protocol was conducted to assess mitochondrial coupled and uncoupled oxygen consumption, LEAK respiration, and membrane integrity using a two-chamber polarographic sensor (Oxygraph-2k; Oroboros Instruments, Innsbruck, Austria). $hA\beta_{1-42}$-incubated and control EC samples were assessed simultaneously in both chambers under similar reaction conditions (n = 5 or 6). The measurements of oxygen consumption were performed in MiR05 at 37°C. MiR05 contains (in mM) 0.5 EGTA, 3.0 $MgCl_2 \cdot 6H_2O$, 60 K-lactobionate, 20 taurine, 10 KH_2PO_4, 20 HEPES, 110 sucrose, and 1 g/L BSA (pH 7.1). The oxygen flux was registered and analyzed by the DatLab 7.0 software. Between 2 and 3 mg (wet weight) of treated entorhinal tissue was placed in the Oxygraph and oxygen levels were increased to approximately 480 pmol. Saponin (50 μg/mL) was added to the chambers to permeabilize the tissue before the experiment was begun. In the protocol, non-phosphorylating LEAK-respiration was induced by adding the Complex I-linked substrates malate (2 mM), pyruvate (5 mM), and glutamate (5 mM). Subsequently, the OXPHOS-capacity of Complex I-linked activity was measured after the addition of a saturating concentration of ADP (5 mM). Cytochrome c (10 μM) was then added to assess mitochondrial membrane damage. OXPHOS-capacity with combined Complex I and II-linked substrates was assessed by the addition of succinate (10 mM). This was followed by FCCP (carbonylcyanide-4 (trifluoromethoxy)

phenylhydrazone, 1 μM) to test for uncoupling. The acceptor control ratio (ACR), which measures the degree of coupling between oxidation and phosphorylation, was calculated as the rate of oxygen consumption during ADP phosphorylation divided by the rate of non-phosphorylating LEAK-respiration induced by glutamate administration.

Protein preparation and Western blotting

To perform Western immunoblotting, treated EC tissue was collected into microfuge tubes and snap-frozen. Tissues were disrupted with a tissue sonicator (QSonica: Q55) in homogenization buffer (10 mM Tris, pH 7.4, 1 mM EGTA, 1 mM EDTA, 0.5 DTT, 0.1 μM okadaic acid, 1 mM Na_3VO_4, 1 mM PMSF and 10 μg/mL leupeptin). Mitochondrial protein purification was done following extraction in mitochondrial homogenization buffer (10 mM Tris-HCl, pH 6.7, 10 mM KCl, 0.15 mM $MgCl_2$, 1 mM PMSF, 1 mM DTT) followed by resuspension in mitochondrial suspension buffer (10 mM Tris HCl-pH 6.7, 0.15 mM $MgCl_2$, 0.25 mM sucrose, 1 mM PMSF, 1 mM DTT). The quantity of protein in each sample was determined using BCA Protein Assay (Thermo Fisher: 23,227) and an ELISA Fluorostar Analysis System Plate Reader. Bovine serum albumin (BSA) was used as the standard for protein quantification. Protein samples (20–30 μg) were resolved on Tris-glycine 8–12% SDS-PAGE gels. The resolved proteins were transferred from gels to nitrocellulose membrane (Bio-Rad: 1620112) and blocked for 1–2 h in either 5% milk or 5% BSA (as indicated below for each specific antibody) in Tris-buffered saline (TBS) containing 0.2% Tween-20 (TBST). All antibodies used were solubilized (0.5–2.0 mg/mL) by manufacturers in buffered saline or culture supernatant containing 0.02–0.1% sodium azide (pH 7.2–7.6). Primary antibodies were diluted for overnight incubation of membranes at 4°C, and included total oxidative phosphorylation (OXPHOS) rodent antibody cocktail (1:2,000, 5% milk in TBST, MitoSciences, MS604), rabbit anti-SOD2 antibody (1:4,000, 5% milk in TBST; Proteintech, 24127-1-AP), rabbit anti-Cytochrome c antibody (1:2,000, 5% milk in TBST; Abcam, AB133504), mouse anti-VDAC-1/Porin antibody (1:2,000, 5% BSA in TBST, Abcam, AB14734), mouse anti-synaptophysin (1:3,000, 5% BSA in TBST; Sigma-Aldrich, MAB5258), rabbit anti-PSD95 (1:3,000, 5% milk in TBST; Abcam, AB18258), rabbit anti-choline acetylcholinesterase (1:1,000, 5% milk in TBST; Abcam, AB183591), rabbit anti-vesicular acetylcholine transporter (1:2,000, 5% milk in TBST; Abcam, AB235201), mouse anti-vinculin (1:4,000, 5% milk in TBST; Abcam, AB130007), and mouse anti-β-Actin (1:5,000, 5% BSA in TBST; Abcam, AB8226). Membranes were then washed 3 times for 5 min each in TBST and incubated at room temperature with either peroxidase-conjugated goat anti-mouse secondary antibody (1:4,000; Millipore Sigma, AP124P) or peroxidase-conjugated goat anti-rabbit secondary antibody (1:5,000; Millipore Sigma, AP132P) for 1–2 h. Immunoreactivity was detected using ECL Western blotting substrate (Thermo Fisher Scientific, 32106) and visualized using a CDP-STAR chemiluminescence system (Amersham hyperfilm ECL). All antibody signals were normalized against loading control (β-Actin or vinculin) immunoreactivity. Western blot data were compiled from six animals, and bands were quantified by densitometric analysis using Image-J software (version 1.41).

Data analysis

Results obtained from mitochondrial respiratory measurements were tested statistically using a two-tailed Student's *t*-test. Data from Western blot densitometry were analyzed using either two-tailed Student's *t*-tests or one-way analyses of variance (ANOVA) with Sidak's multiple comparisons tests. All data analyses were done using GraphPad Prism software version 8.0.1 with significance set at $p < 0.05$. Bar graphs indicate the mean and standard deviation, normalized to the largest control value in percentage (for protein analysis), and include plots showing values obtained from individual animals.

Results

Effects of hAβ_{1-42} on entorhinal mitochondrial function and integrity

During the pathogenesis of AD, the EC selectively accumulates neurotoxic Aβ and shows the earliest signs of oxidative impairment and neurodegeneration (Terni et al., 2010; Olajide et al., 2021), but the mechanisms involved are still unclear. We therefore examined the rapid effects of hAβ_{1-42} on mitochondrial functions in entorhinal tissue using high-resolution respirometry. Utilization of respiration substrates in entorhinal samples was significantly reduced by exposing brain slices to 1 μM hAβ_{1-42} for a period of 3 h (**Figure 1A1**). Relative to control, hAβ_{1-42} markedly reduced respiration in EC slices (in pmol/s/mg; n = 5–6) following the addition of glutamate (2.9 ± 1.2 vs. 5.6 ± 1.0 in controls; p = 0.0211), ADP (3.8 ± 3.3 vs. 20.2 ± 2.4; p = 0.0022), cytochrome c (4.2 ± 3.7 vs. 19.4 ± 2.7; p = 0.0036), succinate (13.7 ± 5.9 vs. 36.0 ± 4.7; p = 0.0045), and FCCP (11.7 ± 5.0 vs. 27.0 ± 4.0; p = 0.0070). However, incubation of EC slices with hAβ_{1-42} did not significantly alter the consumption of malate (0.7 ± 0.2 vs. 1.1 ± 0.5 in controls; p = 0.2427), and pyruvate (1.8 ± 1.2 vs. 3.5 ± 0.6; p = 0.0570). hAβ_{1-42} also markedly reduced the ratio between oxidation and phosphorylation which measures the efficiency of the mitochondria in generating ATP per given amount of oxygen, and is shown by assessments of the ACR (1.1 ± 0.6 vs. 3.6 ± 0.4 in controls; $p < 0.0001$; **Figure 1A2**).

10.3389/fnagi.2022.960314

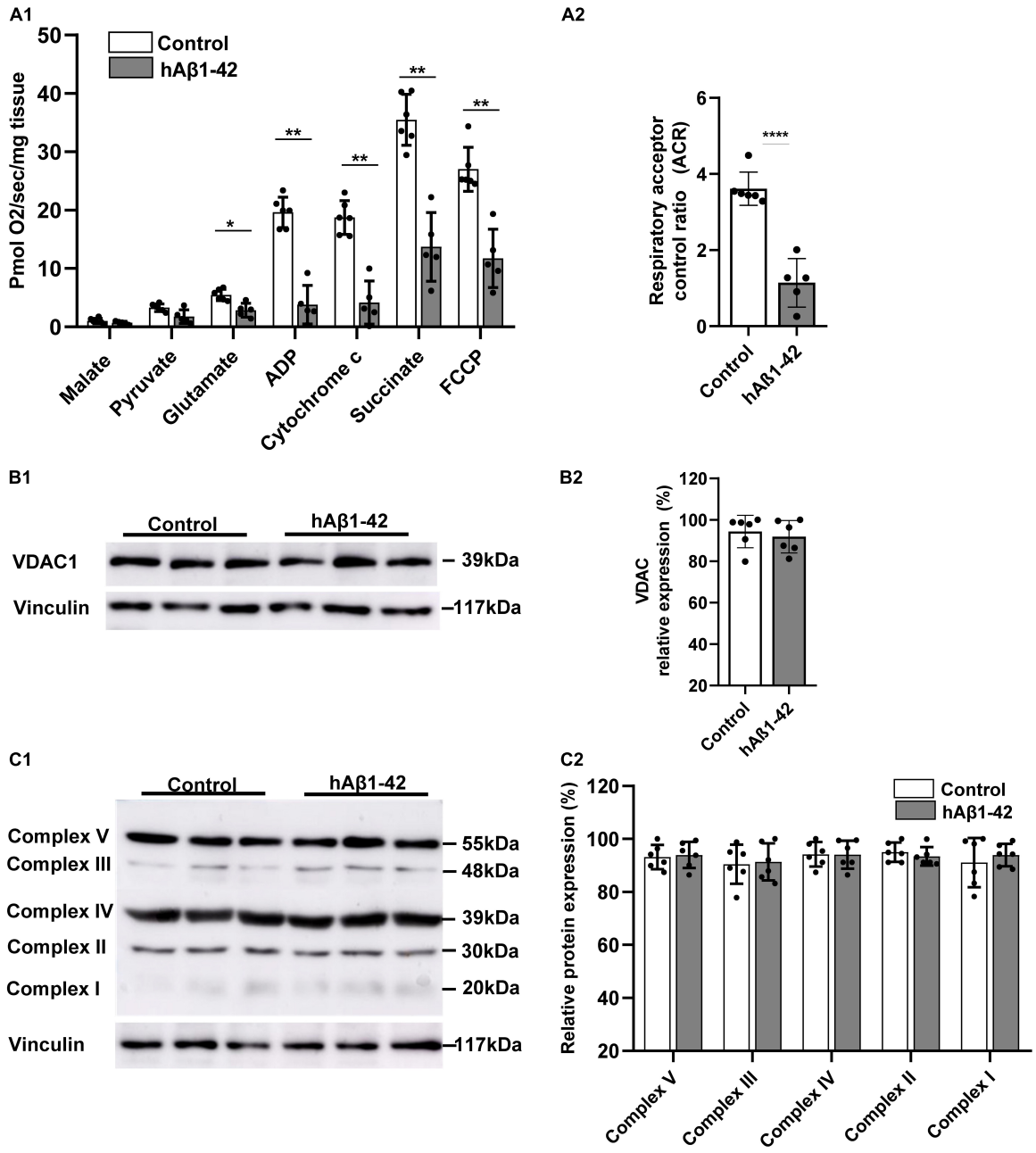

FIGURE 1
Impact of $hA\beta_{1-42}$ on mitochondrial respiration and function in the entorhinal cortex. **(A1)** Bar graphs represent mitochondrial substrate utilization in permeabilized entorhinal tissue previously treated with 1 μM $hA\beta_{1-42}$ for 3 h vs. control tissue, assessed through high-resolution respirometry (n = 5–6). **(A2)** Graph showing the acceptor control ratio (ACR) which measures the relative efficiency of phosphorylation and is determined by dividing ADP by glutamate average rates of respiration. $hA\beta_{1-42}$ treatment significantly reduced the ACR relative to control. **(B1)** Representative immunoblots of mitochondrial membrane and gatekeeper protein voltage-dependent anion channel 1 (VDAC1) and vinculin (loading control) in entorhinal lysates following incubation in control medium or $hA\beta_{1-42}$. **(B2)** Bar graphs showing the normalized protein expression of VDAC1 (n = 6). **(C1)** Representative immunoblots of mitochondrial complex I to V with total OXPHOS rodent antibody cocktail with vinculin serving as a loading control. **(C2)** Graphs showing normalized data for all five mitochondrial subunits in $hA\beta_{1-42}$-treated slices vs. the largest expression in the control group (n = 6) (*$p < 0.05$; **$p < 0.01$; ****$p < 0.0001$).

We next assessed the impact of $hA\beta_{1-42}$ on immunoexpression of markers for the integrity of the mitochondrial membrane and for the five mitochondrial protein complexes that make up the electron transport chain. Compared to control, $hA\beta_{1-42}$ treatment did not alter immunoblot expression of the mitochondrial membrane

and gatekeeper protein voltage-dependent anion channel 1 (VDAC1; 91.9 ± 7.3 vs. 94.3 ± 7.8 in controls; p = 0.6125) (Figure 1B). Similarly, immunoblotting of complexes I to V with total OXPHOS rodent antibody cocktail (Figure 1C) revealed no significant changes (n = 6) in protein expression between control and hAβ_{1-42}-treated entorhinal slices. When compared to control, hAβ_{1-42} (1 μM) treatment for 3 h did not alter the normalized protein expression of Complex V (93.2 ± 4.6 and 94.0 ± 5.0; p = 0.785), Complex III (90.5 ± 7.4 and 91.4 ± 7.0; p = 0.833), Complex IV (94.2 ± 4.6 and 94.1 ± 5.3; p = 0.961), Complex II (95.1 ± 3.6 and 93.4 ± 3.5; p = 0.560), and Complex I (91.1 ± 9.3 and 94.0 ± 4.3; p = 0.589) in entorhinal lysates. Therefore, although hAβ_{1-42} treatment reduces mitochondrial function as reflected in respirometry analysis, it did not significantly affect the expression of protein markers for mitochondrial integrity and for respiratory complexes.

hAβ_{1-42} reduces immunoexpression of mitochondrial enzymes, synaptophysin, postsynaptic density protein-95 and vesicular acetylcholine transporter

Our finding that hAβ_{1-42} rapidly impairs mitochondrial respiration in the EC suggests that a resulting oxidative redox imbalance, due to increased leakage of mitochondrial electrons and ROS formation, could have deleterious effects on the mitochondrial antioxidant system. We therefore characterized the expression of the mitochondrial oxidative scavenger enzyme SOD2, and both mitochondrial and cytosolic cytochrome c protein. Representative immunoblots and quantification data show that, compared to control, hAβ_{1-42} markedly reduced the relative expression of SOD2 (53.3 ± 14.0 vs. 90.4 ± 8.1 in controls; p = 0.0002) (Figure 2A). Mitochondrial cytochrome c expression was also reduced by application of hAβ_{1-42} (33.6 ± 17.2 vs. 86.0 ± 12.3 in controls; p = 0.0001), and this effect was specific to mitochondria because immunoexpression of cytosolic cytochrome c was not significantly affected (81.7 ± 13.6 vs. 89.6 ± 11.3 p = 0.298).

A reduction in the efficiency and energy production capacity of the mitochondrial electron transport chain, increased mitochondrial ROS, and oxidative stress could impact both pre- and post-synaptic elements, and we therefore evaluated the effects of hAβ_{1-42} on the presynaptic marker synaptophysin, and the postsynaptic density protein 95 (PSD95). We found that hAβ_{1-42}-induced mitochondrial dysregulation was accompanied by a marked reduction in relative immunoexpression of both PSD95 (91.9 ± 6.6 and 26.4 ± 11.3; $p < 0.0001$) and synaptophysin (87.5 ± 12.2 and 31.3 ± 21.8; p = 0.0003) (Figure 2B).

Reductions in cholinergic function in the EC is one of the earliest manifestations of AD (Hampel et al., 2018), and we therefore assessed the effects of hAβ_{1-42} on the expression of the vesicular acetylcholine transporter (VAChT) and the degradative enzyme acetylcholinesterase (AChE). Although hAβ_{1-42} did not cause a significant change in AChE immunoexpression when compared to control (97.4 ± 18.2 vs. 91.5 ± 8.7 in controls; p = 0.5433), hAβ_{1-42} markedly reduced the expression of VAChT in entorhinal lysates vs. control (60.0 ± 16.6 vs. 87.7 ± 12.7; p = 0.0312) (Figure 2C), suggesting a disruption in the function of cholinergic terminals in the EC.

Mitochondria-targeted antioxidant mitoquinone mesylate and EUK134 reduce hAβ_{1-42}-induced impairments in synaptic proteins

To determine if increased ROS associated with mitochondrial dysregulation is related to the reductions in mitochondrial enzymes and synaptic proteins induced by hAβ_{1-42}, we tested the ability of two novel, structurally distinct ROS scavengers (MitoQ and EUK134) to block protein reductions induced by hAβ_{1-42}. The mitochondria-targeted antioxidant MitoQ administered alone had no significant effect on the expression of mitochondrial enzymes, but was found to block changes in both SOD2 and mitochondrial cytochrome c induced by hAβ_{1-42} (compare Figure 3A and Figure 2A). There was no significant main effect of treatment on the relative expression of SOD2 between control slices (92.2 ± 6.4) and slices incubated with MitoQ alone (90.4 ± 15.6) or MitoQ with hAβ_{1-42} (88.7 ± 8.9) [$F_{(2,\ 15)}$ = 0.15, p = 0.8646]. Similarly, the expression of mitochondrial cytochrome c protein was not significantly different between control slices (90.7.0 ± 8.3) and slices treated with either MitoQ (94.5 ± 9.8) or MitoQ and hAβ_{1-42} (88.0 ± 11.4) [$F_{(2,\ 15)}$ = 0.65, p = 0.5355] (Figure 3A).

We then assessed if blocking excess ROS induced by hAβ_{1-42} using MitoQ would also block reductions in the immunoexpression of PSD95, synaptophysin, and the vesicular acetylcholine transporter (VChAT). The application of MitoQ had no effect alone, but it prevented reductions in all three proteins induced by hAβ_{1-42} (compare Figure 3B and Figures 2B,C). There were no significant main effects of treatment (n = 6) on the expression of PSD95 [$F_{(2,\ 15)}$ = 0.14, p = 0.8742], synaptophysin [$F_{(2,\ 15)}$ = 0.31, p = 0.7386], and VChAT [$F_{(2,\ 15)}$ = 1.66, p = 0.2226]. Preventing increases in ROS induced by hAβ_{1-42} can therefore prevent degradation of key synaptic proteins.

The idea that increases in mitochondrial ROS induced by hAβ_{1-42} mediate synaptic degeneration in entorhinal slices was further tested by determining if the synthetic SOD and catalase

10.3389/fnagi.2022.960314

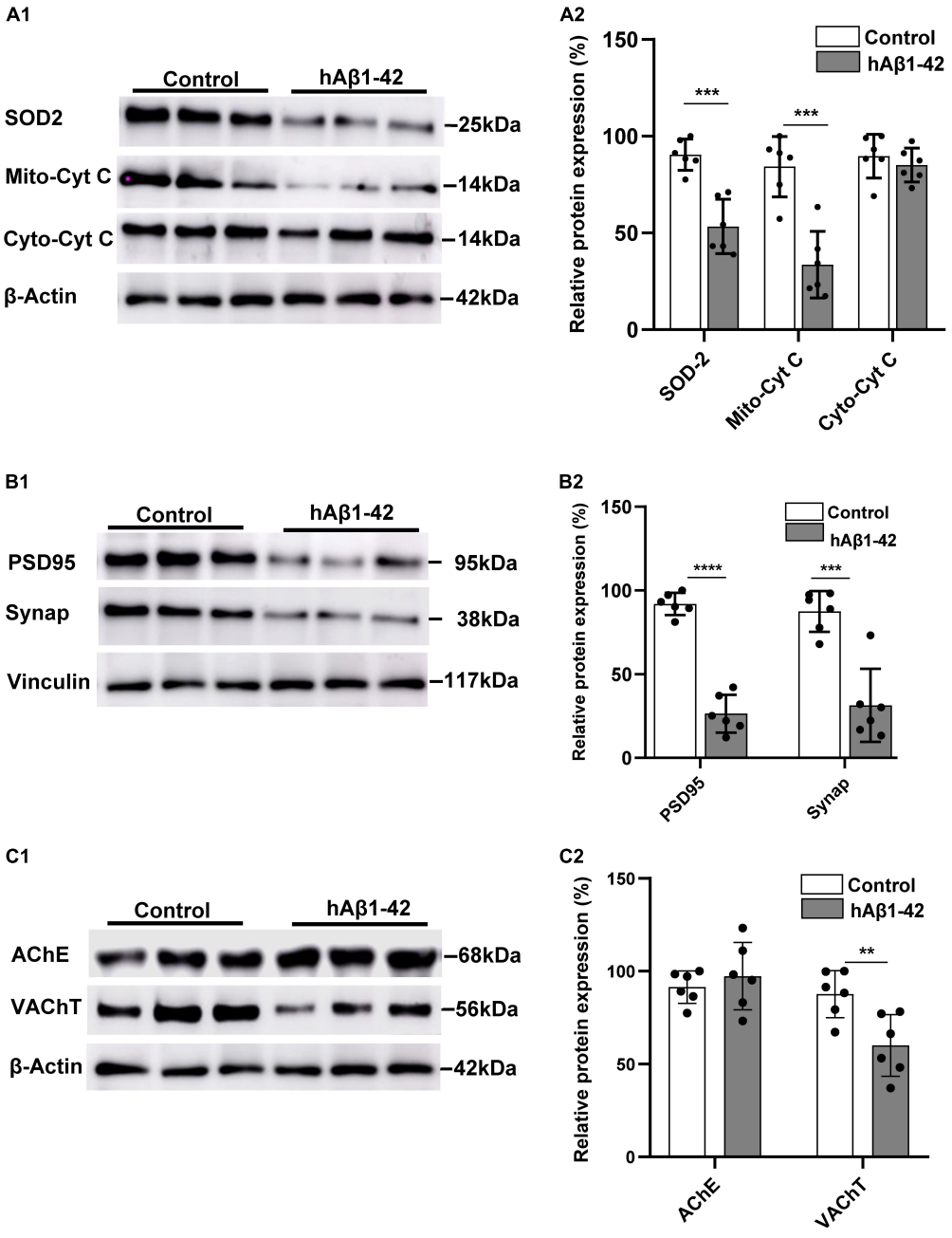

FIGURE 2
Effects of $hA\beta_{1-42}$ on key mitochondrial elements, synaptic proteins, and cholinergic markers in the entorhinal cortex. **(A1)** Representative immunoblots of mitochondrial superoxide dismutase 2 (SOD2), mitochondrial cytochrome c (Mito-cyt C), cytosolic cytochrome c (Cyto-cyt C), and β-actin loading control in entorhinal lysates treated with $hA\beta_{1-42}$ and control medium. **(A2)** Normalized expression of SOD2, Mito-cyt C, and Cyto-cyt C in $hA\beta_{1-42}$-treated entorhinal samples compared to control (n = 6). **(B1)** Representative immunoblots of postsynaptic density protein (PSD95), presynaptic marker synaptophysin (Synap), and vinculin loading control in entorhinal lysates. **(B2)** Quantification data showing the normalized expression of both PSD95 and Synap in slices incubated with $hA\beta_{1-42}$ vs. control (n = 6). **(C1)** Representative immunoblots of cholinergic markers acetylcholinesterase (AChE), vesicular acetylcholine transporter (VAChT), and β-actin (loading control). **(C)** Bar graphs showing normalized expression of AChE and VAChT in $hA\beta_{1-42}$–treated slices and control (n = 6) (**$p < 0.01$; ***$p < 0.005$; ****$p < 0.0001$).

mimetic EUK134 could block the reductions in synaptic and mitochondrial proteins induced by $hA\beta_{1-42}$. Application of EUK134 blocked reductions in both SOD2 and mitochondrial cytochrome c induced by $hA\beta_{1-42}$ (compare Figure 4A and Figure 2A), and there were no significant main effects of treatment with EUK134, or with EUK134 and $hA\beta_{1-42}$, (n = 6),

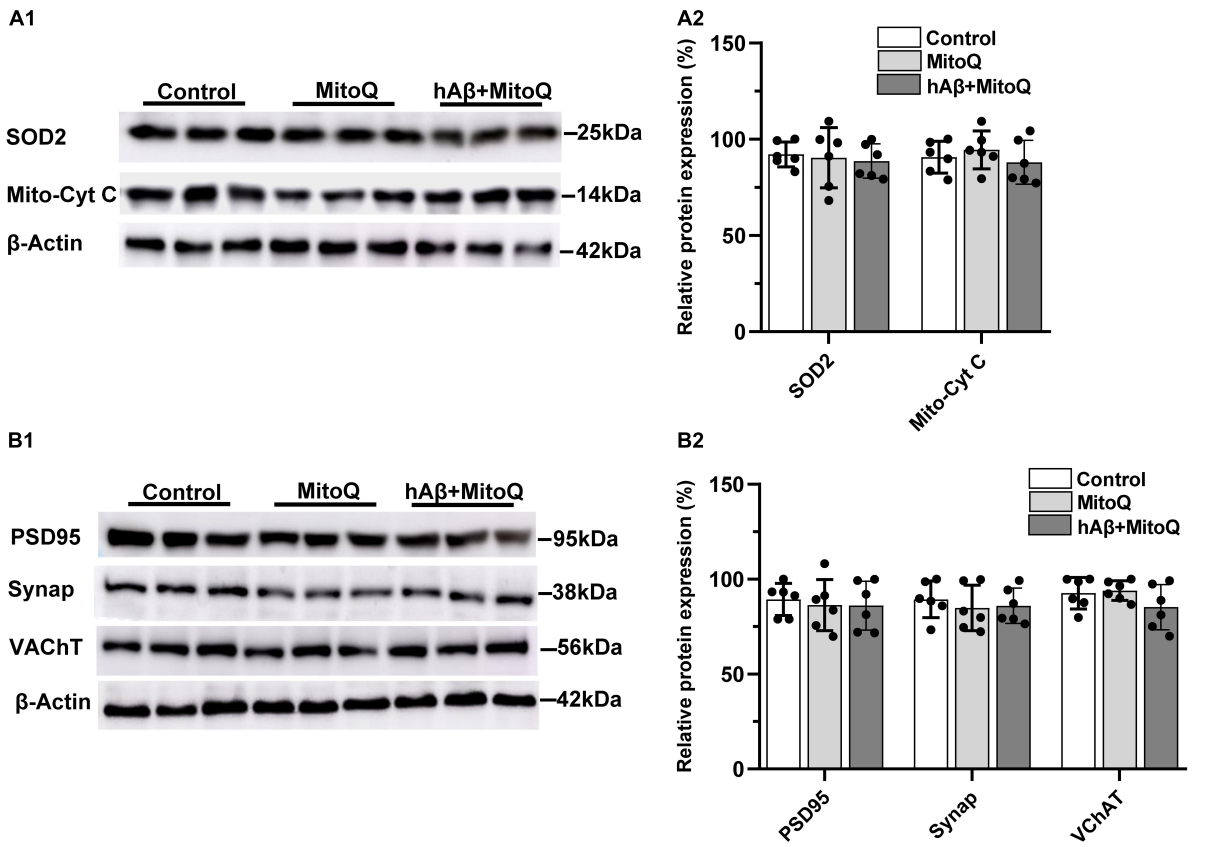

FIGURE 3
Inhibiting increases in reactive oxygen species with MitoQ prevents $hA\beta_{1-42}$-induced changes in mitochondrial and synaptic proteins. **(A1)** Representative immunoblots of superoxide dismutase 2 (SOD2), mitochondrial cytochrome c (Mito-cyt C), and the loading control β-Actin, are shown in slices treated with MitoQ, $hA\beta_{1-42}$ with MitoQ, and control. **(A2)** Normalized relative expression of SOD2 and Mito-cyt C proteins (n = 6). **(B1)** Representative immunoblots of postsynaptic density protein PSD95, presynaptic marker synaptophysin (Synap.), vesicular acetylcholine transporter (VAChT), and the loading control β-Actin are shown in tissue treated with MitoQ, $hA\beta_{1-42}$ with MitoQ, and control. Bar graphs indicate normalized relative expression of PSD95, Synap., and VAChT **(B2)**.

on the relative expression of SOD2 [$F_{(2,\ 15)} = 0.95$, $p = 0.4084$] or mitochondrial cytochrome c [$F_{(2,\ 15)} = 0.61$, $p = 0.5578$].

We also found that EUK134 rescued $hA\beta_{1-42}$-induced reductions in immunoexpression of PSD95 and VChAT, and partially rescued $hA\beta_{1-42}$-induced reductions in the presynaptic protein synaptophysin (compare **Figure 4B** and **Figures 2B,C**). There was no significant effect of treatment with EUK134 or EUK134 and $hA\beta_{1-42}$ on the relative expression of PSD95 [$F_{(2,\ 15)} = 0.04$, $p = 0.9650$] and VChAT [$F_{(2,\ 15)} = 2.83$, $p = 0.0905$]. There was, however, a significant main effect of treatment on synaptophysin immunoexpression [$F_{(2,\ 15)} = 4.44$, $p = 0.0305$] in which the expression of synaptophysin was significantly reduced in slices treated with EUK134 + $hA\beta_{1-42}$ relative to control slices (69.8 ± 21.6 vs. 92.7 ± 5.7 in controls; $p = 0.0480$), but not relative to slices treated with EUK134 alone (90.4 ± 12.1; $p = 0.0811$). The mean expression of synaptophysin following treatment with $hA\beta_{1-42}$ in the presence of EUK134 (69.8 ± 21.6) was greater than that following treatment with $hA\beta_{1-42}$ alone (31.3 ± 21.8; **Figure 2B**), however, suggesting that EUK134 was partially protective in preventing reductions in synaptophysin. These findings suggest that $hA\beta_{1-42}$-induced rapid synaptic impairments in entorhinal tissue can be significantly rescued by inhibiting mitochondrial ROS levels.

Discussion

A previous report from our lab has shown that $hA\beta_{1-42}$ causes rapid degeneration of presynaptic and postsynaptic elements in the EC through activation of GluN2A- and GluN2B-containing NMDA glutamate receptors (Olajide and Chapman, 2021). The selective vulnerability of the EC to early AD-related synaptic damage and neurodegeneration (Du et al., 2004; Velayudhan et al., 2013; Zhou et al., 2016), may reflect the dysregulation of neural mechanisms including NMDA glutamate receptors that contribute to learning and memory (Olajide et al., 2021). Aβ can accumulate in mitochondria where

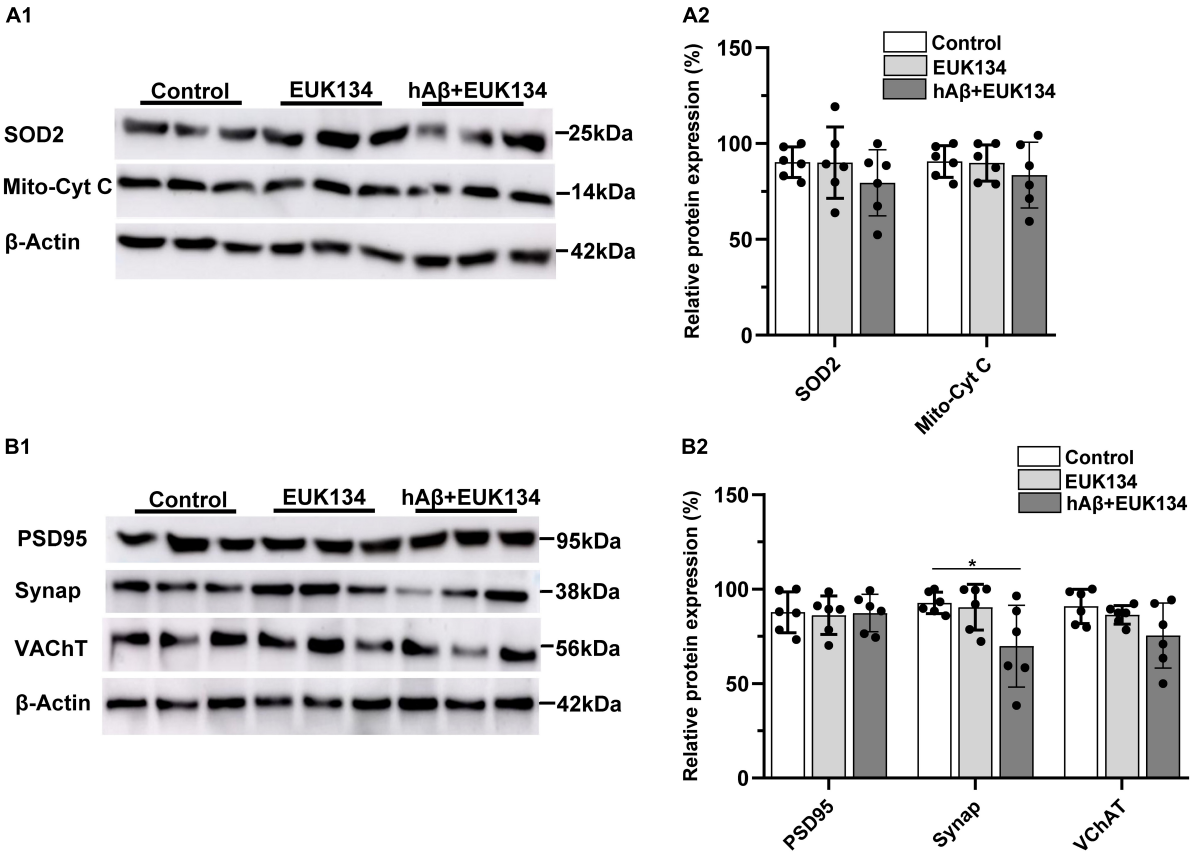

FIGURE 4
Inhibiting increases in reactive oxygen species with EUK134 prevents $hA\beta_{1-42}$-induced changes in mitochondrial and synaptic proteins. **(A1)** Representative immunoblots of superoxide dismutase 2 (SOD2), mitochondrial cytochrome c (Mito-cyt C), and the loading control β-Actin, are shown in slices treated with EUK134, $hA\beta_{1-42}$ with EUK134, and control. **(A2)** Normalized relative expression of SOD2 and Mito-cyt C proteins (n = 6). **(B1)** Representative immunoblots of postsynaptic density protein PSD95, presynaptic marker synaptophysin (Synap.), vesicular acetylcholine transporter (VAChT), and the loading control β-Actin are shown for tissue treated with EUK134, $hA\beta_{1-42}$ with EUK134, and control. Bar graphs indicate normalized relative expression of PSD95, Synap., and VAChT **(B2)** (*$p < 0.05$).

it impairs mitochondrial dynamics and upregulates oxidative stress by impairing mitochondrial respiratory function and the production of adenosine triphosphate (ATP) (Wang et al., 2014, 2020; Ashleigh et al., 2022). Further, activation of NMDA receptors by $hA\beta_{1-42}$ can lead to increases in calcium influx, the rapid facilitation of AMPA glutamate receptor responses, and hyperexcitability that increases metabolic demands on mitochondria, ultimately culminating in oxidative stress and synaptic dysfunction (Findley et al., 2019; Guo et al., 2020; Wang et al., 2020). We have found here that exposure to 1 μM $hA\beta_{1-42}$ for a period of 3 h markedly reduces mitochondrial respiratory function and integrity in the EC. Further, the resulting increase in ROS appears to be a major driver of the rapid degeneration of both pre- and post-synaptic proteins in the EC because the ROS scavengers Mito-Q and EUK134 strongly inhibited reductions in synaptophysin and PSD-95. The reductions in synaptic proteins observed here imply a reduction in number of synapses, but it is not clear if this would be expressed following this relatively brief application of $hA\beta_{1-42}$. However, these results point to a major role of mitochondrial dysregulation in the synaptic degeneration induced by $hA\beta_{1-42}$, which may contribute to the early progression of AD in the EC (Olajide et al., 2021). The present results may reflect mitochondrial dysfunction in glia as well as neurons, and mitochondrial dysfunction in glia is also thought to be a major contributor to the progression of AD (Mulica et al., 2021).

In our experimental model we have applied moderate concentrations of Aβ to wildtype slices for 3 h, but the progression of AD involves circulation of lower concentrations of Aβ over greatly extended periods of time. Although our model may reflect degenerative mechanisms that are expressed early in the progression of AD, and reflect the early selective vulnerability of the EC to Aβ toxicity (Olajide et al., 2021), the changes in mitochondrial function and synaptic proteins that we have observed might also occur in later stages of AD after prolonged exposure to lower concentrations of Aβ.

Human $A\beta_{1-42}$ impairs mitochondrial respiration and function in the entorhinal cortex

We have found here that $hA\beta_{1-42}$ markedly reduces mitochondrial-coupled oxygen consumption, and functional membrane integrity as reflected by oxygen use in the presence of cytochrome c. High-resolution respirometry showed no significant changes in non-phosphorylating LEAK respiration during the addition of the Complex I-linked substrates malate, pyruvate or glutamate, but the OXPHOS capacity of Complex I-linked activity was markedly reduced by $hA\beta_{1-42}$, as shown by the approximately fivefold reduction in oxygen utilization during the addition of ADP. Exposure to $hA\beta_{1-42}$ also impaired the function of Complex II, because the addition of succinate, which reflects the combined OXPHOS capacity of Complex I and Complex II, was also significantly reduced. The rapid defects in mitochondrial-related metabolic pathways provide direct evidence that impaired bioenergetic machinery in mitochondria is an early driver of AD-related pathology in the EC. Similarly, OXPHOS and associated pathways are significantly downregulated within the hippocampus during AD, and reductions in Complex I, III, and IV of OXPHOS have been reported in both early and definite AD brains (Manczak et al., 2004; Brooks et al., 2007).

Further, the indication that $hA\beta_{1-42}$-induced impairments in entorhinal electron transport chain complexes can dysregulate bioenergetics is corroborated by our findings that the efficiency of the link between oxidation and the production of ATP by phosphorylation of ADP was reduced by $hA\beta_{1-42}$, as reflected by both reductions in the uncoupling capacity of the mitochondria during the addition of FCCP, and by a reduction in the ACR. The ACR expresses the rate of oxygen consumption during ADP phosphorylation relative to the rate of non-phosphorylating LEAK-respiration induced by glutamate. Our data corresponds with several reports indicating a large and consistent decline in mitochondrial substrate utilization and energy production in the neocortex during the prodromal stages of AD (Croteau et al., 2018; Wang et al., 2020), suggesting that mitochondrial bioenergetics dysfunction plays an early role in the pathogenesis of AD in the EC.

Mitochondrial cytochrome c transfers electrons to complex IV in the electron transport chain which is the primary site of cellular oxygen consumption (Timón-Gómez et al., 2018). We found that $hA\beta_{1-42}$ caused about a 2.5-fold reduction in mitochondrial cytochrome c function, suggesting alterations to the mitochondrial membrane in entorhinal tissue. We further found that, although total cytoplasmic cytochrome c protein expression was unaffected, the expression of mitochondrial cytochrome c was greatly reduced by treatment with $hA\beta_{1-42}$. An increase in cytosolic cytochrome c could be expected from previous work showing that Aβ can activate intrinsic apoptotic pathways and the release of mitochondrial cytochrome c into the cytosol (Kim et al., 2014), but the lack of an increase in cytosolic cytochrome c in the present study may be due to the relatively brief duration of exposure to Aβ. Deficiency of cytochrome c oxidase (Complex IV) is the most common defect in the mitochondrial electron transport chain in AD, leading to an increase in ROS production, a decrease in energy stores, and a disruption of energy metabolism (Rak et al., 2016). We found a marked reduction in the expression of SOD2, a key antioxidant enzyme that scavenges superoxide in mitochondria, and this is consistent with a rapid increase in mitochondrial ROS production induced by $hA\beta_{1-42}$ that depletes the energy metabolism machinery in the EC.

Although $hA\beta_{1-42}$ significantly reduced respiration and bioenergetics, it did not alter the expression of protein markers for the five mitochondrial Complexes or the expression of the mitochondrial voltage-dependent anion channel 1 (VDAC1). VDAC1 is the most abundant protein on the outer membrane of mitochondria, and it serves as a gatekeeper for the passage of metabolites, and is crucial for the metabolic functions of mitochondria (Camara et al., 2017). It is well established that the expression of mitochondrial proteins and genes are among the most prominent changes in the cortex during AD (Cottrell et al., 2001; Valla et al., 2001; Minjarez et al., 2016; Adav et al., 2019), and the lack of a significant effect of $hA\beta_{1-42}$ on the expression of mitochondrial complex proteins observed here may reflect the resistance of these proteins to rapid degradation over the relativity short incubation time.

Preventing increases in reactive oxygen species inhibits $hA\beta_{1-42}$-induced synaptic changes

Reductions in synaptic proteins induced by $hA\beta_{1-42}$ are likely to have resulted from increased ROS and oxidative stress in entorhinal neurons. Incubation in $hA\beta_{1-42}$ resulted in a marked reduction in SOD2, which is the primary antioxidant enzyme that scavenges superoxide in mitochondria, suggesting that SOD2 may have been depleted due to increases in ROS and overwhelming activity-dependent utilization of SOD2. The reduction in SOD2 may have further impaired ROS scavenging in entorhinal neurons thereby exacerbating oxidative damage and a loss of mitochondrial cytochrome c function. Excessive ROS and oxidative stress have been extensively linked to synaptic loss associated with aging and AD (Patten et al., 2010; Tönnies and Trushina, 2017; Guo et al., 2020), and increases in ROS associated with mitochondrial dysfunction that exceed the scavenging ability of entorhinal neurons is likely to have contributed to the observed loss of synaptic proteins. Consistent with our previous findings in the EC (Olajide and Chapman, 2021), both the presynaptic marker

synaptophysin and the postsynaptic marker PSD-95, were reduced by $hA\beta_{1-42}$.

The degeneration of cholinergic terminals in the EC is one of the earliest neuropathologies in AD (Francis et al., 1999; Gil-Bea et al., 2005; Hamam et al., 2007; Schaeffer and Gattaz, 2008). Although we found that the degradative enzyme acetylcholinesterase was not affected by $hA\beta_{1-42}$, we did observe a reduction in the vesicular acetylcholine transporter (VAChT), suggesting a reduced function in cholinergic terminals. Several other reports have also shown marked reductions in the expression of VAChT following Aβ infusion in rats and in AD models (Ikeda et al., 2000; Pákáski and Kálmán, 2008; Schliebs and Arendt, 2011; Hampel et al., 2018).

ROS-mediated oxidative stress is thought to have a major role in synaptic dysregulation and neurodegeneration in AD, and various antioxidants, and the genetic overexpression of SOD2, have been explored as therapeutic strategies for AD (Dumont et al., 2009; Massaad et al., 2009; Bonda et al., 2010; Olajide et al., 2017a,b, 2018; Tönnies and Trushina, 2017; Misrani et al., 2021). We co-incubated slices with $hA\beta_{1-42}$ and the ROS inhibitors MitoQ or EUK134 to determine if reducing oxidative stress could prevent the degeneration of synaptic proteins in the EC. Both MitoQ and EUK134 inhibited $hA\beta_{1-42}$-induced reductions in both SOD2 and mitochondrial cytochrome c, likely by maintaining a sufficient ROS scavenging capacity in entorhinal neurons and preventing overwhelming demands on SOD2. In addition, co-incubation with MitoQ blocked $hA\beta_{1-42}$-induced decreases in synaptophysin, PSD-95, and VAChT, indicating that oxidative stress arising from insufficient mitochondrial capacity can drive degeneration of these synaptic proteins. Similarly, the ROS inhibitor EUK134 prevented reductions in PSD-95 and VAChT, and greatly attenuated reductions in synaptophysin induced by $hA\beta_{1-42}$. Others have also found that decreasing ROS using MitoQ and EUK134 can prevent synaptic degeneration induced by oxidative stress in cortical and hippocampal neurons (Ma et al., 2011; Mcmanus et al., 2011; Reddy et al., 2012; Sanmartín et al., 2017; Yu et al., 2018; Cenini and Voos, 2019). These studies suggest that the protective effect of ROS inhibition that we have observed following acute application of $hA\beta_{1-42}$ to wildtype slices might be similarly protective for the advancement of neurodegeneration in more chronic models of AD.

Conclusion

Mitochondrial dysfunction resulting in increased ROS production and oxidative stress precedes the formation of neuritic plaques and neurofibrillary tangles, and is thought to contribute substantially to the earliest stages of AD and the onset of cognitive decline and memory loss (Uttara et al., 2009; Wang et al., 2014; Tönnies and Trushina, 2017; Ashleigh et al., 2022). We have shown here that short-term exposure of wild-type EC slices to $hA\beta_{1-42}$ results in deficits in mitochondrial respiration, and have provided evidence that oxidative stress associated with increased ROS is a major factor in the rapid degeneration of key pre- and post-synaptic proteins in the EC. Further, these mechanisms may be a major contributor to the reduction in cholinergic transmission in the EC, which is an early pathology thought to contribute to cognitive decline.

Data availability statement

The raw data supporting the conclusions of this article will be made available by the authors, without undue reservation.

Ethics statement

The animal study was reviewed and approved by Animal Research Ethics Committee, Concordia University.

Author contributions

OO, AB, and CC contributed to conception and design of the study. OO, AB, and CL acquired and analyzed the data. OO wrote the first draft of the manuscript. All authors contributed to manuscript revision and approved the submitted version.

Funding

This research was funded by the Natural Sciences and Engineering Research Council of Canada to CC and AB and the Merit Scholarship to OO from the Fonds de Recherché du Quebec–Nature et Technologies.

Conflict of interest

The authors declare that the research was conducted in the absence of any commercial or financial relationships that could be construed as a potential conflict of interest.

Publisher's note

References

Adav, S. S., Park, J. E., and Sze, S. K. (2019). Quantitative profiling brain proteomes revealed mitochondrial dysfunction in Alzheimer's disease. *Mol. Brain* 12:8. doi: 10.1186/S13041-019-0430-Y/FIGURES/6

Akhter, F., Chen, D., Yan, S. F., and Yan, S. S. (2017). Mitochondrial perturbation in Alzheimer's disease and diabetes. *Prog. Mol. Biol. Transl. Sci.* 146, 341–361. doi: 10.1016/bs.pmbts.2016.12.019

Armand-Ugon, M., Ansoleaga, B., Berjaoui, S., and Ferrer, I. (2017). Reduced mitochondrial activity is early and steady in the entorhinal cortex but it is mainly unmodified in the frontal cortex in Alzheimer's disease. *Curr. Alzheimer Res.* 14, 1327–1334. doi: 10.2174/1567205014666170505095921

Arendt, T. (2009). Synaptic degeneration in Alzheimer's disease. *Acta Neuropathol.* 118, 167–179. doi: 10.1007/s00401-009-0536-x

Ashleigh, T., Swerdlow, R. H., and Beal, M. F. (2022). The role of mitochondrial dysfunction in Alzheimer's disease pathogenesis. *Alzheimers Dement*. doi: 10.1002/alz.12683

Bitan, G., Vollers, S. S., and Teplow, D. B. (2003). Elucidation of primary structure elements controlling early amyloid β-protein oligomerization. *J. Biol. Chem.* 278, 34882–34889. doi: 10.1074/jbc.M300825200

Bonda, D. J., Wang, X., Perry, G., Nunomura, A., Tabaton, M., Zhu, X., et al. (2010). Oxidative stress in Alzheimer disease: A possibility for prevention. *Neuropharmacology* 59, 290–294. doi: 10.1016/j.neuropharm.2010.04.005

Brooks, W. M., Lynch, P. J., Ingle, C. C., Hatton, A., Emson, P. C., Faull, R. L. M., et al. (2007). Gene expression profiles of metabolic enzyme transcripts in Alzheimer's disease. *Brain Res.* 1127, 127–135. doi: 10.1016/J.BRAINRES.2006.09.106

Calkins, M. J., Manczak, M., Mao, P., Shirendeb, U., and Reddy, P. H. (2011). Impaired mitochondrial biogenesis, defective axonal transport of mitochondria, abnormal mitochondrial dynamics and synaptic degeneration in a mouse model of Alzheimer's disease. *Hum. Mol. Genet.* 20, 4515–4529. doi: 10.1093/hmg/ddr381

Camara, A. K. S., Zhou, Y. F., Wen, P. C., Tajkhorshid, E., and Kwok, W. M. (2017). Mitochondrial VDAC1: A key gatekeeper as potential therapeutic target. *Front. Physiol.* 8:460. doi: 10.3389/FPHYS.2017.00460/BIBTEX

Cavallucci, V., Ferraina, C., and D'Amelio, M. (2013). Key role of mitochondria in Alzheimer's disease synaptic dysfunction. *Curr. Pharm. Des.* 19, 6440–6450. doi: 10.2174/1381612811319360005

Cenini, G., and Voos, W. (2019). Mitochondria as potential targets in Alzheimer disease therapy: An update. *Front. Pharmacol.* 10:902. doi: 10.3389/FPHAR.2019.00902/BIBTEX

Coleman, P. D., and Yao, P. J. (2003). Synaptic slaughter in Alzheimer's disease. *Neurobiol. Aging* 24, 1023–1027. doi: 10.1016/j.neurobiolaging.2003.09.001

Cottrell, D. A., Blakely, E. L., Johnson, M. A., Ince, P. G., and Turnbull, D. M. (2001). Mitochondrial enzyme-deficient hippocampal neurons and choroidal cells in AD. *Neurology* 57, 260–264. doi: 10.1212/WNL.57.2.260

Croteau, E., Castellano, C. A., Fortier, M., Bocti, C., Fulop, T., Paquet, N., et al. (2018). A cross-sectional comparison of brain glucose and ketone metabolism in cognitively healthy older adults, mild cognitive impairment and early Alzheimer's disease. *Exp. Gerontol.* 107, 18–26. doi: 10.1016/J.EXGER.2017.07.004

Du, A. T., Schuff, N., Kramer, J. H., Ganzer, S., Zhu, X. P., Jagust, W. J., et al. (2004). Higher atrophy rate of entorhinal cortex than *Hippocampus* in AD. *Neurology* 62, 422–427. doi: 10.1212/01.WNL.0000106462.72282.90

Dumont, M., Wille, E., Stack, C., Calingasan, N. Y., Beal, M. F., and Lin, M. T. (2009). Reduction of oxidative stress, amyloid deposition, and memory deficit by manganese superoxide dismutase overexpression in a transgenic mouse model of Alzheimer's disease. *FASEB J.* 23, 2459–2466. doi: 10.1096/FJ.09-132928

Esposito, L., Raber, J., Kekonius, L., Yan, F., Yu, G. Q., Bien-Ly, N., et al. (2006). Reduction in mitochondrial superoxide dismutase modulates Alzheimer's disease-like pathology and accelerates the onset of behavioral changes in human amyloid precursor protein transgenic mice. *J. Neurosci.* 26, 5167–5179. doi: 10.1523/JNEUROSCI.0482-06.2006

Fan, L., Mao, C., Hu, X., Zhang, S., Yang, Z., Hu, Z., et al. (2020). New insights into the pathogenesis of Alzheimer's disease. *Front. Neurol.* 10:1312. doi: 10.3389/fneur.2019.01312

Findley, C. A., Bartke, A., Hascup, K. N., and Hascup, E. R. (2019). Amyloid beta-related alterations to glutamate signaling dynamics during Alzheimer's disease progression. *ASN Neuro* 11:1759091419855541. doi: 10.1177/1759091419855541

Francis, P. T., Palmer, A. M., Snape, M., and Wilcock, G. K. (1999). The cholinergic hypothesis of Alzheimer's disease: A review of progress. *J. Neurol. Neurosurg. Psychiatry* 66, 137–147. doi: 10.1136/jnnp.66.2.137

Gil-Bea, F. J., García-Alloza, M., Domínguez, J., Marcos, B., and Ramírez, M. J. (2005). Evaluation of cholinergic markers in Alzheimer's disease and in a model of cholinergic deficit. *Neurosci. Lett.* 375, 37–41. doi: 10.1016/j.neulet.2004.10.062

Glovaci, I., and Chapman, C. A. (2019). Dopamine induces release of calcium from internal stores in layer II lateral entorhinal cortex fan cells. *Cell Calcium* 80, 103–111. doi: 10.1016/j.ceca.2019.04.003

Grubman, A., Chew, G., Ouyang, J. F., Sun, G., Choo, X. Y., McLean, C., et al. (2019). A single-cell atlas of entorhinal cortex from individuals with Alzheimer's disease reveals cell-type-specific gene expression regulation. *Nat. Neurosci.* 22, 2087–2097. doi: 10.1038/s41593-019-0539-4

Guo, T., Zhang, D., Zeng, Y., Huang, T. Y., Xu, H., and Zhao, Y. (2020). Molecular and cellular mechanisms underlying the pathogenesis of Alzheimer's disease. *Mol. Neurodegener.* 15:40. doi: 10.1186/s13024-020-00391-7

Haass, C., and Selkoe, D. J. (2007). Soluble protein oligomers in neurodegeneration: Lessons from the Alzheimer's amyloid β-peptide. *Nat. Rev. Mol. Cell Biol.* 8, 101–112. doi: 10.1038/nrm2101

Hamam, B. N., Sinai, M., Poirier, G., and Chapman, C. A. (2007). Cholinergic suppression of excitatory synaptic responses in layer II of the medial entorhinal cortex. *Hippocampus* 17, 103–113. doi: 10.1002/hipo.20249

Hampel, H., Hardy, J., Blennow, K., Chen, C., Perry, G., Kim, S. H., et al. (2021). The amyloid-β pathway in Alzheimer's disease. *Mol. Psychiatry* 26, 5481–5503. doi: 10.1038/s41380-021-01249-0

Hampel, H., Mesulam, M. M., Cuello, A. C., Farlow, M. R., Giacobini, E., Grossberg, G. T., et al. (2018). The cholinergic system in the pathophysiology and treatment of Alzheimer's disease. *Brain* 141, 1917–1933. doi: 10.1093/brain/awy132

Ikeda, E., Shiba, K., Mori, H., Ichikawa, A., Sumiya, H., Kuji, I., et al. (2000). Reduction of vesicular acetylcholine transporter in beta-amyloid protein-infused rats with memory impairment. *Nucl. Med. Commun.* 21, 933–937. doi: 10.1097/00006231-200010000-00007

Ionescu-Tucker, A., and Cotman, C. W. (2021). Emerging roles of oxidative stress in brain aging and Alzheimer's disease. *Neurobiol. Aging* 107, 86–95. doi: 10.1016/J.NEUROBIOLAGING.2021.07.014

Khan, U. A., Liu, L., Provenzano, F. A., Berman, D. E., Profaci, C. P., Sloan, R., et al. (2014). Molecular drivers and cortical spread of lateral entorhinal cortex dysfunction in preclinical Alzheimer's disease. *Nat. Neurosci.* 17, 304–311. doi: 10.1038/nn.3606

Khosravi, S., and Harner, M. E. (2020). The MICOS complex, a structural element of mitochondria with versatile functions. *Biol. Chem.* 401, 765–778. doi: 10.1515/hsz-2020-0103

Kim, J., Yang, Y., Song, S. S., Na, J. H., Oh, K. J., Jeong, C., et al. (2014). Beta-amyloid oligomers activate apoptotic BAK pore for cytochrome c release. *Biophys. J.* 107, 1601–1608. doi: 10.1016/j.bpj.2014.07.074

Li, F., Calingasan, N. Y., Yu, F., Mauck, W. M., Toidze, M., Almeida, C. G., et al. (2004). Increased plaque burden in brains of APP mutant MnSOD heterozygous knockout mice. *J. Neurochem.* 89, 1308–1312. doi: 10.1111/J.1471-4159.2004.02455.X

Ma, T., Hoeffer, C. A., Wong, H., Massaad, C. A., Zhou, P., Iadecola, C., et al. (2011). Amyloid β-induced impairments in hippocampal synaptic plasticity are rescued by decreasing mitochondrial superoxide. *J. Neurosci.* 31, 5589–5595. doi: 10.1523/JNEUROSCI.6566-10.2011

Manczak, M., Park, B. S., Jung, Y., and Reddy, P. H. (2004). Differential expression of oxidative phosphorylation genes in patients with Alzheimer's disease: Implications for early mitochondrial dysfunction and oxidative damage. *Neuromolecular Med.* 5, 147–162. doi: 10.1385/NMM

Marsh, J., and Alifragis, P. (2018). Synaptic dysfunction in Alzheimer's disease: The effects of amyloid beta on synaptic vesicle dynamics as a novel target for therapeutic intervention. *Neural Regen. Res.* 13, 616–623. doi: 10.4103/1673-5374.230276

Massaad, C. A., Washington, T. M., Pautler, R. G., and Klann, E. (2009). Overexpression of SOD-2 reduces hippocampal superoxide and prevents memory deficits in a mouse model of Alzheimer's disease. *Proc. Natl. Acad. Sci. U.S.A.* 106:13576. doi: 10.1073/PNAS.0902714106

Masters, C. L., and Selkoe, D. J. (2012). Biochemistry of amyloid β-protein and amyloid deposits in Alzheimer disease. *Cold Spring Harb. Perspect. Med.* 2:a006262. doi: 10.1101/cshperspect.a006262

Mcmanus, M. J., Murphy, M. P., and Franklin, J. L. (2011). The mitochondria-targeted antioxidant mitoq prevents loss of spatial memory retention and early neuropathology in a transgenic mouse model of Alzheimer's disease. *J. Neurosci.* 31:15703. doi: 10.1523/JNEUROSCI.0552-11.2011

Minjarez, B., Calderón-González, K. G., Rustarazo, M. L. V., Herrera-Aguirre, M. E., Labra-Barrios, M. L., Rincon-Limas, D. E., et al. (2016). Identification of proteins that are differentially expressed in brains with Alzheimer's disease using iTRAQ labeling and tandem mass spectrometry. *J. Proteom.* 139, 103–121. doi: 10.1016/J.JPROT.2016.03.022

Misrani, A., Tabassum, S., and Yang, L. (2021). Mitochondrial dysfunction and oxidative stress in Alzheimer's disease. *Front. Aging Neurosci.* 13:57. doi: 10.3389/FNAGI.2021.617588/BIBTEX

Mucke, L., and Selkoe, D. J. (2012). Neurotoxicity of amyloid β-protein: Synaptic and network dysfunction. *Cold Spring Harb. Perspect. Med.* 2:a006262. doi: 10.1101/cshperspect.a006338

Mulica, P., Grünewald, A., and Pereira, S. L. (2021). Astrocyte-neuron metabolic crosstalk in neurodegeneration: A mitochondrial perspective. *Front. Endocrinol.* 12:668517. doi: 10.3389/fendo.2021.668517

Murphy, M. P. (2009). How mitochondria produce reactive oxygen species. *Biochem J.* 417, 1–13. doi: 10.1042/BJ20081386

Nunomura, A., Perry, G., Aliev, G., Hirai, K., Takeda, A., Balraj, E. K., et al. (2001). Oxidative damage is the earliest event in Alzheimer disease. *J. Neuropathol. Exp. Neurol.* 60, 759–767. doi: 10.1093/JNEN/60.8.759

Olajide, O. J., and Chapman, C. A. (2021). Amyloid-β (1-42) peptide induces rapid NMDA receptor-dependent alterations at glutamatergic synapses in the entorhinal cortex. *Neurobiol. Aging* 105, 296–309. doi: 10.1016/J.NEUROBIOLAGING.2021.05.006

Olajide, O. J., Asogwa, N. T., Moses, B. O., and Oyegbola, C. B. (2017a). Multidirectional inhibition of cortico-hippocampal neurodegeneration by kolaviron treatment in rats. *Metab. Brain Dis.* 32, 1147–1161. doi: 10.1007/s11011-017-0012-6

Olajide, O. J., Fatoye, J. O., Idowu, O. F., Ilekoya, D., Gbadamosi, I. T., Gbadamosi, M. T., et al. (2018). Reversal of behavioral decline and neuropathology by a complex vitamin supplement involves modulation of key neurochemical stressors. *Environ. Toxicol. Pharmacol.* 62, 120–131. doi: 10.1016/j.etap.2018.07.005

Olajide, O. J., Suvanto, M. E., and Chapman, C. A. (2021). Molecular mechanisms of neurodegeneration in the entorhinal cortex that underlie its selective vulnerability during the pathogenesis of Alzheimer's disease. *Biol. Open* 10:bio056796. doi: 10.1242/bio.056796

Olajide, O. J., Yawson, E. O., Gbadamosi, I. T., Arogundade, T. T., Lambe, E., Obasi, K., et al. (2017b). Ascorbic acid ameliorates behavioural deficits and neuropathological alterations in rat model of Alzheimer's disease. *Environ. Toxicol. Pharmacol.* 50, 200–211. doi: 10.1016/j.etap.2017.02.010

O'Nuallain, B., Williams, A. D., Westermark, P., and Wetzel, R. (2004). Seeding specificity in amyloid growth induced by heterologous fibrils. *J. Biol. Chem.* 279, 17490–17499. doi: 10.1074/jbc.M311300200

Overk, C. R., and Masliah, E. (2014). Pathogenesis of synaptic degeneration in Alzheimer's disease and Lewy body disease. *Biochem. Pharmacol.* 88, 508–516. doi: 10.1016/j.bcp.2014.01.015

Pákáski, M., and Kálmán, J. (2008). Interactions between the amyloid and cholinergic mechanisms in Alzheimer's disease. *Neurochem. Int.* 53, 103–111. doi: 10.1016/j.neuint.2008.06.005

Patten, D. A., Germain, M., Kelly, M. A., and Slack, R. S. (2010). Reactive oxygen species: Stuck in the middle of neurodegeneration. *J. Alzheimers Dis.* 20, S357–S367. doi: 10.3233/JAD-2010-100498

Paxinos, G., and Watson, C. (1997). *The rat brain in stereotaxic coordinates*, 3rd Edn. San Diego, CA: Academic Press.

Pickett, E. K., Rose, J., McCrory, C., McKenzie, C. A., King, D., Smith, C., et al. (2018). Region-specific depletion of synaptic mitochondria in the brains of patients with Alzheimer's disease. *Acta Neuropathol.* 136, 747–757. doi: 10.1007/s00401-018-1903-2

Rak, M., Bénit, P. P., Chrétien, D., Bouchereau, J., Schiff, M., El-Khoury, R., et al. (2016). Mitochondrial cytochrome c oxidase deficiency. *Clin. Sci.* 130, 393–407. doi: 10.1042/CS20150707

Reddy, P. H., Tripathi, R., Troung, Q., Tirumala, K., Reddy, T. P., Anekonda, V., et al. (2012). abnormal mitochondrial dynamics and synaptic degeneration as early events in Alzheimer's disease: Implications to mitochondria-targeted antioxidant therapeutics. *Biochim. Biophys. Acta* 1822:639. doi: 10.1016/J.BBADIS.2011.10.011

Sanmartín, C. D., Veloso, P., Adasme, T., Lobos, P., Bruna, B., Galaz, J., et al. (2017). RyR2-mediated Ca2+ release and mitochondrial ROS generation partake in the synaptic dysfunction caused by amyloid β peptide oligomers. *Front. Mol. Neurosci.* 10:115. doi: 10.3389/FNMOL.2017.00115/BIBTEX

Schaeffer, E. L., and Gattaz, W. F. (2008). Cholinergic and glutamatergic alterations beginning at the early stages of Alzheimer disease: Participation of the phospholipase A2 enzyme. *Psychopharmacology* 198, 1–27. doi: 10.1007/s00213-008-1092-0

Schliebs, R., and Arendt, T. (2011). The cholinergic system in aging and neuronal degeneration. *Behav. Brain Res.* 221, 555–563. doi: 10.1016/j.bbr.2010.11.058

Selkoe, D. J. (2002). Alzheimer's disease is a synaptic failure. *Science* 298, 789–791. doi: 10.1126/science.1074069

Shankar, G. M., and Walsh, D. M. (2009). Alzheimer's disease: Synaptic dysfunction and Aβ. *Mol. Neurodegener.* 4:48. doi: 10.1186/1750-1326-4-48

Stine, W. B., Dahlgren, K. N., Krafft, G. A., and LaDu, M. J. (2003). In vitro characterization of conditions for amyloid-β peptide oligomerization and fibrillogenesis. *J. Biol. Chem.* 278, 11612–11622. doi: 10.1074/jbc.M210207200

Terni, B., Boada, J., Portero-Otin, M., Pamplona, R., and Ferrer, I. (2010). Mitochondrial ATP-synthase in the entorhinal cortex is a target of oxidative stress at stages I/II of alzheimer's disease pathology. *Brain Pathol.* 20, 222–233. doi: 10.1111/j.1750-3639.2009.00266.x

Timón-Gómez, A., Nývltová, E., Abriata, L. A., Vila, A. J., Hosler, J., and Barrientos, A. (2018). Mitochondrial cytochrome c oxidase biogenesis: Recent developments. *Semin. Cell Dev. Biol.* 76:163. doi: 10.1016/J.SEMCDB.2017.08.055

Tönnies, E., and Trushina, E. (2017). Oxidative stress, synaptic dysfunction, and Alzheimer's disease. *J. Alzheimers Dis.* 57:1105. doi: 10.3233/JAD-161088

Tu, S., Okamoto, S.-I., Lipton, S. A., and Xu, H. (2014). Oligomeric Aβ-induced synaptic dysfunction in Alzheimer's disease. *Mol. Neurodegener.* 9:48. doi: 10.1186/1750-1326-9-48

Uttara, B., Singh, A., Zamboni, P., and Mahajan, R. (2009). Oxidative stress and neurodegenerative diseases: A review of upstream and downstream antioxidant therapeutic options. *Curr. Neuropharmacol.* 7, 65–74. doi: 10.2174/157015909787602823

van Hoesen, G. W., Hyman, B. T., and Damasio, A. R. (1991). Entorhinal cortex pathology in Alzheimer's disease. *Hippocampus* 1, 1–8. doi: 10.1002/hipo.450010102

Valla, J., Berndt, J. D., and Gonzalez-Lima, F. (2001). Energy hypometabolism in posterior cingulate cortex of Alzheimer's patients: Superficial laminar cytochrome oxidase associated with disease duration. *J. Neurosci.* 21:4923. doi: 10.1523/JNEUROSCI.21-13-04923.2001

Velayudhan, L., Proitsi, P., Westman, E., Muehlboeck, J. S., Mecocci, P., Vellas, B., et al. (2013). Entorhinal cortex thickness predicts cognitive decline in Alzheimer's disease. *J. Alzheimers Dis.* 33, 755–766. doi: 10.3233/JAD-2012-121408

Wang, X., and Michaelis, E. K. (2010). Selective neuronal vulnerability to oxidative stress in the brain. *Front. Aging Neurosci.* 2:12. doi: 10.3389/fnagi.2010.00012

Wang, W., Zhao, F., Ma, X., Perry, G., and Zhu, X. (2020). Mitochondria dysfunction in the pathogenesis of Alzheimer's disease: Recent advances. *Mol. Neurodegener.* 15:30 doi: 10.1186/S13024-020-00376-6

Wang, X., Wang, W., Li, L., Perry, G., Lee, H. G., and Zhu, X. (2014). Oxidative stress and mitochondrial dysfunction in Alzheimer's disease. *Biochim. Biophys. Acta* 1842, 1240–1247. doi: 10.1016/j.bbadis.2013.10.015

Wogulis, M., Wright, S., Cunningham, D., Chilcote, T., Powell, K., and Rydel, R. E. (2005). Nucleation-dependent polymerization is an essential component of amyloid-mediated neuronal cell death. *J. Neurosci.* 25, 1071–1080. doi: 10.1523/JNEUROSCI.2381-04.2005

Xiao, T., Jiao, B., Zhang, W., Pan, C., Wei, J., Liu, X., et al. (2017). Identification of CHCHD10 mutation in chinese patients with Alzheimer disease. *Mol. Neurobiol.* 54, 5243–5247. doi: 10.1007/s12035-016-0056-3

Yu, Q., Wang, Y., Du, F., Yan, S., Hu, G., Origlia, N., et al. (2018). Overexpression of endophilin A1 exacerbates synaptic alterations in a mouse model of Alzheimer's disease. *Nat. Commun.* 9:2968. doi: 10.1038/S41467-018-04389-0

Zhou, M., Zhang, F., Zhao, L., Qian, J., and Dong, C. (2016). Entorhinal cortex: A good biomarker of mild cognitive impairment and mild Alzheimer's disease. *Rev. Neurosci.* 27, 185–195. doi: 10.1515/revneuro-2015-0019

frontiers | Frontiers in Aging Neuroscience

TYPE Original Research
PUBLISHED 28 October 2022
DOI 10.3389/fnagi.2022.974690

OPEN ACCESS

EDITED BY
Rubem C. A. Guedes,
Federal University of Pernambuco, Brazil

REVIEWED BY
Hadi Yousefi,
Khoy University of Medical Sciences, Iran
Weinan Zhou,
University of Illinois Urbana-Champaign, United States
Huaqiu Zhang,
Huazhong University of Science and Technology, China

*CORRESPONDENCE
Hui Fang
fanghui2818@126.com

SPECIALTY SECTION
This article was submitted to Neuroinflammation and Neuropathy, a section of the journal Frontiers in Aging Neuroscience

RECEIVED 21 June 2022
ACCEPTED 07 October 2022
PUBLISHED 28 October 2022

CITATION
Nan X, Sun Q, Xu X, Yang Y, Zhen Y, Zhang Y, Zhou H and Fang H (2022) Forsythoside B ameliorates diabetic cognitive dysfunction by inhibiting hippocampal neuroinflammation and reducing synaptic dysfunction in ovariectomized mice.
Front. Aging Neurosci. 14:974690.
doi: 10.3389/fnagi.2022.974690

Forsythoside B ameliorates diabetic cognitive dysfunction by inhibiting hippocampal neuroinflammation and reducing synaptic dysfunction in ovariectomized mice

Xinyu Nan[1], Qi Sun[2], Xiaoyu Xu[3], Ying Yang[3], Yanfeng Zhen[3], Yameng Zhang[4], Haixia Zhou[4] and Hui Fang[1,3]*

[1]Department of Internal Medicine, Hebei Medical University, Shijiazhuang, Hebei, China, [2]Department of Orthopedics, Hebei General Hospital, Shijiazhuang, Hebei, China, [3]Tangshan Gongren Hospital, Tangshan, Hebei, China, [4]Department of Internal Medicine, North China University of Science and Technology, Tangshan, Hebei, China

Background: Diabetes-associated cognitive impairment (DACI) is a common complication of diabetes, and studies have shown that DACI is more severe in postmenopausal patients with diabetes. Forsythoside B (FTS·B) can inhibit inflammation and reduce synaptic dysfunction, which can improve cognitive function. However, it has not been confirmed whether FTS·B has a reversing or retarding effect on postmenopausal diabetic encephalopathy.

Methods: Seven days after bilateral ovariectomy (OVX) or sham surgery, adult female C57 mice (*n* = 15/group) received intraperitoneal injection of streptozotocin (60 mg/kg/day/L) and citrate buffer for 5 consecutive days to induce diabetes mellitus (DM). Fourteen days later, ovariectomized diabetic mice were given intraperitoneal injection of FTS·B (100, 150 mg/kg/day/L) and subcutaneous injection of 17β-estradiol (1 mg/kg) for 8 weeks [OVX + DM + low-FTS·B group (L-F), OVX + DM + high-FTS·B group (H-F), and OVX + DM + 17β-estradiol (ER)]. In addition, the following control groups were defined: Sham, OVX, DM, and OVX + DM (O + D). Fasting plasma glucose, body weight and blood insulin levels were determined in each group of mice. Next, their cognitive function was tested through behavioral experiments. Hematoxylin & eosin (H&E) and Nissl staining were used to detect the morphological changes in the hippocampus. The aggregation of amyloid beta (Aβ) and the hyperaggregation of p-tau were assessed by immunohistochemistry. Interleukin-1β (IL-1β), interleukin-6 (IL-6), tumor necrosis factor-α (TNF-α), brain-derived neurotrophic factor (BDNF), post-synaptic density-95 (PSD-95), synaptophysin, and synapsin-1 expression in the hippocampus was detected by real-time polymerase chain reaction (RT-PCR) and western blot analysis.

Results: FTS·B can decrease fasting glucose and blood insulin level. Behavioral results showed that cognitive decline was the most severe in the O + D group, and the ER, L-F, and H-F groups revised the cognitive decline. Compared to the O + D group, more normal morphology, which has obvious nucleoli and clear nuclear membrane, was observed by H&E and Nissl staining in the ER, L-F, and H-F groups. FTS·B alleviated DACI by reducing the aggregation of Aβ and the hyperaggregation of p-tau in the hippocampus. Moreover, the protein and mRNA expression showed that FTS·B not only inhibited inflammation by decreasing IL-1β, IL-6, and TNF-α but also modulated synaptic plasticity by increasing BDNF, PSD-95, synaptophysin, and synapsin-1.

Conclusion: These results suggest that FTS·B may be a novel therapeutic target for postmenopausal diabetic encephalopathy treatment.

KEYWORDS

diabetes-associated cognitive impairment, ovariectomy, forsythoside b, inflammation, synaptic dysfunction

Introduction

Diabetes is a chronic metabolic disorder that is currently a serious health problem worldwide. A previous study predicted that the number of patients with diabetes may reach 578 million by 2030 and 700 million by 2045 worldwide (Piatkowska-Chmiel et al., 2022). One of the long-term complications of diabetes in the nervous system is called diabetic encephalopathy (DACI), which is characterized by cognitive impairment and neuropathological changes, mainly manifested by altered synaptic plasticity (Wang B. N. et al., 2021), extracellular plaques of aggregated amyloid beta (Aβ), and neurofibrillary tangles composed of hyperphosphorylated tau protein (Pang et al., 2022). With the intensification of the global aging of society, in recent years, the incidence of diabetes mellitus (DM) has been rising, particularly in post-menopausal women (Bragg et al., 2017; Wang B. N. et al., 2021), which brings huge medical and economic burdens to the world and seriously affects people's daily life and work. Thus, it is necessary to explore the related pathogenesis of menopausal diabetic encephalopathy and to develop an effective drug to treat it.

The inflammatory factors, such as tumor necrosis factor (TNF) and interleukins (IL-1β and IL-6), and free radicals, can lead to cellular damage in the brain, including mitochondrial damage and neuronal apoptosis, which in turn affects cognitive function (Skundric and Lisak, 2003; Chung et al., 2015; Sadeghi et al., 2016). Brain-derived neurotrophic factor (BDNF) is a factor that effectively regulates synaptic plasticity and has a function in promoting learning and memory (Jin et al., 2020). BDNF can modulate synapse-related proteins such as synaptophysin, synapsin-1, and post-synaptic density-95 (PSD-95), which are essential for synaptic plasticity and cognition (Liu et al., 2012; Wang et al., 2016). Therefore, neuroinflammation, neurotrophic factors, and synaptic proteins may be involved in synaptic plasticity damage, which is considered to be the neuropathogenesis of diabetic encephalopathy, to a large extent (Podda et al., 2016).

Forsythoside B (FTS·B) is one of the main active components of the air-dried fruit of Forsythia (Wang et al., 2018), and the current study showed that the neuroprotective effect of FTS·B depends on multiple antioxidant, anti-apoptotic, anti-inflammatory, and neurogenesis-promoting properties (Jiang et al., 2012). However, whether FTS·B can delay menopausal diabetic encephalopathy has not yet been reported and studied. To the best of our knowledge, in this study, we used an ovariectomized diabetic mice model to study the related mechanism of FTS·B in the treatment of menopausal diabetic encephalopathy for the first time. We found that FTS·B could be a potential drug candidate for the treatment of menopausal diabetic encephalopathy by inhibiting hippocampal neuroinflammation and reducing synaptic dysfunction.

Materials and methods

Animals and experimental design

Female C57BL mice (8-weeks-old) were purchased from the Yi Wei Wo Technology Co., Ltd., Shijiazhuang, China. The mice were randomly divided into seven groups as follows: Sham control (Sham); DM; ovariectomy (OVX); ovariectomy and diabetes (O + D); ovariectomy, diabetes, and 17β-estradiol (1 mg/kg) (ER); ovariectomy, diabetes, and low-FTS·B (100 mg/kg) (L-F); and ovariectomy, diabetes and

high-FTS·B (150 mg/kg) (H-F). After anesthesia, each mouse underwent either sham operation (Sham, only a skin incision was made and then sutured) or bilateral ovariectomy. All of the animals were given prophylactic antibiotics (penicillin-G; 20,000 U) beginning soon after surgery and lasting for 3 days. After ovariectomy and 1 week of recovery, 60 mg/kg streptozotocin (freshly prepared, pH 4.5 in citrate buffer) was applied intraperitoneally to induce diabetes. In the control group, ovaries were identified but not removed, and these mice received citrate buffer as a streptozotocin (STZ) vehicle (Wang T. et al., 2021). Forty-eight hours after STZ injections, mice with blood glucose levels above 200 mg/dl were considered diabetic. In addition, the glucose tolerance test was used to convince the success of diabetic model. FTS·B and 17β-estradiol were administered intraperitoneally once per day for 8 weeks. Body weight was measured once 2 weeks. After the treatment, the mice were used to evaluate the fasting blood glucose levels and blood insulin levels, and then the mice were subjected to the Morris water maze test, Y maze test, and novel object recognition test (NORT). After the behavioral tests, the animals were anesthetized with 10% chloral hydrate (3.5 ml/kg) and perfused initially with 0.9% saline solution *via* cardiac puncture. For immunofluorescence, hematoxylin & eosin (H&E), and Nissl staining, the animals were perfused with 4% paraformaldehyde (PFA) in 0.1 M phosphate-buffered saline (PBS) following the initial saline solution perfusion. Next, the brain tissues were rapidly removed and post-fixed by immersion in 4% PFA for 24 h. For real-time polymerase chain reaction (RT-PCR) and western blot analysis, the whole hippocampus was removed and snap-frozen at −80°C. All animal experiments were conducted following the national guidelines and the relevant national laws on the protection of animals. The summary of the experiment's timeline is shown as **Scheme 1**.

Morris water maze test

After 8 weeks of treatment with FTS·B, a water maze test was performed to detect the cognitive level of the mice. The water maze was divided into four quadrants, with a platform placed in the third quadrant. The maze was filled with water containing milk up to 1.5 cm above the platform at a temperature of 22–24°C, with different shapes and colors attached to the walls of the maze. During the training phase, mice were placed into any of the three quadrants without a platform, and it ended when the mice climbed onto the platform. If a mouse did not find the platform within 60 s, the escape latency was recorded as 60 s, and the mouse was carefully guided into the platform, where it remained for 15 s. The mice were then sun-dried and returned to their cages. During the training period, the mice were tested four times a day on the hidden platform for 5 consecutive days to evaluate their learning ability. On the fifth day of training, the platform was removed and the mice were again placed in the maze to test their spatial memory. In the spatial memory ability test, they were placed in water and allowed to swim for 60 s. An IBM computer (Armonk, NY, USA) equipped with a tracking program was used to record the trajectories of the mice, locate the escape latency of the hidden platform, and record the number of times of crossing the platform (Li et al., 2017).

Y maze

Y maze spontaneous alternate behavior is a measure of spatial working memory during exploratory activities. The experiment was carried out in a three-arm maze with three arms of equal size, labeled A, B, and C. Each arm was 34 cm long, 8 cm wide, and 14.5 cm high, at an angle of 120° from the other two arms. Each mouse was placed at the end of one arm and allowed to move freely through the maze for 5 min. The arm entry times and the sequence number (e.g., ABABCC) of each mouse were recorded manually. An arm entry was considered complete when the mouse's hind paw was fully on one arm. The measured parameters included the number of consecutive spontaneous alternate performance (SAP) of mice entering three different arms (i.e., ABC, ACB, BCA, and BAC), the number of mice visiting other arms and returning to the same arm (i.e., ABA, ACA, and BAB), and the number of repeated mice visits to the same arm—returning to the same arm (SAR) (i.e., AA, BB, and CC).

The percentage of SAP was calculated as [(alternating times)/(total arm entry − 2)] × 100.

Novel object recognition test

The NORT is a simple behavioral assay of memory that primarily relies on rodent's innate exploratory behavior in the absence of externally applied rules or reinforcement. The test can be used as a model for the investigation of memory alterations. NORT has habituation, familiarization, and test phases. The experiments were carried out in an isolated chamber, and mice were familiarized with the researcher before the test. The box and objects were cleaned with 70% isopropanol solution before each trial. Habituation phase: the animals were allowed to stay in a box (65 × 45 × 45 cm) for 5 min (**Scheme 2**). Familiarization phase: the animals were first observed for 5 min in the same box with two identical objects (A + A), and their behavior was recorded with a video camera. Test phase: the animals were observed for 5 min in a box containing a familiar object and a novel object, which was different in shape and color (A + B), and their behavior was recorded with a video camera. Evaluation: results were assigned by comparing the time spent with the familiar and novel objects. The calculation formula is as follows:

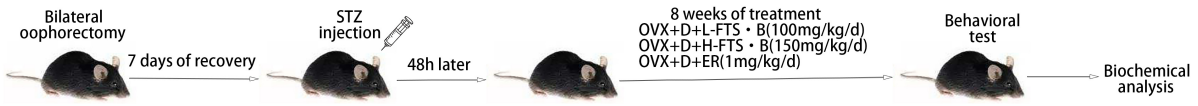

SCHEME 1
The scheme illustrates the stages of the experiment.

Discrimination index (DI) was calculated by dividing the difference in exploration time (seconds) for a familiar object (TF) and a novel object (TN), with the total amount of exploration time for novel and familiar objects: DI = TN/(TN + TF).

Hematoxylin & eosin and Nissl staining

The brain tissues were carefully collected and fixed in 4% PFA solution for 24 h. Next, they were dehydrated in alcohol and embedded in paraffin. After that, the brain tissue sections were dewaxed, hydrated, and stained with H&E solution (Beyotime, China). For Nissl staining, the slides were stained with cresol violet and Nissl differentiation solution in accordance with the manufacturer's instructions (Beyotime, China). Finally, the slides were observed under a light microscope (Nikon, Japan).

Immunofluorescence

The brains were dissected, fixed in PBS with 4% PFA for 2 days, and then frozen into sections. The sections were 10 μm thick and were immunostained with primary Aβ antibody (1:200, Arigobio, China) and tau antibody (1:500, HA, China) at 4°C overnight. The following day, the sections were washed in PBS, incubated with horseradish peroxidase (HRP)–conjugated anti-rabbit secondary antibody at 25°C for 1 h, and incubated with streptavidin-organism HRP complex at 25°C for another 1 h. Next, 5% diaminobenzidine tetrahydrochloride solution and hematoxylin were added as a counterstain (25°C for 5 min). Photomicrographs were obtained using an inverted fluorescence microscope (magnification ×40 and ×200; Nikon, Japan). The intensity of positive staining in the ROI was calculated and defined as the sum of integrated optical density (IOD), and the area of the ROI was also calculated. The average IOD of specific proteins, reported as IOD/mm^2, was defined as the sum of IOD divided by the area of ROI.

Real-time polymerase chain reaction

Hippocampal samples were obtained for this analysis. A Gene Amp 7,700 Sequence Detection System (Applied Biosystems, Foster City, CA, USA) and SYBER® Premix Ex

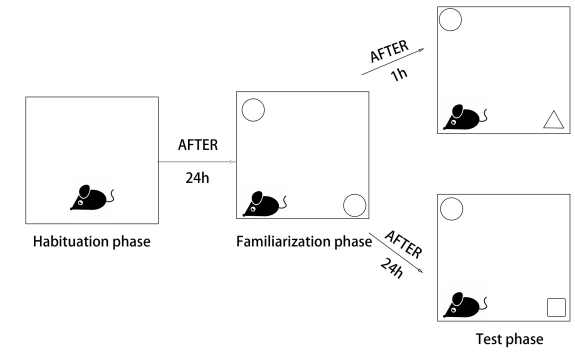

SCHEME 2
The scheme illustrates the phases of the novel object recognition (NOR) test.

Taq^{TM}II kit (Takara, Kusatsu, Japan) were used to perform RT-PCR. The primers for the selected genes are listed in **Table 1**. GAPDH was used as an endogenous control. The changes of relative mRNA transcript levels were reported using the 2 [-Delta C(T)] method as previously described (Mohammadi and Zare, 2020). The experiment was repeated at least three times to ensure accuracy.

Western blot analysis

Tissues were collected and dissolved in a radioimmunoprecipitation analysis buffer using a cocktail of protease inhibitors. Protein lysate was electrophoresed with sodium dodecyl sulfate-polyacrylamide gel and transferred to nitrocellulose membranes. Next, 5% bovine serum albumin was used to block the membranes at 4°C for 2 h. The membranes were subsequently incubated with the following primary antibodies at 4°C overnight: BDNF (1:1,000, Abcam), PSD-95 (1:1,000, Abcam), synaptogenin (1:1,000, Abcam), synapsin-1 (1:1,000, Abcam), TNF-α (1:2,000, HA), IL-6 (1:2,000, HA), IL-1β (1:2,000, HA), and the reference protein β action (1:100,000, HA). After washing with TBST, the membranes were incubated with HRP-conjugated secondary antibody at a dilution of 1:2,000 at 4°C for 4 h. An enhanced chemiluminescence kit (Merck Millipore, Billerica, MA, USA) and imaging system (Bio Spectrum 600; UVP, Upland, CA, USA)

TABLE 1 Sequences of primers used for RT-PCR.

	Forward primer (5′-3′)	Reverse primers (5′-3′)
GAPDH	GGGGAGCCAAAAGGGTCATCATCT	GAGGGGCCATCCACAGTCTTCT
TNF-α	ACTGAACTTCGGGGTGATCG	CCACTTGGTGGTTTGTGAGTG
IL-1β	TTCGGGCAGGCAGTATCACTCATTG	ACACCAGCAGGTTATCATCATCATCC
IL-6	AGACTTCCATCCAGTTGCCTTCTTG	CATGTGTAATTAAGCCTCCGACTTGTG
PSD-95	TCCGGGAGGTGACCCATTC	TTTCCGGCGCATGACGTAG
synaptophysin	AGACATGGACGTGGTGAATCA	ACTCTCCGTCTTGTTGGCAC
synapsin-1	CCAATCTGCCGAATGGGTACA	GCGTTAGACAGCGACGAGAA
BDNF	TCATACTTCGGTTGCATGAAGG	ACACCTGGGTAGGCCAA

were used to visualize the bands. ImageJ (National Institutes of Health, Bethesda, MD, USA) was used to quantify the blots.

Statistical analysis

All data were analyzed using SPSS software (SPSS, Chicago, IL, USA), and the results were expressed as mean ± standard deviation (SD). The Shapiro–Wilk test and the Bartlett's test were used to analyze the normality of distribution and homogeneity of variance. One-way analysis of variance (ANOVA) and Fisher's protected least significant difference test were used to determine statistically significant differences between the groups. The results of radiography scores were analyzed using the Kruskal–Wallis test. $P < 0.05$ was considered to indicate statistical significance.

Results

Glucose tolerance curve and the effects of forsythoside B on blood glucose, body weight, and blood insulin levels (FPI) in ovariectomized diabetic mice were analyzed

We detected the levels of fasting blood glucose and blood insulin levels in each group (Table 2). As shown in Figure 1A, the blood glucose levels in the Sham group at 0, 60, and 120 min were significantly lower than those in the OVX group, and the blood glucose levels in the DM group at 0, 60, and 120 min were significantly lower than those in the O + D group. But there was no significant difference between the groups at 30 min. Among them, the DM group showed the lowest level. This suggests that the diabetes model was established successfully. As shown in Table 2, compared with the Sham group, the levels of fasting blood glucose in the OVX, DM, and O + D groups were higher. However, treatment with FTS·B and 17β-estradiol significantly reversed this trend. Figure 1B demonstrates that compared with Sham group, the fasting weight was significantly reduced in the DM group and significantly increased in the OVX group. Figure 1B also showed that when compared with the O + D group, the fasting weight in the OVX group was significantly increased in the fourth, sixth, and eighth weeks and in the DM group was significantly reduced in the eighth week. However, no significant differences were found between the treatment groups that received different doses of FTS·B and 17β-estradiol. Compared to the Sham group, the FPI level was significantly reduced in the DM and O + D groups (Table 2). After treatment, significant improvements were observed in the ER, L-F, and H-F groups. This suggests that FTS·B has anti-diabetic effects.

Forsythoside B ameliorates cognitive decline of ovariectomized diabetic mice

We used water mazes to evaluate learning and memory in mice. Compared with the Sham group, the OVX, DM, and O + D groups showed more chaotic movements (Figure 2A) and longer escape latency (Figure 2B), and the number of platform crossings decreased (Figures 2C,D). Among them, the O + D group showed the most obvious changes. However, treatment with FTS·B and 17β-estradiol significantly reversed this trend, especially in the H-F group (Figures 2A–D). And there was no significant difference between the groups of swimming speed (Figure 2E). Compared with the Sham group, the target quadrant time was significantly reduced in the OVX, DM, and O + D groups. Among them, the O + D group was the most obvious. However, treatment with FTS·B and 17β-estradiol significantly reversed this trend, especially in the H-F group (Figure 2F).

We assessed working and spatial memory performance by recording spontaneous change behavior in the Y-maze test. As shown in Figure 3, there were significant differences in spatial memory performance among different groups ($P < 0.05$; Figures 3A–C). Compared with the Sham group, the groups OVX, DM, and O + D showed fewer spontaneous alternating movements (Figure 3A). Among them, the O + D group had the fewest spontaneous alternating movements. However,

TABLE 2 Effects of forsythoside B on blood glucose and blood insulin levels in ovariectomized diabetic mice.

Group	Blood glucose (mmol/L)	Blood insulin levels (μIU/ml)
Sham	5.21 ± 0.16	40.85 ± 1.14
OVX	6.22 ± 0.42***	39.68 ± 2.48
DM	19.97 ± 1.18***	25.95 ± 0.79***
O + D	24.03 ± 1.04***	24.22 ± 1.42***
ER	11.13 ± 0.33###	33.49 ± 1.17###
L-F	10.7 ± 1.17###	32.79 ± 1.07###
H-F	8.2 ± 0.67###	34.27 ± 0.69###

Compared to Sham, ***$P < 0.001$. Compared to O + D, ###$P < 0.001$. Data are expressed as mean ± SD ($n = 10$).

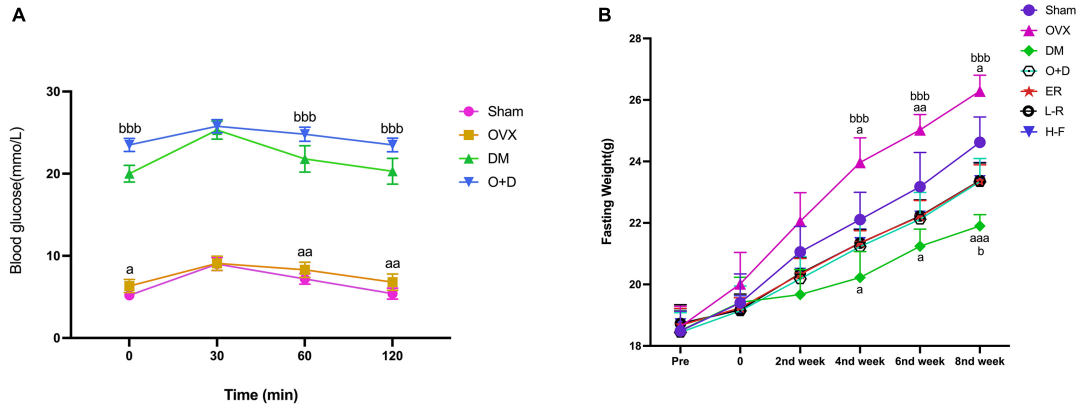

FIGURE 1
Changes of blood glucose and fasting weight. **(A)** Blood glucose and **(B)** fasting weight in Sham, OVX, DM, O+D, ER, L-F, and H-F groups. Before operation (Pre); after operation and streptozotocin injection (0), while FTS•B and 17β-estradiol were administered from the first week to the eighth week on an alternate day. Compared to Sham group, $^{a}P < 0.05$, $^{aa}P < 0.01$, and $^{aaa}P < 0.001$. Compared to O+D group, $^{b}P < 0.05$, $^{bb}P < 0.01$, $^{bbb}P < 0.001$, and ns indicates not significant.

treatment with FTS·B and 17β-estradiol effectively increased the percentage of spontaneous changes (Figure 3D).

To confirm the effect of FTS·B on the menopausal diabetic encephalopathy, a NORT was also performed. The statistical analysis revealed that the groups OVX, DM, and O + D showed a significant reduction in their interest of the objects in the testing stage, especially of a new one, compared to the animals in the Sham group. However, treatment with FTS·B and 17β-estradiol significantly reversed this trend (Figures 4A–D).

Taken together, these data suggest that FTS·B treatment significantly improves learning and cognitive impairment associated with menopausal diabetes.

Forsythoside B reduces hippocampal morphological changes and synaptic dysfunction in ovariectomized diabetic mice

Next, we evaluated whether FTS·B treatment affected hippocampal morphology in each group of mice. We found that the hippocampal region of the Sham group showed normal morphology, with obvious nucleoli and clear nuclear membrane (Figures 5A,B). However, in the OVX, DM, and O + D groups, hippocampal neurons were lost and hippocampal cells were sparsely arranged with blurred boundaries. The O + D group was the most severely affected. Importantly, FTS·B and 17β-estradiol therapy largely reversed these abnormalities, particularly in the H-F group (Figures 5A,B). These results suggest that FTS·B has a significant neuroprotective effect, as it inhibits hippocampal neuron loss and structural changes.

We also assessed the expression levels of synaptic associated proteins (PSD-95, synaptogenin, and synapsin-1) in the hippocampus, which form the molecular basis of synaptic plasticity. PSD-95 (Figures 5C,D), synaptogenin (Figures 5C,E), and synapsin-1 (Figures 5C,F) proteomic levels were significantly decreased in the OVX, DM, and O + D groups compared with the Sham group. Among them, the decrease was most obvious in the O + D group. After treatment with FTS·B and 17β-estradiol, the expression of these three protein groups was significantly increased in ovariectomized diabetic mice, especially in the H-F group (Figures 5C–F). RT-PCR results were consistent with the western blot results (Figures 5G–I). These results suggest that FTS·B enhances the expression level of synaptic associated proteins in the hippocampus, which may indicate the dose-dependent effect of FTS·B *in vivo*.

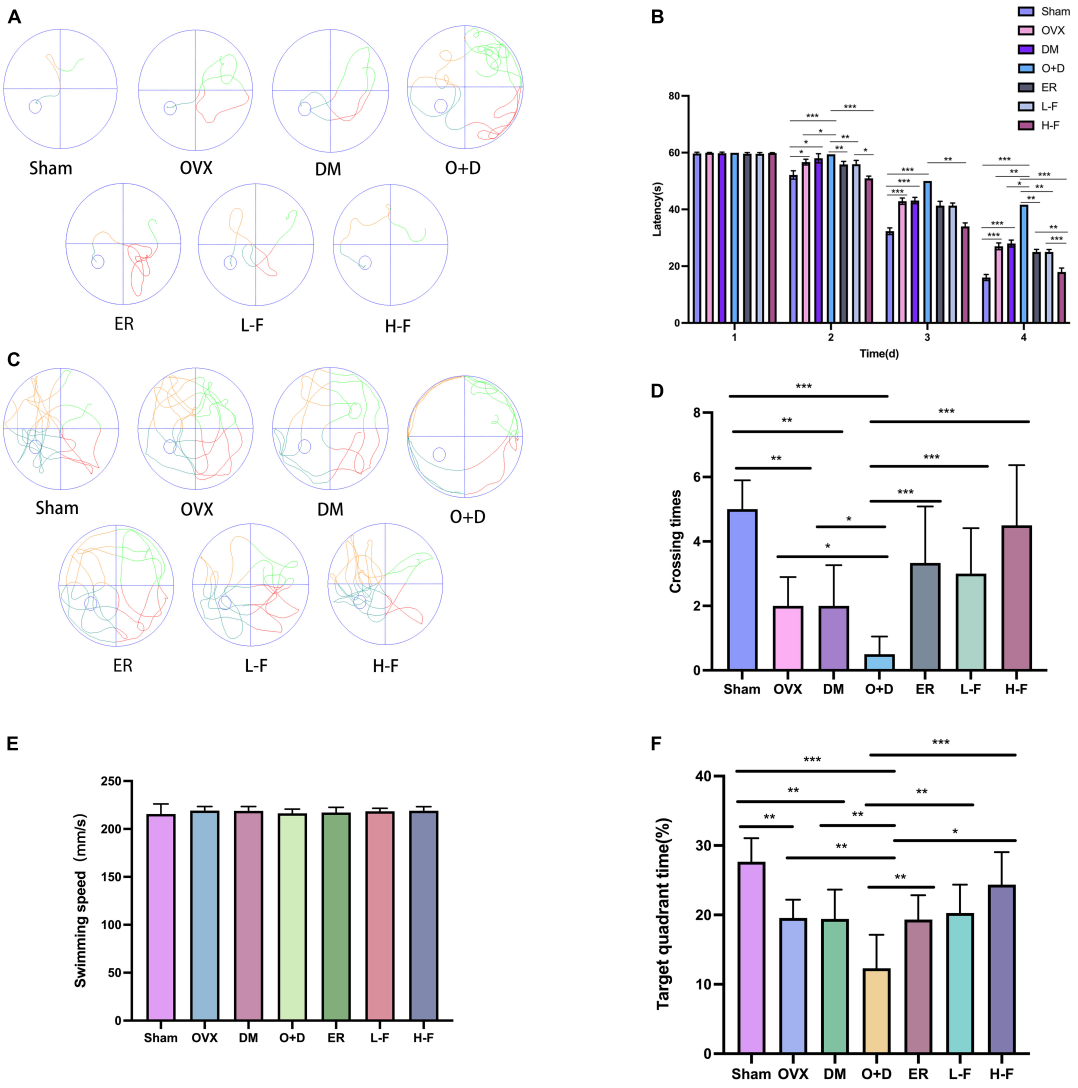

FIGURE 2
FTS•B significantly improves the learning and memory ability of ovariectomized diabetic mice. Behavioral tests and quantitative analyses of C57 mice. **(A)** Representative tracing graphs showing the training trials. **(B)** Escape latency during the platform trials. **(C)** Representative tracing graphs of the probe trials. **(D)** Number of crossings over the original platform location in the probe trials. **(E)** The swimming speed of each group. **(F)** The target quadrant time. $n = 6$. $^{*}P < 0.05$, $^{**}P < 0.01$, $^{***}P < 0.001$, and ns indicates not significant.

Forsythoside B inhibited the aggregation of amyloid beta and the hyperaggregation of p-tau in the hippocampus and increased the level of brain-derived neurotrophic factor in the hippocampus of ovariectomized diabetic mice

The immunohistochemical results showed that the number of Aβ-positive plaques in the hippocampus of the OVX, DM, and O + D groups was significantly higher than that of the Sham group, and the difference was the most significant in the O + D group. However, FTS·B and 17β-estradiol administration significantly reduced the deposition of Aβ in the O + D group, especially at group of H-F (**Figures 6A,C**). As a microtubule-associated protein, tau stabilizes the neuronal cytoskeleton, and its high phosphorylation may lead to the formation of toxic neurofibrillary tangles in diseases such as diabetic encephalopathy and AD (Yan et al., 2018). In this study, hyperaggregation of p-tau was found in the hippocampus of mice in the OVX, DM, and O + D groups compared with the Sham group. The hyperaggregation of p-tau was most severe in the O + D group. These differences were significantly reduced after FTS·B and 17β-estradiol treatment, especially in the H-F group (**Figures 6B,D**).

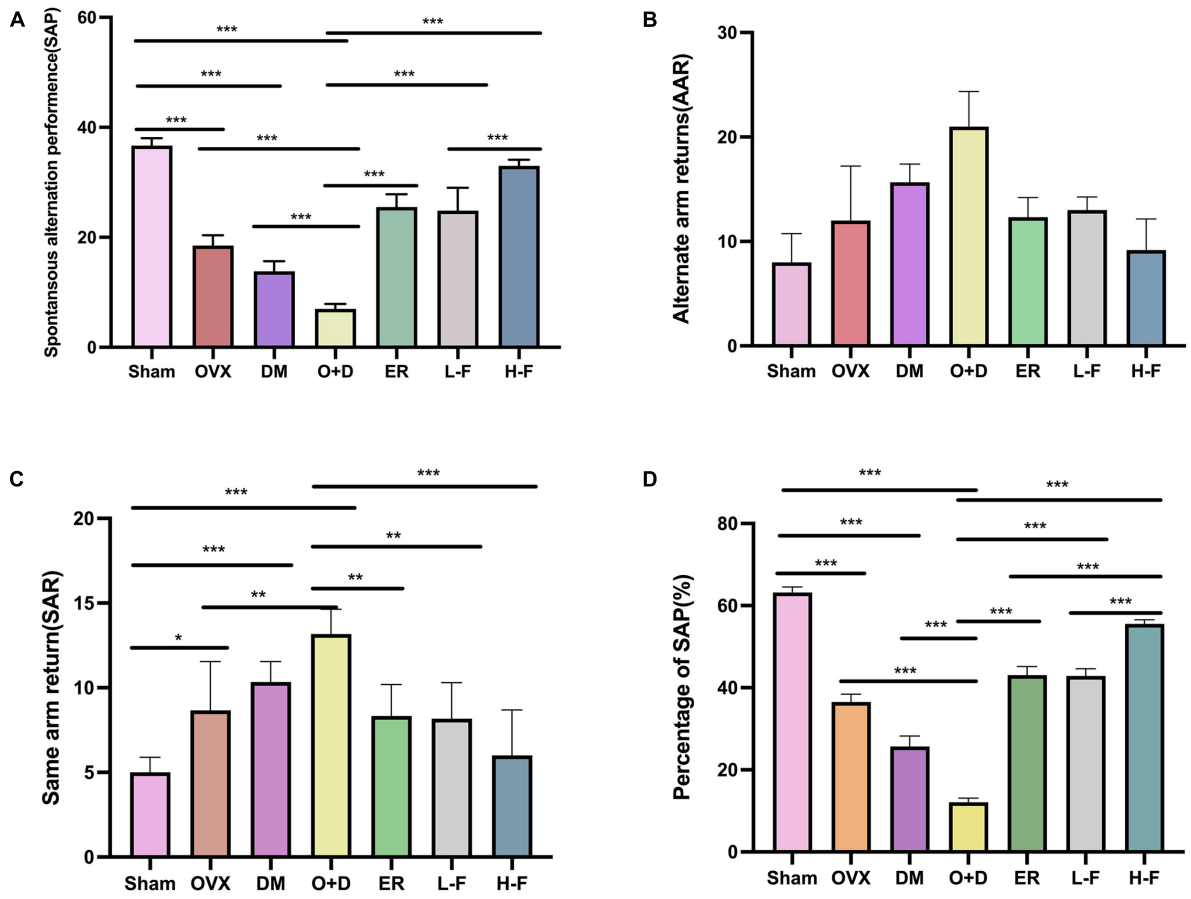

FIGURE 3
FTS•B significantly improves workspace memory impairment in ovariectomized diabetic mice in the Y-maze test. **(A)** Spontaneous alteration performance (SAP) was defined when an animal visited three different arms (i.e., A, B, and C) consecutively (i.e., ABC, ACB, BCA, or BAC). **(B)** Alternate arm returns (AAR) was defined when an animal visited other arms and then returned to the initial arm (i.e., ABA, ACA, and BAB). **(C)** Same arm returns (SAR) was defined as repeated visits of the same arm (i.e., AA, BB, and CC). **(D)** The percentage of SAP (%); $n = 6$. $^{*}P < 0.05$, $^{**}P < 0.01$, $^{***}P < 0.001$, and ns indicates not significant.

Previous studies have found that BDNF is a neurotrophic factor that can promote the development of immature neurons and increase the survival rate of neurons and synaptic plasticity (Tang et al., 2019). We investigated the effect of FTS·B treatment on hippocampal BDNF levels. Our RT-PCR results showed that compared with the Sham group, the mRNA expression levels of BDNF in the hippocampus of the OVX, DM, and O + D groups were significantly reduced, with the lowest mRNA level in the O + D group. However, treatment with FTS·B and 17β-estradiol reversed this reduction. In the H-F group was more effective (**Figure 7A**). Western blot results were consistent with RT-PCR results (**Figures 7B,C**). These data suggest that FTS·B treatment can inhibit the deposition of Aβ and hyperaggregation of p-tau and increase the expression level of BDNF in ovariectomized diabetic mice.

Forsythoside B mediates regulation of neuroinflammation-related protein expression and activation in the hippocampus of ovariectomized diabetic mice

We investigated whether neuroinflammation exists in patients with postmenopausal diabetes and whether FTS·B can prevent neuroinflammation. We assessed the expression levels of TNF-α, IL-6 and IL-1β in the hippocampus using RT-PCR and western blot. RT-PCR results showed that compared with the Sham group, the expression levels of TNF-α, IL-6, and IL-1β in the hippocampus of the OVX, DM, and O + D groups were significantly increased, and the increase was most significant in the O + D group. FTS·B and 17β-estradiol significantly reduced the mRNA expression levels of these factors, especially in the H-F group ($P < 0.05$, **Figures 8A–C**). Western blot results were

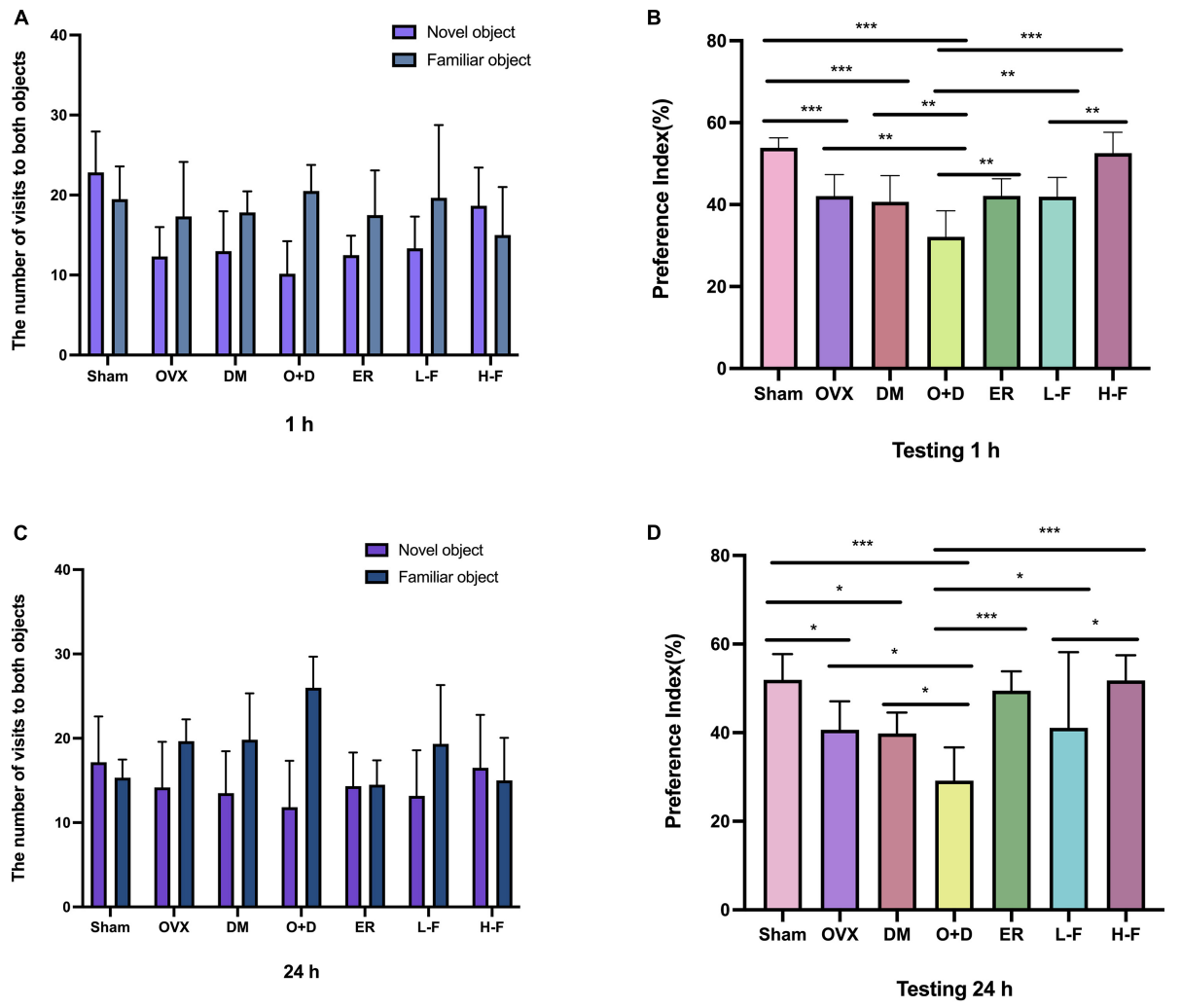

FIGURE 4
FTS•B can significantly reduce memory impairment in ovariectomized diabetic mice, as indicated by the new object recognition test. The recognition memory was measured by the novel object recognition test where the mice were allowed to explore the familiar and novel objects for 5 min. **(A,C)** The bars show the number of times the different groups of mice visited the two objects during the test phase. **(B,D)** The bar chart shows the preference index (%) for each group. $n = 6$. $^{*}P < 0.05$, $^{**}P < 0.01$, $^{***}P < 0.001$, and ns indicates not significant.

consistent with the RT-PCR results ($P < 0.05$, **Figures 9A–D**). These results suggest that FTS·B inhibits neuroinflammation in the hippocampus of ovariectomized diabetic mice.

Discussion

Diabetes is a chronic metabolic disease that can cause structural and functional changes in the central nervous system, leading to cognitive decline (Liu et al., 2020). Previous studies have shown that estrogen deficiency can affect the cognitive function (Albert and Newhouse, 2019). Estrogen plays important roles in the brain regions associated with learning and memory, such as the hippocampus and frontal cortex. These include neurotrophic and neuroprotective effects, increased long-term potentiation (LTP) and dendritic spine density, and upregulation of BDNF and growth receptors (Bansal and Chopra, 2015; Goyal and Garabadu, 2020). There is a synergistic effect between estrogen deficiency and diabetes, which can significantly aggravate the symptoms of cognitive impairment in postmenopausal diabetic patients. Therefore, it is very important to explore the molecular mechanisms behind cognitive impairment in postmenopausal diabetic patients and to identify effective treatment strategies. However, there have been few studies on menopausal diabetic encephalopathy. Therefore, in this study, we performed bilateral ovariectomy in C57 mice and administered intraperitoneal injection of STZ after surgery to simulate a postmenopausal diabetic mouse model. We showed that

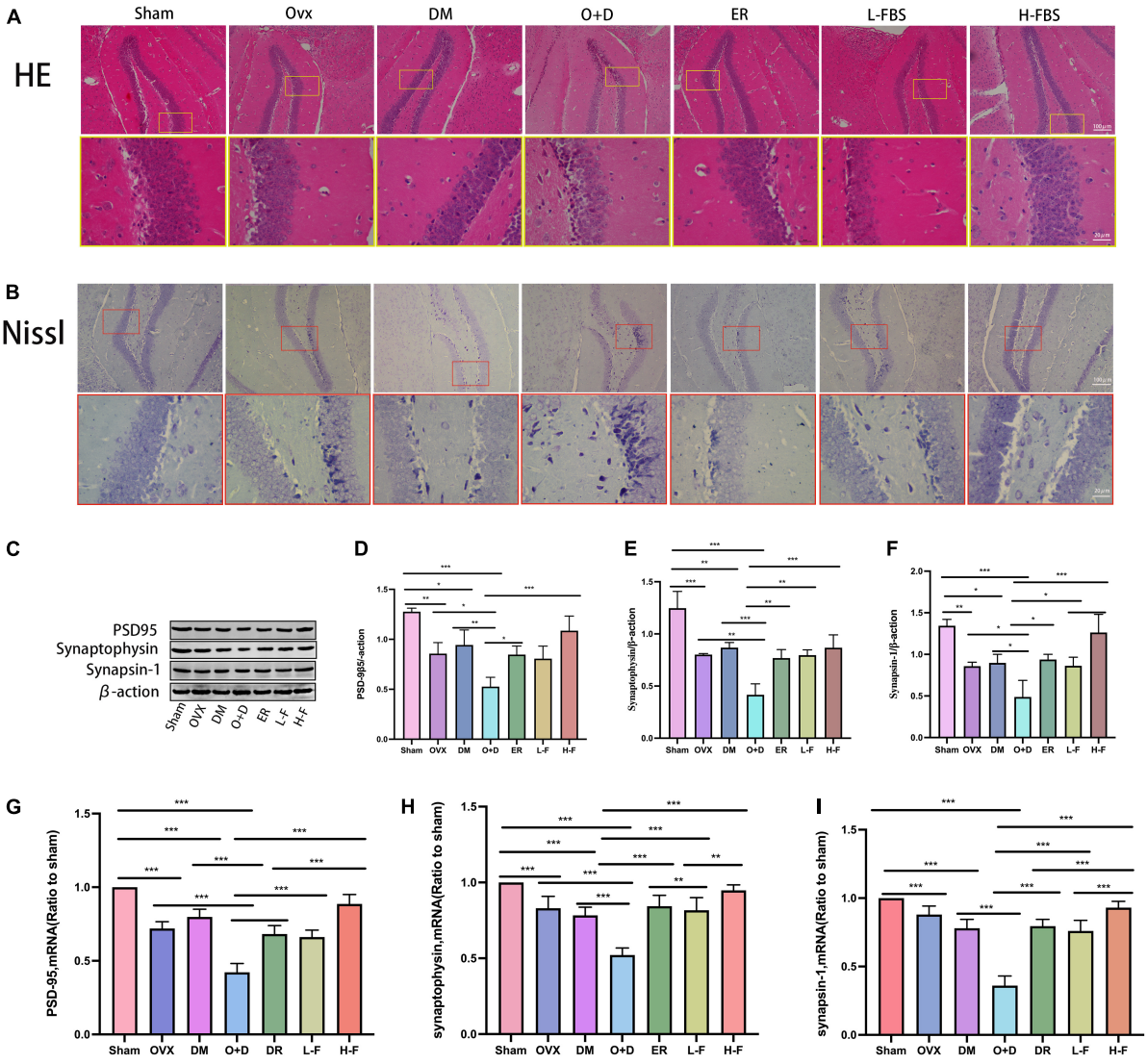

FIGURE 5
FTS•B reduces hippocampal morphologic changes and synaptic dysfunction in ovariectomized diabetic mice. **(A,B)** Representative hematoxylin and eosin (H&E) and Nissl-stained sections of the hippocampus. **(C)** Representative western blotting showing PSD95, synaptophysin, and synapsin-1 expression levels. **(D–F)** Expression levels of PSD95, synaptophysin, and synapsin-1 were quantitatively analyzed. $n = 3$. **(G–I)** Quantitative analysis of the mRNA expression of PSD95, synaptophysin, and synapsin-1. $n = 6$. $^{*}P < 0.05$, $^{**}P < 0.01$, $^{***}P < 0.001$, and ns indicates not significant. Scale bars = 100 and 20 μm as indicated.

postmenopausal diabetic mice developed cognitive impairment and impaired learning and memory functions. We also found that FTS·B could alleviate the symptoms and pathological changes of cognitive dysfunction in the mice by inhibiting hippocampal neuroinflammation and reducing synaptic dysfunction. This study shows that FTS·B can effectively inhibit neuroinflammation of the central nervous system and delay the progression of menopausal diabetic encephalopathy. Thus, FTS·B is a potential therapeutic drug for menopausal diabetic encephalopathy.

Forsythoside B, a phenylethanoid glycoside, is a traditional oriental medicine. Some studies have shown that FTS·B can inhibit inflammation, suppress oxidative stress, and promote blood circulation (Jiang et al., 2010b). Jiang et al. (2010a) found that FTS·B played a significant neuroprotective role in an SD ischemia–reperfusion rat model by inhibiting inflammation. Qu et al. (2021) showed that synaptic plasticity is closely associated with cognitive function. However, it has not been reported whether FTS·B can improve cognitive impairment in menopausal diabetic mice. In this study, we found that FTS·B could reduce cognitive impairment in menopausal diabetic mice, inhibit inflammatory factors, and reduce synaptic dysfunction, which effectively improve their cognitive function.

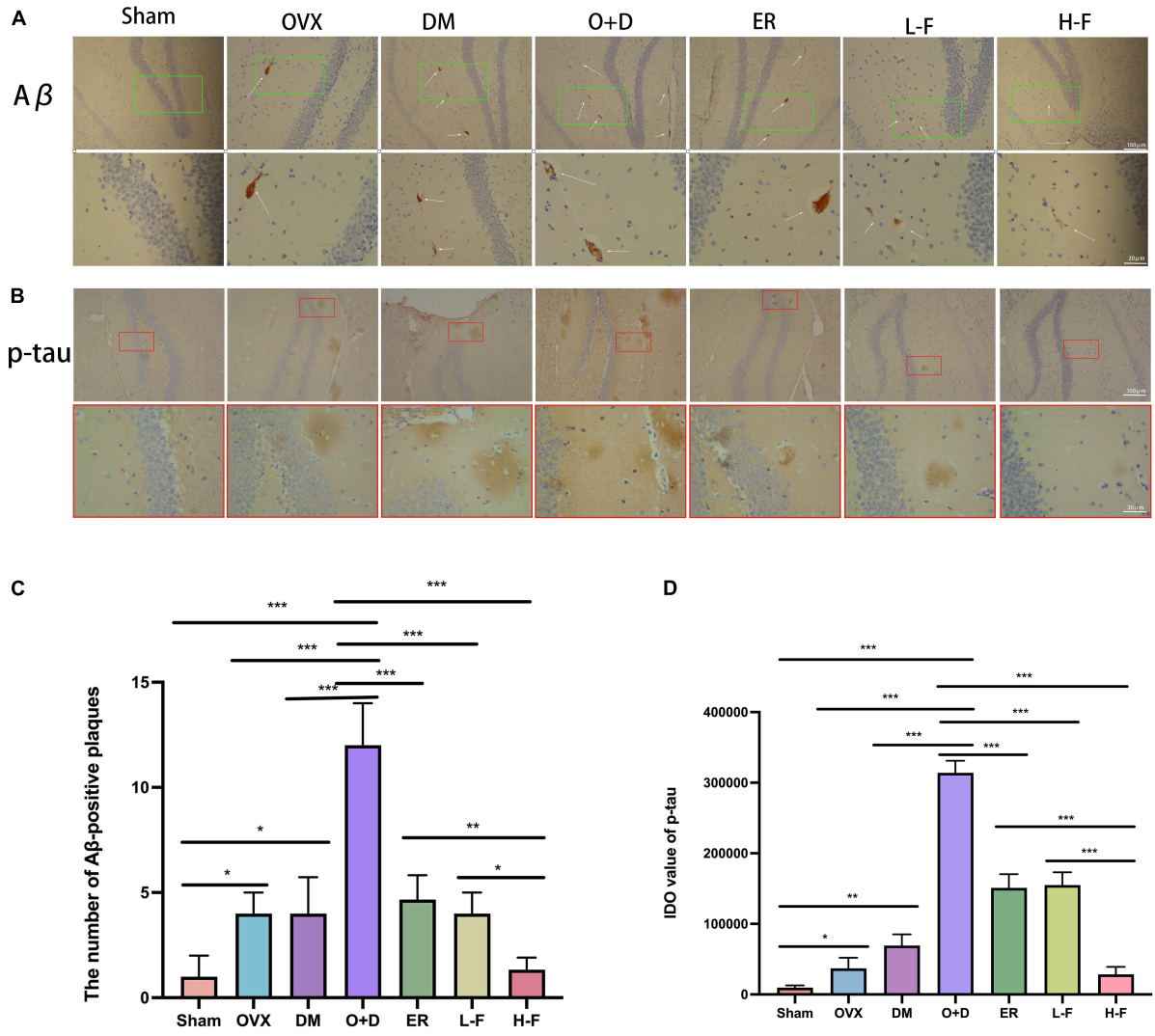

FIGURE 6
FTS•B treatment inhibits the accumulation of Aβ and *p*-tau in the hippocampus of ovariectomized diabetic mice. **(A,B)** Immunohistochemistry assay for Aβ and *p*-tau in the hippocampus in different groups. The thin white arrow indicates Aβ-positive plaques. **(C,D)** Quantitative analysis of Aβ and *p*-tau expression. $n = 3$. $^{*}P < 0.05$, $^{**}P < 0.01$, $^{***}P < 0.001$, and ns indicates not significant. Scale bars = 100 and 20 μm as indicated.

A large number of studies have shown that DACI can cause changes in animal behavior; so, behavioral experiments can be used as an important detection method in the study of diabetic encephalopathy (Yan et al., 2018; Tang et al., 2019; Mohammadi and Zare, 2020; Piatkowska-Chmiel et al., 2022). Piatkowska-Chmiel et al. administered fructose solution + STZ intraperitoneal injection for 4 weeks to induce diabetes in CD-1 mice. Water maze, Y maze, and new object recognition experiment were applied to detect the model group mice. The results showed significant cognitive impairment in the model group. After the treatment with newly synthesized adamantane derivatives and dipeptidyl peptidase 4, the behavioral performance significantly improved (Piatkowska-Chmiel et al., 2022). In addition, it was found by behavioral testing that the learning and memory ability of the high-glucose and high-fat combined with STZ intraperitoneal injection mouse model group was significantly lower compared with the control group. However, after treatment with dihydromyricetin, the learning and memory ability was significantly improved, indicating that dihydromyricetin can significantly improve cognitive dysfunction in type 2 diabetic mice (Zhu et al., 2017). In this study, the behavioral test results were basically consistent with the abovementioned studies. We found that compared with the control group, the postmenopausal diabetic mouse model group exhibited more chaotic movements and longer escape latency in the water maze test, and the number of cross-platforms in the water maze was reduced. In the Y-maze experiment, the

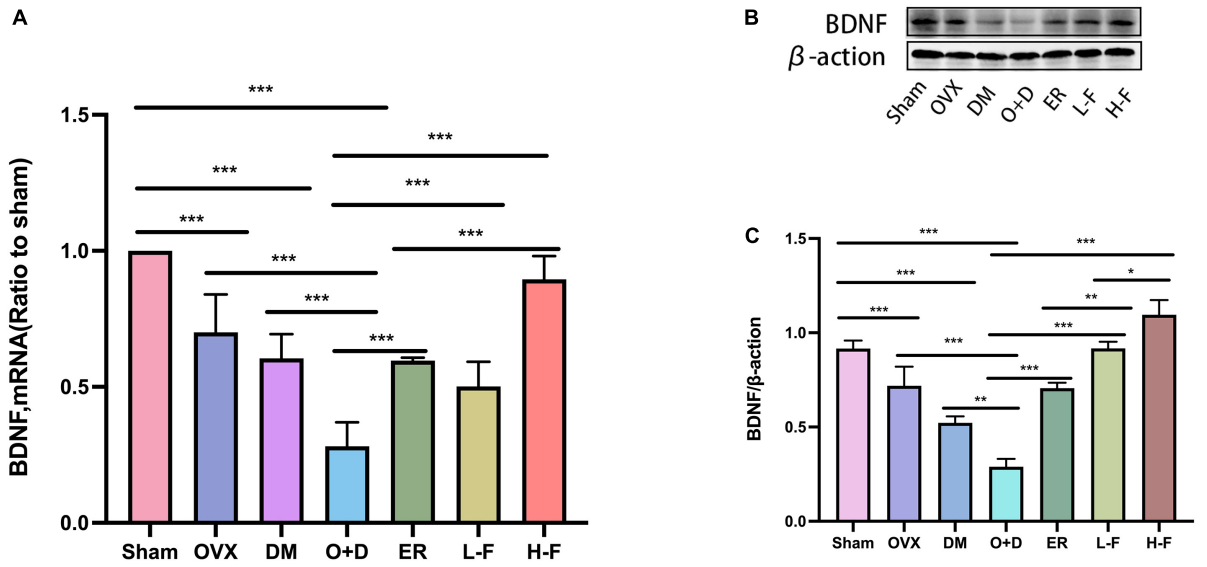

FIGURE 7
FTS•B increases the level of BDNF in the hippocampus of ovariectomized diabetic mice. **(A)** Quantitative analysis of the mRNA expression of BDNF. $n = 6$. **(B)** Representative western blotting showing BDNF expression level. **(C)** Quantitative analysis of BDNF expression. $n = 3$. $^{*}P < 0.05$, $^{**}P < 0.01$, $^{***}P < 0.001$, and ns indicates not significant.

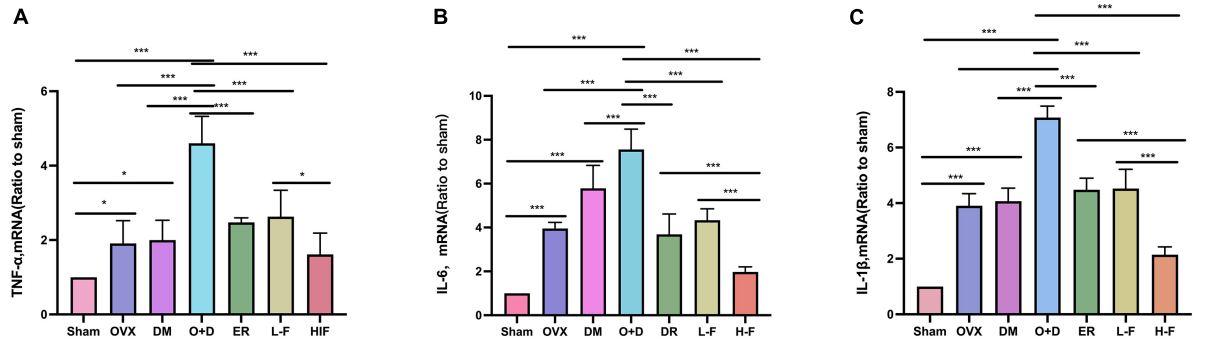

FIGURE 8
FTS•B inhibits the mRNA expression of factors related to hippocampal neuroinflammation in ovariectomized diabetic mice. **(A–C)** Quantitative analysis of the mRNA expression of TNF-α, IL-6, and IL-1β in the hippocampus. $n = 6$. $^{*}P < 0.05$, $^{**}P < 0.01$, $^{***}P < 0.001$, and ns indicates not significant.

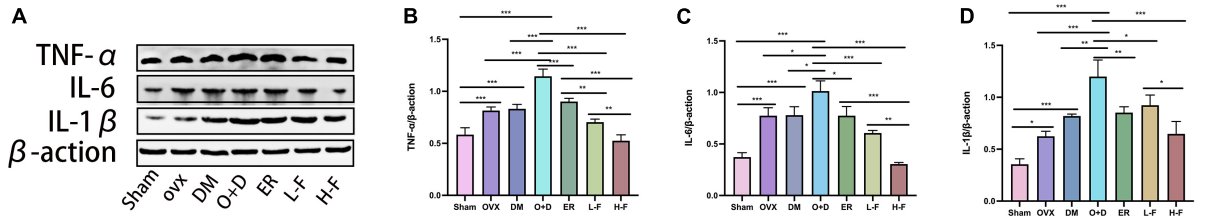

FIGURE 9
FTS•B inhibits the expression of factors related to hippocampal neuroinflammation in ovariectomized diabetic mice. **(A)** Representative western blotting showing TNF-α, IL-6, and IL-1β expression levels in the hippocampus. **(B–D)** Quantitative analysis of TNF-α, IL-6, and IL-1β expression. $n = 3$. $^{*}P < 0.05$, $^{**}P < 0.01$, $^{***}P < 0.001$, and ns indicates not significant.

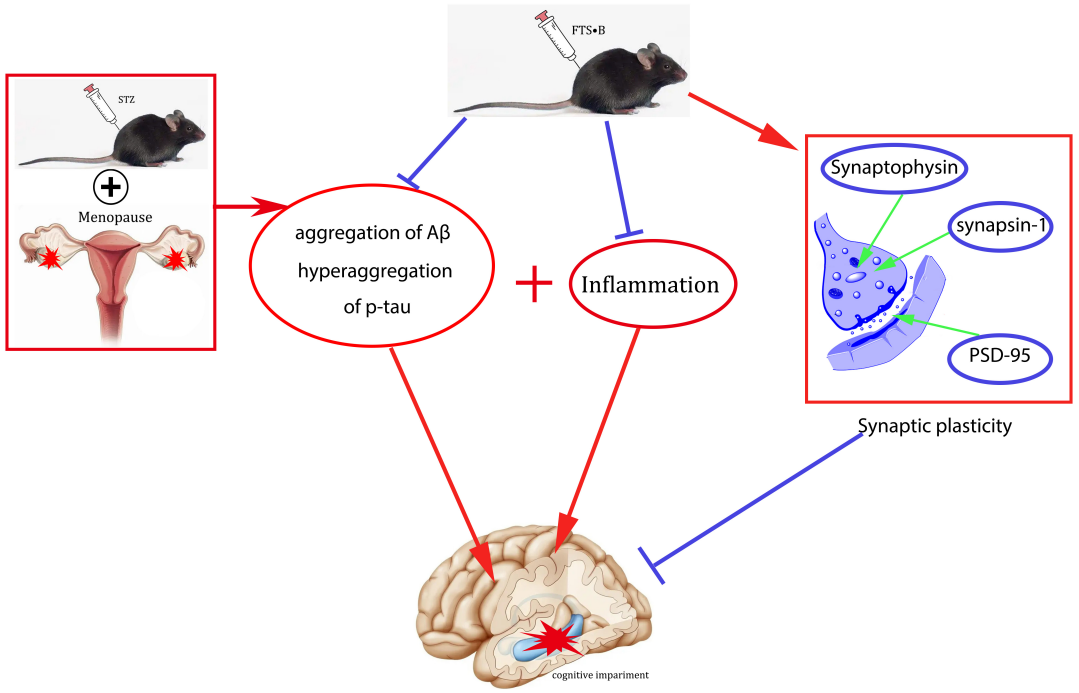

FIGURE 10
Schematic diagram of a potential mechanism of FTS•B in the treatment of cognitive dysfunction in ovariectomized diabetic mice.

spontaneous alternating movements were reduced in the model group. In the novel object recognition experiment, the mice in the model group were significantly less interested in objects in the experimental stage, especially in novel objects. However, FTS·B treatment significantly reversed the above phenomenon, indicating that FTS·B can effectively improve cognitive dysfunction in postmenopausal diabetic mice.

The hippocampus is an important functional region of the brain, and it is mainly involved in memory, learning, executive ability, and attention regulation (Wikenheiser and Schoenbaum, 2016). Arroyo-Garcia et al. (2021) showed that the morphological changes in the hippocampus are closely related to a decline in cognitive function. In addition, some studies used H&E staining to observe the histological changes in the neurons of the hippocampus, which can be used to assess cognitive function (Yang et al., 2022). In this study, we used H&E staining to observe the changes in hippocampal morphology. Fortunately, the results are consistent with other studies. We also used Nissl staining and found that FTS·B significantly improved the hippocampal structure and neuron loss in the ovariectomized diabetic mice model, suggesting that FTS·B can significantly improve the cognitive function of menopausal diabetic mice.

Previous studies have not fully elucidated the specific pathogenesis of cognitive impairment in postmenopausal diabetes. It has been reported that Aβ deposition and neurofibrillary tangles are the main pathological changes in brain cognitive impairment (Zhang et al., 2022). Neurofibrillary tangles consist of intracellular self-assembled p-tau bundles that are induced by Aβ deposition and lead to neuronal degeneration (Kim et al., 2015). Aberrant neurogenesis is considered an important causative event of cognitive impairment (Anacker and Hen, 2017; Cuartero et al., 2019). Neurotrophic factors play a crucial role in neurogenesis (Agrimi et al., 2019). It has been found that BDNF is an important neurotrophic factor and its signaling inhibits autophagy in an adult brain by transcriptionally downregulating key (Patterson, 2015; Chou et al., 2020) components of the autophagy machinery and that genetic ablation of BDNF in the nervous system leads to uncontrolled increases in autophagy in the adult brain and is associated with severe synaptic defect (Nikoletopoulou et al., 2017). Decreased levels of BDNF in the hippocampus can aggravate cognitive impairment. In this study, we found that FTS·B significantly enhanced the learning and memory abilities of postmenopausal diabetic mice and significantly inhibited the deposition of Aβ and neurofibrillary tangles composed of p-tau protein. However, FTS·B significantly increased the expression of BDNF in the hippocampus and effectively improved its cognitive dysfunction.

Neuroinflammation is an important phenotype and a key mediator of DACI and plays an important role in its pathogenesis (Albazal et al., 2021). Neuroinflammation can

amplify itself by increasing tauopathy and Aβ deposition through inflammatory cytokines such as IL-1β, IL-6, and TNF-α (Cavanagh and Wong, 2018). Choi et al. (2019) found that the central nervous system inflammation is closely associated with pathological neurodegenerative diseases. Some studies have shown that proinflammatory cytokines (IL-1β, IL-6, and TNF-α) can interfere with insulin signal transduction and participate in insulin resistance and DACI (Degirmenci et al., 2019). However, the relationship between neuroinflammation and menopausal diabetic encephalopathy is unknown. In this study, we found that FTS·B significantly improved cognitive dysfunction by reducing the expression of inflammatory cytokines IL-1β, IL-6, and TNF-α in the hippocampus of postmenopausal diabetic mice.

In this study, we used bilateral ovariectomy and STZ intraperitoneal injection to create a menopausal diabetes model. FTS·B was found to effectively inhibit the progression of menopausal diabetic encephalopathy through behavioral experiments, histological staining, and mRNA and protein expression levels of inflammation. However, there are some limitations in this study. The specific targets and related mechanisms of FTS·B in the hippocampus have not been fully understood. Furthermore, the subtle morphological changes of synapses were not studied in this experiment. In future studies, we will use a staining technique, such as Golgi staining, to visualize changes in the synaptic structure. Meanwhile, we will focus on *in vitro* experiments and further explore its deeper mechanism by applying anti-inflammatory pathway inhibitors.

Conclusion

In conclusion, this study systematically reports the neuroprotective effects of FTS·B in ovariectomized diabetic mice, including decreased fasting blood glucose, improved behavioral performance, normalized hippocampal morphology, increased synaptic plasticity, and improved Aβ deposition and tau phosphorylation. FTS·B can also increase the expression of BDNF and inhibit the expression of inflammatory factors (**Figure 10**), thereby restoring the cognitive function of postmenopausal diabetes. Therefore, this study suggests that FTS·B may be a potential treatment for postmenopausal diabetic encephalopathy.

Data availability statement

The raw data supporting the conclusions of this article will be made available by the authors, without undue reservation.

Ethics statement

The animal study was reviewed and approved by the North China University of Science and Technology Application.

Author contributions

HF designed the study. XN and QS kept the animal and analyzed the data. XX, YY, YFZ, YMZ, and HZ critically reviewed the data. XN drafted the manuscript. All authors contributed to interpreting the data, critically revising the manuscript, and approved the final version.

Conflict of interest

The authors declare that the research was conducted in the absence of any commercial or financial relationships that could be construed as a potential conflict of interest.

Publisher's note

All claims expressed in this article are solely those of the authors and do not necessarily represent those of their affiliated organizations, or those of the publisher, the editors and the reviewers. Any product that may be evaluated in this article, or claim that may be made by its manufacturer, is not guaranteed or endorsed by the publisher.

References

Agrimi, J., Spalletti, C., Baroni, C., Keceli, G., Zhu, G., Caragnano, A., et al. (2019). Obese mice exposed to psychosocial stress display cardiac and hippocampal dysfunction associated with local brain-derived neurotrophic factor depletion. *EBioMedicine* 47, 384–401. doi: 10.1016/j.ebiom.2019.08.042

Albazal, A., Delshad, A. A., and Roghani, M. (2021). Melatonin reverses cognitive deficits in streptozotocin-induced type 1 diabetes in the rat through attenuation of oxidative stress and inflammation. *J. Chem. Neuroanat.* 112:101902. doi: 10.1016/j.jchemneu.2020.101902

Albert, K. M., and Newhouse, P. A. (2019). Estrogen, stress, and depression: Cognitive and biological interactions. *Annu. Rev. Clin. Psychol.* 15, 399–423. doi: 10.1146/annurev-clinpsy-050718-095557

Anacker, C., and Hen, R. (2017). Adult hippocampal neurogenesis and cognitive flexibility – linking memory and mood. *Nat. Rev. Neurosci.* 18, 335–346. doi: 10.1038/nrn.2017.45

Arroyo-Garcia, L. E., Tendilla-Beltran, H., Vazquez-Roque, R. A., Jurado-Tapia, E. E., Diaz, A., Aguilar-Alonso, P., et al. (2021). Amphetamine sensitization alters

hippocampal neuronal morphology and memory and learning behaviors. *Mol. Psychiatry* 26, 4784–4794. doi: 10.1038/s41380-020-0809-2

Bansal, S., and Chopra, K. (2015). Differential role of estrogen receptor modulators in depression-like behavior and memory impairment in rats with postmenopausal diabetes. *Menopause* 22, 1117–1124. doi: 10.1097/GME.0000000000000435

Bragg, F., Holmes, M. V., Iona, A., Guo, Y., Du, H., Chen, Y., et al. (2017). Association between diabetes and cause-specific mortality in rural and urban areas of China. *JAMA* 317, 280–289. doi: 10.1001/jama.2016.19720

Cavanagh, C., and Wong, T. P. (2018). Preventing synaptic deficits in Alzheimer's disease by inhibiting tumor necrosis factor alpha signaling. *IBRO Rep.* 4, 18–21. doi: 10.1016/j.ibror.2018.01.003

Choi, J., Kim, J., Min, D. Y., Jung, E., Lim, Y., Shin, S. Y., et al. (2019). Inhibition of TNFalpha-induced interleukin-6 gene expression by barley (*Hordeum vulgare*) ethanol extract in BV-2 microglia. *Genes Genomics* 41, 557–566. doi: 10.1007/s13258-018-00781-8

Chou, L. Y., Chao, Y. M., Peng, Y. C., Lin, H. C., and Wu, Y. L. (2020). Glucosamine enhancement of BDNF expression and animal cognitive function. *Molecules* 25:3667. doi: 10.3390/molecules25163667

Chung, W. S., Welsh, C. A., Barres, B. A., and Stevens, B. (2015). Do glia drive synaptic and cognitive impairment in disease? *Nat. Neurosci.* 18, 1539–1545.

Cuartero, M. I., de la Parra, J., Perez-Ruiz, A., Bravo-Ferrer, I., Duran-Laforet, V., Garcia-Culebras, A., et al. (2019). Abolition of aberrant neurogenesis ameliorates cognitive impairment after stroke in mice. *J. Clin. Invest.* 129, 1536–1550. doi: 10.1172/JCI120412

Degirmenci, I., Ozbayer, C., Kebapci, M. N., Kurt, H., Colak, E., and Gunes, H. V. (2019). Common variants of genes encoding TLR4 and TLR4 pathway members TIRAP and IRAK1 are effective on MCP1, IL6, IL1beta, and TNFalpha levels in type 2 diabetes and insulin resistance. *Inflamm. Res.* 68, 801–814. doi: 10.1007/s00011-019-01263-7

Goyal, A., and Garabadu, D. (2020). Roflumilast attenuates cognitive deficits in estrogen insufficient rats. *Behav. Pharmacol.* 31, 671–687. doi: 10.1097/FBP.0000000000000574

Jiang, W. L., Fu, F. H., Xu, B. M., Tian, J. W., Zhu, H. B., and Jian, H. (2010a). Cardioprotection with forsythoside B in rat myocardial ischemia-reperfusion injury: Relation to inflammation response. *Phytomedicine* 17, 635–639. doi: 10.1016/j.phymed.2009.10.017

Jiang, W. L., Tian, J. W., Fu, F. H., Zhu, H. B., and Hou, J. (2010b). Neuroprotective efficacy and therapeutic window of forsythoside B: In a rat model of cerebral ischemia and reperfusion injury. *Eur. J. Pharmacol.* 640, 75–81. doi: 10.1016/j.ejphar.2010.04.055

Jiang, W. L., Yong, X., Zhang, S. P., Zhu, H. B., and Jian, H. (2012). Forsythoside B protects against experimental sepsis by modulating inflammatory factors. *Phytother. Res.* 26, 981–987. doi: 10.1002/ptr.3668

Jin, K., Lu, J., Yu, Z., Shen, Z., Li, H., Mou, T., et al. (2020). Linking peripheral IL-6, IL-1beta and hypocretin-1 with cognitive impairment from major depression. *J. Affect. Disord.* 277, 204–211. doi: 10.1016/j.jad.2020.08.024

Kim, J. Y., Lee, H. K., Jang, J. Y., Yoo, J. K., and Seong, Y. H. (2015). Ilex latifolia prevents amyloid beta protein (25-35)-induced memory impairment by inhibiting apoptosis and Tau phosphorylation in mice. *J. Med. Food* 18, 1317–1326. doi: 10.1089/jmf.2015.3443

Li, Z., Chen, X., Lu, W., Zhang, S., Guan, X., Li, Z., et al. (2017). Anti-Oxidative stress activity is essential for *Amanita caesarea* mediated neuroprotection on glutamate-induced apoptotic HT22 cells and an Alzheimer's disease mouse model. *Int. J. Mol. Sci.* 18:1623. doi: 10.3390/ijms18081623

Liu, Y. W., Zhu, X., Li, W., Lu, Q., Wang, J. Y., Wei, Y. Q., et al. (2012). Ginsenoside re attenuates diabetes-associated cognitive deficits in rats. *Pharmacol. Biochem. Behav.* 101, 93–98. doi: 10.1016/j.pbb.2011.12.003

Liu, Z., Dai, X., Zhang, H., Shi, R., Hui, Y., Jin, X., et al. (2020). Gut microbiota mediates intermittent-fasting alleviation of diabetes-induced cognitive impairment. *Nat. Commun.* 11:855. doi: 10.1038/s41467-020-14676-4

Mohammadi, M., and Zare, Z. (2020). Effects of treadmill exercise on cognitive functions and anxiety-related behaviors in ovariectomized diabetic rats. *Physiol. Behav.* 224:113021. doi: 10.1016/j.physbeh.2020.113021

Nikoletopoulou, V., Sidiropoulou, K., Kallergi, E., Dalezios, Y., and Tavernarakis, N. (2017). Modulation of autophagy by BDNF underlies synaptic plasticity. *Cell Metab.* 26, 230–242.e5. doi: 10.1016/j.cmet.2017.06.005

Pang, K., Jiang, R., Zhang, W., Yang, Z., Li, L.-L., Shimozawa, M., et al. (2022). An App knock-in rat model for Alzheimer's disease exhibiting Aβ and tau pathologies, neuronal death and cognitive impairments. *Cell Res.* 32, 157–175. doi: 10.1038/s41422-021-00582-x

Patterson, S. L. (2015). Immune dysregulation and cognitive vulnerability in the aging brain: Interactions of microglia. IL-1beta, BDNF and synaptic plasticity. *Neuropharmacology* 96, 11–18. doi: 10.1016/j.neuropharm.2014.12.020

Piatkowska-Chmiel, I., Gawronska-Grzywacz, M., Popiolek, L., Herbet, M., and Dudka, J. (2022). The novel adamantane derivatives as potential mediators of inflammation and neural plasticity in diabetes mice with cognitive impairment. *Sci. Rep.* 12:6708. doi: 10.1038/s41598-022-10187-y

Podda, M. V., Cocco, S., Mastrodonato, A., Fusco, S., Leone, L., Barbati, S. A., et al. (2016). Anodal transcranial direct current stimulation boosts synaptic plasticity and memory in mice via epigenetic regulation of BDNF expression. *Sci. Rep.* 6:22180. doi: 10.1038/srep22180

Qu, W., Suazo, K. F., Liu, W., Cheng, S., Jeong, A., Hottman, D., et al. (2021). Neuronal protein farnesylation regulates hippocampal synaptic plasticity and cognitive function. *Mol. Neurobiol.* 58, 1128–1144.

Sadeghi, A., Hami, J., Razavi, S., Esfandiary, E., and Hejazi, Z. (2016). The effect of diabetes mellitus on apoptosis in hippocampus: Cellular and molecular aspects. *Int. J. Prev. Med.* 7:57. doi: 10.4103/2008-7802.178531

Skundric, D. S., and Lisak, R. P. (2003). Role of neuropoietic cytokines in development and progression of diabetic polyneuropathy: From glucose metabolism to neurodegeneration. *Exp. Diabesity Res.* 4, 303–312. doi: 10.1155/EDR.2003.303

Tang, S. S., Ren, Y., Ren, X. Q., Cao, J. R., Hong, H., Ji, H., et al. (2019). ERalpha and/or ERbeta activation ameliorates cognitive impairment, neurogenesis and apoptosis in type 2 diabetes mellitus mice. *Exp. Neurol.* 311, 33–43. doi: 10.1016/j.expneurol.2018.09.002

Wang, B. N., Wu, C. B., Chen, Z. M., Zheng, P. P., Liu, Y. Q., Xiong, J., et al. (2021). DL-3-n-butylphthalide ameliorates diabetes-associated cognitive decline by enhancing PI3K/Akt signaling and suppressing oxidative stress. *Acta Pharmacol. Sin.* 42, 347–360. doi: 10.1038/s41401-020-00583-3

Wang, S., Yu, Y., Feng, Y., Zou, F., Zhang, X., Huang, J., et al. (2016). Protective effect of the orientin on noise-induced cognitive impairments in mice. *Behav. Brain Res.* 296, 290–300. doi: 10.1016/j.bbr.2015.09.024

Wang, T., Wu, J., Dong, W., Wang, M., Zhong, X., Zhang, W., et al. (2021). The MEK inhibitor U0126 ameliorates diabetic cardiomyopathy by restricting XBP1's phosphorylation dependent SUMOylation. *Int. J. Biol. Sci.* 17, 2984–2999. doi: 10.7150/ijbs.60459

Wang, Z., Xia, Q., Liu, X., Liu, W., Huang, W., Mei, X., et al. (2018). Phytochemistry, pharmacology, quality control and future research of *Forsythia suspensa* (Thunb.) Vahl: A review. *J. Ethnopharmacol.* 210, 318–339. doi: 10.1016/j.jep.2017.08.040

Wikenheiser, A. M., and Schoenbaum, G. (2016). Over the river, through the woods: Cognitive maps in the hippocampus and orbitofrontal cortex. *Nat. Rev. Neurosci.* 17, 513–523. doi: 10.1038/nrn.2016.56

Yan, W. H., Zhang, C. X., Xing, T., Gong, X., Yang, Y. X., Li, Y. N., et al. (2018). [Nicorandil improves cognitive dysfunction in mice with streptozotocin-induced diabetes]. *Nan Fang Yi Ke Da Xue Xue Bao* 38, 384–389.

Yang, Y., Song, J., Liu, N., Wei, G., Liu, S., Zhang, S., et al. (2022). Salvianolic acid a relieves cognitive disorder after chronic cerebral ischemia: Involvement of Drd2/Cryab/NF-kappaB pathway. *Pharmacol. Res.* 175:105989. doi: 10.1016/j.phrs.2021.105989

Zhang, Y. Y., Xin, X., Yang, C. Y., Wang, X. Y., Xia, T., and Wang, H. Y. (2022). [The application value of plasma heterogeneous nuclear ribonucleoprotein A2/B1, Abeta42 and P-tau in the preoperative diagnosis of mild cognitive dysfunction]. *Zhonghua Yi Xue Za Zhi* 102, 321–325. doi: 10.3760/cma.j.cn112137-20210830-01977

Zhu, Z. M., Yang, J. H., Yang, S. S., He, J. Q., Zhang, K. F., Feng, S. D., et al. (2017). [The effects of dihydromyricetin on cognitive dysfunction in type 2 diabetes mice]. *Zhongguo Ying Yong Sheng Li Xue Za Zhi* 33, 323–328. doi: 10.12047/j.cjap.5478.2017.079

frontiers | Frontiers in Aging Neuroscience

TYPE Original Research
PUBLISHED 16 March 2023
DOI 10.3389/fnagi.2023.1152065

OPEN ACCESS

EDITED BY
Dario Maschi,
Washington University in St. Louis,
United States

REVIEWED BY
Giovanni Piccoli,
University of Trento, Italy
Francesca Longhena,
University of Brescia, Italy

*CORRESPONDENCE
Fabrizio Gardoni
✉ fabrizio.gardoni@unimi.it

SPECIALTY SECTION
This article was submitted to
Cellular and Molecular Mechanisms
of Brain-aging,
a section of the journal
Frontiers in Aging Neuroscience

RECEIVED 27 January 2023
ACCEPTED 03 March 2023
PUBLISHED 16 March 2023

CITATION
Ferrari E, Salvadè M, Zianni E, Brumana M,
DiLuca M and Gardoni F (2023) Detrimental
effects of soluble α-synuclein oligomers
at excitatory glutamatergic synapses.
Front. Aging Neurosci. 15:1152065.
doi: 10.3389/fnagi.2023.1152065

Detrimental effects of soluble α-synuclein oligomers at excitatory glutamatergic synapses

Elena Ferrari, Michela Salvadè, Elisa Zianni, Marta Brumana, Monica DiLuca and Fabrizio Gardoni*

Department of Pharmacological and Biomolecular Sciences (DiSFeB) "Rodolfo Paoletti", University of Milan, Milan, Italy

Introduction: Oligomeric and fibrillar species of the synaptic protein α-synuclein are established key players in the pathophysiology of Parkinson's disease and other synucleinopathies. Increasing evidence in the literature points to prefibrillar oligomers as the main cytotoxic species driving dysfunction in diverse neurotransmitter systems even at early disease stages. Of note, soluble oligomers have recently been shown to alter synaptic plasticity mechanisms at the glutamatergic cortico-striatal synapse. However, the molecular and morphological detrimental events triggered by soluble α-synuclein aggregates that ultimately lead to excitatory synaptic failure remain mostly elusive.

Methods: In the present study, we aimed to clarify the effects of soluble α-synuclein oligomers (sOligo) in the pathophysiology of synucleinopathies at cortico-striatal and hippocampal excitatory synapses. To investigate early defects of the striatal synapse *in vivo*, sOligo were inoculated in the dorsolateral striatum of 2-month-old wild-type C57BL/6J mice, and molecular and morphological analyses were conducted 42 and 84 days post-injection. In parallel, primary cultures of rat hippocampal neurons were exposed to sOligo, and molecular and morphological analyses were performed after 7 days of treatment.

Results: *In vivo* sOligo injection impaired the post-synaptic retention of striatal ionotropic glutamate receptors and decreased the levels of phosphorylated ERK at 84 days post-injection. These events were not correlated with morphological alterations at dendritic spines. Conversely, chronic *in vitro* administration of sOligo caused a significant decrease in ERK phosphorylation but did not significantly alter post-synaptic levels of ionotropic glutamate receptors or spine density in primary hippocampal neurons.

Conclusion: Overall, our data indicate that sOligo are involved in pathogenic molecular changes at the striatal glutamatergic synapse, confirming the detrimental effect of these species in an *in vivo* synucleinopathy model. Moreover, sOligo affects the ERK signaling pathway similarly in hippocampal and striatal neurons, possibly representing an early mechanism that anticipates synaptic loss.

KEYWORDS

Parkinson's disease, NMDA–receptor, dendritic spine, mice, glutamate

1. Introduction

The molecular mechanisms addressing the role of α-synuclein (αSyn) aggregates in the pathophysiology of Parkinson's disease are mostly elusive; however, a wide range of structurally diverse oligomeric and fibrillar species have been evaluated in *in vivo* and *in vitro* preclinical studies (Bousset et al., 2013; Chen et al., 2015; Pieri et al., 2016).

Prior to being deposited in insoluble inclusions, pre-amyloid αSyn aggregates can spread inter-neuronally, contributing to pathology propagation and synaptic alterations (Hansen et al., 2011; Bengoa-Vergniory et al., 2017; Cascella et al., 2022). However, studying the differential contribution of αSyn toxic aggregates in synucleinopathy progression is complicated by the broad heterogeneity of these pathological forms of the protein. Monitoring their spread and cytotoxic activity *in vivo* is challenging due to their unstable and dynamic nature (Estaun-Panzano et al., 2023). This is especially true for small soluble oligomeric species that can represent both early phases of the αSyn aggregation process or degradation by-products of larger aggregates (Kulenkampff et al., 2021; Bigi et al., 2022).

In recent years, increasing evidence has described the detrimental effects of αSyn protofibrils on various neurotransmitter systems and brain regions (Peelaerts et al., 2015; Lau et al., 2020) and the putative role of oligomeric forms as significant players in disease spread and neurodegeneration (Kulenkampff et al., 2021; Emin et al., 2022). Specifically, small soluble αSyn oligomers (sOligo), generated by *in vitro* reactions or isolated from post-mortem patients' brains, were shown to trigger inflammation and neurotoxicity *in vitro* more efficiently than larger aggregates (Emin et al., 2022). Moreover, fibrillar forms were suggested to induce neurotoxicity, even in an indirect manner, through the release of soluble oligomers. Once taken up by neurons, these aggregates could further sustain the spread of disease through cell-to-cell transfer, seeding, and the formation of new fibrils (Cascella et al., 2022). More specifically, a large number of studies in the past decade have investigated the synaptotoxicity of synuclein aggregates (Bate et al., 2010; Rockenstein et al., 2014; Paumier et al., 2015), identifying detrimental effects not only at the presynaptic level but also at the post-synaptic compartment level (Diogenes et al., 2012; Chen et al., 2015; Ferreira et al., 2017; Sarafian et al., 2017; Trudler et al., 2021). Interestingly, recent studies demonstrated the detrimental effect of αSyn sOligo and αSyn preformed fibrils (αSyn-PFF) on glutamatergic neurotransmission at cortico-striatal synapses in early stages of disease progression, long before the onset of significant dopaminergic nigrostriatal degeneration (Tozzi et al., 2016, 2021; Durante et al., 2019). αSyn-PFF can interfere with bidirectional synaptic plasticity, preventing the induction of both long-term potentiation and long-term depression (Tozzi et al., 2021). In addition, our group recently demonstrated that αSyn-PFF induces dendritic spines loss at cortico-striatal synapses, and this event was correlated with reduced post-synaptic availability of both AMPA receptor (AMPAR) and NMDA receptor (NMDAR) subunits (Ferrari et al., 2022). Conversely, despite evidence that αSyn sOligo can cause synaptic plasticity defects of the cortico-striatal synapse (Durante et al., 2019), their role in driving synucleinopathies at the excitatory glutamatergic synapse and the precise molecular events underlying these defects remain unclear.

We investigated the role of αSyn sOligo in the events underlying early αSyn-driven synaptic dysfunction. To this, sOligo were inoculated in the dorsolateral striatum of 2-month-old wild-type C57BL/6J mice, and molecular and morphological analyses were conducted 42 and 84 days post-injection. Since its first generation in Luk et al. (2012), these rodent models have been extensively characterized to exhibit slow and progressive deterioration of the nigrostriatal tract and dissemination of αSyn neuropathology, making them suitable to reproduce the early disease phases (Henderson et al., 2019; Gómez-Benito et al., 2020). Moreover, *in vivo* experiments were replicated *in vitro* in primary hippocampal neurons to produce a more complete picture of the effect of sOligo in mediating synaptic toxicity at glutamatergic synapses in different brain areas.

2. Materials and methods

2.1. Preparation of αsyn soluble oligomers

α-synuclein oligomers were generated through a recently reported oligomerization protocol with a few modifications (Durante et al., 2019). Recombinant human αSyn monomeric protein (Proteos, Kalamazoo, MI, USA) was thawed on ice, centrifuged at 13,000 × *g* for 10 min at 4°C, and the supernatant was retained (Polinski et al., 2018). After measurement of protein concentration, the solution was diluted to a final concentration of 2 mg/ml in phosphate-buffered saline (PBS) (Sigma-Aldrich) and incubated for 2 h at room temperature (RT) under constant agitation (1,000 rpm) in a benchtop Thermomixer. The solution was then aliquoted and stored at −80°C.

2.2. Transmission electron microscopy validation of sOligo preparation

For each experiment, the presence of oligomeric species in the solution was evaluated by negative staining protocol with a Talos L120C transmission electron microscope (TEM) (Thermo Fisher, Waltham, MA, USA) operating at 120 kV. Digital images were acquired using a 50 CETA-MTM 4k × 4k camera (Thermo Fisher). TEM analyses were performed at the Unitech NOLIMITS imaging facility of the University of Milan.

2.3. Animals

Experimental procedures were conducted following the National Institutes of Health Guide for the Care and Use of Laboratory Animals, the European Community Council Directives 2010/63/EU, and the Italian law 26/2014. Approval of all procedures involving animals were obtained from the local Animal Use Committee and the Italian Ministry of Health (permits 1200/2020-PR, 330/2018-PR and 5247B.N.YCK2018).

Two-month-old male C57BL/6J mice were housed in cages (two to four per cage) in a climate-controlled facility (22 ± 2°C), with *ad libitum* access to food and water throughout and a 12-h light–dark cycle (19:00–07:00 schedule). Each *ex vivo* experimental approach (spine morphology and biochemistry) was conducted using distinct cohorts of mice.

2.3.1. Surgical procedures

C57BL/6J male mice were anesthetized with a mixture of isoflurane/oxygen by inhalation and mounted on a stereotaxic frame (Stoelting) linked to a digital micromanipulator. Brain coordinates for the dorsolateral striatum were chosen as previously described (Luk et al., 2012; Ferrari et al., 2022): anterior–posterior, + 0.2 mm; medial–lateral, ± 2 mm; and dorsal–ventral, – 2.6 mm. For each hemisphere, 2.5 μl of αSyn sOligo (5 μg) (Luk et al., 2012; Tozzi et al., 2021; Ferrari et al., 2022) or PBS was infused through a 10 μl Hamilton syringe using a microinjection pump at a flow rate of 0.25 μl/min. The needle was left in place at the end of the injection for 4 min to allow the solution to flow out entirely.

2.3.2. Isolation of triton-insoluble post-synaptic fractions from mouse striata

To isolate Triton-insoluble post-synaptic fractions highly enriched in post-synaptic density proteins (Stanic et al., 2017), striata were homogenized with a Teflon-glass potter at 4°C in ice-cold buffer (pH 7.4) containing 0.32 M sucrose, 1 mM HEPES, 1 mM $MgCl_2$, 1 mM $NaHCO_3$, and 0.1 mM phenylmethanesulfonylfluoride supplemented with Complete™ protease inhibitor cocktail (Roche Diagnostics) and phosSTOP™ phosphatase inhibitor (Roche Diagnostics). An aliquot of the homogenate was frozen at −20°C and kept subsequent analysis, while the rest of the sample was spun at 13,000 × *g* for 15 min at 4°C. The resulting pellet (P2-crude membrane fraction) was resuspended in Triton-KCl buffer (1% Triton™ X-100 and 150 mM KCl). After 15 min incubation on ice, the solution was centrifuged at 100,000 × *g* for 1 h at 4°C. The pellet (triton-insoluble post-synaptic fraction) was resuspended in 20 mM HEPES buffer supplemented with Complete™ protease inhibitor cocktail tablets and stored at −80°C.

2.3.3. *Ex vivo* spine morphology

For *ex vivo* confocal imaging of the dendritic spines of striatal spiny projection neurons (SPNs), brain slices were labeled with DiI dye (Invitrogen), a fluorescent lipophilic carbocyanine dye that labels spine structures and fine dendritic arborization (Kim et al., 2007). The DiI labeling procedure was performed as previously described (Stanic et al., 2015). Briefly, after mouse cardiac perfusion with 1.5% paraformaldehyde (PFA) in 0.1 M phosphate buffer, DiI solid crystals were applied with a thin needle onto the region of interest on both sides of 3-mm brain slices comprising the striatum. The DiI dye was allowed to diffuse for 16 h in the dark at RT in 0.1 M phosphate buffer; slices were subsequently post-fixed with 4% PFA in 0.1 M phosphate buffer for 45 min at 4°C. Then, 100 μm striatal slices were obtained using a vibratome and mounted on Superfrost glass slides (Thermo Fisher) with Fluoroshield (Sigma) for confocal imaging. The Zeiss Confocal LSM900 system was used to acquire fluorescence images at 555 nm with a 63X objective and Z-stack of 0.45 μm. Analysis of spine morphology and density was performed using Fiji (ImageJ) software. Specifically, spine length and width were manually measured at selected regions of interest in basal dendrites, with a distance from the cell body of up to 300 μm. A total dendritic length of about 200–300 μm from an average of three basal dendrites was considered for each neuron. For each dendritic spine, the spine head and neck width and spine length were measured, and these values were used to classify dendritic spines into three categories (thin, stubby and mushroom) [see also (Harris et al., 1992; Gardoni et al., 2012)]. In particular, the length and the ratio between the width of head and the width of neck (Wh/Wn) were used as parameters for the classification as follows: protrusions having a length of more than 3 μm were considered as filopodia (and therefore excluded from the quantitative analysis), the others as spines; spines with a Wh/Wn ratio bigger than 1.7 were considered mushrooms; spines with a Wh/Wn ratio smaller than 1.7 were divided in stubby, if shorter than 1 μm, and thin if longer than 1 μm.

2.4. Primary hippocampal neuronal cultures

Primary hippocampal neuronal cultures were prepared from embryonic day 18–19 (E18-E19) Sprague–Dawley rat (Charles River, Milan, Italy). In details, the hippocampi were isolated from the embryos' brains under a dissecting microscope. Under a sterile hood, the isolated hippocampi were then washed with ice cold HBSS medium (Hank's balanced salt solution, Sigma) and then incubated at 37°C with HBSS supplemented with trypsin for 13 min to dissociate the tissue. Tissue dissociation was then blocked by washes with plating medium (DMEM) + glutamax (Invitrogen) with 10% Horse Serum (Euroclone) and 1% Pen/Strep (Invitrogen). Finally, neurons were plated on Poli-L-Lysine (Sigma)-coated culture supports/dishes in plating medium at a density of 20,000 and 37,500 cells/cm^2 for imaging and biochemical analyses, respectively. 16 h after plating, the medium was replaced with Neurobasal medium with 2% B27 supplement (Gibco), 1% Glutamax (Invitrogen) and 1% Pen/Strep (Invitrogen).

2.4.1. sOligo treatment of primary hippocampal neurons

α-synuclein sOligo aliquots were thawed at RT and diluted in sterile PBS to a final concentration of 0.1 μg/μl. As previously reported (Wu et al., 2019), a single dose of sOligo was added at *DIV9* (9 days *in vitro*) to the neuronal culture medium at a concentration of 2 μg/ml and was left for 7 days until *DIV16*. Control neurons were treated only with the vehicle solution (PBS).

2.4.2. *In vitro* spine morphology

In vitro spine morphology was performed as previously reported (Gardoni et al., 2012; Stanic et al., 2015; Dinamarca et al., 2016). Briefly, for *in vitro* morphological studies, neurons were transfected with an enhanced green fluorescent protein (EGFP) plasmid at *DIV7* using the calcium-phosphate coprecipitation method. Hippocampal neurons were fixed at *DIV16* for 15 min at RT in 4% PFA in PBS supplemented with 4% sucrose in PBS. Images were acquired using an inverted LSM900 confocal microscope (Zeiss) with a 63X objective (**Supplementary Figure 1**).

Neurons were randomly acquired from different coverslips from three independent experiments and analyzed using Fiji (ImageJ) software. Specifically, spine length and width were manually measured at selected regions of interest in basal dendrites, with a distance from the cell body of up to 300 μm. A total dendritic length of about 200–300 μm from an average of three basal dendrites was considered for each neuron. For quantitative analysis, the same method described above in (Section "2.3.3. *Ex vivo* spine morphology") was used.

2.4.3. Isolation of triton-insoluble post-synaptic fractions from primary hippocampal neurons

Primary hippocampal neurons were harvested at *DIV16* by mechanical scraping in lysis buffer containing 0.32 M sucrose, 1 mM HEPES, 1 mM $MgCl_2$, 1 mM $NaHCO_3$, and 0.1 mM phenylmethanesulfonylfluoride supplemented with Complete™ Protease Inhibitor Cocktail Tablets (Roche Diagnostics) and phosSTOP™ Phosphatase Inhibitor (Roche Diagnostics). Cell lysates were then homogenized using a glass-glass potter in ice-cold lysis buffer, and an aliquot of the total homogenate was stored at −20°C. The sample was centrifuged at 13,000 × *g* for 15 min at 4°C, and the pellet (P2-crude membrane fraction) was resuspended in Triton-KCl buffer (0.5% Triton™ X-100 and 150 mM KCl). After 15-min incubation at 4°C, samples were spun at 100,000 × *g* for 1 h at 4°C. The pellet (TIF) was resuspended in 20 mM HEPES buffer supplemented with Complete™ protease inhibitor cocktail tablets and stored at −80°C.

2.5. SDS-PAGE and Western blotting

The Bradford assay was used to determine the protein content of the homogenate and TIF samples from striatal and primary hippocampal neurons. Samples were then denatured chemically with Laemmli buffer and thermally by heating at 98°C for 10 min. For Western blotting analysis, a total of 10–25 μg of protein was separated by sodium dodecyl sulfate-polyacrylamide gel electrophoresis on 6–12% acrylamide/bisacrylamide gel and transferred to a nitrocellulose membrane (Biorad) by electroblotting. Membranes were blocked for 1 h at RT in blocking solution (I-block, TBS 1X, and 20% Tween-20) on a shaker and incubated with the specific primary antibody diluted in blocking solution overnight at 4°C. The next day, the membranes were washed three times in TBSt (TBS and 0.1% Tween20) and subsequently incubated with the corresponding horseradish peroxidase-conjugated secondary antibody diluted in blocking solution for 1 h at RT. After three washes with TBSt, the membranes were developed with electrochemiluminescence reagents (Biorad) and scanned with a Chemidoc (Biorad Universal Hood III) using Image Lab software (Biorad). Bands were quantified with computer-assisted imaging (Image Lab, Biorad). Protein levels were expressed as relative optical density measurements normalized to a housekeeping protein.

2.6. Antibodies

The primary antibodies used were: mouse anti-tubulin (1:30,000, #T9026, Sigma), rabbit anti-GAPDH (1:5,000, #sc-25778, Santa Cruz), rabbit anti-GluN2A (1:1,000, #M264, Sigma), rabbit anti-GluN2B (1:1,000, #718600, Invitrogen), mouse anti-GluN2D (1:1,000, #MAB5578, Millipore), rabbit anti-GluA1 (1:1,000, #13185, Cell Signaling), mouse anti-GluA2 (1:1,000, #75–002, Neuromab), mouse anti-GluA3 (1:1,000, #MAB5416, Millipore), polyclonal anti-Rph3A (1:2,000, Protein Tech, #11396-1-AP), mouse anti-PSD-95 (1:1,000, #K28/43, Neuromab), rabbit anti-tyrosine hydroxylase (1:10,000, #AB152, Millipore), rabbit anti-phospho-extracellular signal-regulated kinase (ERK) 44/42 (1:1,000, Cell Signaling, #9101), rabbit anti-ERK 44/42 (1:1,000, #9102, Cell Signaling), rabbit anti-phospho-cAMP responsive element binding protein (CREB) (1:1,000, #9198, Cell Signaling), and rabbit anti-CREB (1:1,000, #9197, Cell Signaling). The secondary horseradish peroxidase-linked antibodies used were goat anti-rabbit (1:10,000, #172-1019, Biorad) and goat anti-mouse (1:10,000, #172-1011, Biorad).

2.7. Statistical analyses

Image Lab software (Biorad) was used for the quantification of Western blot experiments. Protein levels are reported as relative optical density normalized on tubulin/GAPDH as housekeeping proteins. Images acquired through confocal microscopy were analyzed using Fiji (ImageJ) software.

Statistical analyses were performed using GraphPad Prism 8 software, and data are presented as mean ± standard error of the mean (SEM). The figure legends include the tests used to evaluate the statistical data significance. Specifically, the following tests were used, as appropriate: two-tailed unpaired Student's *t*-test, Mann–Whitney test, one-way ANOVA, and Kruskal–Wallis test. The numbers of neurons and mice used in each experiment are described in the figure legends.

3. Results

3.1. Post-synaptic molecular alterations of the cortico-striatal synapse induced by *in vivo* striatal injection of sOligo

α-synuclein oligomers were prepared using a validated protocol with some modifications [see section "2. Materials and methods"; (Polinski et al., 2018; Durante et al., 2019)]. The presence and the morphology of sOligo was assessed by TEM prior to their experimental use (**Supplementary Figure 2**). To characterize the impact of sOligo species at the cortico-striatal synapse, we injected sOligo into the dorsolateral striatum of 2-month-old mice (**Figure 1**). Control mice were injected with PBS, the vehicle of αSyn oligomerization. Taking into account previous studies addressing the detrimental effects of αSyn aggregates on glutamatergic synapses (Tozzi et al., 2021; Ferrari et al., 2022), molecular analyses were conducted at 42 and 84 days post-injection (dpi). We first investigated the molecular composition of the striatal glutamatergic post-synaptic compartment in terms of ionotropic glutamatergic receptor (iGluR) levels. To this aim, TIFs enriched in PSD proteins were extracted from mouse striata and iGluR expression was assessed by Western blotting. At 42 dpi, post-synaptic levels of AMPAR subunits GluA1, GluA2, and GluA3

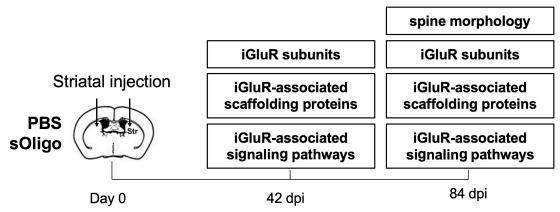

FIGURE 1
Schematic representation of the experimental procedures.

and NMDAR subunits GluN2A, GluN2B, and GluN2D were unchanged in sOligo mice compared with the controls (**Figure 2A**). Interestingly, these findings indicate a lack of toxicity of sOligo on post-synaptic iGluRs at 42 dpi, mirroring what previously reported following *in vivo* PFF-seeding (Ferrari et al., 2022). Considering the fundamental role of scaffolding proteins in regulating post-synaptic retention of iGluRs, we subsequently measured the post-synaptic levels of the most abundant PSD-associated protein, PSD-95, and the NMDAR-scaffolding partner, Rph3A, which were recently demonstrated to contribute to early synaptic dysfunction in experimental models of synucleinopathies induced by αSyn-PFF (Stanic et al., 2015; Ferrari et al., 2022). However, no alterations were observed for either scaffolding element at this time point (**Figure 2A**).

In contrast to the observations at 42 dpi, sOligo-injected mice exhibited a decrease in both AMPAR and NMDAR synaptic levels at 84 dpi (**Figures 2B, C**). In particular, we observed a significant decrease in the AMPAR-GluA1 subunit accompanied by a trend in decrease of the GluA2 and GluA3 subunits compared with PBS mice (**Figure 2B**). In addition, as shown in **Figure 2C**, levels of the NMDAR subunits GluN2A and GluN2D were significantly decreased upon oligomeric αSyn seeding. Again, these alterations in iGluR expression at 84 dpi mirrored findings in the PFF-mouse model (Ferrari et al., 2022), suggesting generalized toxicity of diverse αSyn species toward glutamatergic transmission that anticipates neurodegeneration. However, sOligo inoculation did not affect the integrity of dopaminergic striatal afferents, as shown by unaltered striatal tyrosine hydroxylase expression in sOligo-treated mice compared with controls (**Figure 2D**). Moreover, post-synaptic expression of Rph3A showed a trend in decrease in sOligo-mice compared with controls, while no significant change in the level of PSD-95 was detected (**Figure 2E**). Finally, no modifications of AMPAR and NMDAR subunits were observed in striatal homogenates at dpi 84 thus suggesting an impairment of their synaptic localization in absence of alterations of their total protein levels (**Supplementary Figure 3**).

We next investigated whether the molecular impairments of iGluRs were reflected in alterations of dendritic spine morphology of SPNs, the most abundant neuronal type of the striatum (Graveland and Difiglia, 1985). At 84 dpi, sOligo-mice displayed no variation in dendritic spine density compared to PBS mice, as reported by *ex vivo* morphological analyses (**Figure 2F**). SPNs of treated mice displayed normal spine length but a significant increase in spine width (**Figure 2F**), which could underlie compensatory mechanisms to the previously described modifications at the receptor level.

Considering the observed alteration of post-synaptic levels of iGluRs at 84 dpi, we evaluated possible modifications of downstream signaling pathways at this time point. Synaptic NMDAR activity promoted nuclear signaling to CREB, regulating gene expression of pro-survival factors and anti-apoptotic pathways together with the activity of the ERK (Hardingham and Bading, 2010). Therefore, the levels of phosphorylated ERK (p-ERK) and CREB (p-CREB) were assessed by Western blot analysis in the striatal homogenate. Interestingly, upon sOligo seeding, levels of p-ERK were significantly reduced compared with controls (**Figure 3A**). In contrast, no significant change in p-CREB level was detected at the same time point (**Figure 3B**). Finally, in accordance with the results about NMDAR and AMPAR synaptic localization (**Figure 2A**), no alterations of p-ERK levels were detected at dpi 42 (**Supplementary Figure 4**).

To summarize, at 84 dpi, *in vivo* sOligo seeding caused a reduction in the amount of iGluR complexes at the spines, primarily affecting the AMPAR GluA1 and the NMDAR GluN2A and GluN2D subunits, without altering the number of synaptic contacts. A decrease in p-ERK in these mice suggests that αSyn possibly affects downstream signaling pathways related to ERK activity. Moreover, the concomitant increase in dendritic spine width could represent an early compensatory mechanism to overcome the cortico-striatal signaling defects induced by sOligo.

3.2. Morphological and molecular effects induced by αSyn sOligo at the hippocampal synapse *in vitro*

Data collected using the *in vivo* sOligo-mouse model suggest that soluble αSyn species affect striatal post-synaptic molecular architecture and signaling. To further evaluate possible widespread sOligo toxicity toward glutamatergic neurotransmission, we aimed to evaluate the effect of sOligo on the hippocampal excitatory synapse. To this end, we used primary hippocampal neuronal cultures, a highly validated model for the assessment of synaptic structure and function (Dailey and Smith, 1996; Wu et al., 2019). Hippocampal cultures have been widely exploited to study the modulation of neuronal and synaptic homeostasis following acute and chronic αSyn exposure (Chen et al., 2015; Ferreira et al., 2017; Wu et al., 2019; Shrivastava et al., 2020). In addition, in line with previous findings, we recently demonstrated that 7-day exposure to αSyn-PFFs (2 μg/ml) induced diminished post-synaptic expression of GluN2A-containing NMDARs, leading to early spine loss (Ferrari et al., 2022). Therefore, taking the *in vitro* PFF-neuronal model as a reference, hippocampal primary neurons were treated at *DIV9* by administration of the αSyn sOligo preparation (2 μg/ml) in the culture medium. Control neurons were treated with the vehicle of αSyn solution (PBS). We first evaluated the composition of the glutamatergic post-synaptic compartment of treated hippocampal neurons at *DIV16*. As shown in **Figure 4A**, 7-day administration of sOligo did not significantly alter post-synaptic levels of the AMPAR GluA1, GluA2, and GluA3 subunits and the NMDAR GluN2A and GluN2B subunits, which are the most abundant iGluR subunits in the hippocampus. In line with these data, no alterations in the levels of scaffolding proteins Rph3A and PSD-95 were found in sOligo-treated neurons

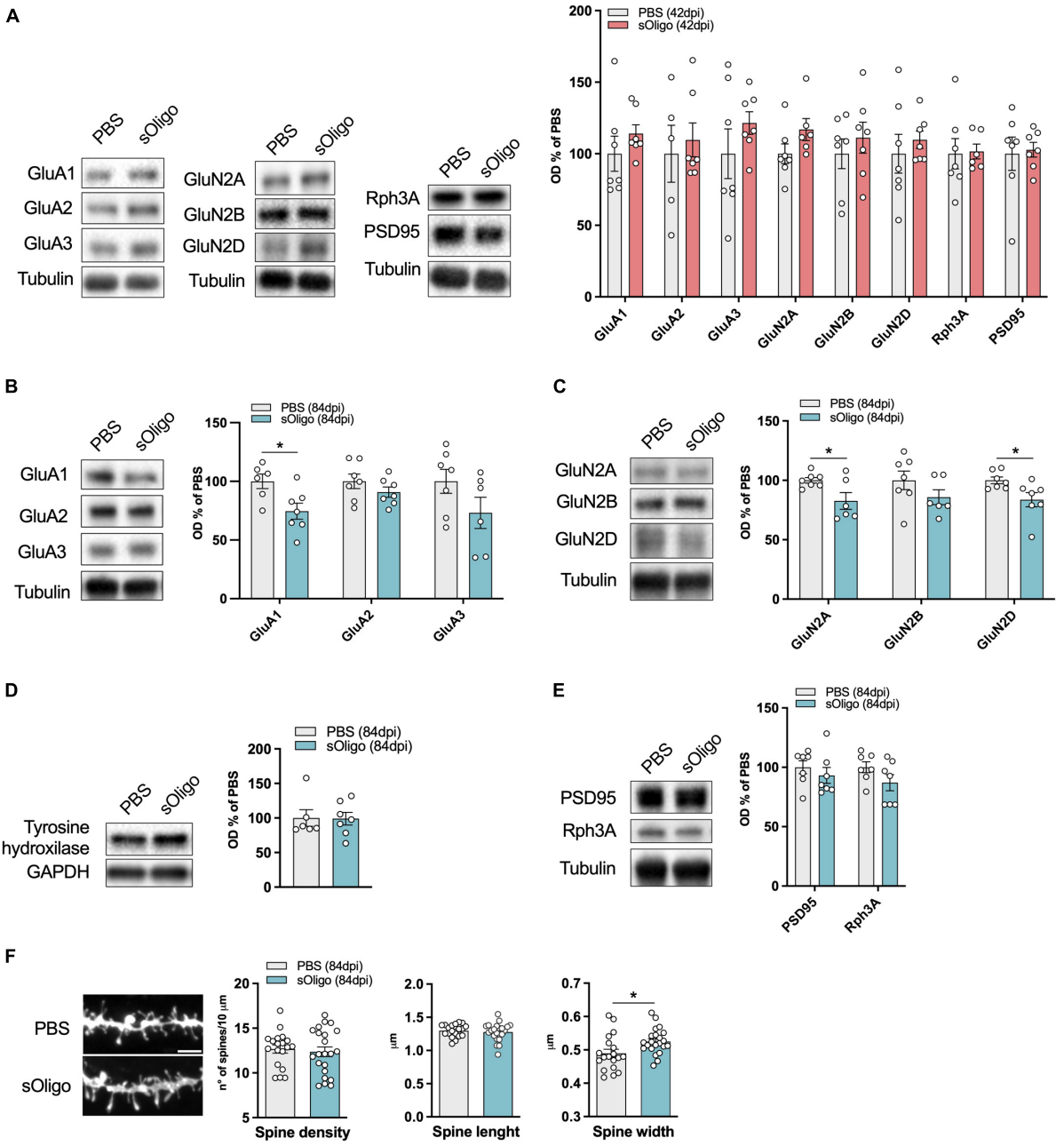

FIGURE 2
Molecular effects induced by *in vivo* striatal injection of αSyn soluble oligomers in mice at the corticostriatal synapse. **(A)** Post-synaptic levels of AMPAR (GluA1, GluA2, and GluA3) and NMDAR (GluN2A, GluN2B, and GluN2D) subunits and scaffolding proteins (Rph3A and PSD95) were evaluated by Western blot in striatal TIF of sOligo- and PBS-injected mice 42 dpi. Protein levels normalized on tubulin were reported as OD% of PBS-mice. n = 5–7 mice. Post-synaptic levels of **(B)** AMPAR (GluA1, GluA2, and GluA3) subunits, **(C)** NMDAR (GluN2A, GluN2B, and GluN2D) subunits and **(E)** scaffolding proteins (Rph3A and PSD95) were evaluated by Western blot in striatal TIF of sOligo- and PBS-injected mice 84 dpi. Protein levels normalized on tubulin were reported as OD% of PBS-mice. n = 5–7 mice. **(D)** Expression of the dopaminergic marker Tyrosine hydroxylase was evaluated by Western blot in striatal homogenates of sOligo- and PBS-injected mice 84 dpi. Protein levels normalized on GAPDH were reported as OD% of PBS-mice. n = 7 mice. **(F)** Representative confocal images and quantification of spine morphology analyses (spine density, spine length and spine width) of SPNs of sOligo- and PBS-injected mice 84 dpi. Scale bar: 3 µm. n = 19–22 neurons from 3 mice. Data are represented as mean ± SEM. *$P < 0.05$ (Student's t-test; data with non-normal distribution were tested with Mann–Whitney test).

compared with controls (Figure 4B). To assess the possible morphological effects of sOligo at dendritic spines at the same time point, hippocampal neurons were transfected with enhanced green fluorescent protein at *DIV7* and subsequently treated with sOligo preparation or PBS at *DIV9*. *In vitro* spine morphology analysis indicated no significant alterations in spine density at *DIV16* upon sOligo exposure compared with PBS administration (Figure 4C). Moreover, sOligo-treated neurons displayed normal spine length and width when compared to controls (Figure 4C), suggesting a lack of early synaptic toxicity of soluble species in this experimental setting. These findings indicate that, at the time point and dose evaluated, soluble αSyn species are incapable of

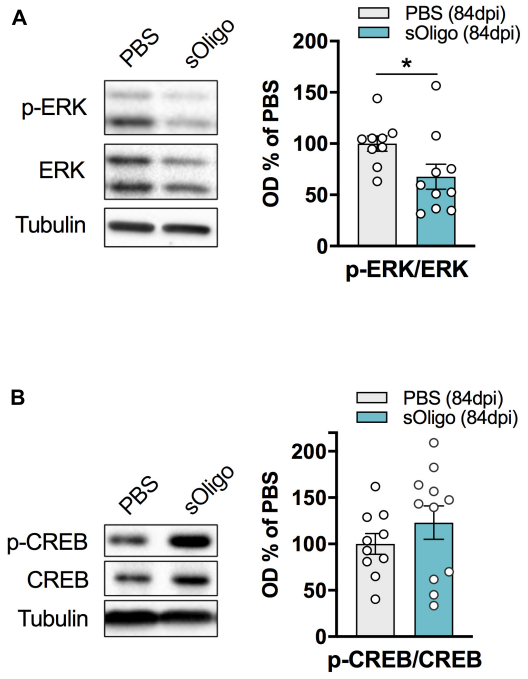

FIGURE 3
Effects of *in vivo* striatal injection of αSyn soluble oligomers in mice on ERK and CREB signaling. **(A)** Levels of pERK were evaluated by Western blot in striatal homogenates of sOligo- and PBS-injected mice 84 dpi. pERK level was normalized on total ERK expression and reported as OD% of PBS-mice. n = 9–10 mice. **(B)** Levels of pCREB were evaluated by Western blot in striatal homogenates of sOligo- and PBS-injected mice 84 dpi. pCREB level was normalized on total CREB expression and reported as OD% of PBS-mice. n = 10–11 mice. Data are represented as mean ± SEM. *$P < 0.05$ (Student's t-test; data with non-normal distribution were tested with Mann–Whitney test).

triggering post-synaptic molecular or morphological alterations at hippocampal excitatory synapses, which contrasts what was recently reported in the αSyn-PFF *in vitro* model (Wu et al., 2019; Ferrari et al., 2022).

Because we detected the impact of sOligo on striatal ERK signaling *in vivo* (**Figure 3A**), we also evaluated p-ERK and p-CREB protein levels in the hippocampal neuronal homogenate by Western blot analysis. In agreement with the *in vivo* data, *in vitro* sOligo administration to neurons induced a decrease in p-ERK at *DIV16* (**Figure 4D**). In contrast, p-CREB levels were not significantly affected by αSyn treatment (**Figure 4E**).

4. Discussion

Few studies are currently available regarding the detrimental effect of αSyn sOligo on post-synaptic glutamate receptors (Hüls et al., 2011; Diogenes et al., 2012; Ferreira et al., 2017; Yu et al., 2019). These reports are mainly focused on the *in vitro* effect of sOligo on rat (Diogenes et al., 2012; Ferreira et al., 2017) or mice (Hüls et al., 2011; Chen et al., 2015) hippocampal synapses and demonstrate that sOligo can alter excitatory synaptic plasticity acting on AMPARs or NMDAR function at glutamatergic synapses. More recently, small αSyn aggregates were reported to reduce the post-synaptic NMDAR-mediated current and impair long-term cortico-striatal potentiation of SPNs (Durante et al., 2019). In the present work, we aimed to elucidate the impact of these species on the molecular and structural organization of dendritic spines both *in vivo* at the cortico-striatal synapse and *in vitro* at the hippocampal synapse. Specifically, pre-fibrillar aggregates (sOligo) were injected into the dorsolateral striata of mice and administered to primary hippocampal neurons.

Here we show that sOligo-injected mice exhibited significant impairments in the molecular composition of the striatal synapse at 84 dpi. In agreement with previous studies (Durante et al., 2019), we observed that αSyn sOligo impacted the striatal post-synaptic availability of GluN2A-containing NMDARs, which are known to be enriched at striatal SPN synapses. However, the significant decrease in the levels of the GluN2D subunit, known to be selectively expressed at cholinergic interneurons (Bloomfield et al., 2007; Mellone et al., 2019), highlighted an overall impairment of NMDARs that was not restricted to striatal SPNs. The toxicity of αSyn toward GluN2D-containing NMDARs was previously suggested in the adeno-associated virus-based αSyn overexpression model and was recently confirmed in mice injected with αSyn-PFF (Tozzi et al., 2016; Ferrari et al., 2022).

In addition to defects in the composition of NMDARs, sOligo mice exhibited significantly decreased expression of the GluA1 subunit of AMPARs. Impaired AMPARs signaling due to decreased synaptic GluA1 localization induced by αSyn mutants has previously been described *in vivo* (Teravskis et al., 2018). Notably, the *in vivo* impairment of the post-synaptic AMPAR and NMDAR levels resembled the alterations caused by striatal injection of αSyn-PFF (Ferrari et al., 2022). In addition, the lack of a post-synaptic effect in both sOligo and PFF mice at dpi 42 suggests that the two diverse aggregated species share a similar timing of toxicity *in vivo* (Luk et al., 2012; Ferrari et al., 2022). However, while PFF mice exhibited a concurrent significant loss of dendritic spines at striatal SPNs at dpi 84 (Ferrari et al., 2022), sOligo inoculation did not lead to synapse loss, and dendritic spines showed only a significantly increased spine head width (Ferrari et al., 2022), possibly underlying a compensatory strategy to overcome early receptor defects. Overall, the data collected on the two αSyn animal models indicate the possible differential toxicity of sOligo and PFF, namely, more severe synaptic dysfunction leading to spine loss induced by PFF at the same time point. This phenomenon could be ascribed to a greater capability of PFFs for transmitting pathology, possibly due to their release of smaller degradation products, such as oligomers. Interestingly, a similar effect was reported comparing the *in vivo* impact of β-sheet oligomers and short fibrils on the dopaminergic system. The authors observed more robust neurotoxicity and a more severe disease phenotype induced by fibrillar fragments than oligomers, supporting the greater efficiency of fibrils in spreading the pathology (Froula et al., 2019).

A large number of possible molecular mechanisms could be involved in the sOligo-mediated effect we observed on synaptic AMPA and NMDA receptors. Several studies identified αSyn docking sites at the excitatory synapses (Shrivastava et al., 2015; Ferreira et al., 2017; Matiiv et al., 2022) and described putative mechanisms mediating αSyn internalization into neurons (Shrivastava et al., 2015; Ihse et al., 2017; Delenclos et al., 2019). Interestingly, other reports put forward the hypothesis of a specific activity of αSyn in promoting NMDAR internalization through

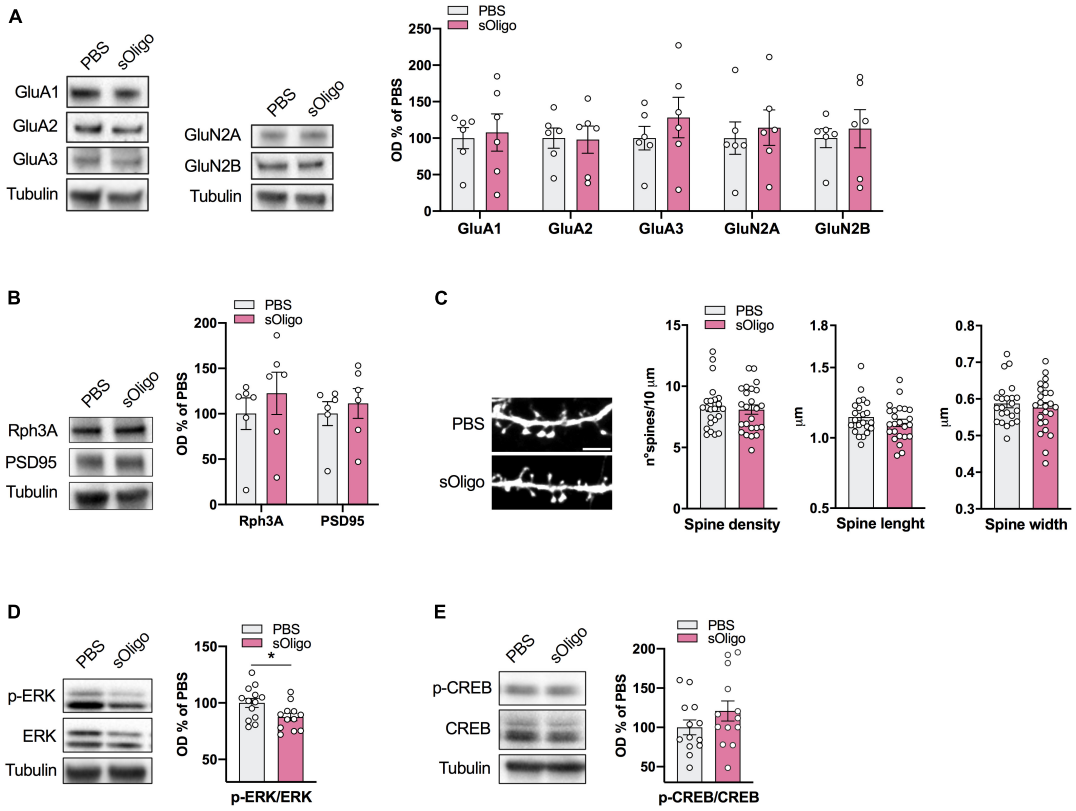

FIGURE 4
Molecular effects induced by αsyn sOligo at the hippocampal synapse *in vitro*. Primary cultures of rat hippocampal neurons were treated at DIV9 with either 2 µg/µl sOligo or PBS and analyses were performed at DIV16. Post-synaptic levels of **(A)** AMPAR (GluA1, GluA2, and GluA3) and NMDAR (GluN2A and GluN2B) subunits and **(B)** the scaffolding protein Rph3A and PSD-95 were evaluated by Western blot in TIF from sOligo- or PBS-neurons. Protein levels normalized on tubulin were reported as OD% of PBS-neurons. *n* = 6 independent cultures. **(C)** Representative confocal images and quantification of spine morphology analyses (spine density, spine length and spine width) of sOligo- and PBS-neurons at DIV16. Scale bar: 3 µm. *n* = 23–24 neurons from 3 independent cultures. **(D)** Levels of pERK were evaluated by Western blot in homogenates of sOligo- and PBS-neurons at DIV16. pERK level was normalized on total ERK expression and reported as OD% of PBS-neurons. *n* = 12–13 independent cultures. **(E)** Levels of pCREB were evaluated by Western blot in homogenates of sOligo- and PBS-neurons at DIV16. pCREB level was normalized on total CREB expression and reported as OD% of PBS-neurons. *n* = 14 independent cultures. Data are represented as mean ± SEM. *$P < 0.05$ (Student's *t*-test; data with non-normal distribution were tested with Mann–Whitney test).

different type of molecular events (Cheng et al., 2011; Chen et al., 2015; Navarria et al., 2015; Yang et al., 2020). In this regard, our group very recently showed that αSyn can directly interact with the NMDAR scaffolding protein Rph3A leading to a reduced membrane retention of GluN2A-containing NMDARs (Ferrari et al., 2022). In line with all these previous observations, here we show that *in vivo* intra-striatal injection of sOligo reduces at dpi 84 both AMPAR and NMDAR subunits at post-synaptic sites. Interestingly, we did not observe alterations of receptors' localization at synapses in primary hippocampal neurons treated with sOligo, thus putting forward the hypothesis of a different sensitivity of specific neuronal populations to αSyn.

Phosphorylation and activity of the mitogen-activated protein kinase ERK and the transcription factor CREB play a fundamental role in coupling synaptic NMDAR and AMPAR function to transcriptional changes underlying many neuroplasticity and pro-survival mechanisms (Wang et al., 2007). Aberrant activation of the ERK pathway was detected in late stages of Parkinson's disease and was correlated with the onset of dyskinesia (Santini et al., 2012). We found decreased levels of p-ERK in mice injected with sOligo at 84 dpi, indicating synaptic signaling defects compatible with decreased post-synaptic expression of NMDAR and AMPAR subunits. Interestingly, 7-day treatment of primary hippocampal neurons with sOligo induced a similar decreased phosphorylation of ERK in the absence of significant alterations in spine density and synaptic localization of NMDAR and AMPAR subunits. Of note, the loss of dendritic spines in cerebrocortical slices was observed upon application of a significantly higher αSyn sOligo concentration responsible for extra-synaptic NMDAR activation (Trudler et al., 2021). Interestingly, we recently demonstrated that 7-day exposure to αSyn-PFFs triggered spine loss coupled with decreased synaptic availability of GluN2A-containing NMDARs (Ferrari et al., 2022). Overall, these data further support different and milder toxicity mechanisms induced by sOligo compared with αSyn-PFF both *in vitro* and *in vivo*.

In conclusion, our data indicate that sOligo are involved in pathogenic molecular changes at the excitatory glutamatergic synapse, confirming the detrimental effect of these αSyn species in an *in vivo* synucleinopathy model. Moreover, sOligo affects the ERK signaling pathway similarly in hippocampal and striatal neurons, possibly representing an early mechanism that anticipates synaptic loss.

Data availability statement

The raw data supporting the conclusions of this article will be made available by the authors, without undue reservation.

Ethics statement

The animal study was reviewed and approved by the Animal Use Committee of University of Milano and the Italian Ministry of Health.

Author contributions

MD and FG contributed to the conception and design of the study. EF performed the statistical analysis. EF and FG wrote the first draft of the manuscript. EF, MS, EZ, and MB performed the *in vitro* and *in vivo* experiments. All authors contributed to manuscript revision, read, and approved the submitted version.

Funding

This work was supported by the grant from Ministero dell'Istruzione, dell'Università e della Ricerca (MIUR)–PRIN (Bando 2017, Prot. 2017ENN4FY to FG), by the Fondazione Cariplo (2021-1516 to FG), and by the Fondazione Regionale per la Ricerca Biomedica (Regione Lombardia), project (3433068_ Linking Park to MD).

Acknowledgments

We thank Anna Grassi and Ilaria Colombini for their excellent practical work. Part of this work was conducted at NOLIMITS, an advanced imaging facility established by the University of Milan.

Conflict of interest

The authors declare that the research was conducted in the absence of any commercial or financial relationships that could be construed as a potential conflict of interest.

Publisher's note

All claims expressed in this article are solely those of the authors and do not necessarily represent those of their affiliated organizations, or those of the publisher, the editors and the reviewers. Any product that may be evaluated in this article, or claim that may be made by its manufacturer, is not guaranteed or endorsed by the publisher.

Supplementary material

The Supplementary Material for this article can be found online at: https://www.frontiersin.org/articles/10.3389/fnagi.2023.1152065/full#supplementary-material

References

Bate, C., Gentleman, S., and Williams, A. (2010). α-synuclein induced synapse damage is enhanced by amyloid-β1-42. *Mol. Neurodegener.* 5:55. doi: 10.1186/1750-1326-5-55

Bengoa-Vergniory, N., Roberts, R. F., Wade-Martins, R., and Alegre-Abarrategui, J. (2017). Alpha-synuclein oligomers: A new hope. *Acta Neuropathol.* 134, 819–838. doi: 10.1007/s00401-017-1755-1

Bigi, A., Cascella, R., Chiti, F., and Cecchi, C. (2022). Amyloid fibrils act as a reservoir of soluble oligomers, the main culprits in protein deposition diseases. *BioEssays* 44:2200086. doi: 10.1002/bies.202200086

Bloomfield, C., O'Donnell, P., French, S. J., and Totterdell, S. (2007). Cholinergic neurons of the adult rat striatum are immunoreactive for glutamatergic N-methyl-d-aspartate 2D but not N-methyl-d-aspartate 2C receptor subunits. *Neuroscience* 150, 639–646. doi: 10.1016/j.neuroscience.2007.09.035

Bousset, L., Pieri, L., Ruiz-Arlandis, G., Gath, J., Jensen, P. H., Habenstein, B. et al. (2013). Structural and functional characterization of two alpha-synuclein strains. *Nat. Commun.* 4:2575. doi: 10.1038/ncomms3575

Cascella, R., Bigi, A., Cremades, N., and Cecchi, C. (2022). Effects of oligomer toxicity, fibril toxicity and fibril spreading in synucleinopathies. *Cell. Mol. Life Sci.* 79:174. doi: 10.1007/s00018-022-04166-9

Chen, S. W., Drakulic, S., Deas, E., Ouberai, M., Aprile, F. A., Arranz, R., et al. (2015). Structural characterization of toxic oligomers that are kinetically trapped during α-synuclein fibril formation. *Proc. Natl. Acad. Sci. U.S.A.* 112, E1994–E2003. doi: 10.1073/pnas.1421204112

Cheng, F., Vivacqua, G., and Yu, S. (2011). The role of alpha-synuclein in neurotransmission and synaptic plasticity. *J. Chem. Neuroanat.* 42, 242–248. doi: 10.1016/j.jchemneu.2010.12.001

Dailey, M. E., and Smith, S. J. (1996). The dynamics of dendritic structure in developing hippocampal slices. *J. Neurosci.* 16, 2983–2994. doi: 10.1523/JNEUROSCI.16-09-02983.1996

Delenclos, M., Burgess, J. D., Lamprokostopoulou, A., Outeiro, T. F., Vekrellis, K., and McLean, P. J. (2019). Cellular models of alpha-synuclein toxicity and aggregation. *J. Neurochem.* 150, 566–576. doi: 10.1111/jnc.14806

Dinamarca, M. C., Guzzetti, F., Karpova, A., Lim, D., Mitro, N., Musardo, S., et al. (2016). Ring finger protein 10 is a novel synaptonuclear messenger encoding activation of NMDA receptors in hippocampus. *eLife* 5:e12430. doi: 10.7554/eLife.12430

Diogenes, M. J., Dias, R. B., Rombo, D. M., Vicente Miranda, H., Maiolino, F., Guerreiro, P., et al. (2012). Extracellular alpha-synuclein oligomers modulate synaptic transmission and impair LTP via NMDA-receptor activation. *J. Neurosci.* 32, 11750–11762.

Durante, V., de Iure, A., Loffredo, V., Vaikath, N., De Risi, M., Paciotti, S., et al. (2019). Alpha-synuclein targets GluN2A NMDA receptor subunit causing striatal synaptic dysfunction and visuospatial memory alteration. *Brain* 142, 1365–1385. doi: 10.1093/brain/awz065

Emin, D., Zhang, Y. P., Lobanova, E., Miller, A., Li, X., Xia, Z., et al. (2022). Small soluble α-synuclein aggregates are the toxic species in Parkinson's disease. *Nat. Commun.* 13:5512. doi: 10.1038/s41467-022-33252-6

Estaun-Panzano, J., Arotcarena, M.-L., and Bezard, E. (2023). Monitoring α-synuclein aggregation. *Neurobiol. Dis.* 176:105966. doi: 10.1016/j.nbd.2022.105966

Ferrari, E., Scheggia, D., Zianni, E., Italia, M., Brumana, M., Palazzolo, L., et al. (2022). Rabphilin-3A as a novel target to reverse α-synuclein-induced synaptic loss in Parkinson's disease. *Pharmacol. Res.* 183:106375. doi: 10.1016/j.phrs.2022.106375

Ferreira, D. G., Temido-Ferreira, M., Vicente Miranda, H., Batalha, V. L., Coelho, J. E., Szegö, ÉM., et al. (2017). α-synuclein interacts with PrPC to induce cognitive impairment through mGluR5 and NMDAR2B. *Nat. Neurosci.* 20, 1569–1579. doi: 10.1038/nn.4648

Froula, J. M., Castellana-Cruz, M., Anabtawi, N. M., Camino, J. D., Chen, S. W., Thrasher, D. R., et al. (2019). Defining α-synuclein species responsible for Parkinson's disease phenotypes in mice. *J. Biol. Chem.* 294, 10392–10406. doi: 10.1074/jbc.RA119.007743

Gardoni, F., Sgobio, C., Pendolino, V., Calabresi, P., Di Luca, M., and Picconi, B. (2012). Targeting NR2A-containing NMDA receptors reduces L-DOPA-induced dyskinesias. *Neurobiol. Aging* 33, 2138–2144.

Gómez-Benito, M., Granado, N., García-Sanz, P., Michel, A., Dumoulin, M., and Moratalla, R. (2020). Modeling Parkinson's Disease with the alpha-synuclein protein. *Front. Pharmacol.* 11:356. doi: 10.3389/fphar.2020.00356

Graveland, G. A., and Difiglia, M. (1985). The frequency and distribution of medium-sized neurons with indented nuclei in the primate and rodent neostriatum. *Brain Res.* 327, 307–311. doi: 10.1016/0006-8993(85)91524-0

Hansen, C., Angot, E., Bergström, A.-L., Steiner, J. A., Pieri, L., Paul, G., et al. (2011). α-Synuclein propagates from mouse brain to grafted dopaminergic neurons and seeds aggregation in cultured human cells. *J. Clin. Invest.* 121, 715–725. doi: 10.1172/JCI43366

Hardingham, G. E., and Bading, H. (2010). Synaptic versus extrasynaptic NMDA receptor signalling: Implications for neurodegenerative disorders. *Nat. Rev. Neurosci.* 11, 682–696. doi: 10.1038/nrn2911

Harris, K., Jensen, F., and Tsao, B. (1992). Three-dimensional structure of dendritic spines and synapses in rat hippocampus (CA1) at postnatal day 15 and adult ages: Implications for the maturation of synaptic physiology and long-term potentiation [published erratum appears in J Neurosci 1992 Aug;12(8):following table of contents]. *J. Neurosci.* 12, 2685–2705. doi: 10.1523/JNEUROSCI.12-07-02685.1992

Henderson, M. X., Cornblath, E. J., Darwich, A., Zhang, B., Brown, H., Gathagan, R. J., et al. (2019). Spread of α-synuclein pathology through the brain connectome is modulated by selective vulnerability and predicted by network analysis. *Nat. Neurosci.* 22, 1248–1257. doi: 10.1038/s41593-019-0457-5

Hüls, S., Högen, T., Vassallo, N., Danzer, K. M., Hengerer, B., Giese, A., et al. (2011). AMPA-receptor-mediated excitatory synaptic transmission is enhanced by iron-induced α-synuclein oligomers: α-Synuclein oligomers alter synaptic transmission. *J. Neurochem.* 117, 868–878. doi: 10.1111/j.1471-4159.2011.07254.x

Ihse, E., Yamakado, H., van Wijk, X. M., Lawrence, R., Esko, J. D., and Masliah, E. (2017). Cellular internalization of alpha-synuclein aggregates by cell surface heparan sulfate depends on aggregate conformation and cell type. *Sci. Rep.* 7:9008. doi: 10.1038/s41598-017-08720-5

Kim, B. G., Dai, H.-N., McAtee, M., Vicini, S., and Bregman, B. S. (2007). Labeling of dendritic spines with the carbocyanine dye DiI for confocal microscopic imaging in lightly fixed cortical slices. *J. Neurosci. Methods* 162, 237–243. doi: 10.1016/j.jneumeth.2007.01.016

Kulenkampff, K., Wolf Perez, A.-M., Sormanni, P., Habchi, J., and Vendruscolo, M. (2021). Quantifying misfolded protein oligomers as drug targets and biomarkers in Alzheimer and Parkinson diseases. *Nat. Rev. Chem.* 5, 277–294. doi: 10.1038/s41570-021-00254-9

Lau, A., So, R. W. L., Lau, H. H. C., Sang, J. C., Ruiz-Riquelme, A., Fleck, S. C., et al. (2020). α-Synuclein strains target distinct brain regions and cell types. *Nat. Neurosci.* 23, 21–31. doi: 10.1038/s41593-019-0541-x

Luk, K. C., Kehm, V., Carroll, J., Zhang, B., O'Brien, P., Trojanowski, J. Q., et al. (2012). Pathological α-synuclein transmission initiates parkinson-like neurodegeneration in nontransgenic mice. *Science* 338, 949–953. doi: 10.1126/science.1227157

Matiiv, A. B., Moskalenko, S. E., Sergeeva, O. S., Zhouravleva, G. A., and Bondarev, S. A. (2022). NOS1AP Interacts with α-synuclein and aggregates in yeast and mammalian cells. *IJMS* 23:9102. doi: 10.3390/ijms23169102

Mellone, M., Zianni, E., Stanic, J., Campanelli, F., Marino, G., Ghiglieri, V., et al. (2019). NMDA receptor GluN2D subunit participates to levodopa-induced dyskinesia pathophysiology. *Neurobiol. Dis.* 121, 338–349. doi: 10.1016/j.nbd.2018.09.021

Navarria, L., Zaltieri, M., Longhena, F., Spillantini, M. G., Missale, C., Spano, P., et al. (2015). Alpha-synuclein modulates NR2B-containing NMDA receptors and decreases their levels after rotenone exposure. *Neurochem. Int.* 85–86, 14–23. doi: 10.1016/j.neuint.2015.03.008

Paumier, K. L., Luk, K. C., Manfredsson, F. P., Kanaan, N. M., Lipton, J. W., Collier, T. J., et al. (2015). Intrastriatal injection of pre-formed mouse α-synuclein fibrils into rats triggers α-synuclein pathology and bilateral nigrostriatal degeneration. *Neurobiol. Dis.* 82, 185–199. doi: 10.1016/j.nbd.2015.06.003

Peelaerts, W., Bousset, L., Van der Perren, A., Moskalyuk, A., Pulizzi, R., Giugliano, M., et al. (2015). α-Synuclein strains cause distinct synucleinopathies after local and systemic administration. *Nature* 522, 340–344. doi: 10.1038/nature14547

Pieri, L., Madiona, K. and Melki, R. (2016). Structural and functional properties of prefibrillar α-synuclein oligomers. *Sci. Rep.* 6:24526. doi: 10.1038/srep24526

Polinski, N. K., Volpicelli-Daley, L. A., Sortwell, C. E., Luk, K. C., Cremades, N., Gottler, L. M., et al. (2018). Best practices for generating and using alpha-synuclein pre-formed fibrils to model Parkinson's Disease in rodents. *JPD* 8, 303–322. doi: 10.3233/JPD-171248

Rockenstein, E., Nuber, S., Overk, C. R., Ubhi, K., Mante, M., Patrick, C., et al. (2014). Accumulation of oligomer-prone α-synuclein exacerbates synaptic and neuronal degeneration *in vivo*. *Brain* 137, 1496–1513. doi: 10.1093/brain/awu057

Santini, E., Feyder, M., Gangarossa, G., Bateup, H. S., Greengard, P., and Fisone, G. (2012). Dopamine- and cAMP-regulated Phosphoprotein of 32-kDa (DARPP-32)-dependent Activation of Extracellular Signal-regulated Kinase (ERK) and Mammalian Target of Rapamycin Complex 1 (mTORC1) Signaling in Experimental Parkinsonism. *J. Biol. Chem.* 287, 27806–27812. doi: 10.1074/jbc.M112.388413

Sarafian, T. A., Littlejohn, K., Yuan, S., Fernandez, C., Cilluffo, M., Koo, B.-K., et al. (2017). Stimulation of synaptoneurosome glutamate release by monomeric and fibrillated α-synuclein: Fibrillated α-Syn Enhances Synaptic Glutamate. *J. Neurosci. Res.* 95, 1871–1887. doi: 10.1002/jnr.24024

Shrivastava, A. N., Bousset, L., Renner, M., Redeker, V., Savistchenko, J., Triller, A., et al. (2020). Differential membrane binding and seeding of distinct α-synuclein fibrillar polymorphs. *Biophys. J.* 118, 1301–1320. doi: 10.1016/j.bpj.2020.01.022

Shrivastava, A. N., Redeker, V., Fritz, N., Pieri, L., Almeida, L. G., Spolidoro, M., et al. (2015). α−synuclein assemblies sequester neuronal α3-Na^+ /K^+ – ATP ase and IMPAIR Na^+ gradient. *EMBO J.* 34, 2408–2423. doi: 10.15252/embj.201591397

Stanic, J., Carta, M., Eberini, I., Pelucchi, S., Marcello, E., Genazzani, A. A., et al. (2015). Rabphilin 3A retains NMDA receptors at synaptic sites through interaction with GluN2A/PSD-95 complex. *Nat. Commun.* 6:10181. doi: 10.1038/ncomms10181

Stanic, J., Mellone, M., Napolitano, F., Racca, C., Zianni, E., Minocci, D., et al. (2017). Rabphilin 3A: A novel target for the treatment of levodopa-induced dyskinesias. *Neurobiol. Dis.* 108, 54–64. doi: 10.1016/j.nbd.2017.08.001

Teravskis, P. J., Covelo, A., Miller, E. C., Singh, B., Martell-Martínez, H. A., Benneyworth, M. A., et al. (2018). A53T mutant alpha-synuclein induces tau-dependent postsynaptic impairment independently of neurodegenerative changes. *J. Neurosci.* 38, 9754–9767. doi: 10.1523/JNEUROSCI.0344-18.2018

Tozzi, A., de Iure, A., Bagetta, V., Tantucci, M., Durante, V., Quiroga-Varela, A., et al. (2016). Alpha-synuclein produces early behavioral alterations via striatal cholinergic synaptic dysfunction by interacting with GluN2D N –Methyl-D-aspartate receptor subunit. *Biol. Psychiatry* 79, 402–414. doi: 10.1016/j.biopsych.2015.08.013

Tozzi, A., Sciaccaluga, M., Loffredo, V., Megaro, A., Ledonne, A., Cardinale, A., et al. (2021). Dopamine-dependent early synaptic and motor dysfunctions induced by α-synuclein in the nigrostriatal circuit. *Brain* 144, 3477–3491. doi: 10.1093/brain/awab242

Trudler, D., Sanz-Blasco, S., Eisele, Y. S., Ghatak, S., Bodhinathan, K., Akhtar, M. W., et al. (2021). α-Synuclein oligomers induce glutamate release from astrocytes and excessive extrasynaptic NMDAR activity in neurons, thus contributing to synapse loss. *J. Neurosci.* 41, 2264–2273. doi: 10.1523/JNEUROSCI.1871-20.2020

Wang, J. Q., Fibuch, E. E., and Mao, L. (2007). Regulation of mitogen-activated protein kinases by glutamate receptors. *J. Neurochem.* 100, 1–11. doi: 10.1111/j.1471-4159.2006.04208.x

Wu, Q., Takano, H., Riddle, D. M., Trojanowski, J. Q., Coulter, D. A., and Lee, V. M.-Y. (2019). α-Synuclein (αSyn) preformed fibrils induce endogenous αSyn aggregation, compromise synaptic activity and enhance synapse loss in cultured excitatory hippocampal neurons. *J. Neurosci.* 39, 5080–5094. doi: 10.1523/JNEUROSCI.0060-19.2019

Yang, W., Li, X., and Yin, N. (2020). Increased α-synuclein oligomerization is associated with decreased activity of glucocerebrosidase in the aging human striatum and hippocampus. *Neurosci. Lett.* 733:135093. doi: 10.1016/j.neulet.2020.135093

Yu, W., Yang, W., Li, X., Li, X., and Yu, S. (2019). Alpha-synuclein oligomerization increases its effect on promoting NMDA receptor internalization. *Int. J. Clin. Exp. Pathol.* 12, 87–100.

frontiers | Frontiers in Aging Neuroscience

TYPE Original Research
PUBLISHED 15 May 2023
DOI 10.3389/fnagi.2023.1152562

OPEN ACCESS

EDITED BY
Dario Maschi,
Washington University in St. Louis,
United States

REVIEWED BY
Sehyoun Yoon,
Northwestern Medicine, United States
Tilmann Achsel,
Université de Lausanne, Switzerland

*CORRESPONDENCE
Bryen A. Jordan
✉ bryen.jordan@einsteinmed.edu

†PRESENT ADDRESSES
Abigail U. Carbonell,
Department of Neurology,
Columbia University Irving Medical Center,
New York, NY, United States
Carmen Freire-Cobo,
Nash Family Department of Neuroscience,
Icahn School of Medicine at Mount Sinai,
New York, NY, United States

RECEIVED 27 January 2023
ACCEPTED 17 April 2023
PUBLISHED 15 May 2023

CITATION
Carbonell AU, Freire-Cobo C, Deyneko IV, Dobariya S, Erdjument-Bromage H, Clipperton-Allen AE, Page DT, Neubert TA and Jordan BA (2023) Comparing synaptic proteomes across five mouse models for autism reveals converging molecular similarities including deficits in oxidative phosphorylation and Rho GTPase signaling. *Front. Aging Neurosci.* 15:1152562. doi: 10.3389/fnagi.2023.1152562

Comparing synaptic proteomes across five mouse models for autism reveals converging molecular similarities including deficits in oxidative phosphorylation and Rho GTPase signaling

Abigail U. Carbonell[1†], Carmen Freire-Cobo[1†], Ilana V. Deyneko[1], Saunil Dobariya[1], Hediye Erdjument-Bromage[2], Amy E. Clipperton-Allen[3], Damon T. Page[3], Thomas A. Neubert[2] and Bryen A. Jordan[1,4*]

[1]Dominick P. Purpura Department of Neuroscience, Albert Einstein College of Medicine, Bronx, NY, United States, [2]Department of Neuroscience and Physiology, New York University Grossman School of Medicine, New York, NY, United States, [3]Department of Neuroscience, The Scripps Research Institute Florida, Jupiter, FL, United States, [4]Department of Psychiatry and Behavioral Sciences, Albert Einstein College of Medicine, Bronx, NY, United States

Specific and effective treatments for autism spectrum disorder (ASD) are lacking due to a poor understanding of disease mechanisms. Here we test the idea that similarities between diverse ASD mouse models are caused by deficits in common molecular pathways at neuronal synapses. To do this, we leverage the availability of multiple genetic models of ASD that exhibit shared synaptic and behavioral deficits and use quantitative mass spectrometry with isobaric tandem mass tagging (TMT) to compare their hippocampal synaptic proteomes. Comparative analyses of mouse models for Fragile X syndrome (*Fmr1* knockout), cortical dysplasia focal epilepsy syndrome (*Cntnap2* knockout), *PTEN* hamartoma tumor syndrome (*Pten* haploinsufficiency), ANKS1B syndrome (*Anks1b* haploinsufficiency), and idiopathic autism (BTBR+) revealed several common altered cellular and molecular pathways at the synapse, including changes in oxidative phosphorylation, and Rho family small GTPase signaling. Functional validation of one of these aberrant pathways, Rac1 signaling, confirms that the *ANKS1B* model displays altered Rac1 activity counter to that observed in other models, as predicted by the bioinformatic analyses. Overall similarity analyses reveal clusters of synaptic profiles, which may form the basis for molecular subtypes that explain genetic heterogeneity in ASD despite a common clinical diagnosis. Our results suggest that ASD-linked susceptibility genes ultimately converge on common signaling pathways regulating synaptic function and propose that these points of convergence are key to understanding the pathogenesis of this disorder.

KEYWORDS

proteomic convergence, PSD, Rho GTPase, Rac, tandem mass tags, TMT, comparative analyses

Introduction

Autism spectrum disorder (ASD) is a neurodevelopmental disorder characterized by social-communication deficits and restrictive and repetitive behaviors. Although the specific cause of ASD is unknown, autism is highly heritable, with a monozygotic twin concordance rate of 40–80% (Gaugler et al., 2014). The genetic architecture of ASD is extraordinarily complex, with common inherited variants and rare *de novo* mutations working together to confer genetic risk (Weiner et al., 2017). This polygenic etiology presents challenges for elucidating the molecular pathogenesis of autism. However, ASD-related syndromes with defined genetic causes for autistic phenotypes present the best opportunities for elucidating the underlying mechanisms of ASD and identifying possible therapeutic targets (Sztainberg and Zoghbi, 2016). These monogenic syndromes, including Fragile X syndrome (*FMR1*), Rett syndrome (*MECP2*), *PTEN* hamartoma tumor syndrome (*PTEN*), tuberous sclerosis complex (*TSC1*/*TSC2*), Phelan McDermid syndrome (*SHANK3*), and cortical dysplasia focal epilepsy syndrome (*CNTNAP2*), play a key role in furthering our understanding of ASD.

Animal models of these syndromes have proven essential for studying the underlying neuropathology of ASD, especially changes in the complex processes of mammalian brain development and function. Studies in rodents have shown that ASD risk genes converge on transcriptional regulation, protein homeostasis, and synaptic structure and function (De Rubeis et al., 2014; Pinto et al., 2014; Ruzzo et al., 2019). Accordingly, mice demonstrating the loss of *Fmr1*, *Mecp2*, *Pten*, *Tsc1*/*Tsc2*, *Shank* genes, or the *Nrxn* and *Nlgn* families all demonstrate changes in synaptic excitability or plasticity, and most also show altered dendritic growth or spine dynamics (Hulbert and Jiang, 2016; Parikshak et al., 2016; Varghese et al., 2017; Verma et al., 2019). Non-syndromic ASD models, such as those induced by valproic acid or maternal immune activation, also reveal structural and functional synaptic deficits, showing that environmental factors can lead to similar synaptic phenotypes (Sui and Chen, 2012; Martin and Manzoni, 2014; Cellot et al., 2016; Patrich et al., 2016; Li et al., 2018; Wang et al., 2018; Andoh et al., 2019).

We recently characterized *ANKS1B* haploinsufficiency, a new genetic syndrome presenting with autism and other neurodevelopmental disorders that is caused by a monogenic deletion in the *ANKS1B* gene (Carbonell et al., 2019). This gene, which encodes for the protein AIDA-1, was previously identified in ASD risk gene networks (Li et al., 2014). To facilitate our work, we developed a mouse model for *ANKS1B* haploinsufficiency and found that it recapitulates behavioral correlates of the syndrome (Carbonell et al., 2019). Altogether, we found that AIDA-1 regulates activity-induced protein synthesis (Jordan et al., 2007), hippocampal synaptic plasticity (Tindi et al., 2015), and NMDA receptor subunit composition (Tindi et al., 2015; Carbonell et al., 2019). AIDA-1 is a core protein of the postsynaptic density and interacts with PSD95 in a complex that contains other factors associated with neurodevelopmental disorders, including *Grin2b*, *Syngap1*, and *Nlgn* (Kaizuka and Takumi, 2018; Carbonell et al., 2019). Our research provides an additional example corroborating the idea that molecular mechanisms regulating synaptic function underlie ASD pathobiology (Zoghbi and Bear, 2012; Bourgeron, 2015).

Despite the heterogeneous genetic architecture of autism and a complex etiology with contributions from environmental factors, ASD is diagnosed by distinct clinical criteria. Therefore, convergent cellular processes at the circuit, synaptic, or molecular level could underlie these shared behavioral phenotypes (Sestan and State, 2018). In seeking convergent mechanisms among syndromic and non-syndromic forms of autism, comparative studies often narrowly focus on selected behaviors, specific synaptic phenomenology, or shared responses to preclinical pharmacological interventions (Barnes et al., 2015; Heise et al., 2018; Schoen et al., 2019). While broader comparisons have been made using transcriptomic analyses (Forés-Martos et al., 2019; Quesnel-Vallières et al., 2019; Hernandez et al., 2020), these changes may not reflect mechanisms of disease due to multiple downstream levels of regulation such as protein translation, degradation, and transport (Vogel and Marcotte, 2012). Indeed, widespread discrepancies between transcript and protein abundance are well-known (Wang et al., 2017; Hoogendijk et al., 2019) but typically ignored when drawing conclusions from discovery-based transcriptomic screens. Proteomic approaches can therefore yield dramatically different results from transcriptomic profiles, as shown in a mouse model of Rett syndrome (Pacheco et al., 2017), and are particularly favored for ASD-linked genes that regulate protein translation (*Fmr1*, *Tsc1*/*Tsc2*, *Pten*) or degradation (*Ube3a*; Louros and Osterweil, 2016). ASD models in which synaptic scaffolding and membrane localization are altered can also be investigated at the proteomic level, especially when the synaptic compartments and complexes are isolated by fractionation or immunoprecipitation (Lee et al., 2017; Reim et al., 2017; Brown et al., 2018; Murtaza et al., 2020). Indeed, analysis of postmortem brain tissue from ASD patients showed that some transcriptomic changes were not observed while changes in synaptic proteins predicted by ASD risk genes and animal models were confirmed (Abraham et al., 2019).

Here, we compare the postsynaptic proteomes of five mouse models for autism using a particularly rigorous quantitative proteomic method employing isobaric tags. The models selected display synaptic deficits and represent models of ASD-related syndromes Fragile X syndrome (*Fmr1* -/Y), *PTEN* hamartoma tumor syndrome (*Pten* +/−), cortical dysplasia focal epilepsy syndrome (*Cntnap2* −/−), ANKS1B syndrome (*Anks1b* +/−), and the BTBR+ inbred model of idiopathic autism. These models have demonstrated face validity for autism, displaying hallmark behavioral correlates of ASD including social interaction deficits and restrictive behaviors (Kazdoba et al., 2016; Zhou et al., 2016; Kabitzke et al., 2018; Carbonell et al., 2019). In each model, we find evidence for upstream regulators that alter synaptic composition with predicted functional effects consistent with clinical phenotypes in ASD and individual syndromes. Mouse models can be clustered according to similarities and differences in upstream regulators, functional effects, and canonical pathways predicted by changes in their synaptic proteomes. Notably, we identified groups of models with shared changes in the synaptic proteome, which may indicate the presence molecular subtypes of ASD. Among diverse and shared molecular deficits observed in all ASD models tested, deficits in oxidative phosphorylation, and RhoA family signaling were predicted by bioinformatic analyses, and functional assays for Rac1 activity corroborate model-specific bioinformatic

predictions. An appreciation of convergent synaptic changes underlying ASD is critical for defining pathogenic mechanisms and prioritizing treatments that can have broad efficacy (Sestan and State, 2018). Our results identify specific druggable pathways that may lead to the design of effective therapeutic interventions for diverse forms of ASD.

Materials and methods

Animal models and fractionation

Fmr1 (stock #003025, MGI:1857169) and *Cntnap2* knockout (stock #017482, MGI: 2677631) mouse models and the BTBR+ (stock #002282), B6129SF2/J (stock #101045), and C57BL/6J (stock #000664) mouse strains were purchased from the Jackson Laboratory. Mice with *Pten* haploinsufficiency (MGI:2151804) and wild-type mice on the C57BL/6J background were obtained from the Page lab at the Scripps Research Institute Florida. Heterozygotes from the *Anks1b* conditional knockout line (stock #035048, MGI:5779292; Tindi et al., 2015) and wild-type mice from the *Nestin-cre* transgenic line (stock #003771, MGI:2176173) were bred in house (Carbonell et al., 2019). Mice from this line expressing the *Nestin-cre* transgene were genotyped for the *Anks1b*^{wt} allele (forward: 5′-CACCCACAGCTCCATAGACAG-3′, reverse: 5′-GCACCTATTCCCTTCACCCTG-3′) and *Anks1b*^{fl} allele (forward: 5′-AGTTGCCAGCCATCTGTTGT-3′, reverse: 5′-GGGTTCCGGATCAGCTTGAT-3′). Postsynaptic density (PSD) enriched fractions were isolated based on the method of Carlin et al. (1980) and Cohen et al. (1977) as we have done before (Jordan et al., 2004, 2007; Zhang et al., 2012; Tindi et al., 2015). Briefly, mice were euthanized in compliance with the Institutional Animal Care and Use Committee of the Albert Einstein College of medicine and both hippocampi were rapidly removed, placed in ice-cold solution A (0.32 M sucrose, 10 mM HEPES pH 7.4, 1 mM $MgCl_2$, 0.5 mM $CaCl_2$, protease and phosphatase inhibitors, and 0.1 mM PMSF), and Dounce homogenized. Samples were then centrifuged at 800*g* for 10 min to remove nuclei and other cellular debris, and the supernatant containing light membrane fractions was subjected to a second centrifugation at 30,000*g* for 25 min. The pellet was then resuspended in solution B (0.32 M sucrose, 10 mM HEPES pH 7.4) and layered on top of a 0.85, 1, and 1.2 M sucrose step gradient and centrifuged at 82,500*g* for 2 h. The synaptosomal fraction was collected at the 1–1.2 M sucrose interface and lysed using an equal volume of 1% Triton X-100 (in 0.32 M sucrose, 12 mM Tris pH 8.1) at 4°C for 15 min. Lysed synaptosomes were then centrifuged at 120,000*g* for 25 min to collect the PSD-enriched fraction.

Antibodies

SDS-PAGE and Western blot were performed under standard conditions using the LI-COR fluorescence-based system with the following antibodies: rabbit anti-Rac1 1:1,000 (Proteintech #24702-1-AP), rabbit anti-RhoA 1:1,000 (ABclonal), rabbit anti-Cdc42 (ABclonal), mouse anti-PSD95 1:1,000 (NeuroMab), and rat anti-tubulin 1:1,000 (Cell Signaling Tech). Statistical analysis for Western blot was performed in JMP 16 (SAS).

Tandem mass tag labeling of peptides and determination of labeling efficiency

PSD-enriched samples isolated from each mouse model were electrophoresed briefly (dye front about 5 mm beyond the gel well) using a 4–12% SDS-PAGE gel to remove SDS and other mass spectrometry (MS)-incompatible chemicals. Proteins were visualized by staining overnight with GelCode® Coomassie blue reagent (Pierce). A gel fragment containing all stacked protein bands was excised, reduced with DTT, alkylated with iodoacetamide, and digested using 5 ng/μL mass spectrometry-grade trypsin (Trypsin Gold, Promega). The resulting peptides were desalted using a Stage Tip manually packed with Empora C18 High Performance Extraction Disks (3 M) (Rappsilber et al., 2007) and eluted peptide solutions were dried under vacuum. Peptides were then resuspended in 18 μL acetonitrile (ACN), 57 μL of 0.2 M HEPES pH 8.5 was added to each sample and were reacted with unique isobaric labels within a 10-plex tandem mass tag set (TMT10-plex; Thompson et al., 2003). TMT10-plex amine reactive reagents (Thermo Fisher, 5 mg per vial) were re-suspended in 1024 μL anhydrous acetonitrile and 25 μL of reagent was added to each sample (TMT label: peptide [w/w] = 12:1). The mixture was incubated at RT for 1 h, quenched by the addition of 10 μL 5% hydroxylamine for 15 min, and acidified by the addition of 10 μL 10% formic acid. To calculate labeling efficiency, a 5-μL aliquot from each reaction was desalted on a StageTip, analyzed by LC–MS/MS with a Q-Exactive Orbitrap HF (high field), and the resulting spectra searched with MaxQuant using its corresponding TMT label as variable modifications on the N-terminus and lysine residues. Labeling efficiency was 95% or greater for all samples labeled (Supplementary Figure 5). To ensure that equal amounts of labeled peptides from each channel were mixed together, a two-step mixing strategy was employed: in the first step, an identical ~1 μL volume of peptides from each channel was mixed and analyzed, and the value of the median ratio (median of the ratios of all peptide intensities of one channel over their corresponding peptide average intensities of all channels) for each channel was determined as the correction factor. In the second step, the rest of the peptides were mixed by adjusting their volume using the correction factors. In this way, median ratios ranging from 0.97 to 1.02 were achieved as previously reported (Erdjument-Bromage et al., 2018). The final mixture of reaction products from 10 TMT channels were desalted on a Sep-Pak tC18 1 mL Vac Cartridge (Waters, #WAT03820). Eluted peptides were dried by vacuum centrifugation and stored at −20°C.

Hydrophilic interaction liquid chromatography fractionation of peptides

The TMT-labeled peptides from the PSD samples were then fractionated by offline HILIC to increase depth of coverage of synaptic proteins and to decrease ratio compression resulting from co-fragmenting peptides (Huang et al., 2017). To do this, the final TMT mixture was dissolved in 90% acetonitrile with 0.1% TFA and peptide separation was carried out on an Agilent pump equipped with a TSK gel amide-80 column (4.6 mm ID, 25 cm long) from TOSOH Bioscience, LLC, PA, United States. A gradient of 90% acetonitrile with 0.1% TFA was introduced over 65 min, and a fraction was

collected every 2 min. Concatenated pools of peptides (10 pools) were finally created by pooling non-adjacent peptide fractions; about 10% of each pool was used for LC–MS/MS analysis.

Liquid chromatography–tandem mass spectrometry

Online chromatography was performed with a Thermo Easy nLC 1000 ultrahigh-pressure UPLC system (Thermo Fisher) coupled online to a Q-Exactive HF with a NanoFlex source (Thermo Fisher). Analytical columns (~23 cm long and 75 µm inner diameter) were packed in-house with ReproSil-Pur C18 AQ 3 µm reversed-phase resin (Dr. Maisch GmbH, Ammerbuch-Entringen). The analytical column was placed in a column heater (Sonation GmbH, Biberach) regulated to a temperature of 45°C. The TMT peptide mixture was loaded onto the analytical column with buffer A (0.1% formic acid) at a maximum backpressure of 300 bar. Peptides were eluted with a 2-step gradient of 3–40% buffer B (100% ACN and 0.1% formic acid) in 180 min and 40–90% B in 20 min, at a flow rate of 250 nL/min over 200 min using a 1D online LC–MS2 data-dependent analysis (DDA) method as follows: MS data were acquired using a data-dependent top-10 method, dynamically choosing the most abundant not-yet-sequenced precursor ions from the survey scans (300–1,750 Th). Peptide fragmentation was performed via higher energy collisional dissociation with a target value of 1×10^5 ions determined with predictive automatic gain control. Isolation of precursors was performed with a window of 1 Th. Survey scans were acquired at a resolution of 120,000 at *m*/*z* 200. Resolution for HCD spectra was set to 60,000 at *m*/*z* 200 with a maximum ion injection time of 128 ms. The normalized collision energy was 35. The underfill ratio specifying the minimum percentage of the target ion value likely to be reached at the maximum fill time was defined as 0.1%. Precursor ions with single, unassigned, or seven and higher charge states were excluded from fragmentation selection. Dynamic exclusion time was set at 30 s. Each of the TMT 10-plex samples was analyzed in triplicate.

All data were analyzed with the MaxQuant proteomics data analysis workflow (version 1.5.5.7) with the Andromeda search engine (Cox et al., 2011; Tyanova et al., 2016). The type of the group specific analysis was set to Reporter ion MS2 with 10plex TMT as isobaric labels for Q Exactive HF MS2 data. Reporter ion mass tolerance was set to 0.01 Da, with activated Precursor Intensity Fraction (PIF) value set at 0.75. False discovery rate (the rate at which identified positives are null) was set to 1% for protein, peptide spectrum match, and site decoy fraction levels. Peptides were required to have a minimum length of eight amino acids and a maximum mass of 4,600 Da. MaxQuant was used to score fragmentation scans for identification based on a search with an allowed mass deviation of the precursor ion of up to 4.5 ppm after time-dependent mass calibration. The allowed fragment mass deviation was 20 ppm. MS2 spectra were used by Andromeda within MaxQuant to search the UniProt mouse database (01092015, 16,699 entries) combined with 262 common contaminants. Enzyme specificity was set as C-terminal to arginine and lysine, and a maximum of two missed cleavages were allowed. Carbamidomethylation of cysteine was set as a fixed modification and N-terminal protein acetylation, deamidated (N, Q), and oxidation (M) as variable modifications. The reporter ion intensities were defined as intensities multiplied by injection time (to obtain the total signal) for each isobaric labeling channel summed over all MS/MS spectra matching to the protein group as previously validated (Tyanova et al., 2016). Following MaxQuant analysis, the protein and peptide .txt files were imported into Perseus (version 1.5.6.0) software which was used for statistical analysis of all the proteins identified.

Experimental samples and bioinformatic analyses

ASD models (*Fmr1*, *Pten*, *Cntnap2*, *Anks1b*, BTBR+) and appropriate controls (C57BL/6J, B6129SF2/J X *Nestin-cre* C57BL/6J) for each model were analyzed in biological triplicates, representing 24 independent samples. Each biological replicate was comprised enriched hippocampal PSD fractions pooled from 2 male mice of each genotype at 6–10 weeks of age ($N = 3$ biological replicates using a total of 6 mice for each genotype). As we could only label 10 samples at a time using the 10-plex TMT isobaric tags, the samples (*Fmr1*, *Pten*, *Cntnap2*, *Anks1b*, BTBR+ models, C57BL/6J controls, and *Nestin-cre* C57BL/6J controls; in triplicate) were analyzed in three independent LC–MS/MS runs, with each run containing the animal model and corresponding control.

Following the identification of proteins and TMT-dependent quantitation of their abundance in each sample, the fold-change was calculated by dividing the relative abundance of a protein in the ASD sample by its abundance in the appropriate control sample. Fold-changes were calculated only between samples within each independent MS analyses. For the *Fmr1*, *Pten*, *Cntnap2*, and BTBR+ models, we used the average of 2 samples of C57BL/6J mice as the control values. For the *Anks1b* Het mice on the *Nestin-cre* C57BL/6J background, we used wild-type littermates on the *Nestin-cre* C57BL/6J background as the control value. The fold-changes were plotted, and values were normalized to a value of 1. To increase the rigor of subsequent analyses, we filtered the protein sets in each experiment for proteins identified and quantified by at least 3 unique peptides, and with a Q-value of 0, representing the highest significance for intensity and score in MaxQuant. We used this list of protein as input in StringDB under the species *Mus musculus* for gene ontology (GO) enrichments analyses (Szklarczyk et al., 2015).

Functional annotation, activation prediction, and regulatory network construction were performed for each mouse model using Ingenuity Pathway Analysis (IPA, QIAGEN Bioinformatics, Fall Release 2022). Fold-change values for each protein in the PSD proteome were used as input for a *Core Analysis* in IPA using the following default settings: Expression Analysis; General Settings = Ingenuity Knowledge Base (Genes Only), Direct Relationships; Networks = Interaction networks, include endogenous chemicals; Node Types = All; Data Sources = All; Confidence = Experimentally Observed; Species = All; Tissues & Cell Lines = All; Mutations = All. To score similarity between models overall and in each domain (Upstream Regulators, Downstream Effects, and Canonical Pathways), *Analysis Match* was used. In *Analysis Match*, activity signatures for each *Core Analysis* are generated by taking the top 50 (Upstream Regulators and Downstream Effects) or 10 (Canonical Pathways) entities that are activated (z-score > 2) and inhibited (z-score < −2) in each domain. Similarity z-scores between

Core Analyses are defined using the following formula, where N is the total number of overlapping entities in each analysis, N_+ is the number of correct matches, and N_- the number of incorrect matches:

$$\text{raw } z\text{-score} = \left(N_+ - N_-\right) / \left(\text{Sqrt}\left(N\right)\right)$$

The raw z-score is divided by a hypothetical perfect match ($N_+ = N <= 100$, $N_- = 0$) and multiplied by 100% to obtain a normalized z-score, where a score of 100 is a perfect match to itself. Raw and normalized z-scores are negative when $N_- > N_+$, yielding an opposite activation signature. To generate overall *value of p* scores, the $-\log_{10}$ of the p-values (maximum value of 50) were calculated for each domain and expressed as a percentage of the maximum possible $-\log_{10}p$ (a perfect match to itself). To compare models, the *Core Analysis* of each model were used as input for a *Comparison Analysis* in IPA. Hierarchical analysis was used to cluster annotations in Upstream Analysis, Downstream Effects, and Canonical Pathways, and to cluster models for similarity relationships.

G-LISA

G-protein linked immunoassays (G-LISA) were used to quantify active Rac1 in hippocampal tissue lysates. Active Rac1 substrate (the G-protein binding domain of Pak1) fused to GST protein (GST-Pak1) was generated in bacteria and purified using glutathione beads. This substrate was added at a concentration of 1 µg to 50 mM Ammonium Carbonate and absorbed onto high-binding 96-well plates overnight to create binding surfaces for GTP-bound Rac1. Hippocampal tissues from the five different mouse models were prepared using the method described by the Cytoskeleton Inc. BK-128 Kit. ($N = 6$ each of BTBR+, *Fmr1*, and *Cntnap2* mice, $N = 5$ *Pten* mice, $N = 9$ *Anks1b* mice, and $N = 9$ each of the two control Mice, C57BL/6J and B6129SF2/J X *Nestin-cre* C57BL/6J mice were used, all prepared from 6 to 10 weeks of age). Briefly, tissues were lysed for 1 min in the kit lysis buffer, and lysates were snap-frozen to preserve GTP-bound active Rac1. All steps were conducted on ice. Lysates were then incubated on the GST-Pak1 coated 96-wells for exactly 30 min on ice. Primary and secondary antibodies as well as HRP-substrate were provided by the BK-128 Kit, and active Rac1 was detected by standard ELISA using immunodetection at 490 OD and HRP-substrate colorimetric measurements.

Results

TMT-MS analyses of postsynaptic density fractions from mouse models of autism

To compare the synaptic proteomes from different ASD mouse models, we obtained *Fmr1* knockout (*Fmr1* KO; Consortium, T.D.-B.F.X, 1994), *Pten* haploinsufficiency (*Pten* Het) (Clipperton-Allen and Page, 2014; Clipperton-Allen and Page, 2015), *Cntnap2* knockout (*Cntnap2* KO; Peñagarikano et al., 2011), *Anks1b* haploinsufficiency (*Anks1b* Het; Carbonell et al., 2019), and the BTBR+ inbred mouse strains (McFarlane et al., 2008). All selected models display abnormal behaviors in domains relevant to ASD, including social approach and interaction, stereotyped movements, learning and memory, and sensorimotor function. These models have also been used to illustrate synaptic dysfunction, including altered synapse formation, excitatory/inhibitory balance, synaptic plasticity, and glutamatergic signaling (Hulbert and Jiang, 2016; Varghese et al., 2017; Bagni and Zukin, 2019; Carbonell et al., 2019). We analyzed changes in the synaptic proteomes of hippocampal postsynaptic density (PSD)-enriched fractions isolated from each of the five mouse models of ASD. PSD-enriched fractions were collected as we have done before (Jordan et al., 2004, 2007; Zhang et al., 2012; Tindi et al., 2015; see Methods) and modified to a single Triton X-100 extraction step (Tindi et al., 2015) as opposed to two. This allowed us to collect enough material from mouse hippocampi at the expense of purity. However, Western blots show that isolated fractions were highly enriched for the post synaptic marker PSD95 (Figure 1A). Moreover, the proteins identified in the three independent experiments (described below) show ~50–80% overlap with the Genes to Cognition database of PSD components (G2Cdb; Croning et al., 2009) and ~30–50% overlap with the Synaptic Gene Ontologies curated synaptic database (SynGO) (Koopmans et al., 2019; Supplementary Table 1). Proteins in each sample were then labeled with a unique isobaric tag within a 10-plex Tandem Mass Tag set (TMT). TMTs are reactive isobaric tags with unique permutations of 14C and 15N stable isotopes that imbue peptides with small differences in mass that can then be resolved by mass spectrometry (MS) (Figure 1B). This approach allows for up to 10 samples to be mixed and analyzed simultaneously by MS, which reduces variability, enables robust quantitation of identified proteins, and allows for rigorous quantitative and comparative analyses between samples. Overall, this method allowed us to overcome poor quantitation traditionally associated with MS-based proteomics. The proteins identified in each run, along with number of unique peptides, scores, and other MS-based information are listed in Supplementary Table 1. Using all genes as a search space, gene ontology (GO) analyses using STRING (Szklarczyk et al., 2019) revealed that isolated fractions are overwhelmingly enriched for synaptic terms (Figure 1C). GO analyses also revealed a similar distribution of Cellular Compartments and Reactome Pathways (Figure 1D) across each of the three independent MS experiments, and that each of the specific pathways was enriched to a similar extent. We used SynGO (Koopmans et al., 2019) to restrict the search space to brain-specific genes and found that *Synapse*, *Process in the synapse*, and *Postsynapse* were the most significant GO terms (Figure 1E). Hierarchical plots for GO terms show an overwhelming enrichment (high Q-scores) for synaptic processes for all three experiments (Figure 1F). Overall, these results show that all experimental samples were highly enriched in synaptic components and were similar to each other, which increases the strength of subsequent comparisons.

Broad comparison of synaptic proteomes across ASD mouse models shows evidence of molecular subtypes

To compare findings across ASD models, we first characterized each model by calculating the ratio of synaptic protein abundance in the model to its appropriate control (fold-change). C57BL/6J (duplicates) mice were used as controls for all models except for the *Anks1b* mice, which used wildtype B6129SF2/J X *Nestin-cre* C57BL/6J

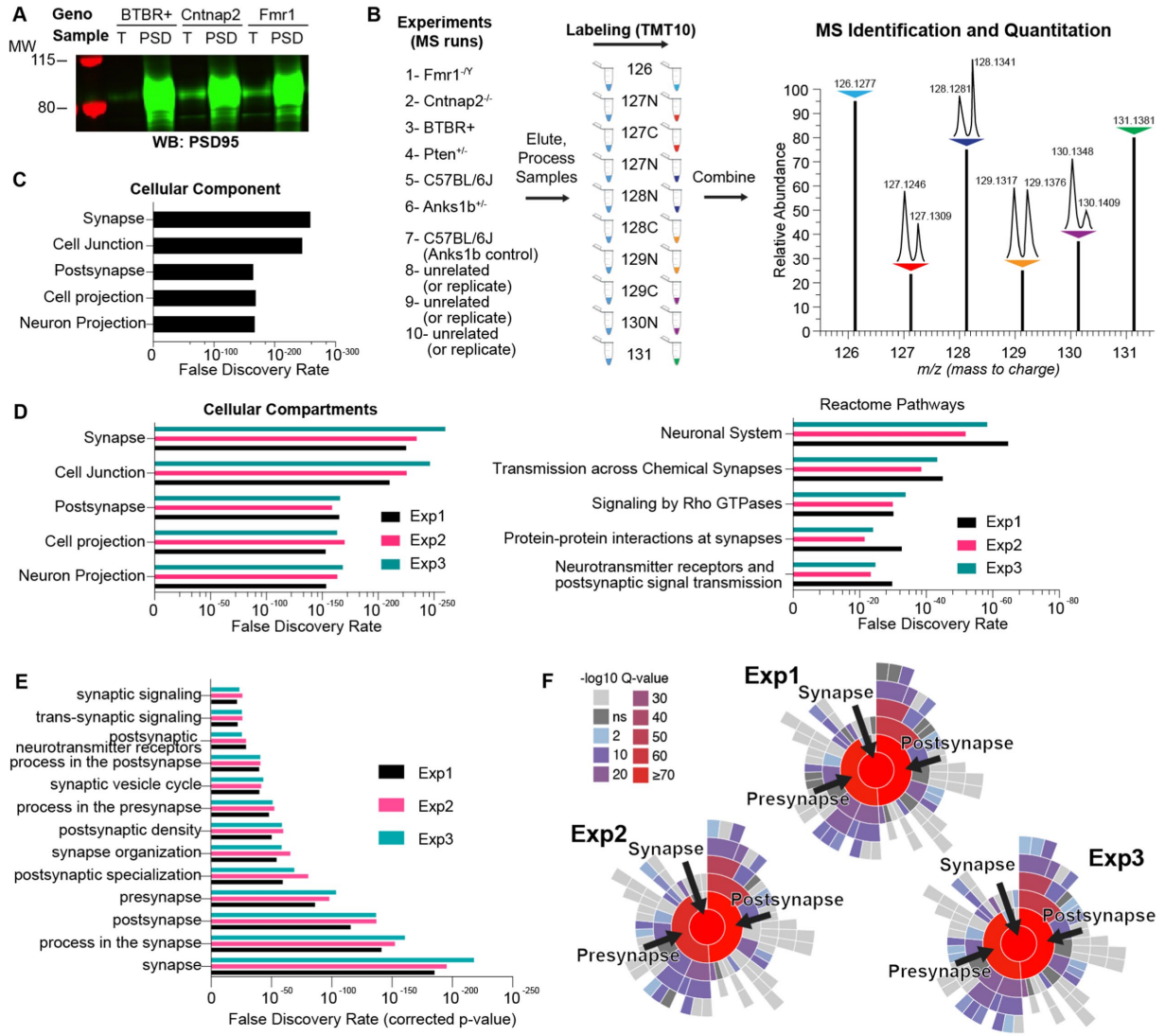

FIGURE 1
Methodology for isobaric-tag based quantitative comparison of synaptic fractions of ASD mouse models. **(A)** Synapse-enriched fractions from sample mouse models of autism spectrum disorder (ASD) demonstrate qualitative enrichment for the synaptic marker PSD95 by Western blot (4μg each sample) compared to total brain fractions (T). **(B)** Isobaric labeling and comparative proteomics schematic showing the ASD mouse models used (De Rubeis et al., 2014; Gaugler et al., 2014; Sztainberg and Zoghbi, 2016; Weiner et al., 2017; Ruzzo et al., 2019) and appropriate control samples (Pinto et al., 2014; Hulbert and Jiang, 2016; Parikshak et al., 2016; Varghese et al., 2017; Verma et al., 2019) modified from the schematic from the Thermo Scientific Catalog for the TMT10plex™ Isobaric Kit. Samples were reacted with unique isobaric tags, whose identifier (e.g., 128N) corresponds to the molecular weight (Daltons) and stable isotope amino acid (N or C) present in that tag. (Right) Idealized MS output showing the same protein in each of the 10 samples identified as 10 contiguous peaks. This permits immediate and rigorous relative quantitation across all samples. m/z represents mass/charge ratio of peptides. *N* =6 total animals for each genotype. **(C)** Bar graph representing the top cellular components sorted by statistical significance (False Discovery Rate), identified by gene ontology (GO) analysis of proteins in a sample MS run (Exp 1) and using all genes as a search space. **(D)** Same as figure **C** but for showing top Cellular Compartment and Reactome Pathways for each MS run. **(E)** Enrichment analyses using SynGO and using only brain-specific genes as a search space. **(F)** Hierarchical plots showing the top GO terms enriched in each experiment and associated *q*-values (*p*-values adjusted for multiple comparisons) for each term.

controls from the same colony. To preserve the quantitative rigor afforded by the isobaric tags, fold-changes were only calculated within experiments (between samples in each independent MS analysis). Moreover, we used a highly stringent filter to increase the significance of findings, considering only proteins identified and quantified by at least 3 unique peptides, and whose MaxQuant calculated Q-values were 0, representing the lowest possible false discovery rate. Finally, only proteins that were identified and quantified in at least 2 independent experiments were considered for subsequent analyses (Supplementary Table 2; 97.6 and 91.2% of proteins found and quantified in Experiment 1 were found and quantified in Experiments 2 and 3, respectively). Distribution plots of protein fold-changes revealed that most proteins were unchanged at hippocampal synapses in the ASD mouse models (fold-changes were normally distributed across a value of 1; Figure 2A). This is expected as large changes in the synaptic proteome would likely be lethal. To measure the overall similarities across models, we performed multivariate analyses using PCA (Principal Components Analyses; Figure 2B) and calculated

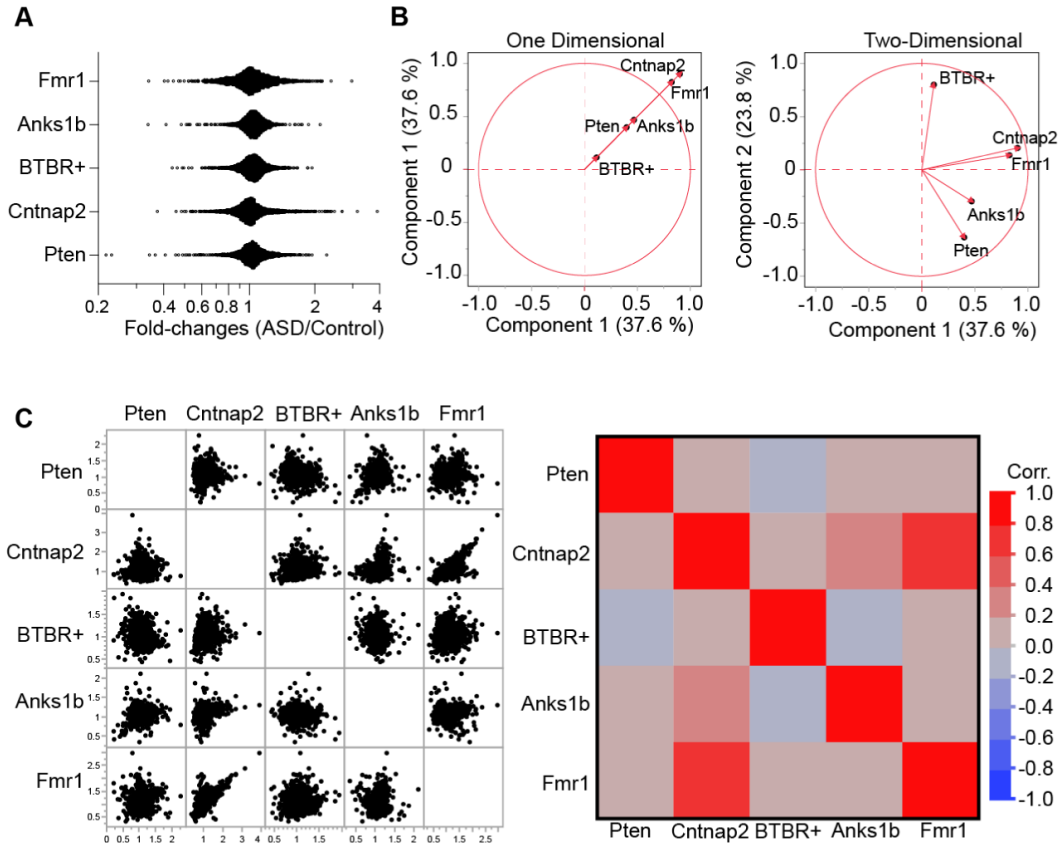

FIGURE 2
Similarity analyses between mouse models of ASD. **(A)** Distribution histograms for all proteins identified each animal model. Results show that fold-values show distribution with outliers. **(B)** Principal components analysis for the five ASD models plotted across (left) one and (right) two dimensions reveal broad similarities between *Cntnap2* and *Fmr1* models, as well as between *Anks1b* and *Pten* models. **(C)** Correlation matrices (left- data points, right- Pearson's correlation) based on genes and fold-changes. For all panels, proteins identified=~1,300–1,500 from n=3 MS runs of n=6 mice per genotype.

correlations using protein identities and fold-changes (Figure 2C). Results show that *Fmr1* and *Cntnap2* models are most similar, with *Anks1b* and *Pten* models appearing to comprise a second molecular subgroup. The inbred BTBR+ strain was most dissimilar.

Dysregulated molecular pathways for oxidative metabolism and Rho GTPase signaling are shared across ASD mouse models

To analyze the functional implications of the altered synaptic proteomes observed, we used Ingenuity Pathway Analysis (IPA, QIAGEN Bioinformatics). IPA derives functional insights and pathway nomenclatures from a continuously updated knowledge base drawn from the literature (Krämer et al., 2014). We first performed a *Comparison Analyses* in IPA. Sorted by overall *z*-scores (standard deviation away from expected values), we found that several canonical pathways were altered across all models in a highly significant manner (Figure 3A; Supplementary Table 3). Moreover, several pathways were predicted to be regulated in the same way (either activated or inhibited) across all ASD models. We hypothesize that these canonical pathways represent critical or potentially causative molecular mechanisms in autism that could serve as novel targets for therapeutic intervention. All tested models show strongly activated (positive *z*-scores) oxidative phosphorylation and strongly downregulated Granzyme A, Sirtuin, RhoGDI, and HIPPO signaling pathways. These results corroborate long-standing research linking neurodevelopmental disorders to mitochondrial dysfunction (oxidative phosphorylation; Giulivi et al., 2010; Rossignol and Frye, 2012) immune regulatory systems (Granzyme A, Sirtuin; Careaga et al., 2017; Meltzer and Van de Water, 2017; Hughes et al., 2018), and cell proliferation and apoptosis (Granzyme A, HIPPO, RhoGDI, Sirtuin; Dong et al., 2018; Courchesne et al., 2019). In addition, our analyses identified specific dysregulated molecules that may represent the core mechanisms linked to deficits within these broad cellular pathways (Supplementary Table 4). Sirtuins, like granzyme signaling, have been implicated in neuroprotection, cognition, and metabolism, as well as Alzheimer's disease and aging (Bonda et al., 2011). Other pathways that were altered in all five models showed multi-directional dysregulation. As expected, based on prevailing literature and samples tested, synaptogenesis signaling and glutamate receptor pathways were also significantly affected in all ASD models, corroborating recent hypotheses classifying ASDs as synaptopathies. We also found a significant number of canonical pathways linked to the activity of the small G-protein family RhoA. Interestingly, these pathways showed a similar pattern where the *Anks1b* model was downregulated while the other four models were upregulated.

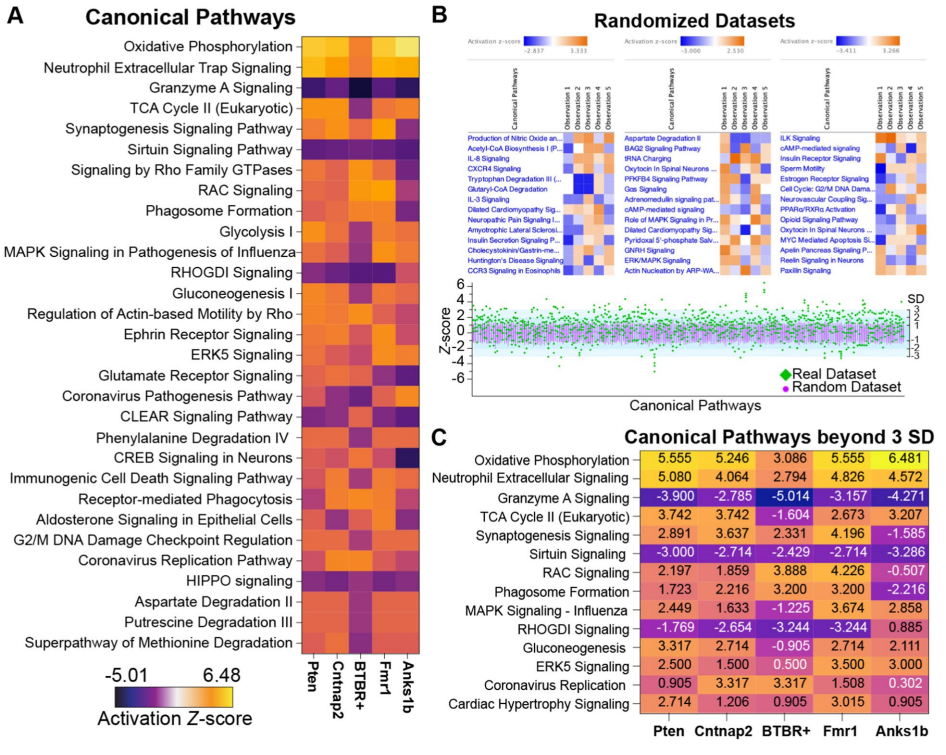

FIGURE 3
Distinct pattern of similarities and differences in Canonical Pathways among mouse models of autism. **(A)** Heat maps showing the predicted activation or inhibition (see LUT legend) of the top 30 significant (*z*-scores) canonical pathways shared in all ASD models. **(B)** Twenty datasets with randomized and normally distributed fold-ratio values were analyzed by IPA. Results reveal top enriched pathways as expected, but with significantly lower *z*-scores, and no pathways show changes in the same direction (*z*-score) for all ASD models. (lower) Plots of *z*-scores (*Y*-axis) for real datasets (green diamonds) for the identified canonical pathways (*X*-axis). Overlaid are the distribution of *z*-scores for the randomized datasets (pink circles; mean±SD). A significant number of outliers were identified in the real datasets (green diamonds outside the light blue area). **(C)** Heat map showing the outlier canonical pathways (>3 standard deviations away from the mean of randomized dataset in at least 2 animal models). **(D)** Analysis Match in IPA to determine the similarities between models based on shared canonical pathways, upstream and downstream regulators. Numbers represent correlation values with 100% representing perfect overlap and −100% being anti-correlated. Results track the broad similarities seen in Figure 2.

While IPA incorporates *p*-values, *z*-scores, and other analyses to address statistical biases based on population subsets (Krämer et al., 2014), the exact methodology is proprietary. To independently test the significance of our findings, we created 20 randomized datasets containing the same proteins as in our real samples, but with randomly assigned fold-ratios. These datasets were generated to reflect the distribution and standard deviations calculated from the real datasets of each animal model. IPA analyses of randomized datasets revealed "significant" canonical pathways, but with *z*-score ranges that were substantially lower than those calculated for the actual sample datasets (average random *z*-score range = ± ~ 2.5; average real *z*-score range = −5.01 to 6.48; Figure 3B). Plotting the *z*-scores for the actual dataset together with the mean and standard deviation of the 20 randomized datasets reveals outlier canonical pathways that were at least three standard deviations removed from the mean (Figure 3B). The standard deviations and *z*-scores calculated for both actual and randomized data were almost identical, suggesting a standardized method for calculating expectation values. Pathways that were greater than three standard deviations removed from the mean include Oxidative phosphorylation, Sirtuin signaling, Granzyme A signaling, Synaptogenesis, and Rho signaling pathways, among others (Figure 3C).

We then used *Analysis Match* to create a similarity matrix for all ASD models tested based on Upstream Regulators, Downstream Effects (Diseases and Functions), Canonical Pathways from each *Core Analysis*, and overall *z*-scores (Figure 3D; Supplementary Figures 1-3). The top pathways in each category and for each animal model were based on *p*-values, *z*-scores, and activation values (Krämer et al., 2014; Supplementary Table 3). Similarity *z*-scores reflect the percentage of maximum similarity to a given model (out of 100%, a perfect match to itself). *Analysis Match* based on functional annotations reveals significant similarities across ASD models, which corroborates results presented in Figure 2 and shows that BTBR+ mice represent a distinct molecular subgroup.

Altered expression and function of Rho GTPases in ASD mouse models validates bioinformatic analyses of synaptic proteomes

To validate our proteomic and bioinformatic analyses, we performed biochemical analyses for one altered cellular pathway among all identified. Across all mouse models tested, RhoA family G-protein signaling pathways are involved in all top canonical pathway hits (Figure 3A) including Synaptogenesis Signaling Pathway, Signaling by Rho family GTPases, Rac Signaling, RhoGDI signaling,

and Regulation of Actin-based motility by Rho. Bioinformatic predictions validate previous studies as Rho GTPases have crucial roles in synaptic function and have been investigated extensively in both human-based experiments and mouse models of ASD (Guo et al., 2020). Directionality of changes was largely consistent among mouse models, predicting activated signaling by Rho GTPases and inhibited regulation by RhoGDI in *Pten*, *Cntnap2*, BTBR+, and *Fmr1* mice, but with opposite changes observed in the *Anks1b* mice (Figure 3A). Depictions of the Rac1 signaling pathways altered in the ASD models show that receptor tyrosine kinases and other synaptic pathways primarily drive changes in Rac activity (Supplementary Figure 6). Components of the WAVE complex and other regulators of actin nucleation and polymerization feature prominently among altered molecules in this pathway. Western blots for Rho family G-proteins Rac1, RhoA, and Cdc42 in synaptic fractions detected Rac1, but not RhoA or Cdc42 in synaptic fractions (Figure 4A). This corroborates the MS analyses showing that Rac1 was identified with more unique peptides in enriched PSD fractions compared to RhoA and CDC42 (Supplementary Table 1). Rac1 expression was increased in the *Fmr1* KO model in synaptic fractions, but largely unchanged across all models (Figures 4A,B). Western blots of whole brain lysates reveal significant changes in several Rho family GTPases across models (Figure 4C). For a more informative test measuring function, we performed G-protein activation ELISAs (G-LISAs) to directly measure Rac1 activity in total hippocampal lysates. As predicted by bioinformatic analyses, Rac1 activity in *Anks1b* model mice was substantially downregulated compared to controls, as well as significantly reduced compared to *Cntnap2*, *Pten*, and *Fmr1* models (Figure 4D). While Rac1 activity in *Pten, Fmr1, Cntnap2*, and BTBR+ mice was not significantly upregulated as predicted, a difference in the variance of the WT and ASD dataset was striking. We used F-test calculations for unequal variances to show the differences were statistically significant (Figure 4E).

Discussion

ASDs are among the most heritable neuropsychiatric conditions, with early epidemiological studies estimating concordance rates of ~90% in monozygotic twins, compared to ~10% for dizygotic twins (Steffenburg et al., 1989; Bailey et al., 1995; Hallmayer et al., 2011). Hundreds of genes and chromosomal loci for ASD susceptibility have been reported, suggesting a highly heterogeneous genetic architecture (Chen et al., 2015; de la Torre-Ubieta et al., 2016). While these studies highlight the notion that there is no single "autism gene," functional and bioinformatic analyses of genetic studies have identified convergent cellular pathways, including those regulating transcription (Sanders et al., 2012; de Rubeis et al., 2013), excitatory/inhibitory (E/I) balance (Blatt et al., 2001; Hussman, 2001; Rubenstein and Merzenich, 2003; Gao and Penzes, 2015; Nelson and Valakh, 2015), and especially synaptic function (Bucan et al., 2009; Glessner et al., 2009; Hussman et al., 2011; Buxbaum et al., 2012; Sanders et al., 2012; Yu et al., 2013; Brett et al., 2014; Buxbaum et al., 2014; Cukier et al., 2014; Iossifov et al., 2014; Pinto et al., 2014; Ronemus et al., 2014; Toma et al., 2014; Yuen et al., 2015). Autism gene databases show clear enrichment for synaptic pathways, and syndromic ASD mouse models are primarily associated with mutations in synaptic proteins or their regulators, such as SHANKs, neurexins, neuroligins, SynGAP1, FMRP, and TSC1/2 (Pinto et al., 2014; Yoo, 2015; Ramaswami and Geschwind, 2018). Indeed, most (if not all) identified ASD mouse models such as those for Fragile X (Bhakar et al., 2012), tuberous sclerosis (Auerbach et al., 2011), Angelman (Mabb et al., 2011) Phelan McDermid (Sarowar and Grabrucker, 2016), and *ANKS1B* syndromes show deficits in diverse forms of synaptic function as well as altered neuronal and synaptic morphology (Tindi et al., 2015; Carbonell et al., 2019). Here, we compared the hippocampal postsynaptic proteomes from five mouse models for autism that display synaptic dysfunction, including altered synapse formation, excitatory/inhibitory balance, synaptic plasticity, and glutamatergic signaling (Hulbert and Jiang, 2016; Varghese et al., 2017; Bagni and Zukin, 2019; Carbonell et al., 2019). The goal of this work was to test the hypothesis that common structural and functional deficits among diverse ASD mouse models are caused by similar underlying synaptic deficits and ASD-linked susceptibility factors that ultimately converge on common signaling pathways. By leveraging widely studied ASD mouse models, we hope to identify high-value therapeutic targets for autism.

Wide-spread genetic- and transcriptomic-based screening and comparative studies of disease models suffer from important caveats that limit their interpretability. Often, little is known about how disease-linked genes or other chromosomal loci ultimately correlate to protein abundance and function. Moreover, multiple studies confirm the weak to nil correlation between transcript and protein abundance (Greenbaum et al., 2003; Maier et al., 2009). Transcriptomes display 100-fold ranges in translation efficiency (Ingolia et al., 2009), proteomes reveal >1,000-fold ranges in half-lives (Doherty et al., 2009), and coupled transcriptomic and proteomic analyses reveal that proteins are ~900 times more abundant than corresponding mRNAs, but with ratios that span over five orders of magnitude (Schwanhäusser et al., 2011). Finally, transcriptomic methods are unlikely to provide meaningful information for ASDs such as Angelman syndrome, Fragile X syndrome, and tuberous sclerosis, where the primary contributors to disease etiology are thought to be altered regulation of protein translation and degradation. These important caveats are often ignored in discovery-based genomic research (Wang et al., 2017; Hoogendijk et al., 2019). To overcome these concerns, we have taken a quantitative proteomic approach based on 10-plex Tandem Mass Tags (TMT; Erdjument-Bromage et al., 2018). By directly measuring synaptic protein abundance, we bypass the concerns about poor transcript and protein correlation, as well as the need to understand the complex functional consequences of altered gene expression.

We have used IPA (Qiagen) to analyze the proteomic data and generate inferences on pathways altered in each disease model. IPA derives functional insights and pathway nomenclatures from a continuously updated knowledge base drawn from the literature (Krämer et al., 2014). While this implies a broad context for functional annotations, it also means that proteins are likely to be associated with scientific trends. Perhaps not surprisingly given the current pandemic, several Diseases and Functions associated with the ASD models are related to viral infections (Supplementary Figure 3). Moreover, there is the possibility for missed hits given the lack of comprehensive annotations for cellular and molecular pathways. One example is the surprising finding that the most downregulated proteins across four of the five ASD models were associated with oligodendrocyte function (Supplementary Table 2). The appearance of proteins related to myelin was surprising in our synaptic fractions but may reflect the presence of neuron-oligodendrocyte synapses that may co-purify using our

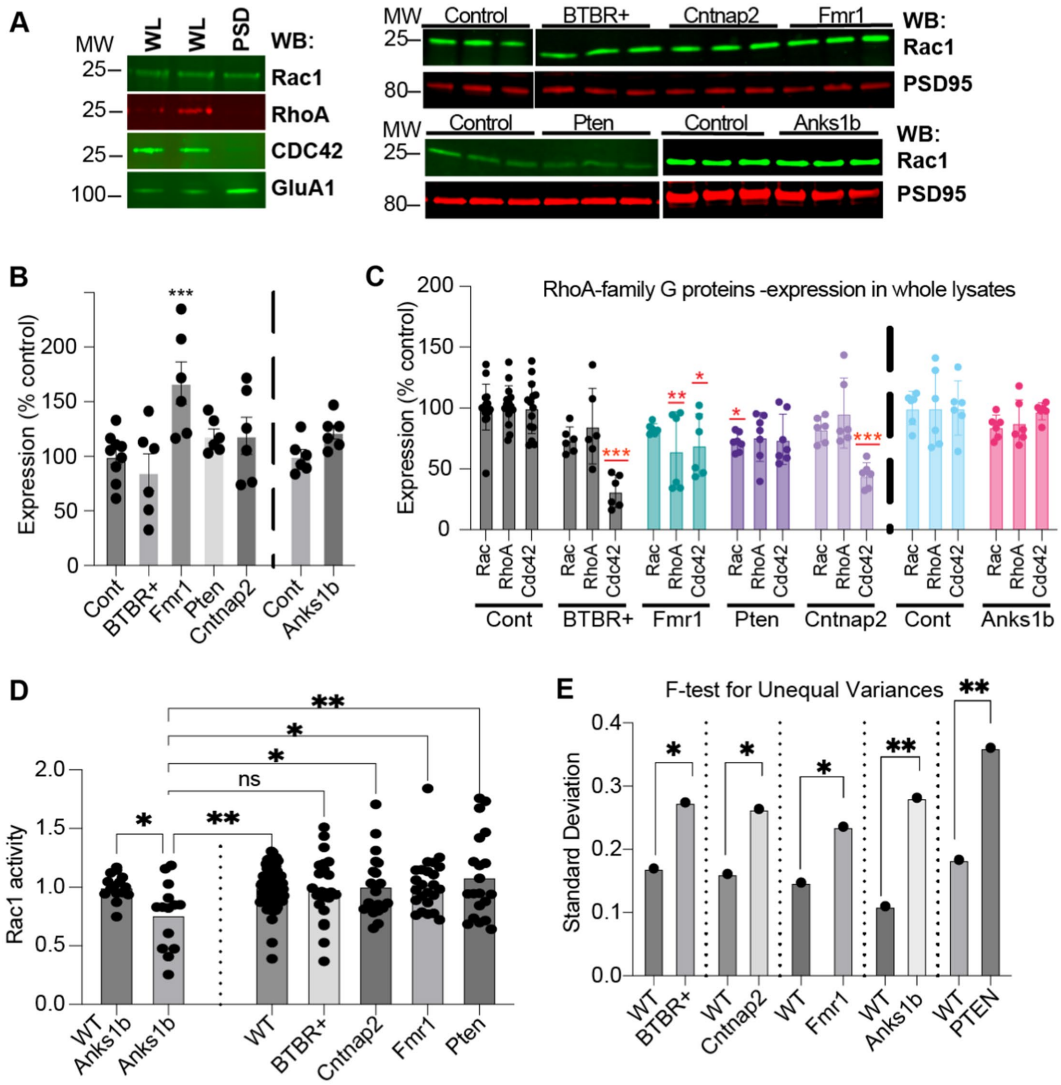

FIGURE 4
Validation of RhoA family GTPases dysfunctions in ASD mouse models **(A)** (Left) Rac1 was the only Rho GTPase detected in whole lysate (WL) and synaptic (PSD enriched) fractions (5 µg each). (Right) Western blots (5µg PSD enriched fraction) showing Rac1 and synaptic marker PSD95 in the different models. **(B)** Quantitation shows increased Rac1 in synaptic fractions from *Fmr1* KO, but not from other mouse models, compared to controls. **(C)** Quantitation of RhoA family GTPases in total lysates shows differences throughout. Expression of Cdc42 in total lysate was reduced for all models except in *Anks1b* Het, where no significant change was observed (30µg whole lysate). **(D)** G-LISA showing difference in fold-change in active Rac1 compared to appropriate controls. Only *Anks1b* showed significant reduction in active Rac1. **(E)** *F*-test calculations for unequal variances show significance. Bar graphs show mean±SEM, n=3–10 samples for each mouse model and wild-type control strain, Student's t-test, *p<0.05 **p<0.01 ***p<0.001. For **B,C** sample values are compared to controls.

methods. Despite these limitations, IPA lists the specific proteins and their fold-changes leading to the assigned pathways. For example, the prediction for activated Oxidative phosphorylation across ASD models is primarily driven by increases in the abundance of ATPases and different subunits of the cytochrome c oxidases and the NADH:ubiquinone oxidoreductase. Changes in synaptogenesis signaling pathways were driven by both increases and decreases in the abundance of regulators of the actin cytoskeleton which include several small G-proteins (Supplementary Table 4).

Regulatory networks predicted by synaptic changes in each model reveal both novel results and patterns consistent with the literature (Figures 3, 4; Supplementary Figures 1-4; Supplementary Tables 1-4). In the *Fmr1* KO model, fold-changes reveal that most altered proteins were upregulated as seen by the rightward skew of the ratio distributions (Figure 2A), which is consistent with the primary role of FMRP as a translational repressor (Darnell et al., 2011). In the model of constitutive *Pten* haploinsufficiency, synaptic dysfunction is likely due to neuronal *Pten*, since altered synaptic composition was also observed in a neuron-specific conditional knockout mouse that displayed changes in activity patterns and repetitive behavior (Lugo et al., 2014). Importantly, we directly compared synaptic proteomes in parallel, a necessary approach for finding shared phenotypes and broadly applicable therapeutic targets (Sestan and State, 2018; Silverman and Ellegood, 2018). Drawn from internally controlled measurements, our results demonstrate quantifiable differences in synaptic composition that support the presence of molecular subtypes in ASD rather than universal changes in the same direction.

In the five autism mouse models chosen for this study, changes in the synaptic proteome highlighted Rho family small GTPase signaling as a commonly altered cellular pathway (Figures 3, 4). These results complement a growing body of evidence showing that altered activation of Rho GTPases is an important mechanism of disease in autism and other neurodevelopmental disorders (Pinto et al., 2010; Zeidán-Chuliá et al., 2013; Guo et al., 2020). Functional validation results showed significantly reduced active Rac1 in *Anks1b* mice compared to wildtype, and compared to *Pten*, *Fmr1,* and *Cntnap2* mice, which was consistent with proteomic analysis (Figures 3, 4). These results suggest that downregulation of Rac1 pathways may inhibit the processes that require GTP-bound Rac1, thereby potentially causing some of the manifestations of *ANKS1B* syndrome, including ASD. Consistent with our findings that synaptic proteins in the Rac pathway (Supplementary Figure 6) and Rac1 itself is differentially regulated in ASD mouse models (Figure 4), further evidence continues to emerge that Rac1 signaling plays an important role in the pathobiology of ASD and other neurodevelopmental disorders. Rac1 mutations associated with intellectual disability impair synaptic plasticity (Tian et al., 2018), and variants in the RhoGEF *TRIO* can cause ASD, intellectual disability, schizophrenia, or macrocephaly, with severe phenotypes predicted by Rac1 overactivation (Katrancha et al., 2017; Sadybekov et al., 2017; Barbosa et al., 2020). Both up- and down-regulation of Rac1 in mice causes social deficits, an important symptom of ASD (Ma et al., 2022). Downstream of Rac1 in actin polymerization, mutations in *PAK*s and *WASF1* can cause macrocephaly, seizures, intellectual disability, or ASD (Ito et al., 2018; Horn et al., 2019). Overall, Rac1 pathways are commonly dysregulated in ASD and other neurodevelopmental disorders and are therefore attractive targets for pharmacotherapy (Zamboni et al., 2018; Guo et al., 2020).

Caveats to our work include comparisons at a single developmental timepoint and single brain region. Models of ASD show behavioral and biological phenotypes that differ based on the spatiotemporal targeting of the gene (Del Pino et al., 2018). A proteomic study of cortical synapses noted smaller differences in *Fmr1* KO mice after 3 weeks of age (Tang et al., 2015), and both Shank3 and Syngap1 show changes in interaction partners throughout development (Li et al., 2016, 2017). Moreover, we focused on hippocampal synapses, but there are important roles for the neocortex, striatum, and cerebellum in the pathophysiology of ASD animal models (Golden et al., 2018). Fractionation of the PSD limits our findings to synaptic profiles in glutamatergic neurons, but ASD risk genes also influence interneuron development (*Cntnap2*; Peñagarikano et al., 2011) and oligodendrocyte maturation (*Pten*; Lee et al., 2019). The number of isobaric tags available in the TMT set limited the number of simultaneous comparisons possible by mass spectrometry. We therefore had to analyze the biological replicates as three independent experiments, which increases variability. To minimize this variability, fold-ratios were calculated only between samples in the same MS run. Future experiments using increased isobaric tags such as the new TMT16-plex system could be used to compare proteomes across cell types and developmental stages, and additional ASD models (Stessman et al., 2016; Sestan and State, 2018; Iakoucheva et al., 2019).

Understanding the molecular mechanisms underlying ASDs is critical for the development of novel therapies. Our proteomic approach overcomes critical confounds associated with gene-based studies of ASD etiology that improperly equate transcript levels, epigenetic modifications, single-nucleotide polymorphisms (SNPs), or copy number variations (CNVs) to changes in protein abundance. This work shows that synaptic proteomes, as identifiable and quantifiable phenotypes of diverse ASD models, can lead to the identification of molecular convergence. We propose that this can lead to important insights into ASD etiology and yield high-value targets to pursue for future therapies.

Data availability statement

The raw mass spectrometry data generated during this study are available at MassIVE (UCSD), https://massive.ucsd.edu/ProteoSAFe/static/massive.jsp under the deposition number MSV000091848.

Author contributions

AC, CF-C, ID, and BJ designed and performed postsynaptic fractionation in autism mouse models. HE-B and TN performed tandem-mass-tag mass spectrometry and protein identification. AC and ID performed bioinformatics analysis and Western blots. ID and SD performed the GLISA assays. AC-A and DP developed and characterized Pten haploinsufficiency mouse model. AC, CF-C, ID, SD, and BJ interpreted results and wrote the paper. All authors contributed to the article and approved the submitted version.

Funding

This work was supported by NIH R01AG039521, NIH R01NS118820, and NIH R56MH115201 to BJ, T32GM007288 to AC, NIH S10RR027990 to TN, and NIH R01MH108519 to DP. Significant support for this work came from the Rose F. Kennedy Intellectual and Developmental Disabilities Research Center (IDDRC), which is funded through the center grant NIH U54HD090260.

Conflict of interest

The authors declare that the research was conducted in the absence of any commercial or financial relationships that could be construed as a potential conflict of interest.

Publisher's note

Supplementary material

The Supplementary material for this article can be found online at: https://www.frontiersin.org/articles/10.3389/fnagi.2023.1152562/full#supplementary-material

References

Abraham, J. R., Szoko, N., Barnard, J., Rubin, R. A., Schlatzer, D., Lundberg, K., et al. (2019). Proteomic investigations of autism brain identify known and novel Pathogenetic processes. *Sci. Rep.* 9:13118. doi: 10.1038/s41598-019-49533-y

Andoh, M., Shibata, K., Okamoto, K., Onodera, J., Morishita, K., Miura, Y., et al. (2019). Exercise reverses behavioral and synaptic abnormalities after maternal inflammation. *Cell Rep.* 27, 2817–2825.e5. doi: 10.1016/j.celrep.2019.05.015

Auerbach, B. D., Osterweil, E. K., and Bear, M. F. (2011). Mutations causing syndromic autism define an axis of synaptic pathophysiology. *Nature* 480, 63–68. doi: 10.1038/nature10658

Bagni, C., and Zukin, R. S. (2019). A synaptic perspective of fragile X syndrome and autism Spectrum disorders. *Neuron* 101, 1070–1088. doi: 10.1016/j.neuron.2019.02.041

Bailey, A., le Couteur, A., Gottesman, I., Bolton, P., Simonoff, E., Yuzda, E., et al. (1995). Autism as a strongly genetic disorder: evidence from a British twin study. *Psychol. Med.* 25, 63–77. doi: 10.1017/S0033291700028099

Barbosa, S., Greville-Heygate, S., Bonnet, M., Godwin, A., Fagotto-Kaufmann, C., Kajava, A. V., et al. (2020). Opposite modulation of RAC1 by mutations in TRIO is associated with distinct, domain-specific neurodevelopmental disorders. *Am. J. Hum. Genet.* 106, 338–355. doi: 10.1016/j.ajhg.2020.01.018

Barnes, S. A., Wijetunge, L. S., Jackson, A. D., Katsanevaki, D., Osterweil, E. K., Komiyama, N. H., et al. (2015). Convergence of hippocampal pathophysiology in Syngap+/− and Fmr1−/y mice. *J. Neurosci.* 35, 15073–15081. doi: 10.1523/JNEUROSCI.1087-15.2015

Bhakar, A. L., Dolen, G., and Bear, M. F. (2012). The pathophysiology of fragile X (and what it teaches us about synapses). *Annu. Rev. Neurosci.* 35, 417–443. doi: 10.1146/annurev-neuro-060909-153138

Blatt, G. J., Fitzgerald, C. M., Guptill, J. T., Booker, A. B., Kemper, T. L., and Bauman, M. L. (2001). Density and distribution of hippocampal neurotransmitter receptors in autism: an autoradiographic study. *J. Autism Dev. Disord.* 31, 537–543. doi: 10.1023/A:1013238809666

Bonda, D. J., Lee, H. G., Camins, A., Pallàs, M., Casadesus, G., Smith, M. A., et al. (2011). The sirtuin pathway in ageing and Alzheimer disease: mechanistic and therapeutic considerations. *Lancet Neurol.* 10, 275–279. doi: 10.1016/S1474-4422(11)70013-8

Bourgeron, T. (2015). From the genetic architecture to synaptic plasticity in autism spectrum disorder. *Nat. Rev. Neurosci.* 16, 551–563. doi: 10.1038/nrn3992

Brett, M., McPherson, J., Zang, Z. J., Lai, A., Tan, E. S., Ng, I., et al. (2014). Massively parallel sequencing of patients with intellectual disability, congenital anomalies and/or autism spectrum disorders with a targeted gene panel. *PLoS One* 9:e93409. doi: 10.1371/journal.pone.0093409

Brown, E. A., Lautz, J. D., Davis, T. R., Gniffke, E. P., VanSchoiack, A. A. W., Neier, S. C., et al. (2018). Clustering the autisms using glutamate synapse protein interaction networks from cortical and hippocampal tissue of seven mouse models. *Mol. Autism.* 9:48. doi: 10.1186/s13229-018-0229-1

Bucan, M., Abrahams, B. S., Wang, K., Glessner, J. T., Herman, E. I., Sonnenblick, L. I., et al. (2009). Genome-wide analyses of exonic copy number variants in a family-based study point to novel autism susceptibility genes. *PLoS Genet.* 5:e1000536. doi: 10.1371/journal.pgen.1000536

Buxbaum, J. D., Bolshakova, N., Brownfeld, J. M., Anney, R. J. L., Bender, P., Bernier, R., et al. (2014). The autism simplex collection: an international, expertly phenotyped autism sample for genetic and phenotypic analyses. *Mol. Autism.* 5:34. doi: 10.1186/2040-2392-5-34

Buxbaum, J. D., Daly, M. J., Devlin, B., Lehner, T., Roeder, K., State, M. W., et al. (2012). The autism sequencing consortium: large-scale, high-throughput sequencing in autism spectrum disorders. *Neuron* 76, 1052–1056. doi: 10.1016/j.neuron.2012.12.008

Carbonell, A. U., Cho, C. H., Tindi, J. O., Counts, P. A., Bates, J. C., Erdjument-Bromage, H., et al. (2019). Haploinsufficiency in the ANKS1B gene encoding AIDA-1 leads to a neurodevelopmental syndrome. *Nat. Commun.* 10:3529. doi: 10.1038/s41467-019-11437-w

Careaga, M., Rogers, S., Hansen, R. L., Amaral, D. G., van de Water, J., and Ashwood, P. (2017). Immune Endophenotypes in children with autism Spectrum disorder. *Biol. Psychiatry* 81, 434–441. doi: 10.1016/j.biopsych.2015.08.036

Carlin, R. K., Grab, D. J., Cohen, R. S., and Siekevitz, P. (1980). Isolation and characterization of postsynaptic densities from various brain regions: enrichment of different types of postsynaptic densities. *J. Cell Biol.* 86, 831–845. doi: 10.1083/jcb.86.3.831

Cellot, G., Maggi, L., di Castro, M. A., Catalano, M., Migliore, R., Migliore, M., et al. (2016). Premature changes in neuronal excitability account for hippocampal network impairment and autistic-like behavior in neonatal BTBR T+tf/J mice. *Sci. Rep.* 6:31696. doi: 10.1038/srep31696

Chen, J. A., Peñagarikano, O., Belgard, T. G., Swarup, V., and Geschwind, D. H. (2015). The emerging picture of autism spectrum disorder: genetics and pathology. *Annu. Rev. Pathol.* 10, 111–144. doi: 10.1146/annurev-pathol-012414-040405

Clipperton-Allen, A. E., and Page, D. T. (2014). Pten haploinsufficient mice show broad brain overgrowth but selective impairments in autism-relevant behavioral tests. *Hum. Mol. Genet.* 23, 3490–3505. doi: 10.1093/hmg/ddu057

Clipperton-Allen, A. E., and Page, D. T. (2015). Decreased aggression and increased repetitive behavior in Pten haploinsufficient mice. *Genes Brain Behav.* 14, 145–157. doi: 10.1111/gbb.12192

Cohen, R. S., Blomberg, F., Berzins, K., and Siekevitz, P. (1977). The structure of postsynaptic densities isolated from dog cerebral cortex. I. Overall morphology and protein composition. *J. Cell Biol.* 74, 181–203. doi: 10.1083/jcb.74.1.181

Consortium, T.D.-B.F.X (1994). Fmr1 knockout mice: a model to study fragile X mental retardation. The Dutch-Belgian fragile X consortium. *Cells* 78, 23–33.

Courchesne, E., Pramparo, T., Gazestani, V. H., Lombardo, M. V., Pierce, K., and Lewis, N. E. (2019). The ASD living biology: from cell proliferation to clinical phenotype. *Mol. Psychiatry* 24, 88–107. doi: 10.1038/s41380-018-0056-y

Cox, J., Neuhauser, N., Michalski, A., Scheltema, R. A., Olsen, J. V., and Mann, M. (2011). Andromeda: a peptide search engine integrated into the MaxQuant environment. *J. Proteome Res.* 10, 1794–1805. doi: 10.1021/pr101065j

Croning, M. D., Marshall, M. C., McLaren, P., Armstrong, J. D., and Grant, S. G. N. (2009). G2Cdb: the genes to cognition database. *Nucleic Acids Res.* 37, D846–D851. doi: 10.1093/nar/gkn700

Cukier, H. N., Dueker, N. D., Slifer, S. H., Lee, J. M., Whitehead, P. L., Lalanne, E., et al. (2014). Exome sequencing of extended families with autism reveals genes shared across neurodevelopmental and neuropsychiatric disorders. *Mol. Autism.* 5:1. doi: 10.1186/2040-2392-5-1

Darnell, J. C., van Driesche, S. J., Zhang, C., Hung, K. Y. S., Mele, A., Fraser, C. E., et al. (2011). FMRP stalls ribosomal translocation on mRNAs linked to synaptic function and autism. *Cells* 146, 247–261. doi: 10.1016/j.cell.2011.06.013

de la Torre-Ubieta, L., Won, H., Stein, J. L., and Geschwind, D. H. (2016). Advancing the understanding of autism disease mechanisms through genetics. *Nat. Med.* 22, 345–361. doi: 10.1038/nm.4071

De Rubeis, S., He, X., Goldberg, A. P., Poultney, C. S., Samocha, K., Ercument Cicek, A., et al. (2014). Synaptic, transcriptional and chromatin genes disrupted in autism. *Nature* 515, 209–215. doi: 10.1038/nature13772

de Rubeis, S., Pasciuto, E., Li, K. W., Fernández, E., di Marino, D., Buzzi, A., et al. (2013). CYFIP1 coordinates mRNA translation and cytoskeleton remodeling to ensure proper dendritic spine formation. *Neuron* 79, 1169–1182. doi: 10.1016/j.neuron.2013.06.039

Del Pino, I., Rico, B., and Marin, O. (2018). Neural circuit dysfunction in mouse models of neurodevelopmental disorders. *Curr. Opin. Neurobiol.* 48, 174–182. doi: 10.1016/j.conb.2017.12.013

Doherty, M. K., Hammond, D. E., Clague, M. J., Gaskell, S. J., and Beynon, R. J. (2009). Turnover of the human proteome: determination of protein intracellular stability by dynamic SILAC. *J. Proteome Res.* 8, 104–112. doi: 10.1021/pr800641v

Dong, D., Zielke, H. R., Yeh, D., and Yang, P. (2018). Cellular stress and apoptosis contribute to the pathogenesis of autism spectrum disorder. *Autism Res.* 11, 1076–1090. doi: 10.1002/aur.1966

Erdjument-Bromage, H., Huang, F. K., and Neubert, T. A. (2018). Sample preparation for relative quantitation of proteins using tandem mass tags (TMT) and mass spectrometry (MS). *Methods Mol. Biol.* 1741, 135–149. doi: 10.1007/978-1-4939-7659-1_11

Forés-Martos, J., Catalá-López, F., Sánchez-Valle, J., Ibáñez, K., Tejero, H., Palma-Gudiel, H., et al. (2019). Transcriptomic metaanalyses of autistic brains reveals shared gene expression and biological pathway abnormalities with cancer. *Mol. Autism.* 10:17. doi: 10.1186/s13229-019-0262-8

Gao, R., and Penzes, P. (2015). Common mechanisms of excitatory and inhibitory imbalance in schizophrenia and autism spectrum disorders. *Curr. Mol. Med.* 15, 146–167. doi: 10.2174/1566524015666150303003028

Gaugler, T., Klei, L., Sanders, S. J., Bodea, C. A., Goldberg, A. P., Lee, A. B., et al. (2014). Most genetic risk for autism resides with common variation. *Nat. Genet.* 46, 881–885. doi: 10.1038/ng.3039

Giulivi, C., Zhang, Y. F., Omanska-Klusek, A., Ross-Inta, C., Wong, S., Hertz-Picciotto, I., et al. (2010). Mitochondrial dysfunction in autism. *JAMA* 304, 2389–2396. doi: 10.1001/jama.2010.1706

Glessner, J. T., Wang, K., Cai, G., Korvatska, O., Kim, C. E., Wood, S., et al. (2009). Autism genome-wide copy number variation reveals ubiquitin and neuronal genes. *Nature* 459, 569–573. doi: 10.1038/nature07953

Golden, C. E., Buxbaum, J. D., and De Rubeis, S. (2018). Disrupted circuits in mouse models of autism spectrum disorder and intellectual disability. *Curr. Opin. Neurobiol.* 48, 106–112. doi: 10.1016/j.conb.2017.11.006

Greenbaum, D., Colangelo, C., Williams, K., and Gerstein, M. (2003). Comparing protein abundance and mRNA expression levels on a genomic scale. *Genome Biol.* 4:117. doi: 10.1186/gb-2003-4-9-117

Guo, D., Yang, X., and Shi, L. (2020). Rho GTPase regulators and effectors in autism Spectrum disorders: animal models and insights for therapeutics. *Cells* 9:835. doi: 10.3390/cells9040835

Hallmayer, J., Cleveland, S., Torres, A., Phillips, J., Cohen, B., Torigoe, T., et al. (2011). Genetic heritability and shared environmental factors among twin pairs with autism. *Arch. Gen. Psychiatry* 68, 1095–1102. doi: 10.1001/archgenpsychiatry.2011.76

Heise, C., Preuss, J. M., Schroeder, J. C., Battaglia, C. R., Kolibius, J., Schmid, R., et al. (2018). Heterogeneity of cell surface glutamate and GABA receptor expression in shank and CNTN4 autism mouse models. *Front. Mol. Neurosci.* 11:212. doi: 10.3389/fnmol.2018.00212

Hernandez, L. M., Kim, M., Hoftman, G. D., Haney, J. R., de la Torre-Ubieta, L., Pasaniuc, B., et al. (2020). Transcriptomic insight into the polygenic mechanisms underlying psychiatric disorders. *Biol. Psychiatry* 89, 54–64. doi: 10.1016/j.biopsych.2020.06.005

Hoogendijk, A. J., Pourfarzad, F., Aarts, C. E. M., Tool, A. T. J., Hiemstra, I. H., Grassi, L., et al. (2019). Dynamic Transcriptome-proteome correlation networks reveal human myeloid differentiation and neutrophil-specific programming. *Cell Rep.* 29, 2505–2519.e4. doi: 10.1016/j.celrep.2019.10.082

Horn, S., Au, M., Basel-Salmon, L., Bayrak-Toydemir, P., Chapin, A., Cohen, L., et al. (2019). De novo variants in PAK1 lead to intellectual disability with macrocephaly and seizures. *Brain* 142, 3351–3359. doi: 10.1093/brain/awz264

Huang, F. K., Zhang, G., Lawlor, K., Nazarian, A., Philip, J., Tempst, P., et al. (2017). Deep coverage of global protein expression and phosphorylation in breast tumor cell lines using TMT 10-plex isobaric labeling. *J. Proteome Res.* 16, 1121–1132. doi: 10.1021/acs.jproteome.6b00374

Hughes, H. K., Mills Ko, E., Rose, D., and Ashwood, P. (2018). Immune dysfunction and autoimmunity as pathological mechanisms in autism Spectrum disorders. *Front. Cell. Neurosci.* 12:405. doi: 10.3389/fncel.2018.00405

Hulbert, S. W., and Jiang, Y. H. (2016). Monogenic mouse models of autism spectrum disorders: common mechanisms and missing links. *Neuroscience* 321, 3–23. doi: 10.1016/j.neuroscience.2015.12.040

Hussman, J. P. (2001). Suppressed GABAergic inhibition as a common factor in suspected etiologies of autism. *J. Autism Dev. Disord.* 31, 247–248. doi: 10.1023/A:1010715619091

Hussman, J. P., Chung, R. H., Griswold, A. J., Jaworski, J. M., Salyakina, D., Ma, D., et al. (2011). A noise-reduction GWAS analysis implicates altered regulation of neurite outgrowth and guidance in autism. *Mol. Autism.* 2:1. doi: 10.1186/2040-2392-2-1

Iakoucheva, L. M., Muotri, A. R., and Sebat, J. (2019). Getting to the cores of autism. *Cells* 178, 1287–1298. doi: 10.1016/j.cell.2019.07.037

Ingolia, N. T., Ghaemmaghami, S., Newman, J. R. S., and Weissman, J. S. (2009). Genome-wide analysis in vivo of translation with nucleotide resolution using ribosome profiling. *Science* 324, 218–223. doi: 10.1126/science.1168978

Iossifov, I., O'Roak, B. J., Sanders, S. J., Ronemus, M., Krumm, N., Levy, D., et al. (2014). The contribution of de novo coding mutations to autism spectrum disorder. *Nature* 515, 216–221. doi: 10.1038/nature13908

Ito, Y., Carss, K. J., Duarte, S. T., Hartley, T., Keren, B., Kurian, M. A., et al. (2018). De novo truncating mutations in WASF1 cause intellectual disability with seizures. *Am. J. Hum. Genet.* 103, 144–153. doi: 10.1016/j.ajhg.2018.06.001

Jordan, B. A., Fernholz, B. D., Boussac, M., Xu, C., Grigorean, G., Ziff, E. B., et al. (2004). Identification and verification of novel rodent postsynaptic density proteins. *Mol. Cell. Proteomics* 3, 857–871. doi: 10.1074/mcp.M400045-MCP200

Jordan, B. A., Fernholz, B. D., Khatri, L., and Ziff, E. B. (2007). Activity-dependent AIDA-1 nuclear signaling regulates nucleolar numbers and protein synthesis in neurons. *Nat. Neurosci.* 10, 427–435. doi: 10.1038/nn1867

Kabitzke, P. A., Brunner, D., He, D., Fazio, P. A., Cox, K., Sutphen, J., et al. (2018). Comprehensive analysis of two Shank3 and the Cacna1c mouse models of autism spectrum disorder. *Genes Brain Behav.* 17, 4–22. doi: 10.1111/gbb.12405

Kaizuka, T., and Takumi, T. (2018). Postsynaptic density proteins and their involvement in neurodevelopmental disorders. *J. Biochem.* 163, 447–455. doi: 10.1093/jb/mvy022

Katrancha, S. M., Wu, Y., Zhu, M., Eipper, B. A., Koleske, A. J., and Mains, R. E. (2017). Neurodevelopmental disease-associated de novo mutations and rare sequence variants affect TRIO GDP/GTP exchange factor activity. *Hum. Mol. Genet.* 26, 4728–4740. doi: 10.1093/hmg/ddx355

Kazdoba, T. M., Leach, P. T., and Crawley, J. N. (2016). Behavioral phenotypes of genetic mouse models of autism. *Genes Brain Behav.* 15, 7–26. doi: 10.1111/gbb.12256

Koopmans, F., van Nierop, P., Andres-Alonso, M., Byrnes, A., Cijsouw, T., Coba, M. P., et al. (2019). SynGO: an evidence-based, expert-curated Knowledge Base for the synapse. *Neuron* 103, 217–234.e4. doi: 10.1016/j.neuron.2019.05.002

Krämer, A., Green, J., Pollard, J. Jr., and Tugendreich, S. (2014). Causal analysis approaches in ingenuity pathway analysis. *Bioinformatics* 30, 523–530. doi: 10.1093/bioinformatics/btt703

Lee, Y., Kang, H., Lee, B., Zhang, Y., Kim, Y., Kim, S., et al. (2017). Integrative analysis of brain region-specific Shank3 Interactomes for understanding the heterogeneity of neuronal pathophysiology related to SHANK3 mutations. *Front. Mol. Neurosci.* 10:110. doi: 10.3389/fnmol.2017.00110

Lee, H., Thacker, S., Sarn, N., Dutta, R., and Eng, C. (2019). Constitutional mislocalization of Pten drives precocious maturation in oligodendrocytes and aberrant myelination in model of autism spectrum disorder. *Transl. Psychiatry* 9:13. doi: 10.1038/s41398-018-0364-7

Li, Y., Missig, G., Finger, B. C., Landino, S. M., Alexander, A. J., Mokler, E. L., et al. (2018). Maternal and early postnatal immune activation produce dissociable effects on neurotransmission in mPFC-amygdala circuits. *J. Neurosci.* 38, 3358–3372. doi: 10.1523/JNEUROSCI.3642-17.2018

Li, J., Shi, M., Ma, Z., Zhao, S., Euskirchen, G., Ziskin, J., et al. (2014). Integrated systems analysis reveals a molecular network underlying autism spectrum disorders. *Mol. Syst. Biol.* 10:774. doi: 10.15252/msb.20145487

Li, J., Wilkinson, B., Clementel, V. A., Hou, J., O'Dell, T. J., and Coba, M. P. (2016). Long-term potentiation modulates synaptic phosphorylation networks and reshapes the structure of the postsynaptic interactome. *Sci. Signal.* 9:rs8. doi: 10.1126/scisignal.aaf6716

Li, J., Zhang, W., Yang, H., Howrigan, D. P., Wilkinson, B., Souaiaia, T., et al. (2017). Spatiotemporal profile of postsynaptic interactomes integrates components of complex brain disorders. *Nat. Neurosci.* 20, 1150–1161. doi: 10.1038/nn.4594

Louros, S. R., and Osterweil, E. K. (2016). Perturbed proteostasis in autism spectrum disorders. *J. Neurochem.* 139, 1081–1092. doi: 10.1111/jnc.13723

Lugo, J. N., Smith, G. D., Arbuckle, E. P., White, J., Holley, A. J., Floruta, C. M., et al. (2014). Deletion of PTEN produces autism-like behavioral deficits and alterations in synaptic proteins. *Front. Mol. Neurosci.* 7:27. doi: 10.3389/fnmol.2014.00027

Ma, B., Shan, X., Yu, J., Zhu, T., Li, R., Lv, H., et al. (2022). Social deficits via dysregulated Rac1-dependent excitability control of prefrontal cortical neurons and increased GABA/glutamate ratios. *Cell Rep.* 41:111722. doi: 10.1016/j.celrep.2022.111722

Mabb, A. M., Judson, M. C., Zylka, M. J., and Philpot, B. D. (2011). Angelman syndrome: insights into genomic imprinting and neurodevelopmental phenotypes. *Trends Neurosci.* 34, 293–303. doi: 10.1016/j.tins.2011.04.001

Maier, T., Guell, M., and Serrano, L. (2009). Correlation of mRNA and protein in complex biological samples. *FEBS Lett.* 583, 3966–3973. doi: 10.1016/j.febslet.2009.10.036

Martin, H. G., and Manzoni, O. J. (2014). Late onset deficits in synaptic plasticity in the valproic acid rat model of autism. *Front. Cell. Neurosci.* 8:23. doi: 10.3389/fncel.2014.00023

McFarlane, H. G., Kusek, G. K., Yang, M., Phoenix, J. L., Bolivar, V. J., and Crawley, J. N. (2008). Autism-like behavioral phenotypes in BTBR T+tf/J mice. *Genes Brain Behav.* 7, 152–163. doi: 10.1111/j.1601-183X.2007.00330.x

Meltzer, A., and Van de Water, J. (2017). The role of the immune system in autism Spectrum disorder. *Neuropsychopharmacology* 42, 284–298. doi: 10.1038/npp.2016.158

Murtaza, N., Uy, J., and Singh, K. K. (2020). Emerging proteomic approaches to identify the underlying pathophysiology of neurodevelopmental and neurodegenerative disorders. *Mol. Autism.* 11:27. doi: 10.1186/s13229-020-00334-5

Nelson, S. B., and Valakh, V. (2015). Excitatory/inhibitory balance and circuit homeostasis in autism Spectrum disorders. *Neuron* 87, 684–698. doi: 10.1016/j.neuron.2015.07.033

Pacheco, N. L., Heaven, M. R., Holt, L. M., Crossman, D. K., Boggio, K. J., Shaffer, S. A., et al. (2017). RNA sequencing and proteomics approaches reveal novel deficits in the cortex of Mecp2-deficient mice, a model for Rett syndrome. *Mol. Autism.* 8:56. doi: 10.1186/s13229-017-0174-4

Parikshak, N. N., Swarup, V., Belgard, T. G., Irimia, M., Ramaswami, G., Gandal, M. J., et al. (2016). Genome-wide changes in lncRNA, splicing, and regional gene expression patterns in autism. *Nature* 540, 423–427. doi: 10.1038/nature20612

Patrich, E., Piontkewitz, Y., Peretz, A., Weiner, I., and Attali, B. (2016). Maternal immune activation produces neonatal excitability defects in offspring hippocampal neurons from pregnant rats treated with poly I:C. *Sci. Rep.* 6:19106. doi: 10.1038/srep19106

Peñagarikano, O., Abrahams, B. S., Herman, E. I., Winden, K. D., Gdalyahu, A., Dong, H., et al. (2011). Absence of CNTNAP2 leads to epilepsy, neuronal migration abnormalities, and core autism-related deficits. *Cells* 147, 235–246. doi: 10.1016/j.cell.2011.08.040

Pinto, D., Delaby, E., Merico, D., Barbosa, M., Merikangas, A., Klei, L., et al. (2014). Convergence of genes and cellular pathways dysregulated in autism spectrum disorders. *Am. J. Hum. Genet.* 94, 677–694. doi: 10.1016/j.ajhg.2014.03.018

Pinto, D., Pagnamenta, A. T., Klei, L., Anney, R., Merico, D., Regan, R., et al. (2010). Functional impact of global rare copy number variation in autism spectrum disorders. *Nature* 466, 368–372. doi: 10.1038/nature09146

Quesnel-Vallières, M., Weatheritt, R. J., Cordes, S. P., and Blencowe, B. J. (2019). Autism spectrum disorder: insights into convergent mechanisms from transcriptomics. *Nat. Rev. Genet.* 20, 51–63. doi: 10.1038/s41576-018-0066-2

Ramaswami, G., and Geschwind, D. H. (2018). Genetics of autism spectrum disorder. *Handb. Clin. Neurol.* 147, 321–329. doi: 10.1016/B978-0-444-63233-3.00021-X

Rappsilber, J., Mann, M., and Ishihama, Y. (2007). Protocol for micro-purification, enrichment, pre-fractionation and storage of peptides for proteomics using StageTips. *Nat. Protoc.* 2, 1896–1906. doi: 10.1038/nprot.2007.261

Reim, D., Distler, U., Halbedl, S., Verpelli, C., Sala, C., Bockmann, J., et al. (2017). Proteomic analysis of post-synaptic density fractions from Shank3 mutant mice reveals

brain region specific changes relevant to autism Spectrum disorder. *Front. Mol. Neurosci.* 10:26. doi: 10.3389/fnmol.2017.00026

Ronemus, M., Iossifov, I., Levy, D., and Wigler, M. (2014). The role of de novo mutations in the genetics of autism spectrum disorders. *Nat. Rev. Genet.* 15, 133–141. doi: 10.1038/nrg3585

Rossignol, D. A., and Frye, R. E. (2012). Mitochondrial dysfunction in autism spectrum disorders: a systematic review and meta-analysis. *Mol. Psychiatry* 17, 290–314. doi: 10.1038/mp.2010.136

Rubenstein, J. L., and Merzenich, M. M. (2003). Model of autism: increased ratio of excitation/inhibition in key neural systems. *Genes Brain Behav.* 2, 255–267. doi: 10.1034/j.1601-183X.2003.00037.x

Ruzzo, E. K., Pérez-Cano, L., Jung, J. Y., Wang, L. K., Kashef-Haghighi, D., Hartl, C., et al. (2019). Inherited and De novo genetic risk for autism impacts shared networks. *Cells* 178, 850–866.e26. doi: 10.1016/j.cell.2019.07.015

Sadybekov, A., Tian, C., Arnesano, C., Katritch, V., and Herring, B. E. (2017). An autism spectrum disorder-related de novo mutation hotspot discovered in the GEF1 domain of Trio. *Nat. Commun.* 8:601. doi: 10.1038/s41467-017-00472-0

Sanders, S. J., Murtha, M. T., Gupta, A. R., Murdoch, J. D., Raubeson, M. J., Willsey, A. J., et al. (2012). De novo mutations revealed by whole-exome sequencing are strongly associated with autism. *Nature* 485, 237–241. doi: 10.1038/nature10945

Sarowar, T., and Grabrucker, A. M. (2016). Actin-dependent alterations of dendritic spine morphology in Shankopathies. *Neural Plast.* 2016:8051861. doi: 10.1155/2016/8051861

Schoen, M., Asoglu, H., Bauer, H. F., Müller, H. P., Abaei, A., Sauer, A. K., et al. (2019). Shank3 transgenic and prenatal zinc-deficient autism mouse models show convergent and individual alterations of brain structures in MRI. *Front. Neural. Circuits* 13:6. doi: 10.3389/fncir.2019.00006

Schwanhäusser, B., Busse, D., Li, N., Dittmar, G., Schuchhardt, J., Wolf, J., et al. (2011). Global quantification of mammalian gene expression control. *Nature* 473, 337–342. doi: 10.1038/nature10098

Sestan, N., and State, M. W. (2018). Lost in translation: traversing the complex path from genomics to therapeutics in autism Spectrum disorder. *Neuron* 100, 406–423. doi: 10.1016/j.neuron.2018.10.015

Silverman, J. L., and Ellegood, J. (2018). Behavioral and neuroanatomical approaches in models of neurodevelopmental disorders: opportunities for translation. *Curr. Opin. Neurol.* 31, 126–133. doi: 10.1097/WCO.0000000000000537

Steffenburg, S., Gillberg, C., Hellgren, L., Andersson, L., Gillberg, I. C., Jakobsson, G., et al. (1989). A twin study of autism in Denmark, Finland, Iceland, Norway and Sweden. *J. Child Psychol. Psychiatry* 30, 405–416. doi: 10.1111/j.1469-7610.1989.tb00254.x

Stessman, H. A., Turner, T. N., and Eichler, E. E. (2016). Molecular subtyping and improved treatment of neurodevelopmental disease. *Genome Med.* 8:22. doi: 10.1186/s13073-016-0278-z

Sui, L., and Chen, M. (2012). Prenatal exposure to valproic acid enhances synaptic plasticity in the medial prefrontal cortex and fear memories. *Brain Res. Bull.* 87, 556–563. doi: 10.1016/j.brainresbull.2012.01.011

Szklarczyk, D., Franceschini, A., Wyder, S., Forslund, K., Heller, D., Huerta-Cepas, J., et al. (2015). STRING v10: protein-protein interaction networks, integrated over the tree of life. *Nucleic Acids Res.* 43, D447–D452. doi: 10.1093/nar/gku1003

Szklarczyk, D., Gable, A. L., Lyon, D., Junge, A., Wyder, S., Huerta-Cepas, J., et al. (2019). STRING v11: protein-protein association networks with increased coverage, supporting functional discovery in genome-wide experimental datasets. *Nucleic Acids Res.* 47, D607–D613. doi: 10.1093/nar/gky1131

Sztainberg, Y., and Zoghbi, H. Y. (2016). Lessons learned from studying syndromic autism spectrum disorders. *Nat. Neurosci.* 19, 1408–1417. doi: 10.1038/nn.4420

Tang, B., Wang, T., Wan, H., Han, L., Qin, X., Zhang, Y., et al. (2015). Fmr1 deficiency promotes age-dependent alterations in the cortical synaptic proteome. *Proc. Natl. Acad. Sci. U. S. A.* 112, E4697–E4706. doi: 10.1073/pnas.1502258112

Thompson, A., Schäfer, J., Kuhn, K., Kienle, S., Schwarz, J., Schmidt, G., et al. (2003). Tandem mass tags: a novel quantification strategy for comparative analysis of complex protein mixtures by MS/MS. *Anal. Chem.* 75, 1895–1904. doi: 10.1021/ac0262560

Tian, C., Kay, Y., Sadybekov, A., Rao, S., Katritch, V., and Herring, B. E. (2018). An intellectual disability-related missense mutation in Rac1 prevents LTP induction. *Front. Mol. Neurosci.* 11:223. doi: 10.3389/fnmol.2018.00223

Tindi, J. O., Chavez, A. E., Cvejic, S., Calvo-Ochoa, E., Castillo, P. E., and Jordan, B. A. (2015). ANKS1B gene product AIDA-1 controls hippocampal synaptic transmission by regulating GluN2B subunit localization. *J. Neurosci.* 35, 8986–8996. doi: 10.1523/JNEUROSCI.4029-14.2015

Toma, C., Torrico, B., Hervás, A., Valdés-Mas, R., Tristán-Noguero, A., Padillo, V., et al. (2014). Exome sequencing in multiplex autism families suggests a major role for heterozygous truncating mutations. *Mol. Psychiatry* 19, 784–790. doi: 10.1038/mp.2013.106

Tyanova, S., Temu, T., and Cox, J. (2016). The MaxQuant computational platform for mass spectrometry-based shotgun proteomics. *Nat. Protoc.* 11, 2301–2319. doi: 10.1038/nprot.2016.136

Varghese, M., Keshav, N., Jacot-Descombes, S., Warda, T., Wicinski, B., Dickstein, D. L., et al. (2017). Autism spectrum disorder: neuropathology and animal models. *Acta Neuropathol.* 134, 537–566. doi: 10.1007/s00401-017-1736-4

Verma, V., Paul, A., Amrapali Vishwanath, A., Vaidya, B., and Clement, J. P. (2019). Understanding intellectual disability and autism spectrum disorders from common mouse models: synapses to behaviour. *Open Biol.* 9:180265. doi: 10.1098/rsob.180265

Vogel, C., and Marcotte, E. M. (2012). Insights into the regulation of protein abundance from proteomic and transcriptomic analyses. *Nat. Rev. Genet.* 13, 227–232. doi: 10.1038/nrg3185

Wang, J., Ma, Z., Carr, S. A., Mertins, P., Zhang, H., Zhang, Z., et al. (2017). Proteome profiling outperforms Transcriptome profiling for Coexpression based gene function prediction. *Mol. Cell. Proteomics* 16, 121–134. doi: 10.1074/mcp.M116.060301

Wang, R., Tan, J., Guo, J., Zheng, Y., Han, Q., So, K. F., et al. (2018). Aberrant development and synaptic transmission of cerebellar cortex in a VPA induced mouse autism model. *Front. Cell. Neurosci.* 12:500. doi: 10.3389/fncel.2018.00500

Weiner, D. J., Wigdor, E. M., Ripke, S., Walters, R. K., Kosmicki, J. A., Grove, J., et al. (2017). Polygenic transmission disequilibrium confirms that common and rare variation act additively to create risk for autism spectrum disorders. *Nat. Genet.* 49, 978–985. doi: 10.1038/ng.3863

Yoo, H. (2015). Genetics of autism Spectrum disorder: current status and possible clinical applications. *Exp. Neurobiol.* 24, 257–272. doi: 10.5607/en.2015.24.4.257

Yu, T. W., Chahrour, M. H., Coulter, M. E., Jiralerspong, S., Okamura-Ikeda, K., Ataman, B., et al. (2013). Using whole-exome sequencing to identify inherited causes of autism. *Neuron* 77, 259–273. doi: 10.1016/j.neuron.2012.11.002

Yuen, R. K., Thiruvahindrapuram, B., Merico, D., Walker, S., Tammimies, K., Hoang, N., et al. (2015). Whole-genome sequencing of quartet families with autism spectrum disorder. *Nat. Med.* 21, 185–191. doi: 10.1038/nm.3792

Zamboni, V., Armentano, M., Berto, G., Ciraolo, E., Ghigo, A., Garzotto, D., et al. (2018). Hyperactivity of Rac1-GTPase pathway impairs neuritogenesis of cortical neurons by altering actin dynamics. *Sci. Rep.* 8:7254. doi: 10.1038/s41598-018-25354-3

Zeidán-Chuliá, F., Rybarczyk-Filho, J. L., Salmina, A. B., de Oliveira, B. H. N., Noda, M., and Moreira, J. C. F. (2013). Exploring the multifactorial nature of autism through computational systems biology: calcium and the rho GTPase RAC1 under the spotlight. *NeuroMolecular Med.* 15, 364–383. doi: 10.1007/s12017-013-8224-3

Zhang, G., Neubert, T. A., and Jordan, B. A. (2012). RNA binding proteins accumulate at the postsynaptic density with synaptic activity. *J. Neurosci.* 32, 599–609. doi: 10.1523/JNEUROSCI.2463-11.2012

Zhou, Y., Kaiser, T., Monteiro, P., Zhang, X., van der Goes, M. S., Wang, D., et al. (2016). Mice with Shank3 mutations associated with ASD and schizophrenia display both shared and distinct defects. *Neuron* 89, 147–162. doi: 10.1016/j.neuron.2015.11.023

Zoghbi, H. Y., and Bear, M. F. (2012). Synaptic dysfunction in neurodevelopmental disorders associated with autism and intellectual disabilities. *Cold Spring Harb. Perspect. Biol.* 4:a009886. doi: 10.1101/cshperspect.a009886

frontiers | Frontiers in Aging Neuroscience

TYPE Original Research
PUBLISHED 05 June 2023
DOI 10.3389/fnagi.2023.1180987

OPEN ACCESS

EDITED BY
Philippe Léon Louis Poindron,
NeuroSys, France

REVIEWED BY
Jeronimo Jurado Arjona,
King's College London, United Kingdom
Antonella Tramutola,
Sapienza University of Rome, Italy

*CORRESPONDENCE
Alejandra Álvarez Rojas
✉ aalvarez@bio.puc.cl

†These authors have contributed equally to this work and share first authorship

RECEIVED 06 March 2023
ACCEPTED 12 May 2023
PUBLISHED 05 June 2023

CITATION
León R, Gutiérrez DA, Pinto C, Morales C, de la Fuente C, Riquelme C, Cortés BI, González-Martin A, Chamorro D, Espinosa N, Fuentealba P, Cancino GI, Zanlungo S, Dulcey AE, Marugan JJ and Álvarez Rojas A (2023) c-Abl tyrosine kinase down-regulation as target for memory improvement in Alzheimer's disease.
Front. Aging Neurosci. 15:1180987.
doi: 10.3389/fnagi.2023.1180987

c-Abl tyrosine kinase down-regulation as target for memory improvement in Alzheimer's disease

Rilda León[1†], Daniela A. Gutiérrez[1†], Claudio Pinto[1], Cristian Morales[2,3], Catalina de la Fuente[1], Cristóbal Riquelme[1], Bastián I. Cortés[4], Adrián González-Martin[1], David Chamorro[1], Nelson Espinosa[3], Pablo Fuentealba[3], Gonzalo I. Cancino[4], Silvana Zanlungo[5], Andrés E. Dulcey[6], Juan J. Marugan[6] and Alejandra Álvarez Rojas[1*]

[1]Cell Signaling Laboratory, Department of Cellular and Molecular Biology, Biological Sciences Faculty, Millennium Institute on Immunology and Immunotherapy, Pontificia Universidad Católica de Chile, Santiago, Chile, [2]Laboratory for Brain-Machine Interfaces and Neuromodulation, Facultad de Ingeniería, Instituto de Ingeniería Biológica y Médica, Pontificia Universidad Católica de Chile, Santiago, Chile, [3]Laboratory of Neural Circuits, Department of Psychiatry, Neuroscience Interdisciplinary Centre, Pontificia Universidad Católica de Chile, Santiago, Chile, [4]Department of Cellular and Molecular Biology, Biological Sciences Faculty, Pontificia Universidad Católica de Chile, Santiago, Chile, [5]Department of Gastroenterology, Faculty of Medicine, Pontificia Universidad Catolica de Chile, Santiago, Chile, [6]Early Translation Branch, National Center for Advancing Translational Sciences (NCATS), NIH, Rockville, MD, United States

Background: Growing evidence suggests that the non-receptor tyrosine kinase, c-Abl, plays a significant role in the pathogenesis of Alzheimer's disease (AD). Here, we analyzed the effect of c-Abl on the cognitive performance decline of APPSwe/PSEN1ΔE9 (APP/PS1) mouse model for AD.

Methods: We used the conditional genetic ablation of c-Abl in the brain (c-Abl-KO) and pharmacological treatment with neurotinib, a novel allosteric c-Abl inhibitor with high brain penetrance, imbued in rodent's chow.

Results: We found that APP/PS1/c-Abl-KO mice and APP/PS1 neurotinib-fed mice had improved performance in hippocampus-dependent tasks. In the object location and Barnes-maze tests, they recognized the displaced object and learned the location of the escape hole faster than APP/PS1 mice. Also, APP/PS1 neurotinib-fed mice required fewer trials to reach the learning criterion in the memory flexibility test. Accordingly, c-Abl absence and inhibition caused fewer amyloid plaques, reduced astrogliosis, and preserved neurons in the hippocampus.

Discussion: Our results further validate c-Abl as a target for AD, and the neurotinib, a novel c-Abl inhibitor, as a suitable preclinical candidate for AD therapies.

KEYWORDS

c-Abl inhibitors, tyrosine kinases, Alzheimer's disease, memory, Hippocampi

1. Introduction

Alzheimer's disease (AD) is a neurodegenerative disorder characterized by cognitive decline primarily affecting memory (Lane et al., 2018; Knopman et al., 2021) being the leading form of dementia with a contribution in 60–70% of worldwide cases.

AD patient's brains have a loss of neuronal populations in regions related to memory and cognition, such as the hippocampus, amygdala, and frontal regions (Gomez-Isla et al., 2008; Viola and Klein, 2015), and are characterized by extracellular aggregates of the Amyloid-β peptide (Aβ) and intracellular neurofibrillary tangles aggregates form by hyper-phosphorylated cytoskeletal Tau protein (Walsh and Selkoe, 2004). The earliest changes in AD are associated with the accumulation of oligomeric forms of the Aβ peptide (AβOs), leading to progressive reduction in connectivity and loss of plasticity followed by synaptic loss, neurotransmitter depletion, cytoskeletal alterations, abnormal protein phosphorylation, and finally, neuronal death (Davies et al., 1987; Hsia et al., 1999; Atwood and Bowen, 2015). AD typically presents with prominent amnestic cognitive impairment and short-term memory difficulty, but impairment in expressive speech, visuospatial processing, and executive functions also occurs. Most AD cases are not dominantly inherited and have a complex relationship to genetics.

The c-Abl protein has been involved in the pathogenesis of many neurodegenerative diseases. It belongs to the ABL family of non-receptor tyrosine kinases that comprises c-Abl (ABL1) and Arg (ABL2). c-Abl can regulate the actin cytoskeleton in dendrites (Jones et al., 2004; Chandía-Cristi et al., 2023) and interact with p73 to promote neuronal death (Wang, 2014; Khatri et al., 2016; Gutiérrez et al., 2023). Neurons treated with AβOs or fibrils show c-Abl activation, and this activation correlates with AD pathology in patients' brains (Alvarez et al., 2004; Jing et al., 2009). Inhibition of c-Abl with imatinib (ATP binding site orthosteric inhibitor) prevented tau phosphorylation, the blockade of LTP induction, dendritic spine reduction, and neuronal apoptosis caused by Aβ (Cancino et al., 2011; Vargas et al., 2014). c-Abl inhibition increased the expression of several synaptic genes in AD models through HDAC2 stabilization (González-Zuñiga et al., 2014), while c-Abl null neurons showed reduced susceptibility to synaptic contacts elimination caused by AβOs (Gutiérrez et al., 2019). González-Martín and colleagues have published the effect of c-Abl ablation in cognitive training as c-Abl KO mice had improved performance when subjected to learning tasks such as the Morris water maze test (González-Martin et al., 2021).

Chronic intraperitoneal administration of imatinib in the AD mouse model APPSwe/PSEN1ΔE9 (APP/PS1) reduced behavioral deficits and decreased AβOs accumulation in the APP/PS1 mice brain and blood (Cancino et al., 2008; Estrada et al., 2016). Therefore, c-Abl inhibition can modulate mice's cognitive performance. However, one of the limitations of using current FDA-approved c-Abl inhibitors is that they have a poor blood–brain barrier (BBB) permeability and target other kinases (Greuber et al., 2013; Aghel et al., 2017; Zukas and Schiff, 2018). In AD, a nilotinib (c-Abl orthosteric inhibitor) trial of 37 patients using the maximal daily tolerated dose of 300 mg showed that after 6–12 months of treatment, the group had reduced $A\beta_{40}$ and $A\beta_{42}$ cerebrospinal fluid levels compared to the placebo group, displaying also reduced Tau phosphorylation (Turner et al., 2020). Although the pathological biomarkers were reduced, the severity and progression of cognitive impairment did not change. However, patients only reached 2–4 nM CSF levels of nilotinib, 10–20 times less than its IC50 against cAbl. These low levels of exposure in CNS might be the cause behind the discrepancies regarding observed cognitive improvement in animal models and human clinical trials. Recently, our group has designed and characterized neurotinib, a new c-Abl allosteric inhibitor binding at the myristoyl pocket of the kinase with excellent BBB permeability and brain pharmacokinetics, and showed that neurotinib decreases cognitive decline in Niemann-Pick A mice (Marin et al., 2022).

Here, we have ultimately confirmed the role of c-Abl in the pathogenesis of AD by generating a new AD transgenic mice strain with genetic ablation of c-Abl in neurons. The APPswe/PSEN1ΔE9/c-Abl-KO (APP/PS1/c-Abl KO) mice had improved performance in hippocampus-dependent tasks than the APP/PS1 mice. Interestingly, APP/PS1/c-Abl KO mice null for c-Abl or APP/PS1 mice fed with neurotinib showed better performance in hippocampus-dependent tasks and reduced brain amyloid burden.

Altogether, our results suggest that c-Abl exerts an important role in the loss of hippocampal-dependent memory in AD. Moreover, we show that c-Abl is a relevant player in AD pathology and that its absence is beneficial for AD, strengthening the use of c-Abl inhibitors as potential disease-modifying drugs for this neurodegenerative disorder and validating neurotinib as a suitable preclinical development candidate for the treatment of AD.

2. Materials and methods

2.1. Animals

Animals were housed in a temperature and humidity-controlled room (22 ± 2°C) with food and water *ad libitum*. c-Abl-KO mice ($Abl^{loxP/loxP}$/Nestin-CRE) mice were bred from $Abl^{loxP/loxP}$ (these floxed mutant mice possess loxP sites flanking exon 5 of the *Abl1* gene) mice with Nestin-CRE+ mice (Jackson Laboratory), resulting in a brain-specific c-Abl conditional knock-out mouse. This strain originated and was maintained on a mixed B6.129S4, C57BL/6 background and did not display any gross physical or behavioral abnormalities. The APPswe/PSEN1ΔE9 mice were purchased from Jackson Laboratory (Bar Harbor, ME, United States), number 34829-JAX. The trade name B6;C3-Tg(APPswe,PSEN1dE9)85Dbo/Mmjax and genetic background is C57BL/6;C3H (Finnie et al., 2017).

To obtain the four genotypes used in this work, we initially crossed APPswe/PSEN1ΔE9 mice with $Abl^{loxP/loxP}$ mice, resulting in APPswe/PSEN1ΔE9/$Abl^{loxP/loxP}$ mice. Then the APPswe/PSEN1ΔE9/$Abl^{loxP/loxP}$ mice were bred with $Abl^{loxP/loxP}$/Nestin-CRE mice, resulting in the four genotypes of interest: APPswe/PSEN1ΔE9/$Abl^{loxP/loxP}$ mice (APP/PS), APPswe/PSEN1ΔE9/$Abl^{loxP/loxP}$/Nestin-CRE mice (APP/PS1/Abl-KO), $Abl^{loxP/loxP}$ mice (WT), and $Abl^{loxP/loxP}$/Nestin-CRE mice (c-Abl-KO). PCR was used to confirm the genotypes of all animals. The animal study protocol #170616008 was approved by the Bioethics and Care of Laboratory Animals Committee of the Pontificia Universidad Católica de Chile and CIBEM.

2.2. Neurotinib diet administration

16-month-old WT and APP/PS1 mice began being fed a control diet or diet containing 67 ppm of neurotinib. At 20-month-old the animals started sequential cognitive tests with resting periods between tests, during which the respective diets were maintained until mice were sacrificed and tissues collected for immunofluorescence. The mice were fed with control or neurotinib (patent number

WO2019/173761 A1) containing diet *ad libitum*. The rodent diet was manufactured by Envigo/Teklad (Madison, Wisconsin) by incorporation of neurotinib ppm at 67 ppm into the NIH-31 Open Formula Mouse/Rat Sterilizabile Diet (7017), followed by irradiation handling of the final product.

2.3. Behavioral testing

Before behavioral testing, all animals were familiarized with the testing room, and the tests were performed from less anxiogenic to most anxiogenic (Open Field, Novel Object Recognition, Object Location Memory, Barnes maze, Memory Flexibility, Morris water maze), between 3 days from each other to let the animals rest.

2.3.1. Open field, novel object recognition, and object location memory tests

The task procedure consisted of three sessions: habituation, sample, and test. The habituation session was repeated on two consecutive days. On the first habituation day, we recorded animals' performance in the Open Field, an empty space in which mice are allowed to freely move for 10 min while being recorded, used to evaluate the general activity levels, such as exploration habits and locomotor activity (Seibenhener and Wooten, 2015). The identical to-be-familiarized objects were placed in the apparatus during the sample session. The animal was positioned at the wall's midpoint opposite the sample objects. After the sample-object exposure time (10 min), the animal was removed and returned to its home cage. The test session was performed 24 h after the sample day. One familiar object and a novel object were placed in the apparatus (Figure 1B). The testing session lasted for 5 min. The exploration time of both objects was measured, and the recognition index (RI) was calculated as the time spent exploring the novel object relative to the total time spent exploring both objects. RI above 0.5 means that the animal can differentiate the novel object from de familiar one. On the other hand, RI below 0.5 means that the animal cannot distinguish between objects.

The task procedure of the OLM is like the NOR procedure. The difference is that one object is displaced to a new position in the test session (Figure 1A). In the OLM, the RI is interpreted as the animal's capacity to recognize the displaced object. Another difference with the NOR is that the OLM task has intra-maze visual cues. The maze used to perform Open Field, NOR, and OLM tests was a gray acrylic rectangular box (46°×°27 cm). Objects used in the NOR and OLM tests were previously equilibrated (to avoid innate preference) and were distinct in each test.

2.3.2. Barnes maze

In this test, animals should learn and remember the location of an escape hole in an anxiogenic, elevated, and illuminated circular open field (Barnes, 1979; Toledo and Inestrosa, 2010). The maze is a white circular platform of 70 cm diameter elevated at 70 cm from the floor with 20 equally spaced holes along the perimeter (7 cm diameter each) located at 2 cm from the platform's edge. The platform has 20 equally spaced holes along the perimeter. Visual cues were located on the walls of the room. A black plexiglass escape box (17 × 13 × 7 cm) was located under one of the holes. The maze was illuminated with two incandescent lights to yield a light level of ~600 lux impinging on the circular platform. The location of the escape box was consistent for a given mouse but randomized across mice (Figure 1C). Each mouse was given four daily trials with an intertrial interval (ITI) of 15 min for four consecutive days. The mouse was placed in the start box for every training trial for 10 s, with the room lights turned off. After time had elapsed, the chamber was lifted, the lights turned on, and the mouse was free to explore the maze. The session ended when the mouse found the hole and entered the escape box or after 3 min. When the mouse entered the escape box, the lights were turned off, and the mouse remained in the dark for 1 min before the next trial began. If the mouse did not find the escape box within 3 min, the experimenter guided the mouse to the escape. We measured latency to enter the escape box (Negrón-Oyarzo et al., 2015).

2.3.3. Morris water maze, memory flexibility, and open field tests

MWM (Morris, 1984) consisted of a round pool made of white plastic of 100 cm diameter, filled to 16 cm depth with water maintained at 19–21°C and colored with white dye to hide the platform. The platform was transparent acrylic (9 cm diameter) in the corresponding quadrant center. Briefly, mice were trained to find the platform three times at different quadrants for 8 days. Animals that found the platform within 60 s were allowed to remain on the platform for 30 s. Those that did not were manually placed on the platform for 30 s.

The MF was performed as described by Toledo and Inestrosa (2010). Each animal was trained in a circular water maze for 4 days. Each day, the platform was changed to the next subsequent quadrant. The animal was considered to finish the training when reaching the criterion: three consecutive trials with an escape latency of 20 s on each training day, up to 15 trials. Once finished testing, the animal was removed from the maze, dried, and returned to its cage.

2.3.4. Data collection

The BM, OLM, and NOR behavioral tests were carried out in the Behavioral Room at the Animal Care facility of the Centro de Investigaciones Médicas (CIM) Each mouse was recorded with a video camera (ImageLab, model CB3200) fixed above the behavioral apparatus. Videos were acquired by Lab View software and analyzed offline using the idTracker video-tracking software (Pérez-Escudero et al., 2014) and Matlab for the analyses. The MWM and MF tests were performed in the Behavioral Room at the Departamento de Biología Celular y Molecular, PUC. The videos were acquired and analyzed using the ANY-maze video tracking system.

2.4. Immunofluorescence staining

Mice were anesthetized with a mix of xylazine, ketamine, and acepromazine (4:4:1), then perfused with a peristaltic bomb (Velp Scientifica SP311) with 100 mL of ice-cold PBS and later with 50 mL of PFA 4%. Brains were removed and post-fixed with PFA 4% at 4°C O/N, followed by Sucrose 30% in PBS at 4°C O/N. Brains were cut into a cryostat (Leica CM1850) with 25 µm coronal sections.

Immunofluorescence was done on floating sections. Sections from different brain areas were selected, mainly the hippocampus and prefrontal cortex, and washed with PBS 1X for 10 min. Sections were permeabilized with Triton X-100 0.4% for 30 min. Then, incubated with Glycine 0.15 M for 15 min and fresh $NaBH_4$ 10 mg/mL for 15 min, washed with PBS 1X for 10 min, and incubated with NH_4Cl 50 mM for 10 min. Sections were incubated with blocking solution (Triton X-100 0.4% + BSA 3%) for 1 h, and O/N with

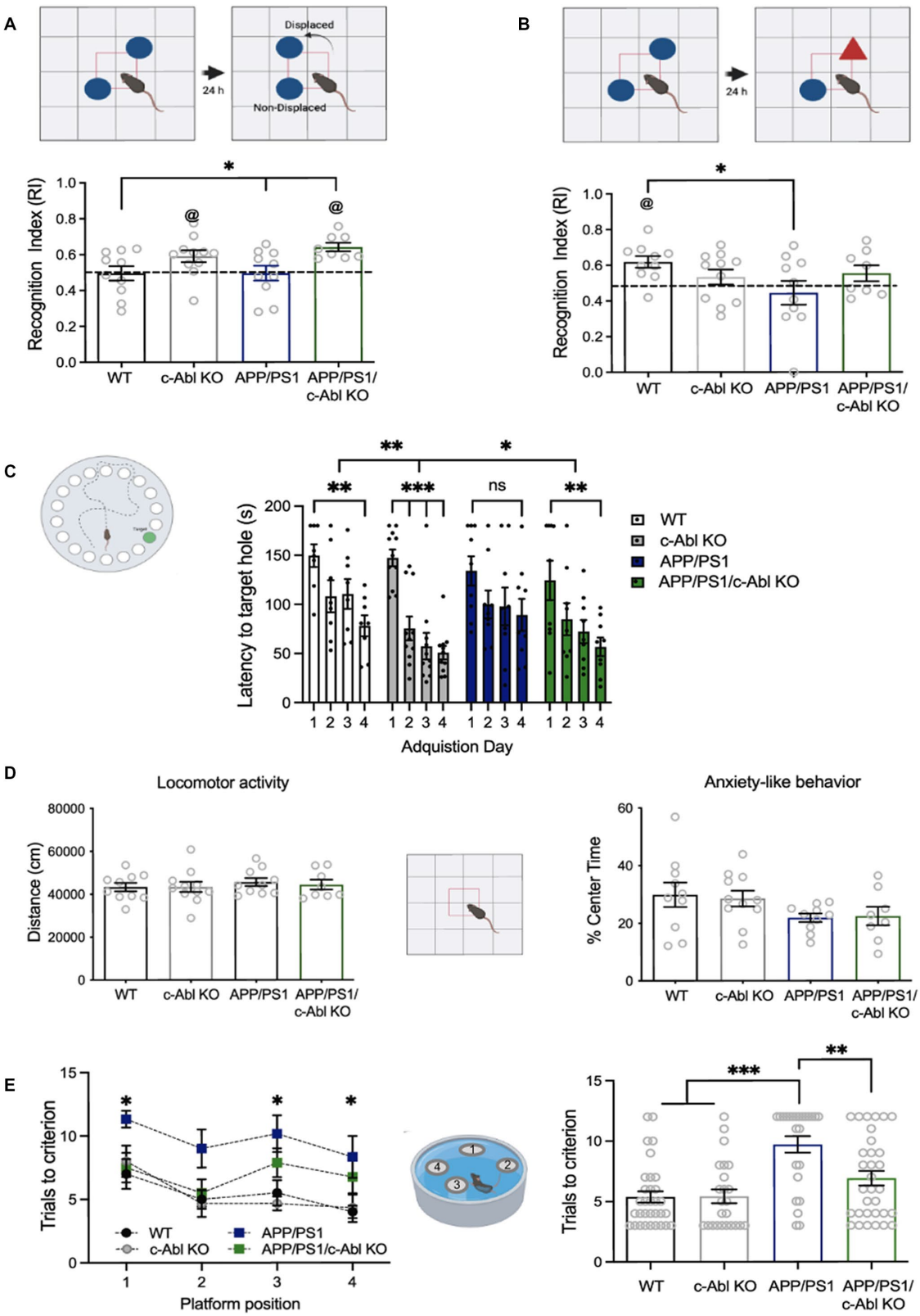

FIGURE 1
c-Abl absence improves behavioral performance in hippocampus-dependent tasks. 10-month-old wild-type (WT), c-Abl conditional knock-out mice (c-Abl KO), and AD mice either WT for c-Abl (APP/PS1) or knock-out for c-Abl (APP/PS1/c-Abl KO) were sequentially subjected to learning tasks as indicated by each cartoon. **(A)** Object Location Memory test. The graph shows the time spent on the relocated object compared to the total exploration time. APP/PS1 vs. APP/PS1/c-Abl KO $p=0.0506$ Tukey's *post-hoc* test. Two-way ANOVA $p^{**}=0.0024$ genotype effect, Tukey's multiple comparison test @ $p<0.05$ vs. chance level (0.5). **(B)** Novel Object Recognition test. Graph shows the time spent smelling the new object, compared with total exploration time. APP/PS1 vs. APP/PS1/c-Abl KO $p=0.4407$ Tukey's *post-hoc* multiple comparison test. Two-way ANOVA $p=0.0552$ genotype

(Continued)

FIGURE 1 (Continued)
and APP condition effect; @ $p<0.05$ vs. chance level (0.5). **(C)** Graph shows the time spent finding the target hole each day of the Barnes maze test. Two-way ANOVA $p^{**}=0.0054$ genotype effect, $p^{***}<0.0001$ acquisition day effect, Tukey's *post-hoc* multiple comparison test. **(D)** Open Field tests. In each case, the bar shows the percent of time spent exploring the center zone (Anxiety-like behavior, $p=0.7625$) and the distance traveled during the whole exploratory time (basal locomotor activity, $p=0.7690$). Two-way ANOVA, Tukey's *post-hoc* multiple comparison test. Same $n=10$ WT, 10 APP/PS1, 8 APP/PS1/c-Abl KO, and 11 c-Abl KO animals on each test. **(E)** Memory flexibility test of 10-month-old mice. Left: graph show the number of mice attempts to find the platform in each position at different training days. Asterisks indicate WT vs. APP/PS1 significance through training days (1st day $p=0.0419$, 3rd day $p=0.0242$, 4th day $p=0.0419$; APP vs. APP/PS1/c-Abl KO 1st day $p=0.089$, 3rd day $p=0.4904$, 4th day $p=0.7607$). Two-way ANOVA, $p=0.0063$ training day's effect, $p<0.0001$ genotype effect, Tukey's multiple comparison test. Right: graph shows the total number of trials to reach the learning criterion for each group. Two-way ANOVA genotype and trials needed effect: $p=0.0164$. $n=8$ WT, 6 APP/PS1, 8 APP/PS1/c-Abl KO, and 6 c-Abl KO animals. Data are presented as mean±SEM. $p^{*}<0.05$.

primary antibody anti-WO2 (Millipore, MABN10), NeuN (ab177487, Abcam), Sox2 (Cell Signaling, 3728S), Doublecortin (Santa Cruz Biotechnology, sc-271,390) or GFAP (GA5, Cell Signaling, 3670S) (all 1:1000 dilution) at 4°C. The next day, sections were washed 3×10 min, and incubated with anti-mouse 488, the AlexaFluor-conjugated secondary antibody (1:1,000 dilution) for 2 h RT, and Hoechst staining for nuclei visualization. Once finished, the sections were washed 3°×°15 min per time and mounted on a slide.

Fluorescence images were captured under a Zeiss Axioscope 5 microscope. Images were always acquired using the same settings and quantified using ImageJ (Fiji).

2.5. Statistics

Data sets were tested for normality using the Kolmogorov–Smirnov test and then compared with the appropriate test. All statistical tests were performed using GraphPad Prism 8 software (GraphPad Software, San Diego, CA, United States). When corresponding, the behavior, plaque's area, and number were analyzed using one-way ANOVA, two-way ANOVA, three-way ANOVA, Tukey's *post-hoc* test, and one-sample *t*-test, as indicated in each figure. All statistical assessments were considered significant when $p < 0.05$. All data are expressed as mean ± SEM.

3. Results

We have shown that the absence of c-Abl (c-Abl KO) in the brain improves the performance of mice in learning tasks involving spatial memory (González-Martin et al., 2021). To assess the effect of brain-specific genetic ablation of c-Abl on the cognitive performance of 10-month-old AD mice, we carried on a battery of behavioral tests mainly depending on hippocampal activity. Tests were performed sequentially, first Open Field to control locomotor activity and anxiety, followed by Object Location Memory (OLM) and Novel Object Recognition (NOR) which are less stressful tests, and then the Barnes Maze (BM).

We used the OLM task to evaluate spatial memory (Murai et al., 2007). Here, we used the factor Recognition Index (RI) to evaluate the mice's capacity to recognize the displaced object. As expected, 10-month-old APP/PS1 mice cannot recognize the displaced object (RI: 0.49). Unexpectedly, aged WT mice neither recognized the displaced object (RI: 0.49). Indeed, 4-month-old WT mice recognized the displaced object (Supplementary Figure S1A, RI: 0.60). Thus, this cognitive impairment was associated with mice aging. Interestingly, both aged c-Abl KO and APP/PS1/c-Abl KO mice were able to identify the displaced object (RI: 0.59 and 0.64, respectively). Moreover, there is a significant difference between APP/PS1/c-Abl KO and APP/PS1 groups (Figure 1A).

Literature suggests that adult neurogenesis is reduced in AD in both humans and mice (Babcock et al., 2021), and that the generation of new adult neurons in the dentate gyrus (DG) of the hippocampus specifically, in the subgranular zone (SGZ), affects rat's performance in behavioral tasks like the NOR (Jessberger et al., 2009). Indeed, it has been described that adult neurogenesis is important for learning and memory (Cancino et al., 2013; Toda et al., 2019). During aging, recognition memory is affected as young, middle-aged and senile rats have compromised object location and recognition-associated memory with marked decrease of adult-born immature neurons in the DG (Canatelli-Mallat et al., 2022). Thus, we addressed adult neurogenesis in brain slices by immunofluorescence for the neural stem cell marker Sox2, and the newly-born neuronal marker DCX (doublecortin) (Supplementary Figure S2), and found no positive cells in aged groups (10 and 22-month-old mice). We also used 3-month-old WT mice as a positive control for neurogenesis, and, as expected, found Sox2+ or DCX+ cells in the SGZ, that were consistently lost in AD mice; further suggesting that the behavioral improvement observed during conditional ablation or pharmacological inhibition of c-Abl is independent of adult neurogenesis.

Therefore, the absence of c-Abl improves a subset of spatial memory: remembering objects and their position in space. Even healthy mice conditionally knock-out for c-Abl in the brain had improved performance (González-Martin et al., 2021). These data indicate that c-Abl absence improves spatial learning and memory performance in AD mice.

To dissect if c-Abl affects hippocampal-associated learning, we also carried out the NOR test, a hippocampus-independent test that evaluates rodents' recognition memory where the factor RI means the recognition of a novel object (Antunes and Biala, 2012). We found that WT mice could recognize the novel object (RI: 0.62). However, APP/PS1, c-Abl KO (RI: 0.53), and APP/ PS1/c-Abl KO (RI: 0.55) mice did not recognize novelty (Figure 1B). According to previous reports, WT vs. APP/PS1 (RI: 0.44) groups were significantly different, indicating that AD mice had a deficit in the NOR tests ($p=0.0315$) (Zhang et al., 2012). Our data indicate that c-Abl absence does not improve recognition memory in APP/c-Abl KO-aged animals.

Interestingly, when we evaluated mice behavior in the BM we found that c-Abl absence in APP/PS1 mice reduced the memory decline (Sunyer et al., 2007). The BM is a hippocampus-dependent

task assessing rodents' spatial learning and memory; in which the latency to the escape hole was measured for 4 days. A significant difference between the first and the next 3 days is a learning indicator. Here, we found that WT mice effectively learned the location of the escape hole, showing a significant reduction in latency between the first and the fourth day (149.6 and 78.2 s, respectively, $p^{**} = 0.0047$). In contrast, APP/PS1 mice were unable to learn (1st day: 134.1 s, 4th day: 89.3 s, $p = 0.1110$) (Figure 1C, Supplementary Figure S1B). Interestingly, c-Abl KO mice showed a marked reduction in latency since day two (1st day: 147.2 s, 2nd day: 75.5 s, $p^{***} = 0.0006$, 4th day: 50.9 s, $p^{***} < 0.0001$) (Figure 1C). APP/PS1/c-Abl KO mice also showed a significantly reduced latency between the first day and day four (1st day: 124.4 s, 4th day: 56.8 s, $p^{**} = 0.0044$). The APP/PS1/c-Abl KO and c-Abl KO group presented a better learning performance and showed lower latency than the WT group in the whole test regardless of the acquisition day (Figure 1C).

Finally, the mice's general motor activity was assessed as control using an Open Field test (Seibenhener and Wooten, 2015), where the animal explored an empty arena. We did not find any differences between groups in locomotor activity measured as traveled distance ($p = 0.7625$) or the time spent in the center zone as an indicator for anxiety-like behavior ($p = 0.7690$), discarding any motor disability or basal stress (Figure 1D). Thus, the differences shown here are just the product of cognitive processes.

To confirm that c-Abl genetic ablation reduces the hippocampal-dependent memory deficits in AD mice we used a new set of mice and applied the Memory Flexibility (MF) test, which is a variation of the Morris Water Maze (MWM) as it has been seen to be more sensitive to hippocampal dysfunction in older mice (Chen et al., 2000). We measured the number of trials to reach the learning criterion over 4 days. As expected, APP/PS1/c-Abl KO mice performed better than APP/PS1 mice, which took more trials to learn the platform's position on a single experimental day (Figure 1E, left). We found that WT mice needed fewer trials (5.38 ± 0.63 trials from 15 daily trials), while APP/PS1 mice needed almost all attempts (9.71 ± 0.66 trials per day) to reach the criterion. Similar to the WT group, c-Abl KO mice needed a few trials to reach the criterion (5.42 ± 0.86 trials per day). More importantly, the APP/PS1/c-Abl KO mice needed almost half of the total trials to reach the criterion (6.91 ± 0.52 trials per day) and were no different from WT (Figure 1E, right). With this more sensitive test, we observed a clear effect of c-Abl absence in AD preventing cognitive decline.

Altogether, our results suggest that the effect of c-Abl absence on cognition is selective, mostly impacting memories that depend on the hippocampus.

3.1. A neurotinib diet improves hippocampal-dependent memory in AD, the same as c-Abl absence in AD

To continue our investigation, we assessed spatial learning and memory in AD mice, both conditional knock-out for c-Abl in the brain or fed with neurotinib, a recently designed and disclosed allosteric c-Abl inhibitor with improved CNS permeability (Marin et al., 2022), to perform additional hippocampus-dependent tests.

In mice, neurotinib has preferential distribution toward CNS reaching single-digit micromolar levels in the brain and a t½ in the range of 8 h upon oral gavage administration at 12.5 mg/kg. Similar single-digit micromolar levels are constantly maintained in the brain after supplementing the molecule in the chaw diet at 67 ppm for 2 weeks, equivalent to daily ingestion of 12.5 mg/kg of neurotinib (Marin et al., 2022, Supplementary Figure S5). Therefore, to approximate our study to the AD clinical testing and pharmaceutical approach, we evaluated "elder" mice as considered by JAX laboratory around 18–24 months old, similar to 56–69 years human (Flurkey et al., 2007), after feeding them for a total of 6 months with a neurotinib-containing diet.

As before, we sequentially performed the learning tasks: Open Field to control locomotor activity and anxiety, followed by NOR, less stressful tests. Then the MWM, a task broadly used to evaluate spatial memory, and finally the more sensitive MF test (Figure 2A). As for the genetic ablation of c-Abl in AD mice, we found no significant difference among groups in animals fed with neurotinib when we evaluated recognition memory in the NOR test (Figure 2B). Like APP/PS1/c-Abl KO animals (Figure 1B), we found no changes in the time spent recognizing novelty in neurotinib-fed WT or APP/PS1-aged fed mice (RI: 0.59 and 0.54, respectively, $p = 0.9129$). Therefore, neither c-Abl ablation nor neurotinib improves mice's performance in hippocampus-independent tasks.

We then performed the MWM, a task broadly used to evaluate spatial memory (Morris, 1984; Vorhees and Williams, 2006), in which amyloid pathology causes impaired performance in 12-month-old mice (Lalonde et al., 2005), and found that WT mice had significantly reduced escape latency across training days than APP/PS1 (5th day 12.21 ± 2.0 s vs. 34.77 ± 5.0 s, $p^{*} = 0.0104$; 8th day 8.23 ± 2.6 s vs. 31.61 ± 5.9 s, respectively, $p^{*} = 0.0217$) (Figure 2C). APP/PS1 mice displayed poor performance, while neurotinib-fed APP/PS1 mice significantly reduced escape latency across training days (5th day 16.15 ± 3.8 s, $p^{*} = 0.0477$; 8th day 14.78 ± 1.8 s, $p = 0.0958$). No differences were found among WT, WT-neurotinib, and APP/PS1-neurotinb groups since day 3 of the MWM test. Interestingly, WT-neurotinib mice had no differences from WT mice (5th day 12.20 ± 1.6 s, $p > 0.9999$; 8th day 11.34 ± 1.3 s, $p = 0.7241$), meaning that the neurotinib diet did not modify basal performance in WT mice (Figure 2C).

Importantly, the MF analysis for APP/PS1-neurotinib-fed mice showed the same trend as the MF for APP/PS1/c-Abl KO (Figure 1E). Interestingly, in the MF mice had to find the hidden platform in a different location each day. Thus, at day 4, APP/PS1-neurotinib fed mice showed short-term memory improvements (1st vs. 4th-day trial $p^{*} = 0.0353$), and behaved significant different from APP/PS1 mice ($p^{**} = 0.0027$) (Figure 1D, left). We also found that WT-neurotinib-fed mice and WT mice needed fewer trials to reach the criterion (5.5 ± 0.3 and 5.1 ± 0.3 trials, respectively), while APP/PS1 mice needed 2-times more trials (10.9 ± 0.6 trials) to reach the criterion (Figure 2D, right). More interestingly, APP/PS1-neurotinib-fed mice needed significantly fewer trials to reach the hidden platform than APP/PS1 mice to reach the criterion (8.1 ± 0.6 trials) (Figure 2D, right). As in BM and OLM tests, the MF data suggest that c-Abl absence or its inhibition improves hippocampus-dependent memory.

As before, we used the Open Field test for mice's general motor activity assessment and found no differences in their anxiety-like behavior ($p = 0.1385$, Figure 2E, left). Overall, mice's locomotor activity was not affected by the neurotinib diet ($p = 0.7167$). The APP/PS1 model showed hyperactivity as animals were prone to walk around and away from the center; a characteristic described for APP

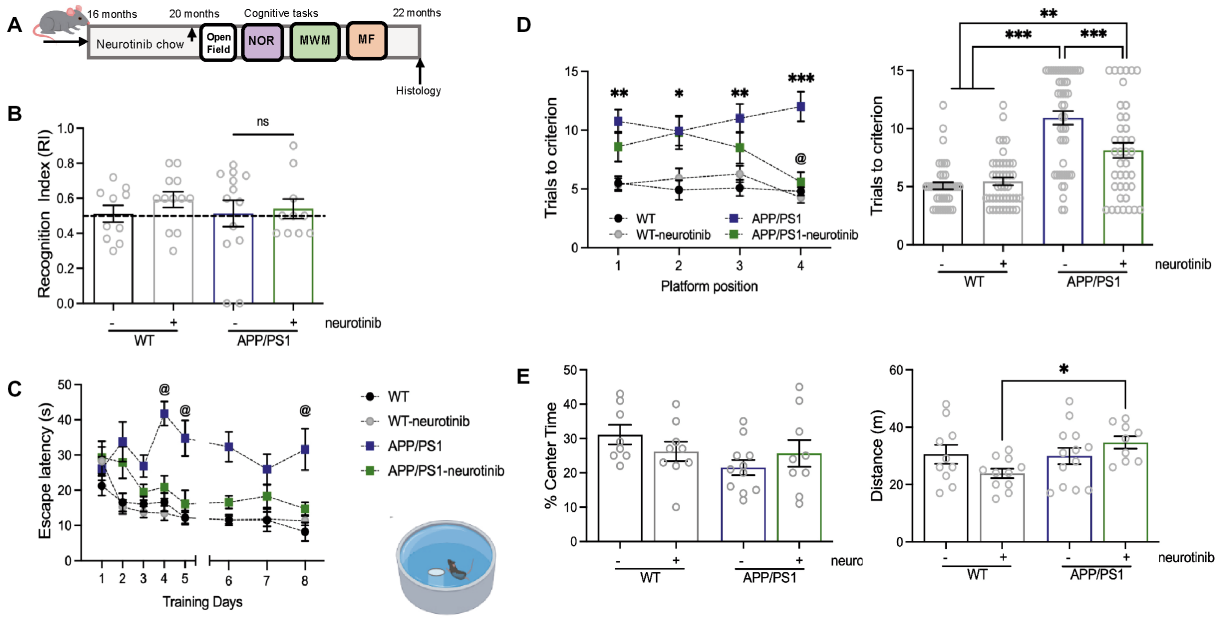

FIGURE 2
c-Abl absence and neurotinib-diet improve the cognitive performance of AD mice in hippocampus-dependent tasks. **(A)** WT and APP/PS1 mice were fed for 4 months with a control diet or diet containing 67ppm of neurotinib before starting the cognitive tests. At 20-month-old, mice were subjected to learning tasks with resting periods between them, and maintenance of *ad libitum* respective diets until tissues were collected. **(B)** Novel Object Recognition test. Graph shows the time spent around the new object, compared to the total exploration time. The dotted line represents the chance. Two-way ANOVA genotype effect: p=0.9573, treatment effect: p=0.5689. **(C)** Morris Water Maze test. Graph shows the time to find the platform during 8-training days (escape latency) @ mean significantly different from 0.5. α: days in which APP/PS1 is different in comparison to another group. Three-way ANOVA, Tukey *post-hoc* multiple comparison test, genotype effect: p<0.0001, treatment effect: p=0.0361, day: p<0.0001, days × treatment: p=0.0237. **(D)** Graphs show the memory flexibility task results as the number of attempts to find the platform in each position at different training days (left), and the number of trials to reach the learning criterion for each group (right, treatment and acquisition day effect p=0.1195, neurotinib effect p<0.0001). Significance was annotated for APP/PS1 vs. WT mice (1st day p**=0.0016, 2nd day p**=0.016, 3rd day p**=0.0033, 4th day p**=0.0033). @ mean significant different between APP/PS1 vs. APP/PS1-neurotinib fed mice p**=0.0027. Two-way ANOVA, Tukey's *post-hoc* multiple comparison test. **(E)** Open field test for anxiety-like behavior (left, p=0.8962) and locomotor activity evaluation (right, p=0.7167) of neurotinib-fed mice. Bar shows the percent of time spent exploring the center zone, and the distance traveled during the whole exploratory time. Two-way ANOVA, Tukey *post-hoc* multiple comparison test: WT-neurotinib vs. APP/PS1-neurotinib: p*=0.0378. Same n=10 WT-control diet, 12 APP-control diet, 11 WT-neurotinib diet, and 10 APP-neurotinib fed animals for each test. Data are shown as mean±SEM.

animals with the APP Swedish and PSEN1 mutation (Lalonde et al., 2005). Similarly, APP/PS1-neurotinib fed mice traveled longer distances (34.67 ± 2.2 m) (Figure 2E, right). However, WT-neurotinib fed mice traveled a few meters of the empty arena in the same amount of time (23.82 ± 1.6 m, p^* = 0.0378), in correlation with their reduced walking speed (Supplementary Figure S3). Further suggesting increased hyperactivity for the APP/PS1-neurotinib fed mice instead of motor affections with the chow.

Altogether, the data presented here indicate that treating an animal model of AD with high brain penetrant c-Abl inhibitor neurotinib improves memory performance in a hippocampus-dependent task, replicating the same pattern observed in the AD mice model knock-out for c-Abl.

3.2. APP/PS1/Abl-KO mice and neurotinib-fed mice have reduced accumulation of Aβ plaques in the brain

It has been shown that c-Abl overexpression in the mouse brain is responsible for gliosis and neuronal loss (Schlatterer et al., 2011), which can be further detrimental in AD. Thus, we analyzed the pathological hallmarks of AD: Aβ aggregation, astrogliosis, and neuronal loss in relation to the genetic ablation of c-Abl and neurotinib-diet. As expected, 10-month-old APP/PS1 mice brain sections involving the brain cortex and hippocampus showed widespread Aβ accumulation as WO2-positive amyloid plaques (Figure 3A, p < 0.0001) compared with WT and c-Abl KO control animals. Also, APP/PS1 mice had important astrogliosis followed by GFAP-positive cells (Figure 3C, p^{***} < 0.0001). Interestingly, APP/PS1/c-Abl KO mice display significantly less number of WO2-positive amyloid plaques, with reduced area in the brain (APP/PS1: 224 ± 40.6 mm² vs. APP/PS1/c-Abl KO: 107.5 ± 16.2 mm², p^{**} = 0.0048) (Figure 3A, left). Also, less astrocytosis, at similar basal levels of c-Abl KO and WT mice (c-Abl KO: 68 ± 5.0 astrocytes/ mm²; APP/PS1: 100 ± 3.2 vs. APP/PS1/c-Abl KO: 76.25 ± 2.1 astrocytes/mm², p^{**} = 0.0031) (Figure 3C). Thus, data suggest that the absence of c-Abl could reduce the Aβ burden in the AD mice model.

Studies in APP/PS1 mice and AD patients treated with c-Abl inhibitors like imatinib and nilotinib diminished Aβ deposits in the brain and blood (Cancino et al., 2008; Estrada et al., 2016; Turner et al., 2020). As before, we analyzed similar brain sections of APP/PS1 control and neurotinib-fed mice and found a significant reduction in the amount and area of WO2-positive amyloid plaques

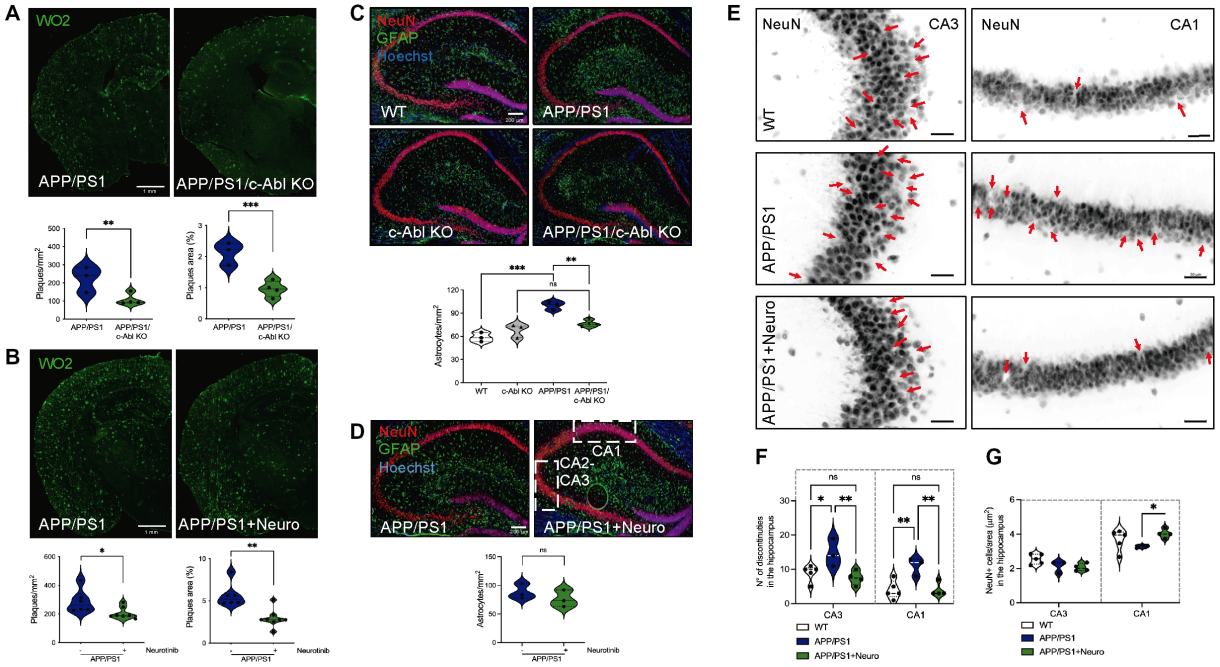

FIGURE 3
c-Abl absence and inhibition reduced amyloid-beta burden, neuroinflammation, and reduced neuronal loss in the APP/PS1 mice model of AD. **(A,B)** Representative immunofluorescences from coronal brain sections stained with WO2 antibody for amyloid-beta plaques in green. Graph shows the number of amyloid-beta plaques per mm^2 and the percentage area of each plaque in relation to the cortex and hippocampus brain area. *n*=4 animals, 2 slices per genotype or treatment. Scale bar=1mm. **(A)** 10-month-old APP/PS1 and APP/PS1/c-Abl KO mice, *n*=3–4 animals per genotype. Two-way ANOVA, *post-hoc* Tukey's multiple comparison test, p^{**}=0.0073 for plaques/mm^2, left; p^{***}=0.0005 for plaques area (%), right. **(B)** 22-month-old APP/PS1 mice fed with control or neurotinib diet. Non-parametric Mann–Whitney *t*-test p^{*}=0.0350 for plaques/mm^2, left; p^{**}=0.0040 for plaques area (%), right. **(C,D)** Representative immunofluorescences from coronal brain sections for the astrocyte marker GFAP (green), NeuN marker for neurons in the hippocampus (red), and the nucleus (Hoechst, blue). Graphs show the number of astrocytes per mm^2. *n*=3–4 animals per genotype or treatment. Scale bar=200µm. **(C)** 10-month-old WT, c-Abl KO, APP/PS1, and APP/PS1/c-Abl KO mice. Two-way ANOVA, *post-hoc* Tukey's multiple comparison test, c-Abl absence effect *p*=0.0651. c-Abl KO vs. APP/PS1/c-Abl KO *p*=0.3509. **(D)** 22-month-old APP/PS1 mice fed with control or neurotinib diet. Non-parametric Mann–Whitney *t*-test *p*=0.4. **(E)** Same immunofluorescences for the neuronal marker in **(D)**, NeuN, of 22-month-old mice fed with control or neurotinib diet are presented in grayscale. Red arrows indicate the discontinuities found in the CA3 and CA1 areas of the hippocampus augmented from the coronal brain sections shown in **(D)** (dotted white square). *n*=3–5 animals per condition. Scale bar=10µm. **(F)** Graph shows the number of discontinuities in the CA3 or CA1 hippocampi. Two-way ANOVA, *post-hoc* Tukey's multiple comparison test, p^{***}=0.0001 treatment effect. **(G)** Graph shows the total number of NeuN$^+$ positive cells counted and normalized per CA3 or CA1 areas (µm^2). Two-way ANOVA, *post-hoc* Tukey's multiple comparison test, *p*=0.1335 treatment effect. Data are presented as mean±SEM. p^{***}<0.0001.

(APP/PS1: 288 ± 33 mm^2 vs. APP/PS1 + neurotinib: 205.7 ± 15.9 mm^2, p^{*} = 0.0350) (Figure 3B). Although no differences were found in the amount of GFAP-positive cells (Figure 3D, *p* = 0.4), APP/PS1 seem to have more GFAP-positive cells when compared with WT controls, but again, non-significant in the reduced sample analyzed (Supplementary Figure S4, *p* = 0.0571).

Finally, we analyzed the neuronal loss using the NeuN marker for mature neurons in APP/PS1 mice fed with the control or neurotinib-supplemented chow (Figure 3E). No differences were found in the dentate gyrus of the hippocampus (Supplementary Figure S5). As expected, the hippocampi of APP/PS1 animals showed an increased number of discontinuities in CA1–CA3 areas (CA1: WT: 4 ± 1.2 vs. APP/PS1: 11 ± 1.5, p^{**} = 0.0046) (Figures 3E,F). Interestingly, APP/PS1-neurotinib fed mice had reduced neuronal loss, similar to WT levels (CA1: 4 ± 1, p^{**} = 0.0065). In accordance, the number of NeuN$^+$ cells per CA1 area was maintained (CA1: APP/PS1: 3.3 ± 0.1 vs. APP/PS1 + neurotinib: 4.03 ± 0.3 cells/µm^2, p^{*} = 0.0442) (Figures 3E–G). The number of NeuN$^+$ cells was not altered in the hippocampi CA3 area (*p* = 0.9621).

Altogether, our results have shown a positive effect of the allosteric inhibitor for c-Abl, neurotinib, over the AD pathology displayed by aged 22-month-old APP/PS1 mice, further validating c-Abl as a key player in the development of AD pathology and cognitive impairment of AD.

4. Discussion

Herein we have found that the genetic ablation and inhibition of c-Abl improves the cognitive performance in hippocampus-dependent tasks of AD and healthy mice. The hippocampus plays a crucial role in learning, memory, and spatial navigation and is the first structure to show senile plaques and tau tangles, parameters correlated with AD patients' cognitive decline (Lane et al., 2018). Thus, our work encourages research of c-Abl as a feasible candidate for memory improvement in AD.

Previous reports have shown that deficiency of some proteins activated in the AD brain that are linked with the progression of AD pathology can reduce the memory alterations characteristic of transgenic mouse models of AD. Active caspase-6 is associated with

AD pathological lesions and is present at the early stages of tangle formation. Behavioral examinations of the 5xFAD mouse AD model with caspase-6-KO showed improved spatial learning, memory, and anxiety/risk assessment behavior (Angel et al., 2020). The p75 neurotrophin receptor (p75NTR) has been increasingly co-localized with hyperphosphorylated tau in AD brains, and one report shows that p75NTR-KO diminished the MWM latency in AD mice (Mañucat-Tan et al., 2019). The PLD1 ablation and chronic inhibition using a well-tolerated PLD1-specific small molecule inhibitor prevent the progression of synaptic dysfunction during early stages in the 3xTg-AD mouse model (Bourne et al., 2019).

As widely reported in the literature, the APP/PS1 model displayed a notorious deficiency in recognition memory and different components of spatial memory (Figure 1, Sierksma et al., 2014; Cheng et al., 2019; Li et al., 2019). Nevertheless, the new model, APP/PS1/c-Abl KO mice, has significantly improved performance in all spatial memory tests, indicating that c-Abl absence attenuates AD-associated memory impairment.

When c-Abl was inhibited with neurotinib in a daily diet, none of our groups showed differences in the NOR test nor APP/PS1/c-Abl KO mice. All groups displayed similar values near the chance. WTs spent 11 s on average in the familiar object and 13 s in the novel object. APP/PS1 spent 16 s on average in the familiar object and 23 s in the novel object. Further suggesting that their natural curiosity behavior is unexpected at 22 months old. As seen by Yang et al. (2019), aging severely impacts working memory recognition in 19–21 months old mice. This result was not unpredictable since the NOR test evaluates recognition and working memory and the central brain region involved in the perirhinal cortex (Antunes and Biala, 2012). Microinjections of anisomycin, a protein synthesis inhibitor, in the perirhinal cortex impaired the NOR test. However, the same injection on the hippocampus does not alter recognition memory (Balderas et al., 2008). On another hand, BM is a well-known hippocampus-dependent task that evaluates spatial learning and memory (Barnes, 1979) as well as the MF test (Chen et al., 2000). Therefore, it is very interesting that in the absence of c-Abl, prominently expressed in the hippocampus and cerebellum (Experiment Detail: Allen Brain Atlas: Mouse Brain, n.d.), APP/PS1 mice overcome the characteristic memory impairment of AD. On the 4th day of the BM, WT vs. APP/PS1 latency was 78.2 vs. 89.3 s; with mice behaving differently among both groups. When we dissected their behavioral response to the BM, we found that the 8 WTs behave evenly in a range of 119.5–36.3 s. Only one did not learn the location of the escape hole (Supplementary Figure S1B, gray). While APP/PS1 mice were divided into two populations: 4 mice from 179.3–114 s, a group that did not learn the location of the escape hole; and one population of 4 mice that indeed learned the location of the escape hole with a latency of 71 to 34 s. However, we have considered one mouse that started well but did not learn (Supplementary Figure S1B, light blue), as behavior followed Gaussian distribution. APP/PS1 mice showed variable responses that suggest adding new animals, as we cannot also discard that 10-month-old APP/PS1 mice could be at different stages of the pathology; effect that might cause the differences observed in APP/PS1 population.

c-Abl-KO 4-month-old young mice displayed improved memory performance in the MWM and BM (González-Martin et al., 2021). Similarly, 10-month-old c-Abl KO mice still performed better than WT mice, even in the APP/PS1 model. Interestingly, we show that old WT mice do not recognize the displaced object in the OLM test, but c-Abl KO does. It has been described that hippocampal function declines age-dependently, and WT-aged mice performed worse than WT-young in the OLM test (Murai et al., 2007; Wimmer et al., 2012). Since the c-Abl KO mice recognized the displaced object, not like the age-matched group, it suggests that c-Abl absence reverts the impairment associated with aging, but its absence or kinase activity did not alter adult neurogenesis as a factor for memory improvement. Further, the impairment presented in aged WT mice in the OLM test could be related to task characteristics. The OLM relies on an animal's innate preference for novelty without additional external reinforcement (Denninger et al., 2018). BM and MF tests use negative external reinforcement to promote spatial learning. In each case, rodents seek an escape from an aversive situation, exposed on a brightly-lit platform or immersed in water, respectively (Denninger et al., 2018). Thus, the cognitive decline observed in the WT group performing the OLM is a typical feature of aged WT mice, abolished in more challenging tasks.

Studies with c-Abl inhibitors have shown improvement in the cognitive status of animal models of AD (Cancino et al., 2008; Estrada et al., 2016; La Barbera et al., 2021). Our laboratory previously showed that treatment with the c-Abl inhibitor, imatinib, reduces path length and escape latency in the MWM of Aβ fibrils injected in rat's hippocampi and APP/PS1 mice (Cancino et al., 2008). Also, imatinib prevented LTP impairment induced by Aβ oligomers in hippocampal slices (Vargas et al., 2014). Other authors have also shown amelioration of the AD phenotype with nilotinib, which is perceived to be the most CNS penetrating c-Abl inhibitor among the FDA-approved drugs (Turner et al., 2020; La Barbera et al., 2021). However, while animal evaluation of FDA-approved c-Abl inhibitors can be carried out at high doses, clinically observed on-target and off-target toxicities limit the maximal human-tolerated doses for these drugs. Cerebrospinal fluid data upon 6-month administration of nilotinib at its maximal daily tolerated dose during the clinical evaluation with AD patients indicated that this drug is only able to achieve CNS levels 10–20 times below its IC50 against c-Abl, pointing toward severe limitations for the use of FDA-approved c-Abl inhibitors to treat neurodegenerative disorders (Turner et al., 2020). To address this liability, here we evaluate a novel allosteric c-Abl inhibitor, neurotinib, with high brain penetration at a low dose and found that AD mice fed with this inhibitor had reduced escape latency and required fewer trials to reach the learning criterion, improving the cognitive decline impairments seen in AD mice (Figure 2).

The extracellular accumulation of Aβ plaques is a significant histopathological marker of AD (Atwood and Bowen, 2015) as the increased neuroinflammation and astrogliosis are presented in AD mouse models and patients (Schlatterer et al., 2011). In correlation with memory improvements, we have found that APP/PS1/c-Abl KO mice had significantly fewer amyloid plaques and astrogliosis than APP/PS1 in the brain cortex and hippocampus. The same was observed in neurotinib-fed mice (Figures 3A–D). Since c-Abl activity regulates the APP proteolytic processing (Yáñez et al., 2016), and its inhibition has been correlated with the decrease of amyloid burden in *in vivo* models of AD (Cancino et al., 2008; Estrada et al., 2016), a reduction of Aβ toxic species could underlie the reduction in memory impairments of AD mice. On the other hand, Aβ oligomeric species are the first to produce synaptic dysfunction by damaging dendritic spines and removing synaptic contacts (Gomez-Isla et al., 2008; Viola and Klein, 2015). In this context, we have seen that c-Abl participates

in synaptic contact removal, increasing susceptibility to AβOs damage (Vargas et al., 2014; Gutiérrez et al., 2019). The resilience given by c-Abl absence might be present in aging and AD as 10-month-old mice showed differences (Supplementary Figure S1). However, it remains to be addressed. Also, it has been recently reported that the inhibition of ABL family leads to increased synaptic strength, especially since $A\beta_{1\text{-}42}$ species reduce spontaneous synaptic activity (Reichenstein et al., 2021). Moreover, the expression of active c-Abl in adult mouse forebrain neurons leads to neuronal loss, neuroinflammation, and interferon signaling pathways activation, especially, in the CA1 region of the hippocampus (Schlatterer et al., 2011, 2012). Interestingly, our results showed that inhibiting c-Abl with neurotinib protects neurons from damage, maintaining levels of $NeuN^+$ cells similar to WTs, in correlation with fewer discontinuities in the CA1–CA3 regions of the hippocampus (Figures 3E–G).

These results fully support c-Abl as a feasible therapeutic target for AD and validate neurotinib as a preclinical development candidate.

Data availability statement

The datasets presented in this study can be found in online repositories. The names of the repository/repositories and accession number(s) can be found at: 10.6084/m9.figshare.22217734.

Ethics statement

The animal study was reviewed and approved by Bioethics and Care of Laboratory Animals Committee of the Pontificia Universidad Católica de Chile and CIBEM. The animal study protocol #170616008 was approved by the Bioethics and Care of Laboratory Animals Committee of the Pontificia Universidad Católica de Chile and CIBEM.

Author contributions

RL, PF, and AÁ contributed to the conception and design of the study. RL and CP performed all the learning tests in APP/PS1 x c-Abl animals. CM and NE analyzed data from learning tests. CP performed all the experiments in neurotinib-fed mice. AD synthesized the neurotinib chow. CP and CR performed WO2 and GFAP immunofluorescences. BC and GC performed DCX and Sox2 immunofluorescences. CF, DC, and AG-M generate the APP/PS1/c-Abl KO transgenic mice strain. RL and DG wrote the first version of the manuscript and discussed the results. DG analyzed data and generated the figures. JM and SZ wrote sections of the manuscript.

Funding

This work was supported by the Agencia Nacional de Investigación y Desarrollo (ANID): Fondecyt grant [1201668 (AÁ)], Fondecyt [grants 1190334 and 1230337 (SZ)], Fondecyt [grant 1210507 (GC)], Fondef [grant ID21I10347 (AÁ, SZ)], Fondef [grant D10E1077 (AÁ, SZ)], Program ICM-ANID-ICN2021 045 (AÁ). Part of this work was supported by intramural funding of the National Center for Advancing Translational Sciences.

Acknowledgments

The authors thank the Advanced Microscopy Facility UMA UC, and the CIBEM Facility for animal housing and care. Cartoons for learning tasks were created with BioRender.com.

Conflict of interest

The authors declare that the research was conducted in the absence of any commercial or financial relationships that could be construed as a potential conflict of interest.

Neurotinib is under the patent WO2019/173761 A1.

Publisher's note

Supplementary material

The Supplementary material for this article can be found online at: https://www.frontiersin.org/articles/10.3389/fnagi.2023.1180987/full#supplementary-material

References

Aghel, N., Delgado, D., and Lipton, J. H. (2017). Cardiovascular toxicities of BCR-ABL tyrosine kinase inhibitors in chronic myeloid leukemia: preventive strategies and cardiovascular surveillance. *Vasc. Health Risk Manag.* 13, 293–303. doi: 10.2147/VHRM.S108874

Alvarez, A. R., Sandoval, P. C., Leal, N. R., Castro, P. U., and Kosik, K. S. (2004). Activation of the neuronal c-Abl tyrosine kinase by amyloid-beta-peptide and reactive oxygen species. *Neurobiol. Dis.* 17, 326–336. doi: 10.1016/j.nbd.2004.06.007

Angel, A., Volkman, R., Royal, T. G., and Offen, D. (2020). Caspase-6 knockout in the 5xFAD model of Alzheimer's disease reveals favorable outcome on memory and neurological hallmarks. *Int. J. Mol. Sci.* 21:1144. doi: 10.3390/ijms21031144

Antunes, M., and Biala, G. (2012). The novel object recognition memory: neurobiology, test procedure, and its modifications. *Cogn. Process.* 13, 93–110. doi: 10.1007/s10339-011-0430-z

Atwood, C. S., and Bowen, R. L. (2015). A unified hypothesis of early- and late-onset Alzheimer's disease pathogenesis. *JAD* 47, 33–47. doi: 10.3233/JAD-143210

Babcock, K. R., Page, J. S., Fallon, J. R., and Webb, A. E. (2021). Adult hippocampal neurogenesis in aging and in Alzheimer's disease. *Stem Cell Rep.* 16, 681–693. doi: 10.1016/j.stemcr.2021.01.019

Balderas, I., Rodriguez-Ortiz, C. J., Salgado-Tonda, P., Chavez-Hurtado, J., McGaugh, J. L., and Bermudez-Rattoni, F. (2008). The consolidation of object and context recognition memory involve different regions of the temporal lobe. *Learn. Mem.* 15, 618–624. doi: 10.1101/lm.1028008

Barnes, C. A. (1979). Memory deficits associated with senescence: a neurophysiological and behavioral study in the rat. *J. Comp. Physiol. Psych.* 93, 74–104. doi: 10.1037/h0077579

Bourne, K. Z., Natarajan, C., Perez, C. X. M., Tumurbaatar, B., Taglialatela, G., and Krishnan, B. (2019). Suppressing aberrant phospholipase D1 signaling in 3xTg

Alzheimer's disease mouse model promotes synaptic resilience. *Sci. Rep.* 9:18342. doi: 10.1038/s41598-019-54974-6

Canatelli-Mallat, M., Chiavellini, P., Lehmann, M., Goya, R. G., and Morel, G. R. (2022). Age-related loss of recognition memory and its correlation with hippocampal and perirhinal cortex changes in female Sprague Dawley rats. *Behav. Brain Res.* 435:114026. doi: 10.1016/j.bbr.2022.114026

Cancino, G. I., Perez de Arce, K., Castro, P. U., Toledo, E. M., von Bernhardi, R., and Alvarez, A. R. (2011). C-Abl tyrosine kinase modulates tau pathology and Cdk5 phosphorylation in AD transgenic mice. *Neurobiol. Aging* 32, 1249–1261. doi: 10.1016/j.neurobiolaging.2009.07.007

Cancino, G. I., Toledo, E. M., Leal, N. R., Hernandez, D. E., Yévenes, L. F., Inestrosa, N. C., et al. (2008). STI571 prevents apoptosis, tau phosphorylation and behavioural impairments induced by Alzheimer's β-amyloid deposits. *Brain* 131, 2425–2442. doi: 10.1093/brain/awn125

Cancino, G. I., Yiu, A. P., Fatt, M. P., Dugani, C. B., Flores, E. R., Kaplan, D. R., et al. (2013). p63 regulates adult neural precursor and newly born neuron survival to control hippocampal-dependent behavior. *J. Neurosci.* 33, 12569–12585. doi: 10.1523/JNEUROSCI.1251-13.2013

Chandía-Cristi, A., Stuardo, N., Trejos, C., Leal, N., Urrutia, D., Bronfman, F. C., et al. (2023). C-Abl tyrosine kinase is required for BDNF-induced dendritic branching and growth. *IJMS* 24:1944. doi: 10.3390/ijms24031944

Chen, K. S., Knox, J., Inglis, J., Bernard, A., Martin, S. J., Morris, R. G. M., et al. (2000). A learning deficit related to age and b-amyloid plaques in a mouse model of Alzheimer's disease. *Nature* 408, 975–979. doi: 10.1038/35050103

Cheng, W. H., Martens, K. M., Bashir, A., Cheung, H., Stukas, S., Wellington, C. L., et al. (2019). CHIMERA repetitive mild traumatic brain injury induces chronic behavioural and neuropathological phenotypes in wild-type and APP/PS1 mice. *Alz Res Therapy* 11:6. doi: 10.1186/s13195-018-0461-0

Davies, C. A., Mann, D. M., Sumpter, P. Q., and Yates, P. O. (1987). A quantitative morphometric analysis of the neuronal and synaptic content of the frontal and temporal cortex in patients with Alzheimer's disease. *J. Neurol. Sci.* 78, 151–164. doi: 10.1016/0022-510x(87)90057-8

Denninger, J. K., Smith, B. M., and Kirby, E. D. (2018). Novel object recognition and object location behavioral testing in mice on a budget. *J. Vis. Exp.* 141:e58593. doi: 10.3791/58593

Estrada, L. D., Chamorro, D., Yañez, M. J., Gonzalez, M., Leal, N., Alvarez, A. R., et al. (2016). Reduction of blood amyloid-β oligomers in Alzheimer's disease transgenic mice by c-Abl kinase inhibition. *JAD* 54, 1193–1205. doi: 10.3233/JAD-151087

Experiment Detail: Allen Brain Atlas: Mouse Brain. (n.d.). Available at: https://mouse.brain-map.org/experiment/show?id=68844474.

Finnie, G. S., Gunnarsson, R., Manavis, J., Blumbergs, P. C., Mander, K. A., Finnie, J. W., et al. (2017). Characterization of an 'amyloid only' transgenic (B6C3-Tg(APPswe, PSEN1dE9)85Dbo/Mmjax) mouse model of Alzheimer's disease. *J. Comp. Pathol.* 156, 389–399. doi: 10.1016/j.jcpa.2017.03.001

Flurkey, K., Currer, J. M., and Harrison, D. E. (2007) in *The mouse in biomedical research*. eds. J. G. Fox, S. W. Barthold, M. T. Davisson, C. E. Newcomer, F. W. Quimby and A. L. Smith, vol. *3. 2nd* ed (New York: Elsevier), 637–672. Available at: mouseion.jax.org/stfb2000_2009/1685

Gomez-Isla, T., Spires, T., De Calignon, A., and Hyman, B. T. (2008). Neuropathology of Alzheimer's disease. *Handb. Clin. Neurol.* 89, 233–243. doi: 10.1016/S0072-9752(07)01222-5

González-Martin, A., Moyano, T., Gutiérrez, D. A., Carvajal, F. J., Cerpa, W., Alvarez, A. R., et al. (2021). C-Abl regulates a synaptic plasticity-related transcriptional program involved in memory and learning. *Prog. Neurobiol.* 205:102122. doi: 10.1016/j.pneurobio.2021.102122

González-Zuñiga, M., Contreras, P. S., Estrada, L. D., Chamorro, D., Villagra, A., Alvarez, A. R., et al. (2014). C-Abl stabilizes HDAC2 levels by tyrosine phosphorylation repressing neuronal gene expression in Alzheimer's disease. *Mol. Cell* 56, 163–173. doi: 10.1016/j.molcel.2014.08.013

Greuber, E. K., Smith-Pearson, P., Wang, J., and Pendergast, A. M. (2013). Role of ABL family kinases in Cancer: from leukemia to solid tumors. *Nat. Rev. Cancer* 13, 559–571. doi: 10.1038/nrc3563

Gutiérrez, D. A., Chandía-Cristi, A., Yáñez, M. J., Zanlungo, S., and Álvarez, A. R. (2023). C-Abl kinase at the crossroads of healthy synaptic remodeling and synaptic dysfunction in neurodegenerative diseases. *Neural Regen. Res.* 18, 237–243. doi: 10.4103/1673-5374.346540

Gutiérrez, D. A., Vargas, L. M., Chandia-Cristi, A., de la Fuente, C., Leal, N., and Alvarez, A. R. (2019). C-Abl deficiency provides synaptic resiliency against Aβ-oligomers. *Front. Cell. Neurosci.* 13:526. doi: 10.3389/fncel.2019.00526

Hsia, A. Y., Masliah, E., McConlogue, L., Yu, G. Q., Tatsuno, G., Mucke, L., et al. (1999). Plaque-independent disruption of neural circuits in Alzheimer's disease mouse models. *Proc. Natl. Acad. Sci. U. S. A.* 96, 3228–3233. doi: 10.1073/pnas.96.6.3228

Jessberger, S., Clark, R. E., Broadbent, N. J., Clemenson, G. D. Jr., Consiglio, A., Lie, D. C., et al. (2009). Dentate gyrus-specific knockdown of adult neurogenesis impairs spatial and object recognition memory in adult rats. *Learn. Mem.* 16, 147–154. doi: 10.1101/lm.1172609

Jing, Z., Caltagarone, J., and Bowser, R. (2009). Altered subcellular distribution of c-Abl in Alzheimer's disease. *JAD* 17, 409–422. doi: 10.3233/JAD-2009-1062

Jones, S. B., Lu, H. Y., and Lu, Q. (2004). Abl tyrosine kinase promotes dendrogenesis by inducing actin cytoskeletal rearrangements in cooperation with rho family small GTPases in hippocampal neurons. *J. Neurosci.* 24, 8510–8521. doi: 10.1523/JNEUROSCI.1264-04.2004

Khatri, A., Wang, J., and Pendergast, A. M. (2016). Multifunctional Abl kinases in health and disease. *J. Cell Sci.* 129, 9–16. doi: 10.1242/jcs.175521

Knopman, D. S., Amieva, H., Petersen, R. C., Chételat, G., Holtzman, D. M., Jones, D. T., et al. (2021). Alzheimer disease. *Nat. Rev. Dis. Primers.* 7:33. doi: 10.1038/s41572-021-00269-y

La Barbera, L., Vedele, F., Nobili, A., Krashia, P., Spoleti, E., D'Amelio, M., et al. (2021). Nilotinib restores memory function by preventing dopaminergic neuron degeneration in a mouse model of Alzheimer's disease. *Prog. Neurobiol.* 202:102031. doi: 10.1016/j.pneurobio.2021.102031

Lalonde, R., Kim, H. D., Maxwell, J. A., and Fukuchi, K. (2005). Exploratory activity and spatial learning in 12-month-old APP695SWE/co+PS1/ΔE9 mice with amyloid plaques. *Neurosci. Lett.* 390, 87–92. doi: 10.1016/j.neulet.2005.08.028

Lane, C. A., Hardy, J., and Schott, J. M. (2018). Alzheimer's disease. *Eur. J. Neurol.* 25, 59–70. doi: 10.1111/ene.13439

Li, C., Shi, J., Wang, B., Li, J., and Jia, H. (2019). CB2 cannabinoid receptor agonist ameliorates novel object recognition but not spatial memory in transgenic APP/PS1 mice. *Neurosci. Lett.* 707:134286. doi: 10.1016/j.neulet.2019.134286

Mañucat-Tan, N. B., Shen, L. L., Bobrovskaya, L., Al-hawas, M., Zhou, F. H., Wang, Y. J., et al. (2019). Knockout of p75 neurotrophin receptor attenuates the hyperphosphorylation of tau in pR5 mouse model. *Aging* 11, 6762–6791. doi: 10.18632/aging.102202

Marin, T., Dulcey, A. E., Campos, F., Castro, J., Pinto, C., Zanlungo, S., et al. (2022). C-Abl activation linked to autophagy-Lysosomal dysfunction contributes to neurological impairment in Niemann-pick type a disease. *Front. Cell Dev. Biol.* 10:844297. doi: 10.3389/fcell.2022.844297

Morris, R. (1984). Developments of a water-maze procedure for studying spatial learning in the rat. *J. Neurosci. Methods* 11, 47–60. doi: 10.1016/0165-0270(84)90007-4

Murai, T., Okuda, S., Tanaka, T., and Ohta, H. (2007). Characteristics of object location memory in mice: behavioral and pharmacological studies. *Physiol. Behav.* 90, 116–124. doi: 10.1016/j.physbeh.2006.09.013

Negrón-Oyarzo, I., Neira, D., Espinosa, N., Fuentealba, P., and Aboitiz, F. (2015). Prenatal stress produces persistence of remote memory and disrupts functional connectivity in the hippocampal -prefrontal cortex axis. *Cerebral Cortex* 25, 3132–3143. doi: 10.1093/cercor/bhu108

Pérez-Escudero, A., Vicente-Page, J., Hinz, R. C., Arganda, S., and de Polavieja, G. G. (2014). idTracker: tracking individuals in a group by automatic identification of unmarked animals. *Nat. Methods* 11, 743–748. doi: 10.1038/nmeth.2994

Reichenstein, M., Borovok, N., Sheinin, A., Brider, T., and Michaelevski, I. (2021). Abelson kinases mediate the depression of spontaneous synaptic activity induced by amyloid Beta 1-42 peptides. *Cell. Mol. Neurobiol.* 41, 431–448. doi: 10.1007/s10571-020-00858-7

Schlatterer, S. D., Suh, H. S., Conejero-Goldberg, C., Chen, S., Acker, C. M., Lee, S. C., et al. (2012). Neuronal c-Abl activation leads to induction of cell cycle and interferon signaling pathways. *J. Neuroinflammation* 9:208. doi: 10.1186/1742-2094-9-208

Schlatterer, S. D., Tremblay, M. A., Acker, C. M., and Davies, P. (2011). Neuronal c-Abl overexpression leads to neuronal loss and neuroinflammation in the mouse forebrain. *J Alz Dis.* 25, 119–133. doi: 10.3233/JAD-2011-102025

Seibenhener, M. L., and Wooten, M. C. (2015). Use of the open field maze to measure Locomotor and anxiety-like behavior in mice. *JoVE* 96:e52434. doi: 10.3791/52434

Sierksma, A. S. R., van den Hove, D. L. A., Pfau, F., Philippens, M., Bruno, O., Prickaerts, J., et al. (2014). Improvement of spatial memory function in APPswe/PS1dE9 mice after chronic inhibition of phosphodiesterase type 4D. *Neuropharmacology* 77, 120–130. doi: 10.1016/j.neuropharm.2013.09.015

Sunyer, B., Patil, S., Frischer, C., Höger, H., Selcher, J., Brannath, W., et al. (2007). Strain-dependent effects of SGS742 in the mouse. *Behav. Brain Res.* 181, 64–75. doi: 10.1016/j.bbr.2007.03.025

Toda, T., Parylak, S. L., Linker, S. B., and Gage, F. H. (2019). The role of adult hippocampal neurogenesis in brain health and disease. *Mol. Psychiatry* 24, 67–87. doi: 10.1038/s41380-018-0036-2

Toledo, E. M., and Inestrosa, N. C. (2010). Activation of Wnt signaling by lithium and rosiglitazone reduced spatial memory impairment and neurodegeneration in brains of an APPswe/PSEN1ΔE9 mouse model of Alzheimer's disease. *Mol. Psychiatry* 15, 272–285. doi: 10.1038/mp.2009.72

Turner, R. S., Hebron, M. L., Lawler, A., Mundel, E. E., Yusuf, N., Moussa, C., et al. (2020). Nilotinib effects on safety, tolerability, and biomarkers in Alzheimer's disease. *Ann. Neurol.* 88, 183–194. doi: 10.1002/ana.25775

Vargas, L. M., Leal, N., Estrada, L. D., González, A., Serrano, F., and Alvarez, A. R. (2014). EphA4 activation of c-Abl mediates synaptic loss and LTP blockade caused by amyloid-β oligomers. *PLoS One* 9:e92309. doi: 10.1371/journal.pone.0092309

Viola, K. L., and Klein, W. L. (2015). Amyloid b oligomers in Alzheimer's disease pathogenesis, treatment, and diagnosis. *Acta Neuropathol.* 129, 183–206. doi: 10.1007/s00401-015-1386-3

Vorhees, C. V., and Williams, M. T. (2006). Morris water maze: procedures for assessing spatial and related forms of learning and memory. *Nat. Protoc.* 1, 848–858. doi: 10.1038/nprot.2006.116

Walsh, D. M., and Selkoe, D. J. (2004). Deciphering the molecular basis of memory failure in Alzheimer's disease. *Neuron* 44, 181–193. doi: 10.1016/j.neuron.2004.09.010

Wang, J. Y. (2014). The capable ABL: what is its biological function? *Mol. Cell. Biol.* 34, 1188–1197. doi: 10.1128/MCB.01454-13

Wimmer, M. E., Hernandez, P. J., Blackwell, J., and Abel, T. (2012). Aging impairs hippocampus-dependent long-term memory for object location in mice. *Neurobiol. Aging* 33, 2220–2224. doi: 10.1016/j.neurobiolaging.2011.07.007

Yáñez, M. J., Belbin, O., Estrada, L. D., Leal, N., Contreras, P. S., Lleó, A., et al. (2016). c-Abl links APP-BACE1 interaction promoting APP amyloidogenic processing in Niemann-Pick type C disease. *Biochem. Biophys. Acta.* 1862, 2158–2167.

Yang, W., Zhou, X., and Ma, T. (2019). Memory decline and behavioral inflexibility in aged mice are correlated with Dysregulation of protein synthesis capacity. *Front. Aging Neurosci.* 11:246. doi: 10.3389/fnagi.2019.00246

Zhang, X. G., Wang, S., Zhang, L., Shi, C., and Xie, X. (2012). Novel object recognition as a facile behavior test for evaluating drug effects in AβPP/PS1 Alzheimer's disease mouse model. *JAD* 31, 801–812. doi: 10.3233/JAD-2012-120151

Zukas, A. M., and Schiff, D. (2018). Neurological complications of new chemotherapy agents. *Neuro-Oncology* 20, 24–36. doi: 10.1093/neuonc/nox115

Frontiers in
Aging Neuroscience

Explores the mechanisms of central nervous system aging and age-related neural disease

The third most-cited journal in the field of geriatrics and gerontology, with a focus on understanding the mechanistic processes associated with central nervous system aging.

Discover the latest Research Topics

See more →

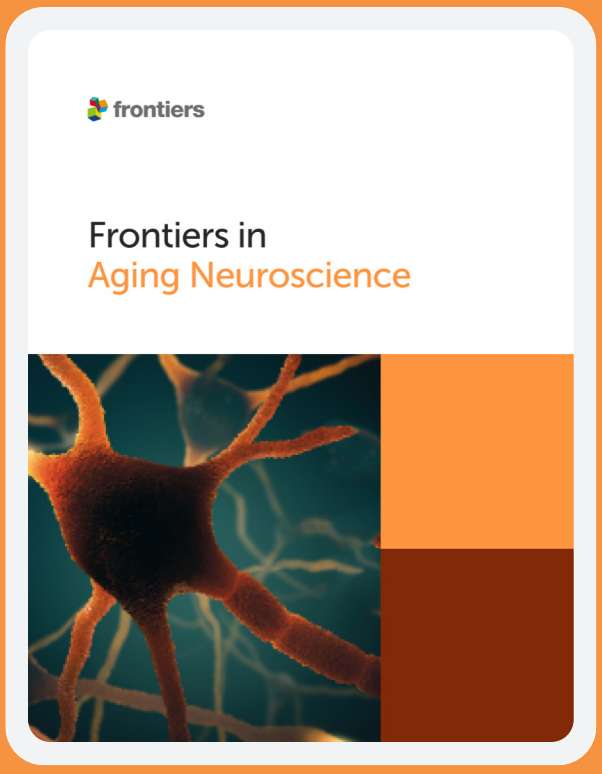

Frontiers

Avenue du Tribunal-Fédéral 34
1005 Lausanne, Switzerland
frontiersin.org

Contact us

+41 (0)21 510 17 00
frontiersin.org/about/contact